Energy Reconstruction in Highly Granular Calorimeters for Future Electron-Positron Colliders

DISSERTATION

by

YASMINE ISRAELI

Max-Planck-Institut für Physik

Munich, October 2018

Fakultät für Physik der

TECHNISCHE
UNIVERSITÄT
MÜNCHEN

Energy Reconstruction in Highly Granular Calorimeters for Future Electron-Positron Colliders

Yasmine Israeli

Vollständiger Abdruck der von der Fakultät für Physik der Technischen Universität München zur Erlangung des akademischen Grades eines

Doktors der Naturwissenschaften (Dr. rer. nat.)

genehmigten Dissertation.

Vorsitzender: Prof. Dr. Andreas Weiler
Prüfende der Dissertation:
1. Hon.-Prof. Dr. Allen C. Caldwell
2. Prof. Dr. Elisa Resconi

Die Dissertation wurde am 31.10.2018 bei der Technischen Universität München eingereicht und durch die Fakultät für Physik am 24.01.2019 angenommen.

To Jerry

ABSTRACT

Future linear electron-positron colliders offer a unique opportunity to precisely study the particles and interactions described by the Standard Model and to search for new physics beyond it. Two accelerator concepts are currently under investigation: the International Linear Collider (ILC) and the Compact LInear Collider (CLIC). More futuristic concepts investigate the possibility of using plasma wakefield accelerators for a further upgrade of the collision energy in these future linear colliders.

For precision measurements at future linear colliders, the CALICE collaboration develops different imaging calorimeters with high granularity. Among the CALICE physics prototypes are the silicon-tungsten electromagnetic calorimeter, the scintillator-SiPM based analog hadron calorimeter and the scintillator-steel tail catcher and muon tracker. These prototypes were operated together as a combined calorimeter system in hadron beams at the CERN and FNAL test beam facilities. In this thesis, the performance of the combined system in terms of energy response and energy resolution is investigated.

The energy reconstruction is performed with a standard reconstruction method based on calibrated sub-detector energy sums and a software compensation (SC) method making use of the local energy density information provided by the high granularity of the detectors. The results obtained with the SC method show an improvement in the energy resolution of up to 30% compared to the standard reconstruction results. These results are comparable to the ones achieved for data with showers starting only in the AHCAL and therefore demonstrate the success of the inter-calibration of the different sub-systems, despite their different geometries and different readout technologies. In addition, with SC reconstruction, results obtained from GEANT4-based detector simulations are compatible with the results obtained from data.

The last part of the thesis discusses the concept of plasma wakefield acceleration as an acceleration alternative in the further future. A preliminary study performed by means of particle-in-cell simulations demonstrates an energy gain of approximately 2 GeV in half a meter when using this technique.

TABLE OF CONTENTS

CHAPTER 1

INTRODUCTION

The *Standard Model of Particle Physics*, which describes all fundamental particles known today and their interactions, has been established and confirmed by a wide range of experiments in the past 50 years. This has culminated in the discovery of the Higgs boson in 2012, which completed the experimental observation of all particles in the Standard Model. Despite this remarkable success, there is overwhelming observational evidence that the Standard Model alone is insufficient, motivating a continuing study of particles and interactions in high-energy physics experiments.

At present, the most powerful collider in the world is the *Large Hadron Collider (LHC)*, colliding hadrons at a center-of-mass energy of 13 TeV. A high energy lepton collider would complement the LHC physics program, providing more precise measurements. In collisions of elementary particles the initial states and the precise collision energies are well defined, leading to a model independent interpretation of measurements. For collisions at the TeV-scale, a linear electron-positron collider is the preferred alternative, due to inherently limited energy reach of circular accelerators. Two accelerator concepts are being considered for this purpose: the *International Linear Collider (ILC)* and the *Compact Linear Collider (CLIC)*.

Exploiting the full potential of such a collider requires a large multi-purpose detector with unprecedented resolutions for achieving the best possible measurement precision. Of great importance is the performance of the calorimeter system, which is responsible for measuring the particle energies and the overall energy flow. This system is divided into electromagnetic and hadronic calorimeters, which target different particle types, and are typically characterized by a relatively poor energy resolution for hadrons.

In order to measure jet energies to around 3% to 4% precision, a modern approach has been developed for combining the measurements of the tracking system and the calorimeters, aiming at a separate reconstruction of each particle in a jet. This approach, referred to as the *Particle Flow Algorithm (PFA)*, requires calorimeter systems with high spatial granularity. Several calorimeter prototypes optimized for the application of PFAs have been developed by the *Calorimeter for Linear Collider Experiment (CALICE)* collaboration. The performance of a calorimeter system consisting of three of CALICE prototypes – an electromagnetic calorimeter, a hadronic calorimeter and a tail catcher and muon tracker – is presented in this thesis.

The CALICE calorimeter system has been operated in test beam experiments at *Conseil Européen pour la Recherche Nucléaire (CERN)* in 2007 and at *Fermi National Accelerator Laboratory, Batavia IL, USA (FNAL)* in 2008. The detection of hadron data with the system is investigated thoroughly in this thesis, using several reconstruction schemes for studying the hadronic energy resolution: a standard reconstruction method based on calibrated sub-detector energy sums, and three *Software Compensation* (SC) reconstruction schemes making use of the local energy density information provided by the high granularity of the detectors. The performance of the system has been studied as well with GEANT4-based detector simulations for testing the robustness of the reconstruction methods and validating the simulation models. The obtained results demonstrate the feasibility of a full 4π detector system of the same technologies as well as the possible performance achievable with each of the reconstruction schemes.

The *High Energy Physics (HEP)* research demands for increasingly high energy collisions. For this reason, it is expected that a further increase of the collision energy of linear colliders will be required in the future. Since the common acceleration techniques are limited to acceleration gradients of about 100 MV/m, such an upgrade would required either the extension of the acceleration paths or the use of alternative acceleration methods which can achieve higher acceleration gradients. The latter option is being investigated by the development of *Plasma Wakefield Accelerators (PWFAs)*, in which electric fields associated with electron plasma waves are used to accelerate electron beams with much higher acceleration gradients, in the order of $10-100$ GV/m. An acceleration scheme that includes a PWFA after the conventional linear accelerator might be a viable option for increasing the beam energies in linear colliders, leading to a substantial increase in the collision energies.

This thesis is structured as follows. Chapter 2 gives a brief introduction to the Standard Model and an overview of modern experimental techniques for producing and detecting elementary particles. A description of particle interactions with matter and the basics of calorimetry are given in chapter 3. The combined calorimeter system of CALICE prototypes is introduced in chapter 4, which details the system readout technologies, the prototype structures and the test beam experiment facilities. Chapter 5 describes the selection of pion events from the data recorded in both test beam experiments. The calibration of the detector signals to an energy scale and the different reconstruction methods are detailed in chapter 6. In chapter 7 the results of the data analysis are presented and compared with previous analyses. A detailed study of simulated events and its comparison to real-data results is given in chapter 8. Finally, the concept of plasma wakefield acceleration is presented in chapter 9, including a preliminary study of a PWFA implementation in a *Free Electron Laser (FEL)* design.

CHAPTER 2

INTRODUCTION TO HIGH ENERGY PHYSICS

Elementary particle physics has achieved remarkable progress during the last 50 years in investigating the fundamental structure of matter. The currently best description of the constituents of matter and three of the four known forces is given by the Standard Model of particle physics. The Standard Model has predicted a wide range of phenomena, nearly all of which have been validated and confirmed by means of particle physics experiments. Besides experiments with cosmic rays, particle accelerators emerged as the tool par excellence to discover and create new components of matter, allowing for testing the predictions of the Standard Model and for searching for signatures of new physics. Modern experiments at particle accelerators are equipped with an advanced detection system, covering much of the solid angle around the collision point.

This chapter gives a short overview of HEP, introducing the Standard Model as well as modern experimental possibilities for acceleration and detection of particles.

2.1 The Standard Model of Particle Physics

The Standard Model of particle physics is a successful theoretical framework which classifies all known subatomic particles and describes their interactions. The model emerged in the 1960s and the 1970s from the incorporation of the *Quantum Electrodynamics (QED)* theory [1], the *Glashow-Weinberg-Salam (GWS)* theory of electroweak processes [2–4] and the *Quantum Chromodynamics (QCD)* theory [5].

The Standard Model includes 24 elementary particles and anti-particles with spin $\frac{1}{2}$ that follow Fermi-Dirac statistics. These particles form all known matter − the *fermions*. The fermions are divided into two groups: *leptons* and *quarks*. Each group consists of 3 generations of particles, ordered by increasing particles' mass. In addition, to each particle in a group corresponds an anti-particle with the same mass but with opposite quantum numbers.

Leptons are classified via their electric charge (-1,0,1) and their lepton family numbers (electron number, muon number, tau number). The negative charged leptons are: *electron* (e^-), *muon* (μ^-) and *tau* (τ^-), whereas the positively charged ones are the anti-leptons: *positron* (e^+), *anti-muon* (μ^+) and *anti-tau* (τ^+). The electrically neutral leptons are: *neutrinos* (ν_e, ν_μ *and* ν_τ) and *anti-neutrinos*

$(\bar{\nu}_e, \bar{\nu}_\mu \text{ and } \bar{\nu}_\tau)$. The only stable leptons are the electron, the neutrinos and their anti-leptons, muons and taus decay with a mean lifetime of 2.2×10^{-6} s and 2.9×10^{-13} s, respectively.

The quark group is divided into up-type and down-type quarks. The up-type quarks (*up (u)*, *charm (c)* and *top (t)*) have an electric charge of $\frac{2}{3}$, while the down-type quarks (*down (d)*, *strange (s)* and *bottom (b)*) have an electric charge of $-\frac{1}{3}$. The corresponding anti-quarks carry an electric charge of $-\frac{2}{3}$ and $\frac{1}{3}$, respectively. Each up-type and down-type quark occurs in three flavors, referred to as '*color*': quarks carry a 'red', 'green' or 'blue' color, while anti-quarks carry 'anti-red', 'anti-green' or 'anti-blue' color. So far, only colorless bound states of 2-3 quarks have been observed. These bound states form new particles, namely the *hadrons*: two quarks that carry one unit of color and the corresponding unit of anti-colour form a *meson*, and three quarks carry three different units of (anti-) color form a *baryon*. All the hadrons are unstable, except for the proton, which consists of quarks of the 1st generation - two up-quarks and one down-quark (uud).

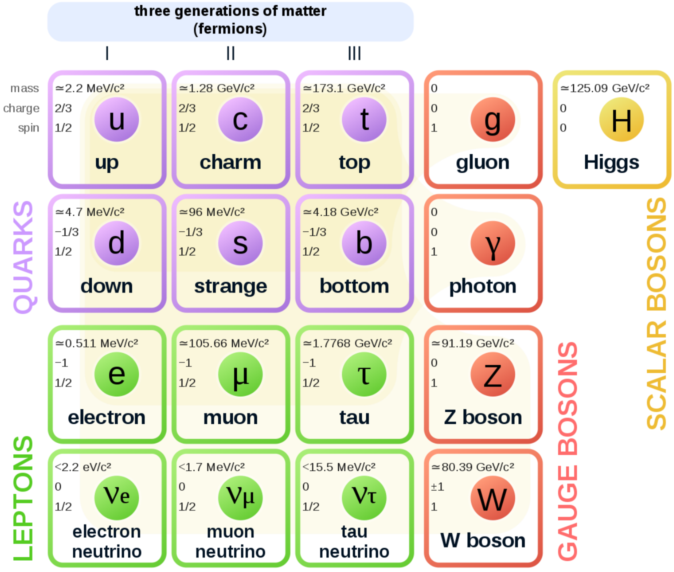

Figure 2.1: The elementary particles of the Standard Model: quarks (purple), leptons (green), Gauge bosons (red) and the Higgs boson (yellow). The mass, charge and spin of each particle is noted in the upper left corner of each particle frame. Adapted from reference [6].

In addition to the fermions, the Standard Model includes particles with spin 1 – the *Gauge bosons* – which function as the force carriers of the three fundamental forces that the Standard Model considers: the weak nuclear force, the electromagnetic force and the strong nuclear force. The Standard Model does not include a description of the gravitational force, since no consistent description of gravity as a *Quantum Field Theory (QFT)* has been devised yet; however, at the level of experimental precision of today's measurements it is negligible at the subatomic scale.

The weak nuclear force has two charged mediators, the W^- and W^+ bosons, and one neutral mediator, the Z^0 boson. These bosons are massive with $\mathrm{m}_{W^\pm} = 80.4\,\mathrm{GeV}$ and $\mathrm{m}_{Z^0} = 91.2\,\mathrm{GeV}$ and therefore the reach of the weak force is limited. The electromagnetic force, acting on any particle with electric charge, is mediated via the photons γ, which are massless particles with no electric charge. The strong nuclear force, acting on any particle with color charge, is mediated by eight massless gluons, which carry both color and anti-color and therefore can be self-coupled.

All of the interactions between the fermions obey several conservation laws from the conservations of energy, momentum and angular momentum to charge, color, quark number, flavor (except to weak interactions) and lepton number conservation.

All the elementary particles of the Standard Model and their properties are shown in figure 2.1. The last elementary particle in the Standard Model is the Higgs boson, which is a spin 0 boson with no electric charge, no color charge and a mass of 125.09 GeV [7]. This boson is produced by fundamental excitation of the Higgs field, a complex scalar field with a non-zero vacuum expectation value. The Higgs field, which is introduced by the Higgs mechanism [8, 9], gives mass to the Standard Model particles.

2.2 Collider Experiments

The experimental evidence for the existence of each of the elementary particles of the Standard Model, culminating in the discovery of the Higgs boson in 2012, have made the Standard Model one of the most successful theories in physics. Nowadays the most common way to produce unstable elementary particles is by experiments at accelerators in which a beam of particles is accelerated and smashed at almost light speed into either a target (*fixed-target experiments*) or another accelerated particle beam (*collider experiments*). The type of particles produced in such a collision is limited by the center-of-mass energy of the collision, as the emerged particles must have lower rest-mass-energies. This has motivated the development of more powerful particle accelerators with the years for discovering heavier particles.

One way to accelerate particles is by using a synchrotron ring in which the particle beams are guided by powerful magnets to circulate in accelerating fields for gaining more and more energy. The ring structure enables acceleration of particles to higher energies during many circulations and increases the collision rates, since the particles which did not interact can be focused again and used for further collisions; however, since the magnets, which are responsible for stabilizing and focusing the beams and for bending the paths of the particles, have a limited strength, the possible acceleration in a given synchrotron ring is restricted. Moreover, when charged particles are bent in a magnetic field they emit synchrotron radiation, which causes an energy loss per cycle, given by

$$\Delta \mathrm{E} = \frac{(\mathrm{Z}e)^2 \cdot \mathrm{E}^4}{\varepsilon_0 \cdot 3\mathrm{R} \cdot (\mathrm{m}_0 c^2)^4}, \tag{2.1}$$

in which $\mathrm{Z}e$, E and m_0 are the charge, energy and mass of the accelerated particle, respectively, ε_0 is the vacuum permittivity and R is the radius of the accelerator. As one can see, the dominant terms are the energy of the accelerated particle and its mass. Since electrons are rather light, for energetic electrons this energy loss is substantial, severely limiting the efficiency of a circular acceleration.

The largest and most powerful collider in the world to date is the LHC [10] at CERN, colliding protons (and occasionally heavy ions) at a current center-of-mass energy of $\sqrt{s} = 13\,\mathrm{TeV}$ in a synchrotron ring with a circumference of 26.7 km. The LHC has been specially designed for exploring the Standard Model at previously unreached energies and for searching for yet unknown particles beyond the Standard Model. The LHC achieved a crowning success with the discovery of the Higgs boson at the ATLAS and CMS experiments [11, 12]. However, in proton-collision experiments, such as the LHC, the precision of the measurements is intrinsically limited, since protons are composite objects comprising quarks and gluons. As such, the proton constituents are the actual colliding objects. Since these constituents carry only a fraction of the overall proton momentum, the exact energy of each individual collision is unknown. Furthermore, the strong force in these collisions gives rise to a large QCD background and exposes the detectors to a considerable radiation.

Considering the quark-confinement on one hand and the relative short lifetimes of muons and taus on the other hand, the electron - the only stable elementary particle observable in isolation - is the ultimate particle for precise collider experiments. In an electron-positiron collider the initial states of the collisions are well defined and the precise energy and spin orientation (in case of polarized beams) of the colliding particles are known. Furthermore, the clean environment, i.e. less radiation and less background, allows for highly precise measurements. The most powerful and the largest electron-positron collider built so far was the *Large Electron-Positron Collider (LEP)* [13], which was operated between 1989 and 2000 at CERN. The LEP was the circular collider for which the LHC tunnel was originally designed. The large synchrotron ring with a radius of approximately 4.25 km gave the possibility to efficiently accelerate electron beams up to a center-of-mass energy of 209 GeV. Higher collision energies suffered from an excessive energy loss due to synchrotron radiation.

In order to compensate for the radiation losses and to achieve a constant power in a synchrotron ring, the radius needs to increase at least as the square of the energy, $\mathrm{R} \propto \mathrm{E}^2$ (see equation 2.1). This means that for high collision energies the synchrotron machine becomes proportionally large. For linear machines, however, the length is given by the energy over the *acceleration gradient* (i.e. the energy gained per unit length), and therefore increases with energy. For this reason, constructing the next electron-positron collider for acceleration beyond the reached energies as a linear collider is the more reasonable alternative.

In linear colliders, the possibility to reuse the accelerator structure multiple times, as performed in circular accelerators, is eliminated; therefore, linear acceleration of particles requires either very long acceleration paths or very high acceleration gradients. The conventional techniques for acceleration rely on radio-frequency (RF) waves inside metallic cavities (*RF cavities*), which produce accelerating electromagnetic fields. The main constraint of this technology is the upper limit for the accelerating fields, over which the energy of the field ionizes the atoms of the cavities' walls [14]. This constrains the acceleration gradients achieved with this technology to a maximum of about 100 MV/m. Therefore, scaling to higher energies is only possible by increasing the acceleration portion, hence increasing the costs of a project. An alternative technique aiming at achieving much higher acceleration gradients, in the order of $10 - 100$ GV/m, is the *plasma-based acceleration*. In this method, either a relativistic particle beam or a laser pulse is used to excite relativistic waves in a plasma. The electric fields achieved in this way are stronger by several orders of magnitude than the fields produced inside the RF cavities, and thus, can be used to accelerate particles to high energies in much smaller distances. More details about this technology are given in chapter 9.

The idea of a plasma-based accelerator was first proposed in the late 1970s; however, the method has not yet reached a level of maturity appropriate for high-rate HEP. Although current experiments show acceleration of electron beams to the GeV scale [15–17], still more research is needed for improving the beam quality, in particular in terms of low energy spread and low emittance, before the plasma wakefield acceleration method can be implemented in collider experiments. For the nearer future, nonetheless, more precise measurements of higher center-of-mass energies are necessary for the ongoing research of the Standard Model and beyond it complementary to the LHC physics program. For this purpose two accelerator designs are currently being investigated: the ILC [18–22], with a design center-of-mass energy of 250 GeV and possible upgrades to 500 GeV and ultimately to 1 TeV, and the CLIC [23–25] with a center-of-mass energy of up to 3 TeV. One of these future colliders is likely to start its operation in approximately $15 - 20$ years.

2.3 Particle Detectors

All collider experiments are optimized for the identification and energy measurement of the particles produced in high-energy collisions. An individual collision and the particles it produces are referred to as an *event*, while the exact position in which it occurs is known as the *interaction point*. The primary particles produced in an event are of main interest for the HEP study. In order to reconstruct them, it is necessary to identify every particle in the event and to measure its four-momentum.

The particle physics detector systems use a wide range of technologies to detect and measure the properties of each particle. Modern particle detectors are large-scale detectors which cover most of the 4π solid angle around the interaction point. They consists of layers of sub-detectors, each designed either for particular measurements or for specific types of particles. Such a structure is shown in figure 2.2(a) for the *International Large Detector (ILD)*, which is one of the detector concepts developed for the ILC.

The inner region of the detector is devoted to the *vertex detector*, which uses several concentric layers of silicon detectors with a very fine resolution for resolving the secondary vertices of short lived particles from the primary vertex. A *tracking detector* is used to determine the momentum and charge of charged particles. The detector reveals the paths, or *tracks*, of particles in a magnetic field perpendicular to the direction of travel. The Lorentz force exerted on every charged particle in a magnetic field causes the particle to move in a helical orbit with a radius proportional to its momentum. The direction in which the track is bent reveals if the particle is negatively or positively charged.

The next sub-detectors are the *Electromagnetic Calorimeter (ECAL)*, for detecting electrons and photons, and the *Hadronic Calorimeter (HCAL)*, for detecting and measuring the energies of hadrons. The calorimeter system aims at measuring the energy of particles coming from a collision by 'forcing' them to deposit all of their kinetic energy inside of the detector.

Dedicated detectors are positioned at the outer layer for reconstructing and identifying muons and for measuring the energy which leaks through the end of the calorimeter system (*tail catcher*). In order to be able to measure the momenta of charged particles, a detector usually has a solenoid which produces a strong axial magnetic field in the range of $1-4\,\mathrm{T}$.

The presence of particles that leave no signal in the detecor system can be inferred from the presence of *missing transverse momentum*, which is defined by the sum of the measured transverse momenta of all the observed particles in an event (this sum should be zero if all particles produced in the collision have been detected, since the initial transverse momentum was zero).

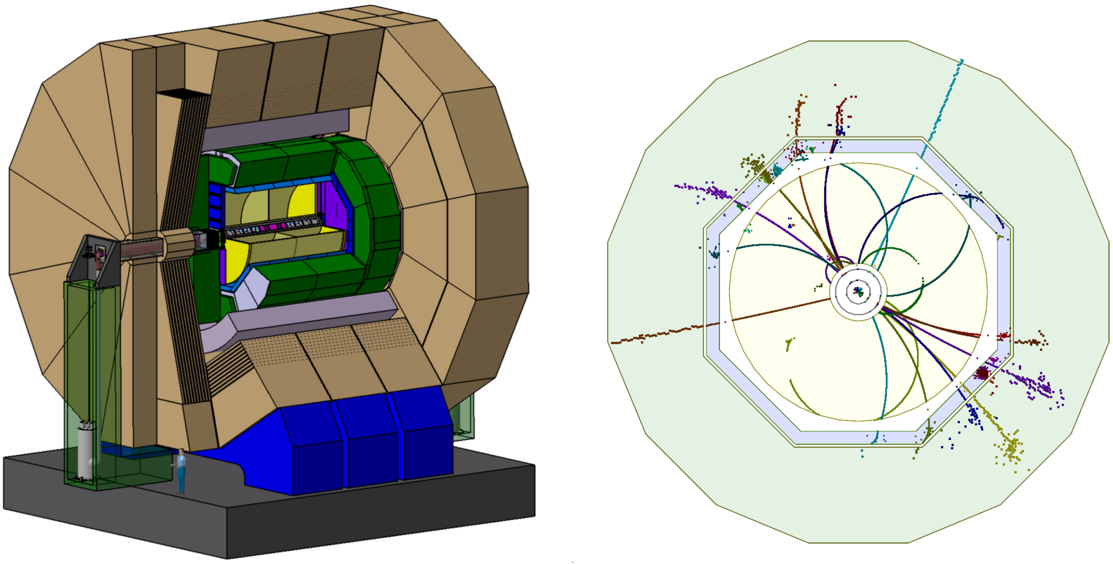

(a) (b)

Figure 2.2: (a) View of the ILD detector concept. The ILD tracker consists of several layers: a multi-layer vertex detector (not visible in the figure), layers of silicon strip detectors (magenta) and the time projection chamber (yellow). In the next layers lies the calorimeter system with an ECAL (blue) and an HCAL (green). A large volume superconducting coil surrounds the calorimeters (gray). The outer detector (brown) measures the magnetic flux and simultaneously serves as a muon detector and a tail catcher [26]. (b) A front view illustration of Particle Flow Algorithm detection of $e^+e^- \rightarrow ZH \rightarrow \mu^-\mu^+H$ process in the ILD tracker and calorimeter systems. Detector signals with same color belong to the same particle. Adapted from reference [27].

Exploiting the full potential of a future electron-positron collider requires the detector system to be capable of detecting the complete event structure with great detail. Many of the interesting physics processes at such a collider will be characterized by multi-jet final states, i.e. narrow cones with multiple hadrons which are generated by the prompt decay of short-lived particles. A particular goal of the detector design is the capability to separate hadronic decays of W and Z bosons which requires a jet energy resolution of $3-4\%$ over a wide range of jet energies.

2.3.1 Particle Flow Algorithms

A typical jet is composed on average of approximately 60% charged hadrons, 30% photons and 10% natural hadrons [28]. Traditionally, the jet energy is obtained from the sum of the energy depositions in the calorimeter system as illustrated in figure 2.3(a). This means that approximately

70% of the jet energy is measured in the HCAL which is typically characterized by a relatively poor energy resolution (see sub-section 3.4.2 for details).

A modern approach to reconstruct the jet energy with high precision is the PFA, which employs advanced pattern recognition techniques for reconstructing the jet energy from the energy sum of individual particles. The Particle flow approach improves the jet energy resolution by limiting the use of the HCAL to the reconstruction of neutral hadrons (and possible energy leakages of photons from the ECAL), whilst the large fraction of charged hadrons in the jet is reconstructed in the tracking system. The PFA scheme is illustrated in figure 2.3(a). Since the tracking system provides very precise measurements, the jet energy resolution, given by a weighted sum of the individual resolutions of the tracking system, the ECAL and the HCAL, can improve substantially.

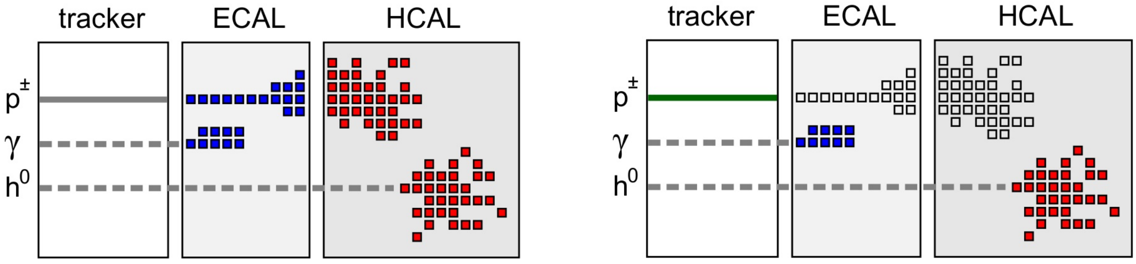

(a) Simple Calorimetry (b) PFA Calorimetry

Figure 2.3: (a) The calorimeter system measures all the energy depositions of a jet regardless of the particle type (charged particles $p^{\pm}$, photons γ, or neutral hadrons h^0). (b) Charged particles are measured in the tracker and their energy depositions in the calorimeters are ignored. Photons are measured in the ECAL and neutral hadrons are measured in the HCAL [29].

A successful implementation of the PFA requires an excellent tracking system with >99% efficiency to reconstruct a single track within the jet. Matching correctly reconstructed tracks with the calorimeter clusters is essential to distinguish between charged and neutral hadrons (the latter have no tracks). In addition, each energy deposition in the calorimeter should be associated with the correct particle to avoid missing or double counting energy. The calorimeter system should have the capability to separate overlapping calorimeter depositions of neutral and charged particles, otherwise part of the energy of the neutral hadron might be lost and/or part of the energy of the charged hadron may be double counted.

This *confusion*, rather than the calorimetric performance, is the limiting factor in Particle Flow calorimetry, placing stringent requirements on the granularity of the ECAL and the HCAL. To maximize the PFA performance, all detector concepts for future linear colliders are instrumented with high granularity calorimeters, a tracker with an exceptional good momentum resolution and a high magnetic field. Moreover, the tracker and the full calorimeter stack are located inside the magnet to avoid extended uninstrumented regions which would deteriorate the ability to associate energy depositions in the calorimeters with the corresponding particles.

Figure 2.2(a) presents the design of ILD, one of the detector concepts that fulfills the PFA requirements [26]. The high granularity of the ILD calorimeters is depicted in figure 2.2(b), which gives an example of a PFA reconstruction ($e^+e^- \to \mu^-\mu^+H$ process at center-of-mass energy of 250 GeV). For optimizing the ILD design, in particular the jet energy resolution of the calorimeters, *Monte Carlo Simulations (MC)* reconstructed with the *Pandora Particle Flow Algorithm (PandoraPFA)* have been used. PandoraPFA is the currently best performing algorithm for the ILC detector concepts, providing a sophisticated pattern recognition for different detector designs. Recent studies of PandoraPFA for ILD have shown that a jet energy resolution below 4% for energies in the 50 GeV to 250 GeV range is achievable [30].

CHAPTER 3

CALORIMETRY IN HIGH ENERGY PHYSICS

Calorimetry plays a key role in the detection of collision events in modern particle physics. The electromagnetic and hadronic calorimeters are responsible for measuring the energy of charged and neutral particles as well as for reconstructing jets and measuring their energy. In addition, the calorimeter system is essential for measuring the overall energy flow and for evaluating the missing transverse momentum for reconstructing *invisible particles*, i.e. particles that leave no signal in the detector system.

Calorimeters are blocks of instrumented material in which particles to be measured are fully or partially absorbed and their energy transformed into a measurable quantity. The interaction of a high-energy particle with the calorimeter matter leads to a development of a *particle shower*. First, the primary particle produces secondary particles when crossing through the calorimeter. Then, each secondary particle interacts with the calorimeter matter and produces more particles. As this process continues, the number of particles increases as long as the energy of the secondary particles is sufficient to create new particles.

Any calorimeter consists of active signal generators, the active material that measure the shower energy, and a passive particle absorber, the material that causes the particles to shower. The energy deposited in the active part serves as a measurement of the energy of the incident particle. For accurate measurements, the size of a calorimeter should be large enough to contain the full energy loss of the particle. The required calorimeter thickness corresponds to the shower depth which scales logarithmically with the initial particle energy, and therefore detection of highly energetic particles does not require excessively thick calorimeters.

The interaction processes that play a role in the shower development depend on the energy and the nature of the primary particle. Electrons, positrons and photons will undergo electromagnetic interactions with the atomic fields, generating electromagnetic showers. These electromagnetic interactions are described in detail in section 3.1. As for hadrons, a range of strong interactions with the nuclei will take place, producing hadronic showers. A brief description of the nature of hadronic showers and the relevant strong interactions can be found in section 3.2.

There are several considerations when designing a calorimeter, including cost and performance. The designs differ by the materials, the read-out method and the geometry implemented in each calorimeter. Typically, calorimeters are classified by their construction into *homogeneous* and *sampling* calorimeters, as well as by their use for electromagnetic or hadronic interactions. Details about these definitions and different configurations can be found in section 3.3. The expected performance of calorimeters for electromagnetic and hadronic showers is discussed in section 3.4. Section 3.5 presents some of the current methods used for simulating showers, focusing on the relevant models for the analysis presented in this dissertation.

3.1 Electromagnetic Showers

Electromagnetic showers may be started by photons, electrons or positrons entering a material. These showers grow by electromagnetic interactions with atomic electromagnetic fields, which give increasingly more particles of lower energy, until the energy carried by individual particles cannot sustain the production processes. The characteristic length scale for the longitudinal development of an electromagnetic shower in a material is the *radiation length* X_0, which is usually measured in g cm^{-2}. The radiation length is defined as the mean length over which a high-energy electron has lost $\left(1 - e^{-1}\right) = 63.2\%$ of its initial energy by bremsstrahlung*. This equals $\frac{7}{9}$ of the mean free path of a high-energy photon before undergoing pair-production. A common parametrization of the radiation length of a material as a function of its atomic number and mass, Z and A, respectively, is given in reference [31] as

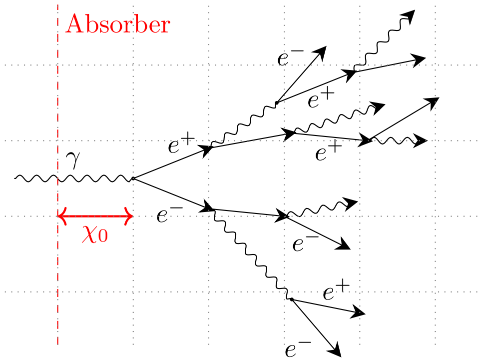

Figure 3.1: An illustration of the development of an electromagnetic shower.

$$X_0 = \frac{716.4\,\mathrm{g\,cm^{-2}A}}{Z(Z+1)\ln(287/\sqrt{Z})}. \tag{3.1}$$

The transverse development of an electromagnetic shower in different materials is measured by the *Molière radius* ρ_M, which stands for the radius of a cylinder containing 90% of the energy of the shower. The Molière radius is given in reference [32] as

$$\rho_M = 21.2\,\mathrm{MeV}\frac{X_0}{\varepsilon_c}, \tag{3.2}$$

where ε_c is the critical energy in which the electron ionization loss per radiation length is equal to the electron energy [33].

---

*Definition in section 3.1.2.

3.1.1 Photon Interactions with Matter

Photons passing through matter interact with the atoms via different processes. The possible interactions are listed in the following:

Coherent Elastic Scattering This category includes Rayleigh and Thompson scattering, which originate from interactions with atomic electrons and the nuclear charge, respectively. In these processes the photon does not lose energy, therefore there is no contribution to the shower development.

Compton Scattering A photon scatters from an atomic electron and transfers some if its energy to the struck electron. The recoiling electron normally acquires sufficient energy to leave the atom.

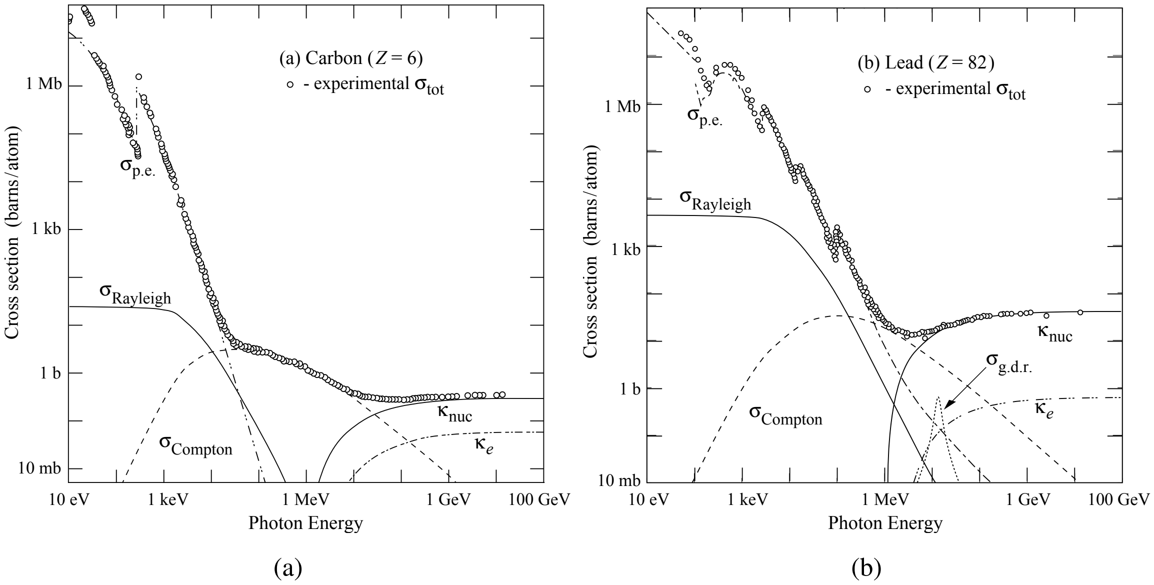

(a) (b)

Figure 3.2: The cross sections of photon interactions with (a) carbon and (b) lead as a function of the photon energy [34]. The photon interactions are Rayleigh scattering (σ_{Rayleigh}), Compton scattering (σ_{Compton}), the photoelectric effect ($\sigma_{\text{p.e}}$), pair production by nuclear fields (κ_{nuc}), pair production by electron fields (κ_{e}) and the photo-nuclear absorption ($\sigma_{\text{g.d.r.}}$).

The Photoelectric Effect A photon with an energy larger than the initial binding energy of the electron is absorbed by atomic interaction and an electron is expelled with kinetic energy equal to the energy difference between the photon energy and the binding energy. The emitted electron is referred to as a *photo-electron*.

Pair Production At energies greater than twice the electron rest mass, a photon passing through a coulomb field may create a pair of electron and positron. These processes are caused predominantly (>99%) by nuclear electromagnetic fields, whereas a slight contribution is due to electron fields.

Photo-nuclear Absorption Photons with energies of the order of 10 MeV or more (mostly in the energy region of the so called Giant Dipole Resonance (g.d.r) [34]) may excite resonant states in the nuclei. When these states decay, an emission of a neutron, a proton or another energetic photon takes place.

Figure 3.2 summarizes these processes and their contributions in a light element (carbon) and a heavy element (lead) at different photon energies. At low energies, contributions from Compton scattering, Rayleigh scattering and the photoelectric effect can be seen, where the latter is the most probable. At high energies pair production is the dominant interaction.

3.1.2 Electron and Positron Interactions with Matter

Electrons and positrons traversing matter lose energy due to the following electromagnetic interactions:

Møller Scattering Electron-electron scattering of the projectile electron with an atomic electron of the matter.

Bhabha Scattering for positrons Positron-electron scattering of the projectile positron with an atomic electron of the matter.

Positron Annihilation A positron collision with an atomic electron leads to annihilation of the electron and the positron and creates two gamma-ray photons.

Ionization In the context of shower development, this process describes an electron or a positron collision with an atomic electron, which transfers sufficient energy to put the atomic electron in an unbound state.

Bremsstrahlung Electromagnetic radiation produced by acceleration or deceleration of an electron or positron in the presence of the electromagnetic field of the atoms in the material (usually the nuclei fields).

The different contributions to the energy loss of electrons and positrons per radiation length X_0 in lead are shown in figure 3.3 as a function of the particle energy. At low energies, electrons and positrons primary lose energy by ionization. Other contributions in this energy range are bremsstrahlung, Møller scattering, Bhabha scattering and positron annihilation. For high energies (approximately larger than 10 MeV), the energy loss is predominantly due to bremsstrahlung.

3.1.3 Electromagnetic Interactions of Heavy Charged Particles with Matter

Heavy charged particles, such as muons and charged hadrons, can undergo ionization and bremsstrahlung when interacting with the atomic fields of matter. The emission of bremsstrahlung scales with the particle mass m and its energy E, as $\mathrm{E} \cdot \mathrm{m}^{-2}$ [35] and therefore is suppressed in particles with energies lower than a few hundred GeVs. The mean rate of energy loss through ionization and

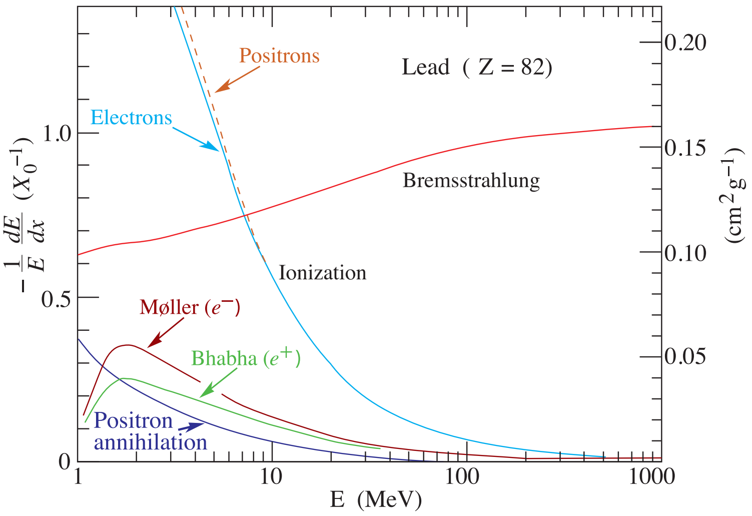

Figure 3.3: The fractional energy loss per radiation length of electrons and positrons in lead as a function of particle energy [34].

atomic excitations for fast particles with speed $v = \beta c$ and charge ze (e being the elementary charge) is well-described by the Bethe-Bloch equation,

$$\left\langle -\frac{dE}{dx} \right\rangle = Kz^2 \frac{Z}{A}\frac{1}{\beta^2}\left[\frac{1}{2}\ln\frac{2m_e c^2\beta^2\gamma^2 T_{\max}}{I^2} - \beta^2 - \frac{\delta(\beta\gamma)}{2}\right], \tag{3.3}$$

in which $T_{\max}$ is the maximum kinetic energy which can be imparted to a free electron in a single collision, K is the proportionality constant[†], Z and A are the atomic and mass number of the material, respectively, I is the mean excitation energy of the dense material and $\delta(\beta\gamma)$ is the density effect correction function [34]. This equation describes with an accuracy of a few percent the mean rate of energy loss in the region $0.1 \lesssim \beta\gamma \lesssim 1000$ for intermediate-Z materials. The energy loss of positive muons on copper as a function of the momentum is shown in figure 3.4. In the relevant range, the energy loss is computed with the Bethe-Bloch equation, while outside of this range additional corrections are applied (more details can be found in reference [34]). A broad minimum in the energy loss is visible around $\beta\gamma \approx 3 - 4$. A particle with an energy corresponding to this range[‡] is referred to as a *Minimum Ionizing Particle (MIP)*.

In thin layers of dense material, less interactions occur and therefore fluctuations in the energy loss are expected. These fluctuations, which are referred to as *Landau fluctuations*, occur due to variations in the number of interactions as well as in the energy transferred in each interaction. The distribution of energy loss in these thin layers, the so called *Landau distribution*, is asymmetric and characterized by a narrow peak with a long tail toward large energy losses. The high-energy-tail comes from a small number of individual collisions, each with a small probability of transferring comparatively large amount of energy. The large weight of these rare events drives the mean value toward the tail of the distribution.

[†] $K = e\pi N_A r_e^2 m_e c^2$, with Avogadro's number N_A, the classical electron radius $r_e = e^2/4\pi\epsilon m_e c^2$ and the electron mass m_e.

[‡] usually muons or other particles with unity charge such as pions [32].

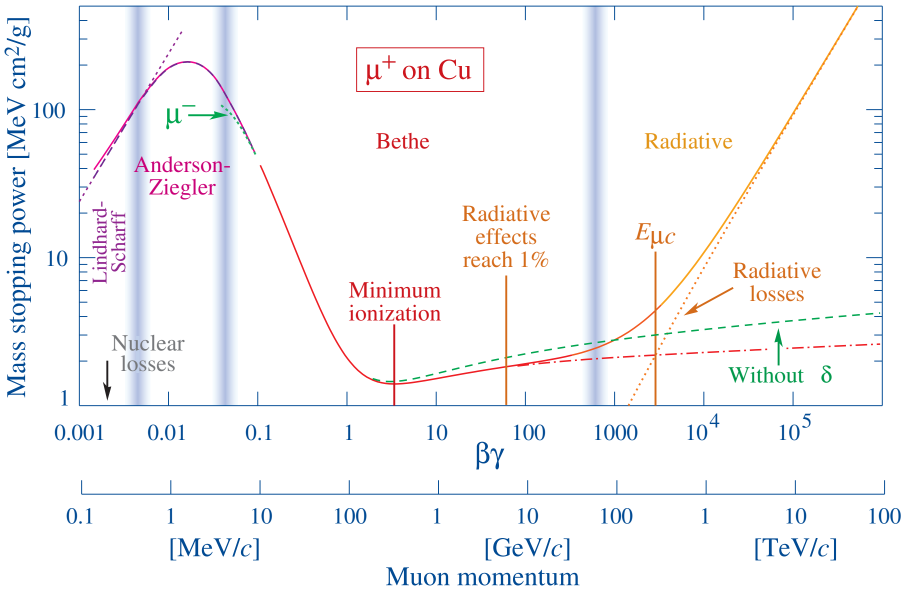

Figure 3.4: The mean energy loss of positive muons in copper as a function of the muon momentum [34]. The solid curves indicate the total energy loss. The vertical bands indicate boundaries between different approximations. Between $0.1 < \beta\gamma < 1000$ the Bethe-Bloch equation (equation 3.3) is used.

It is more common to describe the energy loss of single particles in thin layers with the *Most Probable Value (MPV)* of the energy loss distribution, rather than its mean value. The MPV is a more robust observable with a smaller dependence on the particle energy compared with the mean value [36]. In thin layers, the MPV is lower than the mean value, which increases more rapidly with the particle energy.

3.2 Hadronic Showers

Hadrons passing through matter undergo electromagnetic interactions in the presence of atomic electromagnetic fields along with strong interactions with the nuclei of the material. Among these interactions, inelastic hadronic interactions are the ones that generate hadronic showers by producing secondary particles, which then lose their energy either by ionization and excitation or undergo further inelastic interactions. When the particle production is balanced by the particle absorption, the number of the particles in the shower reaches a maximum, which is followed by a gradual decrease in the energy deposition from that point.

The inelastic interactions with the nuclei induce production of mesons and baryons, spallation, excitation of nuclei and nuclear fission. The characteristic length scale for the development of showers with these interactions is the *nuclear interaction length* λ_I. This length indicates the average distance a high-energy hadron has to travel inside an absorber medium before a nuclear interaction occurs. Consequently, the probability that the particle traverses a distance x in the medium without causing a nuclear interaction is given by

$$P = exp\left(\frac{-x}{\lambda_I}\right). \tag{3.4}$$

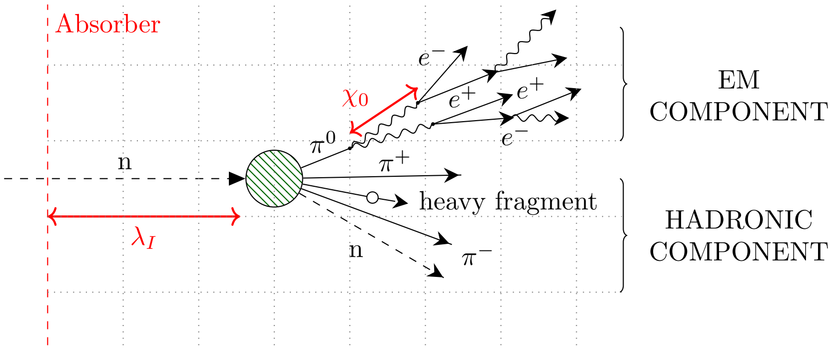

Figure 3.5: Schematic depiction of a hadronic shower starting by neutron-nucleus interaction after a distance of λ_I in the matter.

λ_I value scales with the atomic mass of the material as $A^{1/3}$. Cross-section measurements for interactions of protons and pions with different fixed targets have shown an additional dependence on the projectile's size and result in a correction factor for *pion interaction length* λ_π, which is a factor $\frac{3}{2}$ larger than the proton interaction length (which is usually used to define λ_I) [32]. The nuclear interaction length is typically larger than the radiation length and therefore hadronic showers are usually larger in extension compared to electromagnetic showers.

The level of complexity of hadronic showers is much higher compared to electromagnetic showers, due to the following:

The Electromagnetic Component The neutral particles produced in the shower, in particular π^0 and η mesons, decay into two photons and initiate an electromagnetic sub-shower within the hadronic shower. Since $\lambda_I \gg X_0$ in most materials, this electromagnetic component is typically narrower and denser than the pure hadronic component. The fraction of the electromagnetic component varies strongly from event to event, depending on particular processes occurring in the early phase of the shower development; however, on average, this electromagnetic component increases with the energy of the initial hadron [37].

The Invisible Energy A certain fraction of the deposited energy produced by the strong interactions is undetectable and thus referred to as *invisible energy*. The main source of this phenomenon are energy losses in the excitation or recoil of the target nuclei, which often do not result in a signal in the active medium. In addition, the neutrons generated within the shower lose their energy in elastic scattering processes, which reach an end either by the decay of the neutron or by a neutron capture. In the latter case the excited nucleus releases additional energy by photon emission. Since this process is very slow compared with the shower-time-scale, usually the energy it contributes is not measured. Additional energy might be lost to neutrinos originating from meson decays.

An illustration of the shower development and its two components is shown in figure 3.5.

3.3 Calorimeter Configuration

Calorimeters are classified into two categories according to their read-out implementation: homogeneous calorimeters and sampling calorimeters. In homogeneous calorimeters, the entire detector volume is sensitive to particles, acting simultaneously as the absorbing material and the signal generator. The materials which are usually used for this purpose are dense scintillating crystals, lead loaded glass or liquefied noble gases. Typically, measurements of photons produced in the interactions within these material are used to evaluate the energy of the initial particle. These photons, generated via a process known as scintillation (see section 4.2), are then detected by photo-detectors located at the far-end of the material.

In sampling calorimeters, the different functions of shower generation and particle detection are exercised by different materials in alternating layers. The passive absorber layers which generate the shower are chosen to have a high density and high atomic number to produce more compact showers. Typically, materials such as iron, copper, lead, steel, tungsten or uranium are used. The active read-out layers which record the particles inside the shower can be implemented in different ways using a variety of technologies.

The advantage of sampling calorimeters is the possibility to optimally choose the absorber and active material independently. When choosing a very dense absorber material the calorimeters can be made very compact. Moreover, using sampling calorimeters gives the possibility to study the shower's longitudinal development. On the other hand, these calorimeters detect only a small fraction of the particles and due to sampling fluctuations (see next section for details), they are characterized by an inferior energy resolution of electromagnetic showers compared to homogeneous calorimeters.

The electromagnetic and the hadronic showers extend to different scales due to the difference between the nuclear interaction length and the radiation length in matter. For that reason, calorimeters are often divided into ECALs, for measuring mainly electromagnetic showers, and HCALs, for measuring mainly hadronic showers. The advantage of this separation is the possibility to perform an independent optimization of both calorimeters for their specific needs, resulting in a better performance, in particular for electromagnetic showers. However, the energy reconstruction of hadrons in such a calorimeter system becomes more complex due to transition effects and inter-calibration corrections between the different detectors, as is described in more detail in section 6.1.

3.4 Calorimeter Response

In HEP calorimetry, the energy of an incoming particle is evaluated by the total signal generated by the showering particles. Ideally, the signal amplitude is proportional to the energy E of the primary particle. The concept of calorimeter *linearity* refers to the level of which this proportionality is achieved in practice. The precision with which E can be measured is evaluated by the relative width of the signal distribution $\frac{\sigma}{\mathrm{E}}$, which defines the *energy resolution* of the calorimeter. The calorimeter response for electromagnetic and hadronic showers, evaluated with the linearity and the energy resolution of the calorimeter, is discussed in this sub-section.

3.4.1 Electromagnetic Response

The simple development of electromagnetic showers, which is described in sub-section 3.1, and the capability to efficiently detect secondary particles of such showers, allow a high degree of linearity in ECALs. Homogeneous calorimeters are the most efficient in this respect, using the entire kinetic energy of the incoming particle to generate the calorimeter signal. However, due to non-linear effects such as saturation and shower leakage, deviations from linearity may be observed.

The development of an electromagnetic shower is a stochastic process and therefore fluctuations from shower to shower are unavoidable. These fluctuations follow the Poissonian statistics. In general, the number of particles that constitute the calorimeter signal $\mathrm{N_{sig}}$ is proportional to the total measured signal. Moreover, as the number of particles in the shower $\mathrm{N_{sho}}$ grows with E, so do $\mathrm{N_{sig}}$ and the measured signal. For that reason, for higher energies a more precise measurement is expected.

For homogeneous calorimeters, $\mathrm{N_{sig}} \approx \mathrm{N_{sho}}$ and therefore the *intrinsic shower fluctuations*, i.e. the fluctuations of $\mathrm{N_{sho}}$, are the dominant contribution to the energy resolution. Due to these fluctuations, the width of the signal distribution is $\sigma \propto \sqrt{\mathrm{N_{sho}}} \propto \sqrt{\mathrm{E}}$.

In sampling calorimeters, the showers are sampled at finite number of points, where the active medium is located, rather than recorded for their entire length. For these calorimeters, $\mathrm{N_{sig}}$ is described by the number of different shower particles in the active calorimeter layers, $\mathrm{N_{samp}} \approx \mathrm{f_{samp}} \cdot \mathrm{N_{sho}}$, where $\mathrm{f_{samp}}$ represents the *sampling fraction*, i.e. the fraction of the total absorbed energy deposited in the active material. The fluctuations in $\mathrm{N_{samp}}$, convoluted with fluctuations in the amount of energy deposited by individual particles, are referred to as *sampling fluctuations*. They depend both on $\mathrm{f_{samp}}$ and on the *sampling frequency*, which is determined by the number of different sampling elements in the region where the showers develop. The energy uncertainty caused by sampling fluctuations may be expressed as $\sigma_{\mathrm{samp}} \propto \sqrt{\mathrm{d}/\mathrm{f_{samp}} \cdot \mathrm{E}}$, in which d represents the thickness of an individual active sampling layer [32, 34].

All the statistics-related contributions to the energy resolution are described by the stochastic component of the energy resolution, given by

$$\left(\frac{\sigma}{\mathrm{E}}\right)_{\mathrm{stochastic}} = \frac{a}{\sqrt{\mathrm{E}}}. \tag{3.5}$$

a is called the *stochastic term* and used commonly with the energy E given in units of GeV. Other influences on the signal distribution are non-uniformities in the detector, such as dead regions or inhomogeneities in the detector material, and the calibration uncertainty. The signal uncertainties introduced by these factors scale with the energy and result in a constant energy resolution, defined with the *constant term* b as

$$\left(\frac{\sigma}{\mathrm{E}}\right)_{\mathrm{constant}} = b. \tag{3.6}$$

Additional consideration for a full description of the energy resolution of a calorimeter is the energy-independent noise contribution arising from electronic noise of the readout chain. This is described with the *noise term* c by

$$\left(\frac{\sigma}{\mathrm{E}}\right)_{\mathrm{noise}} = \frac{c}{\mathrm{E}}. \tag{3.7}$$

As the sources of fluctuations described above are mutually uncorrelated, their contributions to the energy resolution may be added in quadrature. The total energy resolution then can be written as

$$\frac{\sigma}{\mathrm{E}} = \sqrt{\left(\frac{a}{\sqrt{\mathrm{E}}}\right)^2 + (b)^2 + \left(\frac{c}{\mathrm{E}}\right)^2} = \frac{a}{\sqrt{\mathrm{E}}} \oplus b \oplus \frac{c}{\mathrm{E}} \tag{3.8}$$

3.4.2 Hadronic Response

Hadronic calorimetry is considerably more difficult than electromagnetic calorimetry. The reason for this is the complex development of hadron-induced showers (discussed in sub-section 3.2): the presence of two components, electromagnetic and pure hadronic, and invisible energy.

The calorimeter response for the total energy deposited by a hadron shower, marked as π, can be written as

$$\pi = f_{em} \cdot e + (1 - f_{em}) \cdot h, \tag{3.9}$$

in which e and h denote the calorimeter response to the electromagnetic[§] and the pure hadronic components, respectively, and f_{em} represents the electromagnetic fraction. The response π is non-linear for two reasons. First, due to the invisible energy the calorimeter response to the hadronic sub-shower is typically smaller than the electromagnetic response ($\frac{e}{h} > 1$). Second, f_{em} increases on average with the hadron energy E. The ratio $\frac{e}{h}$ classifies calorimeters into two types: *compensating* calorimeters with $\frac{e}{h} = 1$ and *non-compensating* with $\frac{e}{h} \neq 1$. Since $\frac{e}{h}$ cannot be measured experimentally, commonly the ratio $\frac{e}{\pi}$ is used. It is, however, important to note that $\frac{e}{\pi}$ decreases in higher hadron energies since the response π increases as f_{em} with E.

In addition to the fluctuations considered for electromagnetic showers, other sources of fluctuations take part and deteriorate the energy resolution of hadron calorimeters. The most significant fluctuations that play a role are the event-to-event fluctuations in f_{em} [32]. These fluctuations are large and are not described by Poisson statistics. Another critical influence arises from the fluctuations in the visible energy, which are strongly correlated with the f_{em} fluctuations. These additional fluctuations result in a significantly worse energy resolution of hadron calorimeters compared with that of electromagnetic ones.

Attempts to improve the calorimeter performance include designing of a fully compensating calorimeter with $\frac{e}{h} = 1$. Such a calorimeter design is possible only with the flexibility offered by sampling calorimeters, in which several variables can be chosen or tuned. Several methods are used in this case:

Reducing the electromagnetic response The cross section of the photoelectric effect has a very strong dependence on the atomic number Z, scaling approximately as Z^5 [35]. This dependence can be seen in figure 3.2. For this reason, in a high-Z absorber the photons are more likely to interact with the absorber material than reaching the active medium. The electrons created in such a process contribute to the signal only if the interaction takes place close to

---

[§] The response e is similar to the response for an electromagnetic shower, which was described in the previous sub-section.

the boundary of the absorbing layer. For this reason, by selecting a high-Z absorber, the electromagnetic response e decreases. Further suppression of e can be achieve by shielding the active layers by thin sheets of passive low-Z material, which preferentially absorbs low-energy photons.

Boosting the non-electromagnetic response By selecting an active material which contains hydrogen atoms (such as butane-filled proportional counters or plastic scintillator), it is possible to increase the response to shower-neutrons since the neutrons have large n-p elastic cross sections. The recoiling protons in such an active medium will produce signals and therefore will increase h. Another option is to use an absorber composed partly of U^{238}. In U^{238}, the flux of neutrons and the nuclear photons induce fission processes. The extra energy released in these processes would then compensate for the invisible energy and will increase h.

The most prominent example of a compensating calorimeter is the ZEUS uranium-scintillator calorimeter [38], which achieved the best energy resolution for hadrons of $\frac{\sigma}{E} \approx \frac{35\%}{\sqrt{\mathrm{E/GeV}}} \oplus 2\%$ [39]. The calorimeter layout involved both methods mentioned above along with a careful choice of the absorber-to-readout material thickness ratio. Using these methods for an optimal compensation gave a response ratio of $\frac{e}{\pi} = 1.00 \pm 0.03$ [38].

Aside from equalizing of the responses e and h with design constraints, there are several methods for implementing compensation in non-compensating calorimeters. In these alternative approaches, the energy contributions from the electromagnetic and the pure hadronic components are determined on an event-to-event basis. The compensation is then achieved by applying different weights to the different signal components. For a perfect compensation, the energy depositions are precisely classified and a factor of $\frac{e}{h}$ is applied to energy depositions of the pure-hadronic component. In practice, however, it is difficult to classify precisely the energy sharing between the components. Two methods, which aim at achieving compensation in non-compensating calorimeters, are listed here:

Dual readout calorimeters In a dual readout calorimeter the signal is sensed by two read-out systems to estimate f_{em} on event-to-event basis. One system detects the ionization energy losses, while the other measures Cherenkov light [40], which is strongly correlated to the electromagnetic fraction of the hadron shower.

Software Compensation In fine segmented calorimeters, the electromagnetic component deposits large signals in a small number of cells compared to pure-hadronic component, due to its smaller length scale ($\lambda_I \gg X_0$). Therefore, by down-weighting cells with large signals, compensation can be achieved. In this thesis, a new scheme of software compensation is presented. More details can be found in section 6.3.

3.5 Simulation of Particle Showers

GEANT4 [41] is a software toolkit for simulating particles in matter. The software, which was developed for HEP uses, is widely used in different research fields. GEANT4 simulates the propagation and interactions of particles in matter with MC simulation methods. The interactions of the particles are described by a variety of different physics models, which can be selected by the user. For a complete and consistent modeling of processes in the simulation, the software offers the possibility to combine several models of different energy regimes or/and different particle types by creating (or using pre-defined) *physics lists*.

GEANT4 provides high precision modeling of electromagnetic showers as the physics of these showers is well understood and involves only electrons, positrons and photons. The software standard model for electromagnetic processes reaches precision level of less than 1% in its predictions for observables in sampling calorimeters [42, 43].

As described in section 3.2, the development of hadron-induced showers might include a large variety of physics processes. Among these processes, the strong force interactions of the composite nuclei with the composite shower particles cannot be calculated analytically. GEANT4 uses several models for describing hadronic interactions with matter. These models are based on different approximations and assumptions for limited energy ranges. All models use experimental data to some extent, mainly for modeling final states. The level of this use varies from one model to another, ranging from models that are largely based on evaluated or measured data to models that are predominantly based on theory. Ongoing studies are preformed by the GEANT4 collaboration for improving the precision level of the models; however, no ultimate model of hadronic showers with a similar accuracy to the electromagnetic model has been devised yet.

The modeling scale used for each interaction is depended on the projectile particle momentum. At lower energies the individual nucleons in the target nucleus have to be considered, whereas at higher energies the quark content of the projectile and the single target nucleon are the relevant structures.

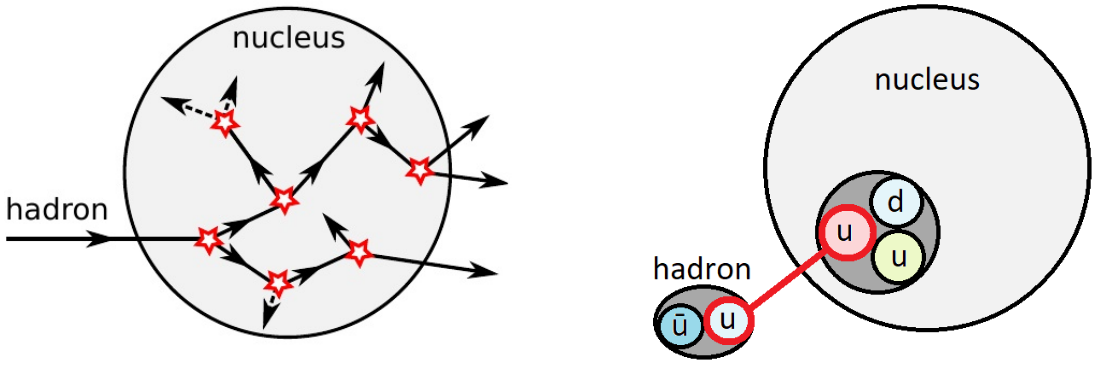

(a) (b)

Figure 3.6: Illustration of the working principle of GEANT4 models. (a) The cascade model [29]. (b) The parton string model.

3.5.1 Cascade models

Cascade models are models optimized for energies of a few hundred MeV to a few GeV. In this energy range, the modeling scale is comparable with the distance between the nucleons and therefore, the quark sub-structure can be neglected. The interactions are then described through the projectile hadron and the nucleons in the target nucleus. The mean free path between the interactions of secondary particles is calculated from parametrized cross sections and nucleon densities, which are modeled differently in different cascade models.

In the *Bertini cascade model* [44, 45] the nuclear potential is represented by several concentric, constant-density shells[¶]. The nucleons in each shell are treated as a Fermi gas, i.e. up to the Fermi energy, the nucleons occupy all possible states of the system. The Pauli exclusion principle imposes a minimum energy for the creation of secondary particles. For each interaction in this model, calculations of the struck nucleon momentum, the type of the reaction taking place and the momentum of the reaction products are performed. The model also includes de-excitation algorithms which take over when all cascade particles have either left the volume or been trapped in a nucleus.

3.5.2 Parton String Models

Parton string models [46] describe interactions of high-energetic hadrons (>5 GeV) with nuclei. The modeling scale in this case is rather small and therefore the quark sub-structure of the projectile and the target nucleons is taken into account. The nucleus is modeled as an ensemble of protons and neutrons. Each nucleon is positioned randomly according to the nuclear density distribution (a Wood-Saxon potential for heavy nuclei with A>16 and a harmonic oscillator potential for lighter nuclei) and assigned with a random momentum chosen up to the Fermi momentum.

Each interaction is described as a collision between the projectile hadron and a single nucleon of the target nucleus. The type of interaction is predicted from the center-of-mass energies, the hadron impact parameter and the diffractive and inelastic cross-sections. In the interaction, a string between one quark of the projectile and one quark of the nucleon is formed, carrying energy and momentum. The string moves according to movement of its constituents and gets excited by other nuclei. Excited strings are fragmented into quark-anti-quark pairs and new strings as long as the energy is sufficient. In the end of this process, the remaining secondary particles are propagated through the nucleus using a cascade model. The de-excitation of the nucleus is further simulated by nuclear fragmentation, pre-compound, and nuclear de-excitation models [47, 48].

GEANT4 includes two parton string models, the *Fritiof (FTF)* model and the *Quark-Gluon String (QGS)* model. These models differ in the string formation and fragmentation. The FTF model considers only momentum exchange between the projectile and the nucleon, while the QGS model includes also inelastic scattering processes mediated by pomerons [49]. More details can be found in [47].

[¶] The number of shells varies from 1 to 6 depends on the nucleus mass [45].

3.5.3 Physics Lists

GEANT4 physics lists are consistent sets of physics models for all sorts of interactions, considering different particle types, energies, and target materials. Various physics lists are possible for different GEANT4 applications, giving the users the possibility to use or write their own preferred physics list. Several pre-defined physics lists, *reference physics lists*, are available in GEANT4 and used by the large majority of users [50].

Nine reference physics lists for hadron-nucleus interactions are provided in release 10.0 of the toolkit. Each of the physics lists combines several models, which are optimized for different energy ranges. A smooth transition between models is achieved by overlapping their energy regions and randomly selecting one of the models for each interaction. In this thesis, the two most popular lists are used [51]:

1. **FTFP_BERT** uses the Bertini cascade model up to 5 GeV incident hadron energy, and the FTF model from 4 GeV upwards.
2. **QGSP_BERT** uses Bertini cascade model until 5 GeV, the FTF model from 4 GeV to 25 GeV, and the QGS model for the high energy range starting at 12 GeV.

A schematic representation of the models used in these lists is shown in figure 3.7. The letter P in the list names indicates the use of the GEANT4 pre-compound mode for de-exciting the nucleus after the high energy interaction of either FTF or QGS model has been completed.

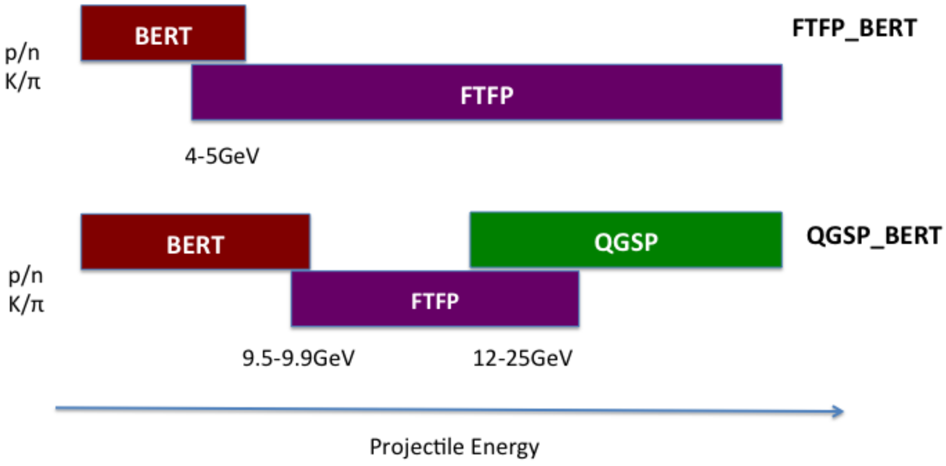

Figure 3.7: Schematic representation of FTFP_BERT and QGSP_BERT physics lists in GEANT4 version G4.10.1.p02 [52]. These physics lists describe hadron-nucleus inelastic interactions.

CHAPTER 4

CALICE PHYSICS PROTOTYPES

The CALICE collaboration has developed and extensively studied highly granular calorimeter prototypes to evaluate detector technologies for future linear collider experiments. These calorimeters have unprecedented granularity which allows high spatial resolution studies of the structure of showers and the testing of particle flow algorithms. Since the foundation of the collaboration in 2001 different calorimeter concepts were developed, testing the efficiency of different absorber materials (tungsten/steel), different granularities, several readout techniques and comparing between analog, digital and semi-digital prototypes.

The first prototypes were developed between 2006 − 2009 with the goal of demonstrating the general feasibility and performances of highly granular calorimeters in test beam experiments. Those calorimeters are focused on the physics aspects rather than the engineering constrains of collider detectors and therefore referred to as the *CALICE physics prototypes*. The physics prototypes have been successfully operated in various test beam experiments in different configurations at *Deutsches Elektronen Synchrotron (DESY)*, CERN and FNAL between 2006 and 2012. Different methods for reconstructing the collected data were developed. From 2015 until the present, new prototypes are being developed taking into account also the engineering challenges involved in integrating such calorimeters in a full 4π detector system. These prototypes are referred to as *CALICE technological prototypes*.

In this dissertation, the discussion is limited to the physics prototypes, with a particular focus on a combined system of the *Silicon-Tungsten Electromagnetic Calorimeter (Si-W ECAL)*, the *Analog Hadron Calorimeter (AHCAL)* and the *Tail Catcher and Muon Tracker (TCMT)* prototypes. This system was installed and tested in test beam experiments at CERN in 2007 and FNAL in 2008. This chapter presents the system readout technologies, the prototype structures and the test beam experiment facilities.

4.1 Silicon Sensors

The continuous need for detectors with finer spatial resolution have made silicon sensors very attractive for particle detectors. In silicon, the energy required to create an electron-hole pair is 3.6 eV (compared to the ionization energy of 15 eV in argon gas). This leads to an ionization yield for MIPs of about 80 pairs per micrometer in a relative short response time. For instance, in a wafer of thickness of 300 μm 23000 pairs are produced and collected in approximately 30 ns [53].

Like other tracking detectors, the working principle of a silicon detector is based on the detection of free charges resulting from ionization or excitation of atoms in a medium by a passing particle. In silicon sensors, the bulk material is an n- (p-) doped silicon wafer with implantation of p^+ (n^+) doped strips or pixels on one side forming a pn-junction [54]. A full depletion bias voltage is applied to the sensor, causing the generated holes to drift along the electric field to the p^+ doped structures (backplane) while the electrons drift to the n^{++} backplane (structures). These charges are collected by capacitive-coupled aluminum readout strips and analyzed by external electronics. The readout chip, a custom *Application Specific Integrated Circuit (ASIC)* digitizes the signal. An illustration of this process is shown in figure 4.1 (taken from reference [54] in which more information can be found).

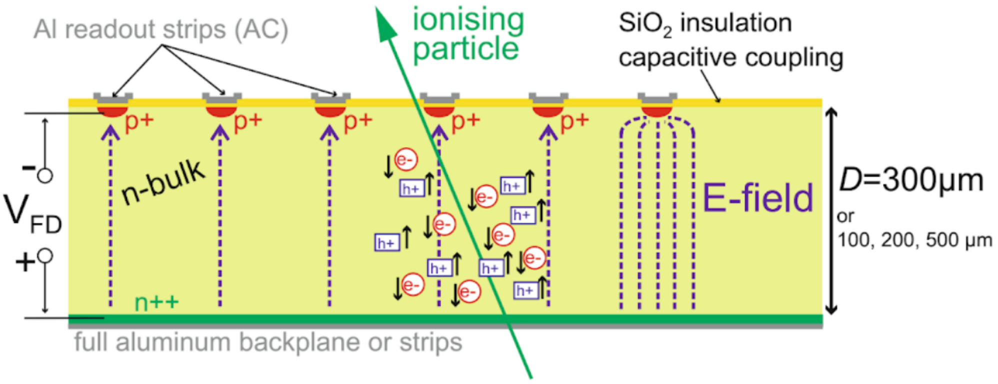

Figure 4.1: The working principle of p-in-n silicon detector, taken from reference [54].

4.2 Scintillators

In addition to ionization, the passage of a fast particle through a medium may excite some of the atoms in the medium to higher atomic levels. The emission of photons originated by the decay of these atoms to their ground state is called scintillation.

The materials which convert γ- and particle-radiation efficiently into light with a wavelength in or near the visible spectrum are referred to as scintillators. These materials are often used, together with a photo-detector, as scintillation detectors. The advantages of such detectors are sensitivity to the deposited energy and cheap and reliable construction and operation.

Although many materials show luminescence, an efficient scintillator is characterized by a high light yield, i.e high efficiency to convert the excitation energy into emission of light, a transparency with respect to its own scintillating light (no re-absorption) and a short decay constant for fast operation time.

There are two commonly used types of scintillators, inorganic crystals and organic scintillators, which are characterized by different scintillation mechanisms. In inorganic crystals, e.g. NaI, CsI

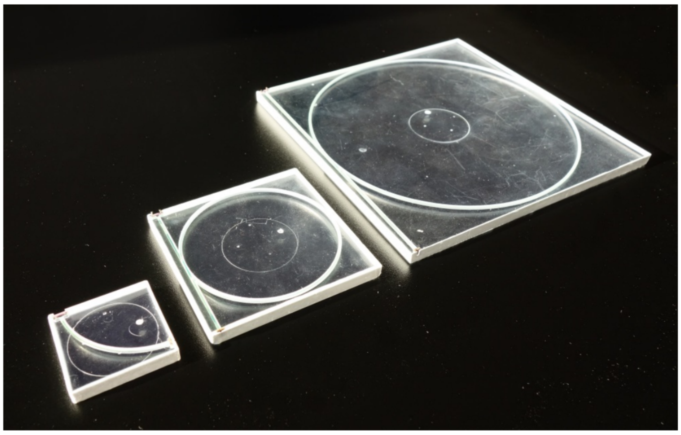

Figure 4.2: The different scintillator tiles used for the AHCAL readout [55]. In each tile, a SiPM coupled to a wavelength-shifting fiber is embedded. Left: $3 \times 3\,\mathrm{cm}^2$ tile. Middle: $6 \times 6\,\mathrm{cm}^2$ tile. Right: $12 \times 12\,\mathrm{cm}^2$ tile.

the scintillation arises due to the electronic band structure found in crystals. However, in organic materials the scintillating light arises from transitions in the energy levels of single molecules. Organic scintillators, often used as plastics, have as large advantages the ease of fabrication, low costs and short decay time (~1 ns). Plastic scintillators were selected as scintillating materials for the CALICE prototypes described in this thesis.

4.3 Silicon Photomultipliers

Silicon Photomultipliers (SiPM) [56] are semiconductor devices [57] for measuring photons in the visible and near-visible ranges with single-photon sensitivity. This relatively new concept of detection offers detectors with smaller size and lower operating voltage in comparison with the more conventional *Photomultiplier Tube (PMT)* detectors [58]. Furthermore, the detectors are insensitive to magnetic fields.

A SiPM consists of a pixel array of Avalanche Photo-Diodes (APDs) with a typical pixel size of $10 - 100\,\mu$m. Each pixel operates in Geiger mode, i.e. the applied reverse bias voltage $\mathrm{U_{bias}}$ is larger than the pixel breakdown voltage $\mathrm{U_{bd}}$. When a photon hits a pixel, an electron-hole pair in the depletion region is released and drifts apart due to the high electric field. Then, each pair ionizes the material along its path, generating more electron-holes pairs. This triggers a self-sustaining avalanche (*Geiger discharge*). Due to the arising current of the avalanche, a quenching resistor in each pixel reduces the effective voltage to below $\mathrm{U_{bd}}$ and therefore stops the avalanche and allows the pixel to recover. A pixel with a Geiger discharge is referred to as a *fired* pixel.

The pixels are connected in parallel to common anode and cathode leads resulting in a linear superposition of the pulses when two or more pixels are fired simultaneously. A similar response can be caused by photons which are created by a Geiger discharge and fire adjacent pixels, this phenomenon is called *optical inter-pixel crosstalk*.

The typical response of a SiPM is shown in figure 4.3b: the first peak is the pedestal created

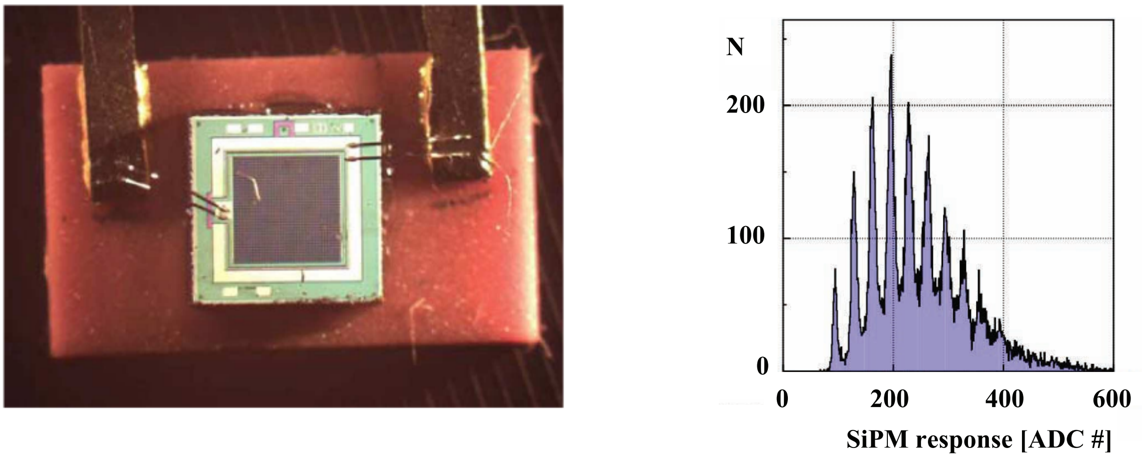

(a) (b)

Figure 4.3: (a) A magnified picture of the SiPM device used in the AHCAL physics prototype, consists of array of 34 × 34 pixels on an area of 1 mm^2. (b) The typical spectrum for low-intensity light [59] of the AHCAL SiPMs.

by random Geiger discharges initiated mostly by thermal excitations and by random noise in the readout electronics (*dark count*), the second peak corresponds to a single Geiger discharge, the third to two Geiger discharges and so on. The gain G of a SiPM is the number of output electrons per detected photon, typically of the order of 10^6. It is given by

$$G = C_{\mathrm{pix}} \cdot (U_{\mathrm{bias}} - U_{\mathrm{bd}}) / e \tag{4.1}$$

in which C_{pix} is the capacitance of a single pixel and e is the elementary charge, and can be measured by the difference between two adjacent peaks. When the U_{bias} is fixed, the gain decreases with increasing temperatures since the U_{bd} increases. Gain stabilization can be pursued tracking the changes of the U_{bd} and adjusting the U_{bias} accordingly or scanning the temperatures all along the measurement and implementing temperature correction in the offline analysis. Another parameter with a strong dependence on the temperature is the dark count rate, which rises with higher temperature and reduces the detector sensitivity and the dynamic range.

The photon detection efficiency is a key characteristic of a SiPM and it can be expressed as the product of three independent parameters: (a) the geometrical fill factor - the fraction between the active area, i.e. the total area occupied by the pixel array, and the total surface of the device, (b) the quantum efficiency - the probability that an incident photon inside the depletion region produces an electron-hole pair and (c) the Geiger efficiency - the voltage-dependent probability of a charge in the depletion region to trigger a Geiger discharge.

The number of incoming photons, the SiPM detection efficiency and the probability for optical inter-pixel cross talk determine the number of the photo-electrons $N_{\mathrm{ph.e.}}$, which are the electrons triggering the Geiger discharges. The SiPM response is not linear and saturates for a large $N_{\mathrm{ph.e.}}$ due to the limited pixel number and the recovery time of a pixel in the pixel array. In order to avoid biased measurements, saturation corrections must be implemented.

4.4 The Silicon-Tungsten Electromagnetic Calorimeter

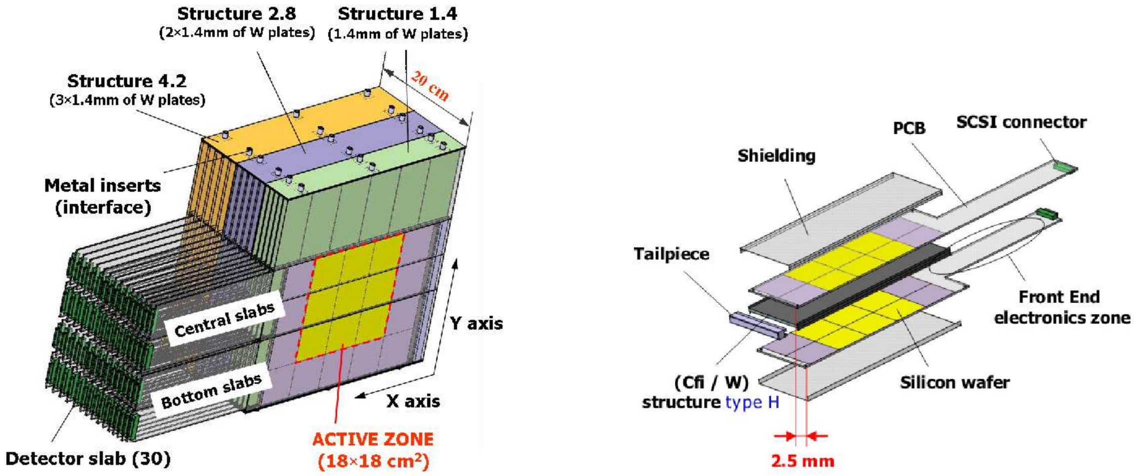

(a) (b)

Figure 4.4: (a) Schematic 3D views of the Si-W ECAL prototype. (b) Schematic diagram showing the components of a detector slab. Taken from reference [60].

The Si-W ECAL [60] is a sampling calorimeter optimized for measuring electromagnetic showers. The absorber structure of this detector consists of 30 layers of tungsten absorber layers arranged in three longitudinal sections, as shown in figure 4.4a. The tungsten layers of the first section are 1.4 mm thick to ensure a good energy resolution at low energy. The layers of the second and third sections are 2.8 mm and 4.2 mm thick, respectively. In total, the Si-W ECAL has a depth of 24.6 radiation length X_0 (1 nuclear interaction length λ_I) to contain high energy electromagnetic showers.

An alveolar composite structure is used for compactness and minimization of non-absorber passive material. This structure supports every second tungsten absorber plate, leaving free gaps between two layers to insert the detection units, called *detector slabs*. One detector slab, shown in figure 4.4b, has a sandwich structure consisting of a silicon layer and readout electronics shielded by a 0.1 mm aluminum foil on both sides of a tungsten layer [61].

Each silicon layer has an active zone of $18 \times 18\,\mathrm{cm}^2$ segmented into 3×3 silicon wafers. A wafer is used to make a module, consisting of 6×6 silicon pads which share a common anode. The silicon sensor size of $1 \times 1\,\mathrm{cm}^2$ is comparable with the tungsten Molière radius of 0.9 cm. To ensure full depletion with a bias voltage of 150 V, wafers with 5 kΩ·cm resistivity are used. The wafer thickness of 525 μm was chosen to obtain approximately 42,000 electron-holes pairs from a traversing MIP, reaching a signal-to-noise ratio of approximately 10 with the readout electronic noise of up to 4000 electrons.

The Si-W ECAL has in total 9720 readout channels. To equalize the channel response, a standard energy scale is assigned to the electronic read-out from the silicon active medium of each pad. This calibration, which is referred to as the MIP calibration, is preformed using muon beams, since muons with momentum from a few hundreds MeV to a few tens GeV lose their energy only by ionization

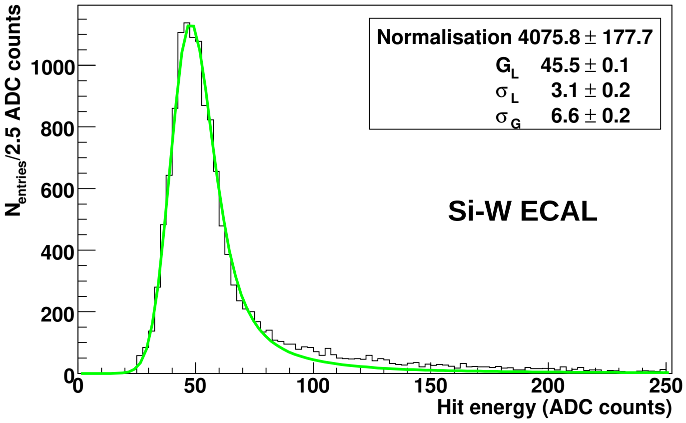

Figure 4.5: The distribution of hit energies in muon events for a particular Si-W ECAL channel. The distribution is fitted with a convolution of a Gaussian and a Landau distribution. The fit parameters are detailed in the legend: normalization, G$_L$ and σ_L refer to the constant value, MPV and width of the Landau function, respectively, while σ_G refers to the width of the Gaussian function [60].

and have minimal ionization energy loss rates, as shown in figure 3.4. The beam is projected on the whole surface of the prototype and the response of each channel is recorded. As a first step, the pedestal peak of each channel, defined by the mean value of the signal recorded with no beam (i.e. coming from electronics) and the corresponding standard deviation, is subtracted from the raw data. Then, selection of muon events is performed as detailed in [60] and the distribution of the remaining signals (in *Analog-to-Digital Converter (ADC)* counts) is fitted with a convolution of a Landau distribution and a Gaussian. A conversion factor to MIP equivalent energies is given by the MPV of the Landau function. An example of the channel calibration procedure (after subtracting the pedestal) is shown in figure 4.5 [60].

4.5 The Analog Hadron Calorimeter

The AHCAL [59] is a highly granular scintillator-steel sampling calorimeter. It is the first detector to use and test the SiPM technology on a large scale in high energy physics. The detector has 7608 scintillator cells spreading over an active area of $90 \times 90\,\text{cm}^2$. It consists of 39 steel absorber layers with an average thickness of 17.4 mm, which are separated by 38 active layers of plastic scintillator tiles. All scintillator tiles in a layer are housed inside a rigid cassette, which is a closed box with steel sheet top and bottom covers, each with a thickness of 2 mm. Considering the alternating structure, the total absorbing material per layer amounts to 21.4 mm. The total thickness of the AHCAL is 5.3 λ_I (47.2 X_0). A picture of all the layers installed is shown in figure 4.6a.

The scintillator tiles are 5 mm thick and their size varies between $3 \times 3\,\text{cm}^2$, $6 \times 6\,\text{cm}^2$ and $12 \times 12\,\text{cm}^2$, as shown in figure 4.2. In each tile, a SiPM coupled to a *wavelength-shifting (WLS)* fiber is embedded. The first 30 active layers contain 216 scintillator tiles with $3 \times 3\,\text{cm}^2$ tiles in the layer core (for an optimal two-particle separation capability [62]), three rings of $6 \times 6\,\text{cm}^2$ tiles around the core and an outer ring of $12 \times 12\,\text{cm}^2$ tiles. This structure is shown on figure 4.6b. The last

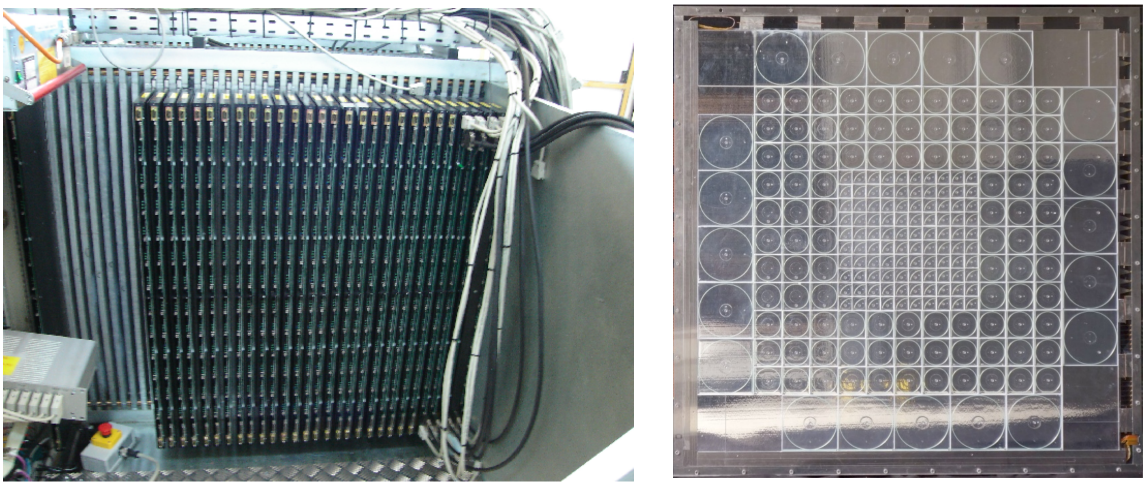

(a) (b)

Figure 4.6: (a) The AHCAL steel stack support with active layers installed [63]. (b) An active layer of the AHCAL prototype, showing the arrangement of different sized tiles [55].

eight layers contain 141 scintillator tiles of $6 \times 6\,\mathrm{cm}^2$ and $12 \times 12\,\mathrm{cm}^2$.

The SiPMs in use are characterized by an active area of $1.1 \times 1.1\,\mathrm{mm}^2$, which consists of 1156 pixels, each $32 \times 32\,\mu\mathrm{m}^2$ in size. A reverse bias voltage of $\sim$50 V, a few volts above the breakdown voltage, is chosen to ascertain a large dynamic range with a good signal-to-noise ratio. Each pixel in the SiPM has a capacitance of 50 fF and a quenching resistor of $0.5\,\mathrm{M}\Omega$ to $20\,\mathrm{M}\Omega$, yielding a recovery time of $25 - 1000$ ns [64].

The AHCAL is operated in two modes:

- *calibration mode* (CM): a readout electronics mode with a high amplification factor and a short pulsing time in which calibration of each individual SiPM is preformed using *Light-Emitting Diode (LED)* light with pulse intensities of single photon emission up to full saturation of the SiPM.

- *physics mode* (PM): a readout electronics mode with a longer pulsing time and lower amplification factor, which is used for beam-data measurements.

In both modes the readout is given in ADC units, however, due to the different setting, the readout units of the calibration and physics modes are referred to as $\mathrm{ADC}^{\mathrm{CM}}$ and $\mathrm{ADC}^{\mathrm{PM}}$, respectively.

Calibration Procedure

In the calibration mode a LED system is used to measure the single photo-electron spectrum and the response of each SiPM in the calorimeter, for evaluation of the gain and correction of non linearity and saturation effects. The single photo-electron spectrum is fitted with a multi-Gaussian function and the gain G_i^{CM} is extracted from the distance between the pedestal and second peak divided by two. The SiPM response is measured over the entire dynamic range (zero to saturation) and described by the response function f_{CM}, which gives the number of fired pixels as a function of the number of incoming photons.

In the physics mode, a calibration of the cell response and cell-to-cell equalization is performed using a broad muon beam to illuminate the entire front face of the AHCAL. Muon events per cell i are selected (after pedestal subtraction from the raw data) as detailed in [59] and the $\mathrm{ADC}^{\mathrm{PM}}$ distribution is fitted with a convolution of Landau and Gaussian functions. The MPV of the fit determines the MIP calibration factor C_i^{MIP}. To account for temperature variations of both the gain and the photo detection efficiency, the visible energy is scaled by -3.7%/K to the average temperature of each measurement [64].

In order to extrapolate the calibration measurements such as gain correction to physics events, an inter-calibration factor between the two operation modes is necessary. On that account, the response function f_{PM} is measured in the physics mode and the given ratio of f_{CM} and f_{PM} provides the inter-calibration factor I_i of channel i in units of $\mathrm{ADC}^{\mathrm{CM}}/\mathrm{ADC}^{\mathrm{PM}}$.

For beam measurements in the physics mode, each SiPM signal A_i^{PM} in $\mathrm{ADC}^{\mathrm{PM}}$ units is accounted for its non linearity and converted to MIP units. This procedure includes the following steps:

1. Converting the signal units from $\mathrm{ADC}^{\mathrm{PM}}$ units to the number of fired pixels in the calibration mode using the following relation:

$$A_i^{\mathrm{CM}}\,[\mathrm{pix}] = \frac{A_i^{\mathrm{PM}} \cdot \mathrm{I}_i}{G_i^{\mathrm{CM}}(T)} \tag{4.2}$$

2. Applying the inverse response function f_{CM}^{-1} to obtain the number of incoming photons in calibration mode:

$$f_{\mathrm{CM}}^{-1}\left(A_i^{\mathrm{CM}}\,[pix]\right) \tag{4.3}$$

3. Converting the results back to $\mathrm{ADC}^{\mathrm{PM}}$ units by using the gain calibration, the inter-calibration factor and the MIP calibration factor:

$$A_i^{\mathrm{PM}}\,[\mathrm{MIP}] = \frac{f_{\mathrm{CM}}^{-1}\left(A_i^{\mathrm{CM}}\,[pix]\right) \cdot G_i^{\mathrm{CM}}}{C_i^{\mathrm{MIP}} \cdot \mathrm{I}_i} \tag{4.4}$$

4.6 The Tail Catcher and Muon Tracker

The TCMT [65] is a scintillator-steel sampling calorimeter designed for detecting muons and tails of hadronic showers. The prototype consists of 16 steel absorber plates divided into a fine section with 8 layers of 21 mm thick plates and a coarse section with 8 layers of 102 mm thick plates. The active layers of $100 \times 100\,\mathrm{cm}^2$ are formed by $100 \times 5\,\mathrm{cm}^2$ plastic scintillator strips with a thickness of 5 mm, which are assembled in 16 modules. They are installed between the absorber plates, alternating between horizontal and vertical orientation in adjacent layers. The light produced in each strip is guided by a WLS fiber to a SiPM. In total, the detector has 320 channels over a depth of 5.8 λ_I.

Channel responses are equalized with a broad muon beam, similarly to the other prototypes, converting each channel ADC count to MIP units. The pedestal is subtracted from the raw data and a muon sample is selected as detailed in [65]. Each ADC distribution is fitted with an asymmetric Gaussian function with a limited range to the right of the peak, setting the MPV as the MIP calibration constant of the channel. The SiPMs calibration, the correction of SiPM signal and the full conversion to MIP units use the same procedures described in the previous section for the AHCAL SiPMs.

4.7 Test Beam Experiments

The full calorimeter system of the Si-W ECAL, the AHCAL and the TCMT amounts to an approximate depth of 12 λ_I with 17648 readout channels in total. This system, presented in figure 4.7(a), was installed in CALICE test beam experiments at CERN in 2007 and at FNAL in 2008. For CERN test beam, from 6 GeV to 180 GeV, the H6 beam line of the *Super Proton Synchrotron (SPS)* north area was used. The SPS provides a proton beam of up to 400 GeV, which is directed on a fixed target to produce a beam of secondary particles: protons, electrons, pions and muons. Tuning magnets, collimators and absorbers were selected and adjusted from the control room to modify beam momentum, particle species and electric charge. The FNAL experiment was operated in section MT6-2B of the MTest beam line, where a primary proton beam of 120 GeV is used [66]. Several targets, absorbers and collimators can be arranged in different configurations to produce different operation modes: the *proton mode* of 120 GeV protons, the *pion mode* of 8 − 60 GeV pions and the *low energy pion mode* of 1 − 32 GeV pions, electrons, kaons and broadband muons.

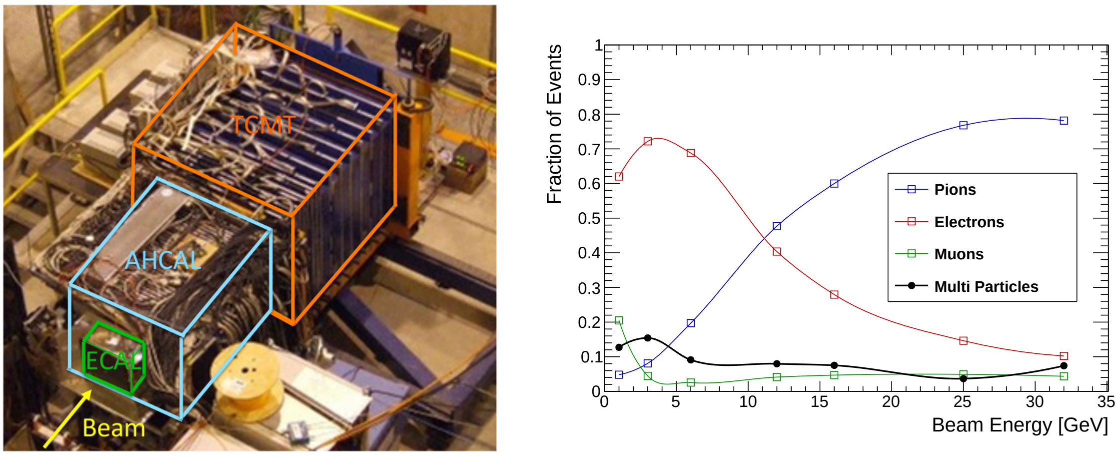

(a) (b)

Figure 4.7: (a) The CALICE detector at the CERN test beam in 2006. The Si-W ECAL, the AHCAL and the TCMT are traced by the labeled green, blue and orange outlines, respectively [59]. (b) The beam composition of low energy pion mode in the FNAL MTest beam line as a function of beam energy [55].

Particles produced by the low energy pion mode are selected for momentum and polarity by a configurable dipole and a collimator setup. Since no other direct selection of the particle type is offered, the delivered particle beam is a mixture of mostly electrons, pions and muons in varying

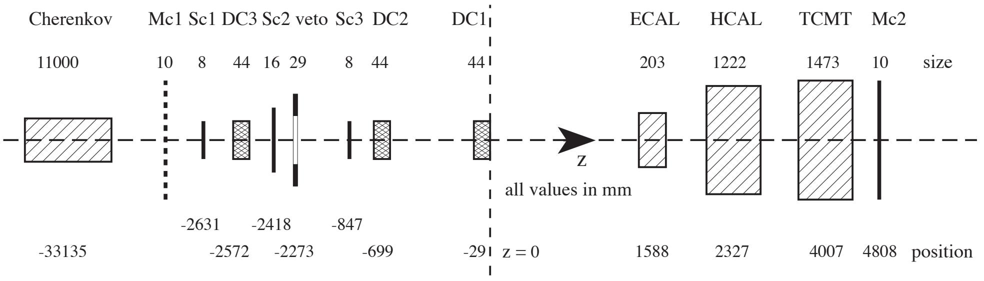

Figure 4.8: CALICE experimental setup at the CERN SPS H6 beam line (top view) [70]. Mc1 and Mc2 are the large muon counters; Sc1, Sc2 and Sc3 are the scintillator triggers; DC1, DC2 and DC3 are the delay wire chambers. The figure is not to scale.

fractions, depending on the beam energy. Measurements with the CALICE setup consisting of the *Scintillator Electromagnetic Calorimeter (ScECAL)* [67], the AHCAL and the TCMT were used to estimate the beam composition of the low energy pion mode. The beam composition as a function of the beam energy is shown in figure 4.7(b). This estimation was done offline by means of selecting muon events, electron events, pion events and multi-particle events (events with more than one incident particle) [29, 66].

In the energy ranges considered in this thesis, the hadronic component of the beams at CERN and FNAL consists primarily of pions, with less than 10% admixture of other hadronic species [68]. However, at energies of 10 GeV and below, electrons dominate the total particle content of the beam at FNAL [69]. For the CERN beam, the muon mixture varies from energy to energy due to effects of the beam optics, with values in excess of 30% in the region of 35 GeV [70].

Since the beam cannot be completely pure, additional detectors such as Cherenkov detectors or a muon veto are used to identify events with the desired particles. The CALICE setups at CERN and FNAL include a muon trigger downstream of the TCMT for muon tagging and a Cherenkov detector for beam particle identification. Additional auxiliary detectors are used for triggering and tracking: two coincidence scintillation plates provide the beam trigger, delay wire chambers determine the position of the beam particles and a veto wall rejects beam halo events. A schematic view of the beam line setup at CERN test beam facility is shown in figure 4.8 [70]. The FNAL setup includes also an analogue multiplicity counter for identifying multi-particle events (see the use of this counter in the offline analysis in figure 5.1). A detailed description and scheme of the FNAL setup can be found in [71].

In both experiments, the coordinate system used for recording the data is right handed with the Z axis pointing into the beam direction. In this dissertation, the detector layers are numbered from 0 to 83: layers 0 to 29 are Si-W ECAL layers, layers 30 to 67 are AHCAL layers and layers 68 to 83 are TCMT layers. The visible signal in each of the detector cells is measured in MIP units (see previous sections). To eliminate electronic noise, only cells in which the signal exceeds half a MIP are considered, these are referred to as *hits*. The total energy of the setup is calculated in GeV units, as described in section 6.1.

4.7.1 Simulation of Test Beam Experiments

The CALICE test beam experiments at CERN and FNAL are simulated with a GEANT4-based software (see section 3.5) for a better understanding of the data as well as for validation and optimization of the simulation models in use. The full geometry of the test beam setups, which includes the calorimeters and the auxiliary detectors, is modeled in the Mokka framework [72], which is a Monte Carlo application based on GEANT4. Details concerning the simulation procedure for the Si-W ECAL and the AHCAL can be found in [61] and [64], respectively.

For an accurate comparison between data and simulation, realistic detector effects need to be included in the simulation. Mokka includes corrections for the saturation effects of high ionization densities in scintillating materials, which are modeled using Birk's law [73]. Furthermore, the simulation is implemented with timing constrains resembling the integration time of the readout electronics of each detector to reject late energy depositions in hadronic showers, which are usually not measured in data.

Additional detector characteristics are applied to the Mokka simulation during the reconstruction phase by performing the appropriate digitization procedure for each of the sub-detectors. The goal of the digitization is to bring the simulation hits to a similar state as the raw data, so that the hits are reconstructed in the same way as the real data. Since Mokka output is given in units of GeV, the digitization procedure includes conversion of the signal to MIP units for consistency with the calibration process of real data.

The digitization process of the Si-W ECAL is detailed in [61]. In this process, noise is added by smearing of the raw energy depositions in the Si-pads, using a Gaussian function with a mean value of 0.13 MIP and a dispersion of 0.012 MIP, as was measured in the data [61].

The digitization of the AHCAL is described in detail in [29, 64]. The process includes the following steps:

- Realistic detector granularity: Summing up several neighboring virtual grid cells of 1 X 1 cm^2 size that Mokka uses to obtain signals of the actual size of 3 X 3 cm^2, 6 X 6 cm^2 or 12 X 12 cm^2 tiles.

- Light cross-talk between neighboring tiles: simulating the inter-tile light cross-talk by distributing a fraction of the scintillating light in each cell to all neighboring cells. This fraction is taken as 2.5% per 3 cm tile edge, as was measured with two tiles on a test bench.

- Conversion from GeV to MIP scale: using a conversion factor of 0.1225 MIP/MeV, which is estimated from muon beam simulations, to transfer the signal to MIP units.

- Non linearity in the SiPM response: converting the units again, from MIP units into number of fired SiPM pixels, by using the measured light yield for each individual channel and applying the suitable response function f, which is evaluated from the data, to each channel.

- Statistical fluctuations on the pixel scale: the number of firing pixels is smeared with a Poisson distribution to account for statistical fluctuations of the pixel statistics. After this step, the signal is converted to ADC units.

- Readout electronic noise: The noise of the SiPM and the readout system is added to each calorimeter cell by adding the pedestal subtracted amplitude of random trigger events (from the same run that is simulated) to the amplitude of the cell.

A similar process following the same basic ideas is used for the TCMT.

CHAPTER 5

SELECTION OF PION EVENTS

The performance of a full calorimeter system can be best evaluated with a hadron beam. Hadrons which enter the system, would typically deposit significant fractions of their energy in all detector parts. The current analysis uses data of negative pion beams with energies ranging between 4 GeV and 80 GeV. This data was taken with the full calorimeter system consisting of the Si-W ECAL, the AHCAL and the TCMT at CERN and FNAL test beam facilities. The datasets used in this analysis are described in section 5.1.

This study addresses detection in a full calorimeter system and therefore uses either events in which the possible shower starts in the Si-W ECAL and extends to the AHCAL or events with a primary track in the Si-W ECAL and a possible shower-start in the AHCAL. For the selection of single pion events two sets of cuts are applied: starting with the *quality cuts*, described in section 5.2, to increase the purity of the sample and continuing with cuts optimized for *pion selection* in section 5.3.

5.1 Datasets

In this analysis, CERN data of beams of 10 GeV to 80 GeV and FNAL data of beams of 4 GeV to 60 GeV are used. Table 5.1 summarizes the runs used for the analysis and gives the number of events with a beam trigger and the number and percentage of selected events for each run. For validation studies, most of the runs are simulated using the simulation software Mokka with GEANT4 version 10.1 and FTFP BERT and QGSP BERT physics lists.

Since the data are taken in two test beam experiments under different conditions and with different beam structures and energy ranges, different sets of calibration factors, from MIP to energy units, are derived and applied to energy depositions in CERN and FNAL events (see section 6.1).

The reconstruction methods, which are detailed in the next chapter, are applied separately to CERN and FNAL events. Different runs taken with the same initial momentum in the same test beam experiment are merged in the reconstruction process. From this, a separated evaluation of the detection system performance in the different experiments is given. To study the full energy range, the reconstruction methods are applied to all the events of both experiments, which are referred to as the *combined* data. In this case as well, the respective energy-calibration factors are applied

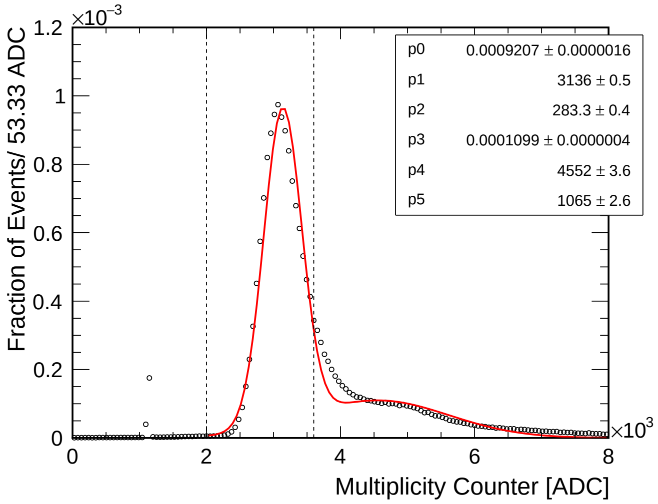

Figure 5.1: A distribution of FNAL multi-particle counter signal from the entire FNAL data. The first peak originates from single particle events, while the second peak originates from multi-particle events. The distribution is fitted to a multi-Gaussian function (red solid line). The fit parameters are given in the legend: p0 (p3), p1 (p4), p2 (p5) are the constant, the mean and the sigma values of the first (second) peak. The vertical lines at 2000 ADC and 3600 ADC indicate two of the event selection cuts: the empty event and the multi-particle cuts, respectively.

to CERN and FNAL events. Measurements of CERN and FNAL events with the same initial momentum are reconstructed separately and therefore produce two results, which are then averaged when evaluating the system performance in the full energy range.

5.2 Quality Cuts

Several cuts are applied as a first step to improve the purity of the data sample, rejecting noise and unidentified events, reducing contamination of electron and multi-particle events and removing events with a high probability for substantial longitudinal or lateral leakage.

Noise Reduction: The first criterion to remove noise events is given by the beam trigger, which is defined by the coincidence signal of two plastic scintillator counters, as described in section 4.7. Hence only events with valid beam trigger are analyzed. Then, events with more than 100 hits in a single Si-W ECAL layer are rejected, as well as events with more than 7 hits in a particular noisy wafer (wafer in the bottom section of the 29th layer [74]) or simultaneous hits in two particularly noisy pads of this wafer. Moreover, in each event, individual hits in the Si-W ECAL are removed, when no hit in the 26 neighboring pads (eight from the same layer and nine from each adjacent layer) is found.

Empty Events Rejection: Empty events, namely events with only partial detection of the incoming particle, are removed from the sample in several steps. First, events with a total reconstructed energy, E_{reco}, lower than 15% of the known beam energy, E_{beam} are removed. Then, particles which hit the Si-W ECAL at a large angle near the acceptance limits are rejected by requiring

Table 5.1: Summary of the data samples, giving the number of events with a beam trigger $N_{\text{Events}}^{\text{full}}$ and the number of events entering the analysis after event selection $N_{\text{Events}}^{\text{selected}}$. Runs starting with 330 refer to CERN datasets and runs starting with 500 refer to FNAL datasets.

Run Number	Energy [GeV]	$N_{\text{Events}}^{\text{full}}$	$N_{\text{Events}}^{\text{selected}}$	$\frac{N_{\text{Events}}^{\text{selected}}}{N_{\text{Events}}^{\text{full}}}$ [%]
330332	10	127465	47701	37.4
330643	10	88322	35998	40.8
330328	15	113246	53713	47.4
330327	18	107897	56599	52.5
330649	20	78543	46299	58.9
330325	25	90439	52353	57.9
330650	25	70735	41841	59.1
330551	35	103217	55650	53.9
330960	35	68181	38832	56.9
330390	40	78012	49262	63.1
330550	45	86423	50367	58.3
330961	45	58252	37893	65.0
330391	50	69159	45771	66.2
330392	80	57188	33795	59.1
330962	80	47633	31573	66.3
500778	4	8371	2075	24.8
500779	4	94252	24564	25.3
500780	4	97810	24503	26.1
500868	6	97742	35245	36.1
500666	8	131164	45815	34.9
500656	8	30343	10410	34.3
500642	10	131444	49532	37.7
500644	12	135487	58185	42.9
500650	15	25335	9752	38.5
500679	20	27363	11899	43.5
500881	30	88270	36104	40.9
500811	60	6071	2623	43.2

a minimum of 25 hits in the Si-W ECAL [75]. An additional selection in the FNAL sample is done via the information available from the multiplicity counter. Storing the signal of this detector in a histogram for all the events in the FNAL data sample, it is possible to fit a multi-Gaussian function, as shown in figure 5.1. The first peak originates from single particle events, while the second peak originates from multi-particle events. Events with a signal more than ~4 σbelow the mean value of the first particle peak are rejected (corresponds to 2000 ADC counts).

Lateral Shower Leakage Reduction: In order to avoid selecting events in which there may be lateral shower leakage, the barycentres (energy-weighted mean positions) $\overline{x}$ and $\overline{y}$ of all the hits in the Si-W ECAL volume are calculated:

$$\overline{x} = \frac{\sum\limits_{\text{hits}} x_{\text{hit}} \cdot \text{E}_{\text{hit}}}{\sum\limits_{\text{hits}} \text{E}_{\text{hit}}} \quad \text{and} \quad \overline{y} = \frac{\sum\limits_{\text{hits}} y_{\text{hit}} \cdot \text{E}_{\text{hit}}}{\sum\limits_{\text{hits}} \text{E}_{\text{hit}}} \tag{5.1}$$

and are required to lie in the central part of the detector: -50 mm < $\overline{x}$ < 50 mm and -50 mm < $\overline{y}$ < 50 mm.

Multi-Particle Rejection: The initial multi-particle rejection is performed in several steps. An algorithm based on the Primary Track Finder algorithm [76] is used to reconstruct the primary track in each event. A primary track is not identified when several parallel incoming tracks are identified in the layers before the shower starting position or in case of a shower starting in the first two layers of the Si-W ECAL. Events without a reconstructed track are rejected. In addition, the selection of FNAL events uses the multi-particle counter distribution, which is shown in figure 5.1. Events with a signal that is at least 1.64 standard deviations greater than the mean value of the single particle peak are rejected (corresponds to 3600 ADC counts).

Electron Event Rejection: Rejection of electron events from the 4 GeV − 30 GeV FNAL data sample is performed using the information recorded by the Cherenkov detector veto. A further removal of the electron contamination for CERN and FNAL test beams is performed and described in sub-section 5.3.2.

The effect of these quality cuts is shown in figure 5.2 for 10 GeV pion beams recorded at CERN and FNAL. In order to combine the energy contributions from the different calorimeters, the calibration procedure detailed in sub-section 6.1 is used for reconstructing the energy in GeV units*. The figure presents the independent energy distributions of different rejected events along with the energy distributions before and after the cuts are applied.

---

*There are several methods to reconstruct the energy. For selecting events, a simple sum of the calibrated contributions of the sub-detectors is computed.

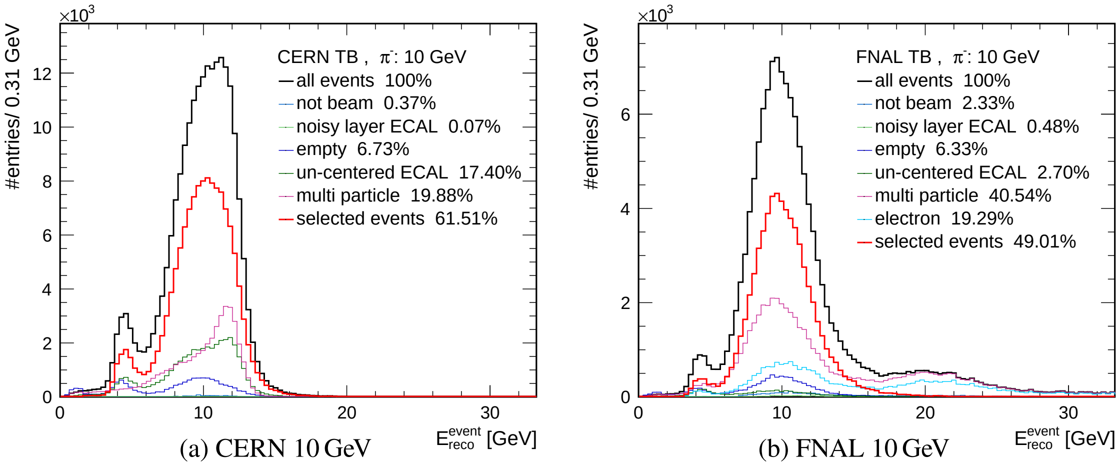

(a) CERN 10 GeV (b) FNAL 10 GeV

Figure 5.2: First selection of 10 GeV events with the quality cuts. Black: energy distribution of the raw data. Red: energy distribution of after applying quality cuts. Other colors: energy distributions of different rejected events, the percentage of these events of the full sample is given in the legend.

5.3 Pion Selection

For the purpose of pion selection, additional conditions are required to suppress multi-particle, electron and muon events and to avoid events with a high probability of substantial leakage. These additional conditions are as follows:

5.3.1 Clustering for Multi-Particle Rejection

One particular class of multi-particle events is an event in which two aligned particles enter the Si-W ECAL simultaneously. To reject such events, a clustering algorithm is used to cluster hits in the first 8 layers of the Si-W ECAL calorimeter. The algorithm introduces a distance criterion d_{th} which is calculated from the three dimensional distance between centers of those cells that carry a signal. The optimal value for d_{th} was found to be 12 mm [74]. Neighboring hits within this distance are merged into a single cluster, with a minimum requirement of three hits to form such cluster. Events with multiple beam-aligned clusters or without any beam-aligned cluster are rejected.

5.3.2 First Hadronic Interaction Layer

The layer of the *First Hadronic Interaction (FHI)* is characterized by a significant increase of the total deposited energy compared to the previous layers. The reconstruction process of the FHI layer in the full calorimeter system uses several techniques for which detailed descriptions can be found in appendix A.

In order to suppress electron events and events with particle showers upstream of the calorimeters, all events with a reconstructed FHI layer < 5 are rejected. In addition, to avoid late-starting showers with a high probability for longitudinal leakage and showers that primarily develop in the less granular part of the setup, only events with FHI layer < 56[†] are selected.

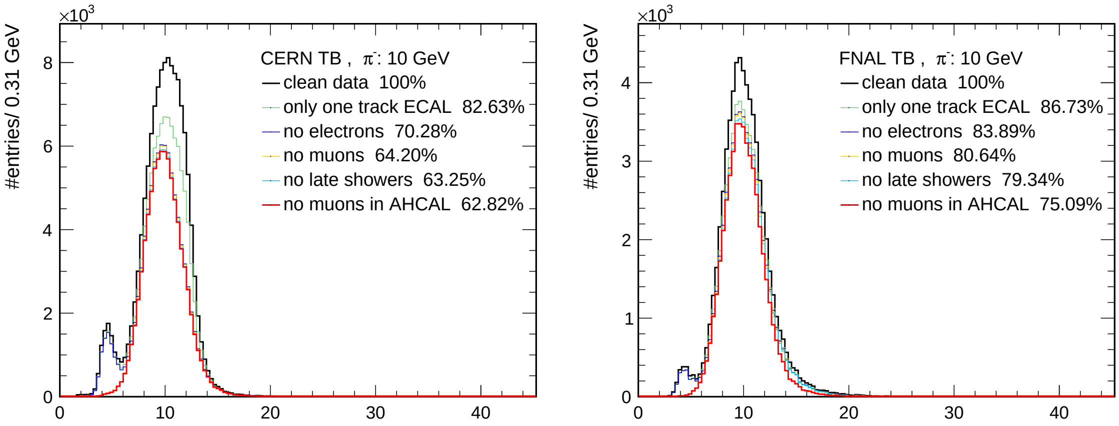

(a) CERN 10 GeV (b) FNAL 10 GeV

Figure 5.3: Pion selection of 10 GeV data events. Black: energy distribution of "clean data", corresponds to the result after the quality cuts shown in figure 5.2. Red: energy distribution of selected events. Other colors: energy distributions of different steps of the applied pion selection, the event percentage for the these steps is given in the legend.

5.3.3 Muon Contamination

The muon contamination is divided into two categories: single-muon events and multi-particle-events in which one particle is a muon. The former are rejected by removing events with depositions along the calorimeters without an identified FHI layer, since muons travel through the detector without producing showers. In addition, low-energy muons, that travel only through some of the layers, are suppressed in events with $E_{beam} \geqslant 15$ GeV by removing events with a reconstructed energy lower than $E_{beam}/2.6$, a threshold based on cut optimization.

Muons as additional particles can enter the calorimeter system through the Si-W ECAL or outside of its coverage ($x > 90$ mm, $x < -90$ mm, $y < -90$ mm or $y > 90$ mm) through the AHCAL. The clustering process described in sub-section 5.3.1 removes the Si-W ECAL muons, while further steps are required for rejecting the AHCAL muons. These muons are recognized and removed if their initial detection is in the first three layers of the AHCAL and (a) a track of at least 5 consecutive hits in the same transverse position (including one layer gap after a minimum of two hits) is reconstructed or (b) the total number of hits in this position exceeds 25 (in reference [59] the mean value of muon hits in the AHCAL was evaluated to be 26 hits).

Figure 5.3 shows the pion selection for 10 GeV beams in CERN and FNAL, depicting the energy distributions of the clean data, i.e. after the quality cuts were applied (corresponding to the red distribution in figure 5.2), and selected events.

[†] Layer 56 is the 27th layer of the AHCAL in which the particles reach a depth of approximately 4.7 λ_I in the full system.

5.4 Events with Anomalously High Visible Energy

The distributions of selected events show a slight asymmetric behavior with a tail towards high energies, including events with a reconstructed energy up to approximately 10 GeV higher than the beam energy. This tail, particularly prominent on a logarithmic scale, can be reproduced as well in distributions of simulated events (both physics lists) and therefore arises from physics processes rather than beam contamination. To understand this feature, the fraction of hits with signals larger than a moving threshold E_{hit} is calculated for three event samples:

1. Full sample: all selected events.
2. Central events: selected events with reconstructed energy in an interval of 20% relative deviation off the mean energy.
3. Tail events: selected events with reconstructed energy shifted by 10 GeV with respect to the energies of the central events.

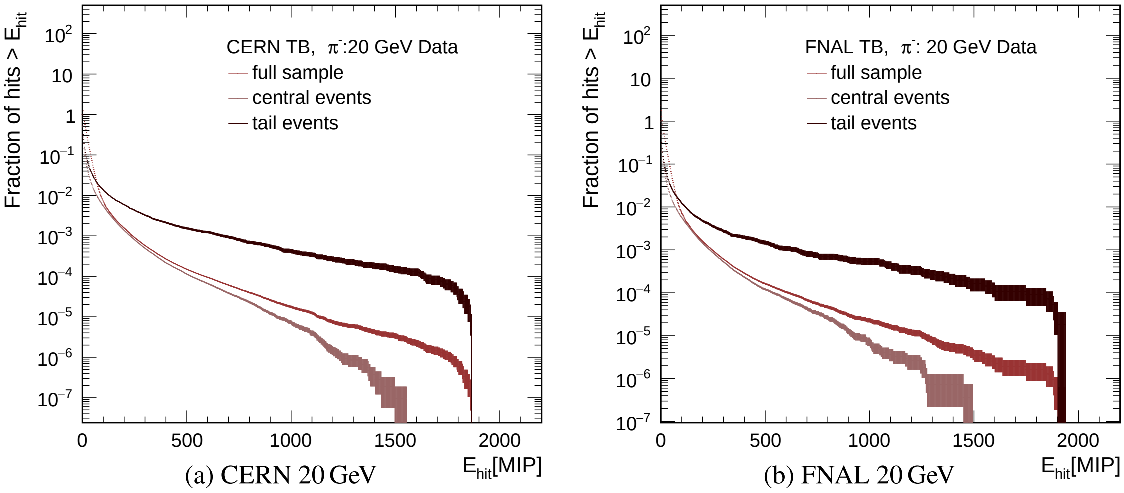

(a) CERN 20 GeV (b) FNAL 20 GeV

Figure 5.4: The fraction of hits larger than a moving threshold E_{hit} calculated for all selected events (red), central events (light brown) and tail events (dark brown) recorded at CERN (left) and FNAL (right) with 20 GeV beams.

Figure 5.4 presents an example of these distributions for all hits in the calorimeter system as a function of the moving threshold for 20 GeV data events (simulated events result in figures with similar trends). The fraction of hit signals larger than 500 MIP[‡], which corresponds to 2.4 GeV in the Si-W ECAL, is larger by several orders of magnitude for tail events than for central events, hence the possibility to explain tail events as multi-particle event is excluded. Since the hit fraction for higher thresholds is fairly low, it seems that the large reconstructed energy of tail events is dominated by a few hits responsible for large depositions. This scenario can occur when a nuclear interaction

---

[‡] Including the correction for the varying thickness of the absorber layers in the Si-W ECAL and the TCMT, as explained in sub-section 6.1.

takes place right at the edge of an absorber plate, leading to direct detection of a nuclear fragment or other highly charged particles in the subsequent active layer.

CHAPTER 6

RECONSTRUCTION METHODS

In this analysis, three sampling calorimeters with different geometries and different readout technologies are used concurrently to detect single pion events. The advantages of the use of sampling calorimeters and calorimeter systems were discussed in section 3.3, while the complexity of the detection of hadronic showers was discussed in section 3.4. The calorimeters and the test beam construction were described in details in the previous chapter.

In such a system, energy reconstruction is a significant challenge. To reconstruct the pion energy in energy units from the visible energy of each sub-detector (MIP units), weights are applied to the energy depositions. The reconstructed energy per event $\mathrm{E}_{\mathrm{reco}}^{\mathrm{event}}$ is determined by the sum of all the weighted depositions. The weights are derived differently from one reconstruction method to another, however for any chosen energy reconstruction algorithm, they can be optimized by minimizing the quadratic sum of the residuals of the reconstructed event energy to the known beam energy, resembling a χ^2 function:

$$\chi^2 = \sum_{\mathrm{events}} \frac{\left(\mathrm{E}_{\mathrm{reco}}^{\mathrm{event}} - \mathrm{E}_{\mathrm{beam}}^{\mathrm{event}}\right)^2}{\left(55\%\sqrt{\mathrm{GeV}}\right)^2 \cdot \mathrm{E}_{\mathrm{beam}}^{\mathrm{event}} \cdot \mathrm{N}_{\mathrm{beam}}^{\mathrm{events}}}. \tag{6.1}$$

The term $\left(55\%\sqrt{\mathrm{GeV}}\right)^2 \cdot \mathrm{E}_{\mathrm{beam}}^{\mathrm{event}}$ in the denominator refers to the square of the expected energy resolution, with a stochastic term of $55\%/\sqrt{\mathrm{E}_{\mathrm{beam}}/\mathrm{GeV}}$ and the term $\mathrm{N}_{\mathrm{beam}}^{\mathrm{events}}$ representing the number of selected pion events with the same energy.

This chapter presents the different reconstruction algorithms used in this analysis: section 6.1 discusses the calibration of the sub-detector contributions to energy units, section 6.2 introduces the standard reconstruction method with different weights for the primary track hits and section 6.3 details the software compensation method. Details about the systematic uncertainties which are included in the analysis are found in section 6.4.

6.1 Energy Calibration

The signals of each sub-detector are given in MIP units (as was discussed in sections 4.4, 4.5 and 4.6). To equalize the sub-detector responses, calibration factors from MIP to GeV units are determined for each technological or geometrical distinct region of the system.

In this analysis, the same calibration is applied to the AHCAL and the TCMT, since these calorimeters use the same active and passive materials and have essentially the same longitudinal sampling structure; therefore, two calibration factors, one for the Si-W ECAL and one for the AHCAL and the TCMT, are determined in two steps. First, for each beam energy, the minimization of the χ^2 function in equation 6.1 is used, where the reconstructed energy for a given event is defined as

$$\mathrm{E}_{\mathrm{reco}}^{\mathrm{event}} = C_{\text{Si-W ECAL}} \cdot \sum_{j}^{\text{hits}} c_t \mathrm{E}_j^{\text{Si-W ECAL}} + C_{\text{AHCAL}} \cdot \left(\sum_{j}^{\text{hits}} \mathrm{E}_j^{\text{AHCAL}} + \sum_{j}^{\text{hits}} c_t \mathrm{E}_j^{\text{TCMT}} \right). \tag{6.2}$$

Here, hits of each sub-detector are summed and weighted using the calibration factors $C_{\text{Si-W ECAL}}$ and C_{AHCAL}. In addition, another factor c_t is used in order to take into account the varying thickness of the absorber structure in the Si-W ECAL and in the TCMT. In the Si-W ECAL, c_t is 1, 2 and 3 for the first, second and third longitudinal segment, respectively, and in the TCMT it is 1 and 5 for the first and second longitudinal segment. Moreover, the difference between the thickness of the odd and even layers in the Si-W ECAL is corrected by adding 7.2%* to the calibration of the odd layers, as was measured in reference [61].

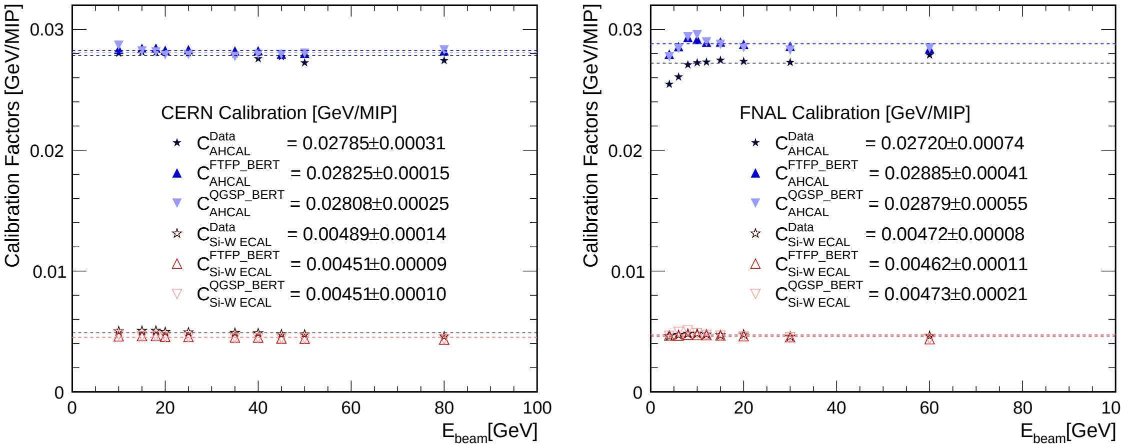

Figure 6.1: The results of the calibration process for CERN (left) and FNAL (right) data. Red: The calibration factors for the Si-W ECAL hits. Blue: The calibration factors for the AHCAL and the TCMT hits. The average factors are marked by the corresponding dashed lines. The 4 GeV data-points are excluded from FNAL average to prevent bias. The statistical uncertainties are smaller than the marker size.

The obtained calibration factors show a slight energy dependence, with deviations on the level of 1%-3% over the energy ranges considered here. A set of global calibration factors is determined by averaging the factors over all energies for a given beam period. In this average, the statistical uncertainties of each of the individual calibration factors is taken into account. Since the 4 GeV AHCAL calibration factor is a relative low, the 4 GeV point is excluded from the FNAL average in order to prevent a bias in the final calibration factors. For low energies, the activity in the AHCAL is

---

*This value was evaluated from electron measurements; however due to the differences in λ_I vs X_0, a larger difference for the first hadronic interaction layer (up to approximately 28%) is expected.

limited and located mostly in the first few layers and therefore the AHCAL calibration in the lower energy range is less reliable and more susceptible to noise.

Figure 6.1 shows the calibration factors determined for each energy separately, as well as the averages used as the global calibration factors. The resulting calibration constants are also summarized in table 6.1. The Si-W ECAL weights obtained from the data have higher values than the weights obtained from the simulations for both CERN and FNAL datasets (approximately up to 8% and 2%, respectively). However, for the AHCAL weights, an opposite trend of lower values for data is observed (approximately up to 1.5% for CERN dataset and 6% for FNAL dataset). These results are compatible with the studies of the longitudinal shower profile in the data and simulation (presented in section 8.1), which show that mean depositions in the Si-W ECAL layers are mostly higher in the simulations than that in the data and mean depositions in the AHCAL layers are mostly higher in the data than that in the simulation.

Table 6.1: The calibration factors obtained from CERN and FNAL data for hits in the different detectors.

Dataset		$C_{\text{Si-W ECAL}}$ [GeV/MIP]	C_{AHCAL}[GeV/MIP]
CERN	Data	0.00489±0.00015	0.02785±0.00031
	FTFP BERT	0.00451±0.00009	0.02825±0.00015
	QGSP BERT	0.00451±0.00010	0.02808±0.00025
FNAL	Data	0.00472±0.00008	0.02720±0.00074
	FTFP BERT	0.00462±0.00011	0.02885±0.00041
	QGSP BERT	0.00473±0.00021	0.02879±0.00055

6.2 Standard Reconstruction

In the sampling calorimeters in which the density of the absorber material is larger than the density of the active medium, the response to the electromagnetic showers is smaller than the response to MIPs [32]. Accordingly, in reference [70] the sampling fraction of the Si-W ECAL was evaluated as approximately 25% higher for MIPs than for electromagnetic showers. This aspect is taken into account in the following reconstruction method in which different weighting of primary track and shower hits in the Si-W ECAL are implemented.

The calibration factors which were discussed in the previous section are used for shower hits. For the calibration of primary track hits, new factors are determined by means of comparing a calculation of the mean energy loss (in energy units) of a MIP in the Si-W ECAL from material properties with a measurement of mean energy loss (in MIP units) in events with showers starting in the first layers of the AHCAL. The calculation gives a mean energy loss of approximately 213 MeV[†], whereas the measurements give 83.79 MIPs for CERN data and 84.84 MIPs for FNAL data. Therefore the new

---

[†] Total energy loss of 6.1 MeV in silicon, 185.6 MeV in tungsten, 1.3 MeV in aluminum and 20 MeV in the PCBs (Printed circuit boards) [34].

calibration scheme uses a factor of $0.52 \cdot C_{\text{Si-W ECAL}}$ for primary-track hits. This scheme yields an improvement in the system linearity of up to 3% predominantly for lower beam energies[‡]. A similar method used for primary hits in the AHCAL did not result in an improvement and therefore, for the simplicity of the analysis, was not implemented.

For this reconstruction method, the event reconstructed energy in equation 6.2 was transformed to

$$\tilde{\mathrm{E}}^{\text{event}}_{\text{reco}} = C_{\text{Si-W ECAL}} \cdot c_t \cdot \left(\sum_{j}^{\text{shower}} \mathrm{E}_j^{\text{Si-W ECAL}} + \sum_{k}^{\text{track}} 0.52 \cdot \mathrm{E}_k^{\text{Si-W ECAL}} \right) + \\ + C_{\text{AHCAL}} \cdot \left(\sum_{j}^{\text{hits}} \mathrm{E}_j^{\text{AHCAL}} + \sum_{j}^{\text{hits}} c_t \cdot \mathrm{E}_j^{\text{TCMT}} \right). \quad (6.3)$$

6.2.1 Fit of the Reconstructed Energy

The distributions of the reconstructed energies for each test beam energy are fitted with a Gaussian function in two steps, following the procedure used in reference [70]. First, the full range is fitted and then, using the mean and standard deviation of the first fit, a new fit is applied in the interval of ±2 standard deviations around the mean value. The mean value obtained from the second fit represents the reconstructed energy E_{reco}, and the energy resolution is given by the standard deviation σ_{reco} divided by E_{reco}. Figure 6.2 shows the standard reconstructed energies for 4 GeV and 80 GeV pions, marked in blue. The figure also includes red curves for the reconstructed energy distributions obtained from the SC method, which is described in the following section.

In addition to the fitting method mentioned above, the distributions of the reconstructed energies are fitted with the asymmetric Novosibirsk function [77] for comparison with previous analyses [69]. In this case, the energy response and resolution are extracted from the fitted function as its mean and *Root Mean Square (RMS)*, which are calculated using Monte-Carlo integration.

6.3 Software Compensation Schemes

As the sub-detectors in the calorimeter system are non-compensating calorimeters, their response for hadronic showers is typically smaller than for electromagnetic showers and therefore overall smaller for hadrons ($\frac{e}{\pi} > 1$). This characteristic in combination with the event-to-event fluctuations of the electromagnetic fraction of the hadronic shower (which originates from π^0/η production and their subsequent decay to two photons) results in a deterioration of the energy resolution in hadron detection (more details in section 3.4.2).

A reconstruction technique which was shown previously to improve the energy resolution for the AHCAL [70, 78] and for a combined scintillator-SiPM calorimeter system [69] is the software compensation method. In this method, different weights are assigned to different calorimeter cells based on the energy content, which is taken as a measure for the local shower energy density.

[‡] The absolute value of the correction is independent of the energy and therefore it is more substantial for lower energies.

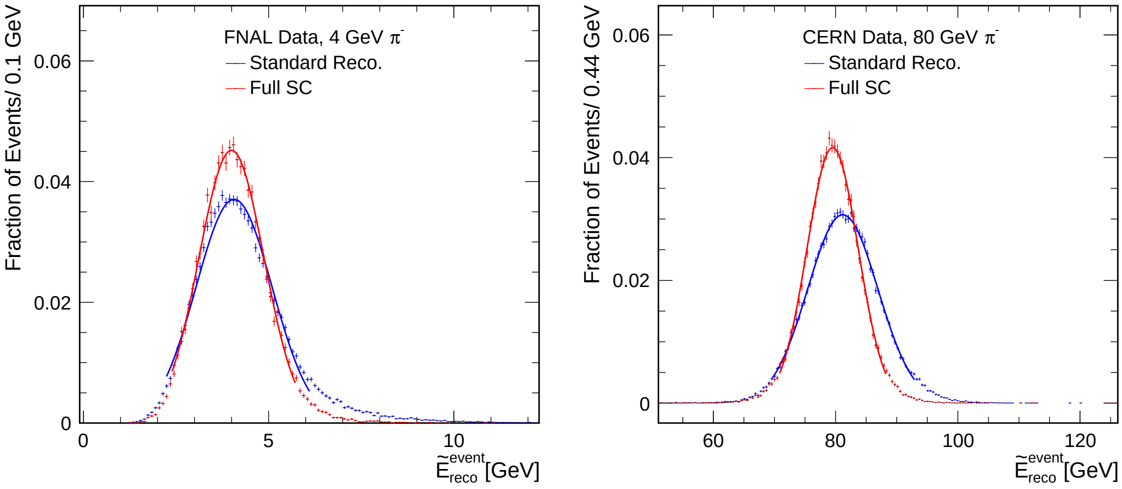

Figure 6.2: The distributions of the reconstructed energy for 4 GeV (left) and 80 GeV (right) beams obtained from the standard (blue) and Full SC (red) reconstruction methods. The distributions are fitted with a two-step fit of a Gaussian function as described in sub-section 6.2.1.

The SC scheme in this study includes each of the sub-detectors in the combined system, using the parametrization developed in reference [69] for a full calorimeter system. The distribution of the hits in MIP units (excluding the primary track hits) in each sub-detector is divided into several bins for different energy ranges as follows: eight bins for the Si-W ECAL, eight bins for the AHCAL and one bin for the TCMT. The bin boundaries, which are given in table 6.2, were optimized for a similar relative fraction of the total energy in each bin. Since the local energy density depends on the beam energy as well as on the region in the shower, this condition is met only for a specific energy in each sub-detector. For the bins in the Si-W ECAL, approximately equal fractions of the total energy are obtained at 6 GeV, while the AHCAL binning is chosen such that approximately equal fractions are obtained at 50 GeV. These different optimization points in energy are motivated by the different relative importance of the Si-W ECAL and AHCAL in the overall energy sum in the detector with the changing beam energy. Tests with different binning have confirmed that the precise number of bins as well as the exact location of the bin boundaries do not have a sizable effect on the final energy resolution. Figure 6.3 presents an example of the Si-W ECAL and AHCAL hit distributions for 25 GeV π^- at the CERN test beam. The different colors represent the different bins and the primary track hits (red).

The total energy contribution E_i for each bin i in the distribution is evaluated with two different methods. For bins $i = 3-8$ in the Si-W ECAL and AHCAL, and $i = 1$ in the TCMT, E_i is calculated from the sum of the individual hit signals scaled with the appropriate weighting for the absorber thickness c_t as well as the appropriate calibration factor for the sub-detector. For bins $i = 1-2$ in the Si-W ECAL and AHCAL, E_i is taken as the number of hits multiplied by the suitable calibration factor [§]. This method for the first two bins is similar to the one used for energy reconstruction in the

---

[§] The units are adjusted to energy units in the next step by applying weights to these bins.

Table 6.2: SC bin boundaries used in the Si-W ECAL and AHCAL in this analysis.

Bin	Si-W ECAL [MIP]	AHCAL [MIP]
1	0.0 – 3.5	0.0 – 2.0
2	3.5 – 6.7	2.0 – 4.0
3	6.7 – 12.0	4.0 – 6.6
4	12.0 – 19.0	6.6 – 11.0
5	19.0 – 30.0	11.0 – 18.2
6	30.0 – 50.0	18.2 – 30.2
7	50.0 – 98.0	30.2 – 50.0
8	98.0 – ∞	50.0 – ∞

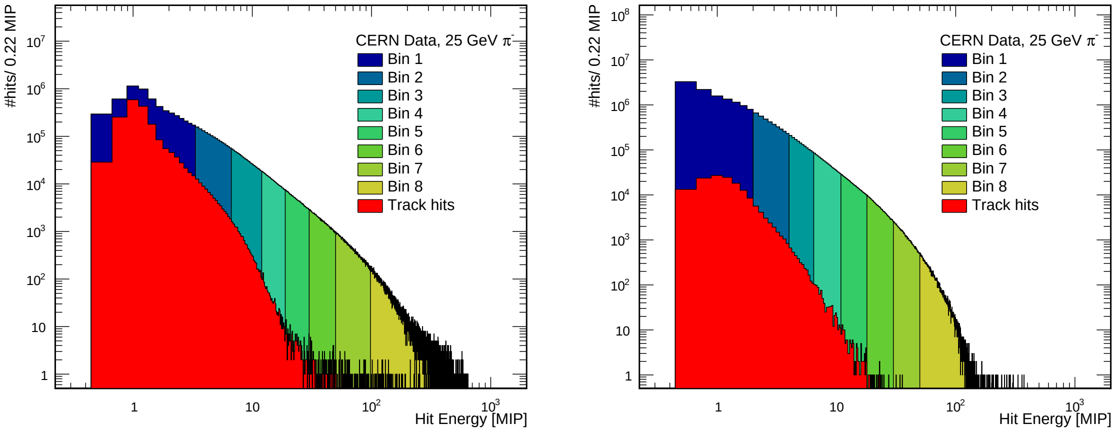

(a) Si-W ECAL (b) AHCAL

Figure 6.3: The hit energy spectra of CERN data of 25 GeV beams. Left: Hit energy spectra in the Si-W ECAL. Right: Hit energy spectra in the AHCAL. The different colors show the different energy range of the bins and the track hits (red).

Semi-Digital Hadronic Calorimeter (SDHCAL) prototype [79] and based on the assumption that the hits falling into these bins primarily originate from a single or a few particles. This is aimed at suppressing Landau fluctuations in the energy deposition (*Landau suppression*) and results in an energy resolution with a stochastic term lower by approximately 2%. The different methods can be described mathematically as

$$\mathrm{E}_i = \begin{cases} C \cdot \sum_{j}^{\text{hits}} 1, & i = 1-2 \ \text{ Si-W ECAL / AHCAL} \\ C \cdot c_t \cdot \sum_{j}^{\text{hits}} \mathrm{E}_j, & i = 3-8 \ \text{ Si-W ECAL / AHCAL}\,, \\ C \cdot c_t \cdot \sum_{j}^{\text{hits}} \mathrm{E}_j, & i = 1 \ \text{ TCMT} \end{cases} \tag{6.4}$$

in which C is the corresponding calibration factor.

The energy depositions of the primary track, from the first Si-W ECAL layer up to two layers before the reconstructed FHI layer, are excluded from the SC weighting. These hits are multiplied with the appropriate weighting for the absorber thickness and the suitable calibration factor, which is derived in the standard method (see section 6.2).

The energy/hit sums in different bins (E_is) are multiplied with bin-dependent weights. These weights are energy dependent since both the shower density profile and the average electromagnetic fraction of the shower are energy dependent. Their dependence is parametrized by second order Chebyshev polynomials [80] as a function of the estimated energy of the particle $\mathrm{E}_{\mathrm{est.}}$. The polynomials have three free parameters (a, b, c) and a scale factor S = 100 GeV (to preserve the orthogonality properties of Chebyshev polynomials), as in the following equation:

$$\omega_i\left(\mathrm{E}_{\mathrm{est.}}\right) = a_i + b_i \times \frac{\mathrm{E}_{\mathrm{est.}}}{S} + c_i \times \left(2 \times \left(\frac{\mathrm{E}_{\mathrm{est.}}}{S}\right)^2 + 1\right). \tag{6.5}$$

In total, for deriving the weights for the 17 bins of the full system, 51 parameters are needed (24 each for the Si-W ECAL and the AHCAL, 3 for the TCMT). To avoid confusion, the weights for Si-W ECAL, AHCAL and TCMT are referred to as $\omega_i = \alpha_i, \beta_i, \gamma$ respectively in the following. To optimized these parameters, a minimization of the χ^2 function in equation 6.1 is calculated over multiple runs at multiple energies using the appropriated beam energies. The reconstructed energy per event in this case is

$$\begin{aligned}\mathrm{E}^{\mathrm{event}}_{\mathrm{Full\ SC}} = \sum_i^{\mathrm{bins}} \alpha_i\left(\mathrm{E}_{\mathrm{est.}}\right) \cdot \mathrm{E}_i^{\mathrm{Si\text{-}W\ ECAL}} + \sum_i^{\mathrm{bins}} \beta_i\left(\mathrm{E}_{\mathrm{est.}}\right) \cdot \mathrm{E}_i^{\mathrm{AHCAL}} + \gamma\left(\mathrm{E}_{\mathrm{est.}}\right) \cdot \mathrm{E}_{\mathrm{sum}}^{\mathrm{TCMT}} \\ + 0.52 \cdot C_{\mathrm{Si\text{-}W\ ECAL}} \cdot c_t \cdot \mathrm{E}_{\mathrm{track}}^{\mathrm{Si\text{-}W\ ECAL}} + C_{\mathrm{AHCAL}} \cdot \mathrm{E}_{\mathrm{track}}^{\mathrm{AHCAL}},\end{aligned} \tag{6.6}$$

using the calibration factors $C_{\mathrm{Si\text{-}W\ ECAL}}$ and C_{AHCAL}, the layer thickness factor c_t, the SC weights $\alpha_i, \beta_i, \gamma$, the sum (or count) of energy depositions in the ith bin E_i and the sum of energy depositions on the primary track $\mathrm{E}_{\mathrm{track}}$.

In the optimization process for the 51 parameters, $\mathrm{E}_{\mathrm{est.}}$ is taken as the known beam energy. After the optimization, these parameters are implemented in the corresponding polynomials, using the corresponding standard reconstructed energy, $\mathrm{E}_{\mathrm{reco}}$, as an input to reconstruct each test beam energy. This way, no prior knowledge of the beam energy is used when applying the SC reconstruction to the data.

To avoid possible biases, half of the event sample is used for the determination of the SC weights and the other half is used to study their performance. The event sample is split into even and odd event numbers, so that possible time-dependent fluctuations are included in both the training and the testing sample. Tests have shown that there are no significant changes of the results of the present analysis when the same event sample is used for both training and testing.

For each test beam energy, a two-step fit of a Gaussian function, as was described in sub-section 6.2.1, is performed on the distribution of the SC reconstructed energies. The mean value of the fit represents the SC reconstructed energy, $\mathrm{E}_{\mathrm{Full\ SC}}$,while its standard deviation, $\sigma_{\mathrm{Full\ SC}}$, is used to obtain the energy resolution by $\sigma_{\mathrm{Full\ SC}}/\mathrm{E}_{\mathrm{Full\ SC}}$. Additional fitting to the Novosibirsk function is performed for comparison with the previous analyses.

6.3.1 Application of Software Compensation to different Detectors

The SC scheme discussed so far includes all three sub-detectors in the combined setups and therefore is referred to as the *Full SC* scheme. To study the application of SC reconstruction to individual parts of the combined systems, two additional SC schemes were used to reconstruct the data: the *HCAL SC* in which SC is applied to the AHCAL and the TCMT and the *ECAL SC*[¶] in which SC is applied only to the Si-W ECAL. These schemes use the same binning technique for the corresponding sub-detectors as the Full SC scheme, while the contributions of the primary track and the additional sub-detectors are reconstructed with the standard method.

The following formulas describe the reconstructed energy of these schemes:

$$\begin{aligned}\mathrm{E}^{\mathrm{event}}_{\mathrm{HCAL\ SC}} = C_{\mathrm{Si\text{-}W\ ECAL}} \cdot c_t \cdot \sum_j^{\mathrm{hits}} \mathrm{E}_j^{\mathrm{Si\text{-}W\ ECAL}} + C_{\mathrm{AHCAL}} \cdot \mathrm{E}^{\mathrm{AHCAL}}_{\mathrm{track}} \\ + \sum_i^{\mathrm{bins}} \beta_i \left(\mathrm{E}_{\mathrm{est.}}\right) \cdot \mathrm{E}_i^{\mathrm{AHCAL}} + \gamma \left(E_{\mathrm{est.}}\right) \cdot \mathrm{E}^{\mathrm{TCMT}}_{\mathrm{sum}} \qquad (6.7)\end{aligned}$$

$$\begin{aligned}\mathrm{E}^{\mathrm{event}}_{\mathrm{ECAL\ SC}} = \sum_i^{\mathrm{bins}} \alpha_i \left(\mathrm{E}_{\mathrm{est.}}\right) \cdot E_i^{\mathrm{Si\text{-}W\ ECAL}} + 0.52 \cdot C_{\mathrm{Si\text{-}W\ ECAL}} \cdot c_t \cdot \mathrm{E}^{\mathrm{Si\text{-}W\ ECAL}}_{\mathrm{track}} \\ + C_{\mathrm{AHCAL}} \cdot \left(\sum_j^{\mathrm{hits}} \mathrm{E}_j^{\mathrm{AHCAL}} + \sum_j^{\mathrm{hits}} c_t \cdot \mathrm{E}_j^{\mathrm{TCMT}} \right) \qquad (6.8)\end{aligned}$$

6.4 Systematic Uncertainties

In this analysis, only systematic effects originating from the event selection are taken into account. Detector effects, such as the saturation behavior of the photon sensors, have been found to be negligible in previous studies [69, 70] and therefore are not considered. In addition, uncertainties of the energy scale of the detector originating from the MIP calibration of the calorimeters are not included, since they are corrected for in the calibration process from MIP to GeV, which is described in section 6.1. The uncertainties are evaluated separately for every reconstruction method (the standard, Full SC, HCAL SC, ECAL SC) and every dataset (CERN data, FNAL data, the combined dataset). The same procedure is applied to both data and simulations (further simulation systematic effects are not included in this work).

To study possible systematic effects of the event selection, the relevant selection cuts are varied from their default values. The relevant cuts, cuts on the total reconstructed energy and cuts on reconstructed FHI layer, are modified separately. Additional systematic tests were performed by varying the clustering distance d_{th}, which is described in sub-section 5.3.1. The following list describes the variations applied to the event selection:

- **Electron rejection**: A tighter electron rejection cut by rejecting events with FHI layer in the first module of the Si-W ECAL (10th layer instead of the 5th layer).

[¶] This scheme, in contrast to the previous schemes, does not use the Landau suppression technique described above.

- **Full shower**: A tighter cut for full shower containment by rejecting events with FHI after the 5th layer of the AHCAL (35th layer of the full calorimeter system, instead of layer 56).
- **Muon rejection**: A looser muon rejection by removing the cut on the reconstructed energy, which is destined for rejecting low-energy muons (including events from $E_{beam} \geqslant 15$ GeV with $E_{reco} < E_{beam}/2.6$).
- **Clustering**: A looser clustering requirement for multi-particle rejection by clustering hits within d_{th}=20 mm (instead of d_{th}=12 mm).

After each modification, selected events are reconstructed with the methods described in the previous sections and systematic uncertainties and their energy dependence are estimated for:

1. The reconstructed energy.
2. The energy resolution.
3. The ratio between the energy resolution obtained from the SC methods and the energy resolution obtained from the standard method (the *relative improvement*).

Tables 6.3, 6.4 and 6.5 display the systematic uncertainties over several representative energies for the standard and the Full SC methods (the uncertainties are evaluated also for other beam energies). The independent influence of each cut as a function of the beam energy is shown in appendix C.

To evaluate the total systematic uncertainty, the individual uncertainties, which are assumed to be uncorrelated, are added in quadrature. The energy dependence of the total systematic uncertainties (for the standard and the Full SC schemes) is shown in figure 6.4. The uncertainties of the reconstructed energy show a relatively flat trend with each reconstruction method; however, the uncertainties for the energy resolution are energy dependent with larger values in the lower energy range. The similar behavior obtained in simulations (shown in appendix C.5) suggests that lower-energy showers are more susceptible to variations in the event selection. Since the 60 GeV data-point is at the end of the energy range of FNAL dataset and has low statistics (in real data), the SC reconstruction of this data-point is also very prone to variations with to small changes in the event selection and therefore results in larger uncertainties. This feature is not present in the reconstruction of the combined dataset.

Table 6.3: Summary of systematic uncertainties for reconstructed energies for standard (Std) and Full SC (SC) reconstructions of the CERN and FNAL data. The uncertainties are relative in units of percentage.

Energy	4 GeV		30 GeV		50 GeV		80 GeV	
Cut	Std	SC	Std	SC	Std	SC	Std	SC
	systematic uncertainty [%]							
Electron rejection	0.27	-0.16	0.04	0.08	0.07	-0.01	0.00	0.07
Full shower	-1.64	-0.81	-0.15	-0.11	0.48	-0.16	0.14	0.20
Muon rejection	0.00	-0.39	0.00	-0.02	0.00	-0.13	0.00	0.11
Clustering	-0.01	-0.03	- 0.01	-0.06	0.00	-0.05	-0.01	0.04
Total	1.67	0.92	0.16	0.15	0.48	0.21	0.14	0.24

Table 6.4: Summary of systematic uncertainties for energy resolutions for standard (Std) and Full SC (SC) reconstructions of the CERN and FNAL data. The uncertainties are relative in units of percentage.

Energy	4 GeV		30 GeV		50 GeV		80 GeV	
Cut	Std	SC	Std	SC	Std	SC	Std	SC
	systematic uncertainty [%]							
Electron rejection	-0.45	-1.91	-0.47	-0.35	-0.57	1.09	-0.90	0.60
Full shower	5.29	6.45	1.30	0.27	-0.07	-1.11	1.50	-2.82
Muon rejection	0.00	0.11	0.00	-0.89	0.00	1.10	0.00	-0.50
Clustering	0.21	-1.04	0.17	-0.06	-0.33	0.61	0.07	0.30
Total	5.31	6.81	1.40	1.00	0.67	2.01	1.75	2.94

Table 6.5: Summary of systematic uncertainties for the relative improvement of the reconstructed energy resolutions of the CERN and FNAL data. The uncertainties are relative in units of percentage.

Energy	4 GeV	30 GeV	50 GeV	80 GeV
	systematic uncertainty [%]			
Electron rejection	-1.47	0.12	1.68	1.52
Full shower	1.10	-1.02	-1.04	-4.26
Muon rejection	0.11	-0.89	1.10	-0.50
Clustering	-1.26	-0.24	0.95	0.22
Total	2.23	1.38	2.45	4.56

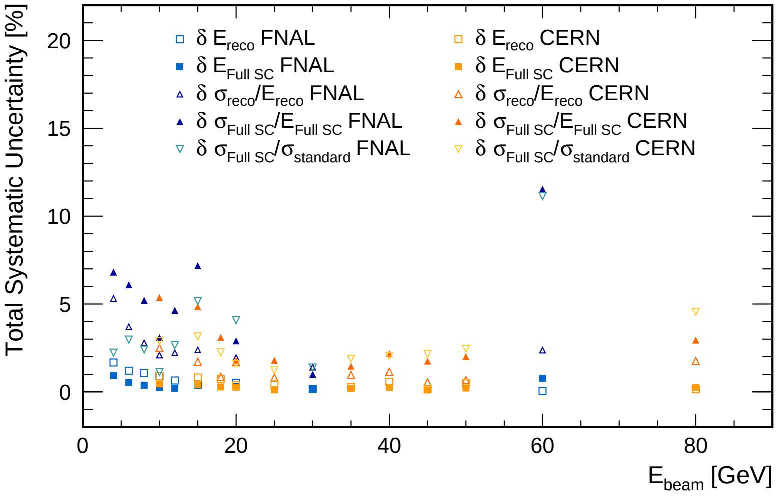

Figure 6.4: Summary of the total systematic uncertainties obtained from the standard and the Full SC reconstruction of the CERN and FNAL data as a function of the beam energy.

CHAPTER 7

RESULTS

The goal of this analysis is a direct comparison of the reconstruction methods described in the previous chapter: the standard reconstruction and the various SC schemes (Full SC, HCAL SC and ECAL SC). The particle energy in each event is reconstructed with every method. The reconstruction assumes no knowledge of the test beam energy, as this information is used only to optimized the weights and to validate the quality of the analysis results.

CERN or FNAL events are reconstructed with their respective set of calibration constants, which have been introduced in section 6.1. The SC weights for each SC scheme and each dataset (CERN, FNAL or the combined dataset) are optimized separately and implemented event-by-event in the corresponding SC reconstruction of the suitable dataset. Since the SC weights are dependent on the runs used for their optimization, the event energy produced by each SC scheme varies slightly when either the CERN data or the FNAL data are used, compared to when the combined data are used. For each experiment and test beam configuration, the reconstruction produces a set of results that are normally distributed due to statistical fluctuations, detector effects and reconstruction inaccuracies.

The fitting methods described in sub-section 6.2.1 are applied to each set to reconstruct the beam energies and determine the respective energy resolutions.

The performance of the calorimeter system is evaluated for each of the test beam periods and for the full energy range (with the combined data) by measuring the linearity and the energy resolution as a function of the beam energy. Since beams of 10 GeV, 15 GeV and 20 GeV were measured both at FNAL and CERN test beam setups, the separated reconstruction of the combined data produces two results for the different test beam locations. An average of these results is taken for the final combined results (more details in section 7.3).

This chapter summarizes the energy reconstruction results. Section 7.1 contains the dependence of the SC weights on the beam and hit energies. A comparison between the standard and the Full SC reconstruction is detailed in section 7.2. Following this, the performance of the detector system for different test beam periods is presented in section 7.3 and a comparison between the different SC schemes is given in section 7.4. Finally, a comparison with previous analyses is discussed in section 7.5 and a test for the SC robustness is presented in section 7.6.

7.1 Software Compensation weights

As described in section 6.3, a parametrization of second order polynomials as a function of the particle energy is used for the SC bin weights. Since these weights are optimized for the energy range of each dataset, the second order polynomial parametrization may produce negative values outside of the energy range used for the optimization, requiring care when extrapolating to larger ranges. The weights for the different bins are highly correlated, in particular for the first two bins in which hits are counted rather than using the full energy information. This often results in opposing trends of the energy dependence of these two weights (convex and concave), which can change between bin 1 and bin 2 depending on the dataset and in particular on the range of energies considered. Figure D.1 shows the bin weights optimized with the CERN dataset as a function of the estimated particle energy E_{est}. The weight values of bin 1 and 2 are divided with the energy corresponding to the center of the respective bin to equalize these weights and make them comparable to the other weights. In figure 7.2, the bin weights optimized with the CERN data for 10 GeV, 35 GeV and 80 GeV beams are presented as a function of the hit energies to which these weights are applied. The weights of the first two bins are inversely proportional to E_{hit}, which results in a constant contribution to the reconstructed energy of each hit in these bins.

The general trend for bins of high hit energies to be down-weighted corresponds to the assumption that the hits in these bins are originating predominantly from electromagnetic sub-showers which are typically narrower and denser than hadronic sub-showers.

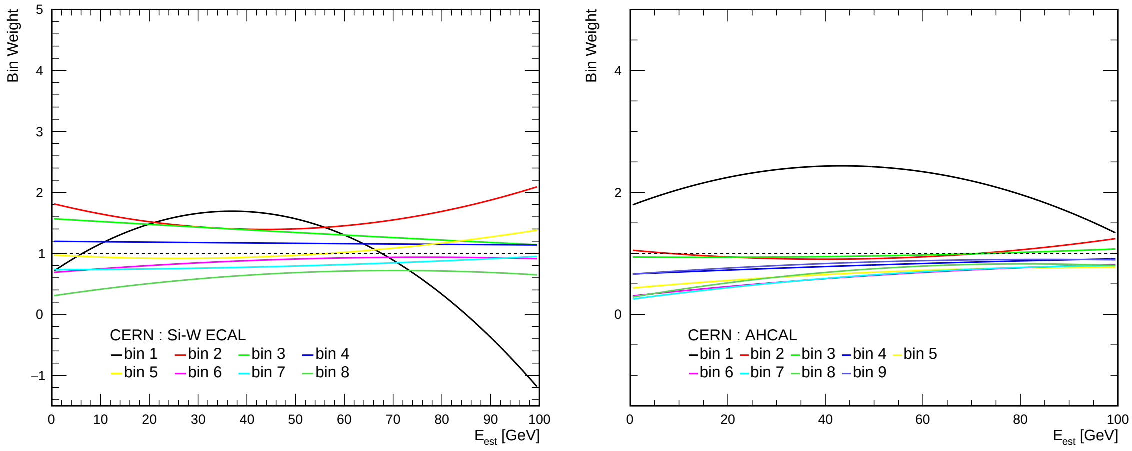

Figure 7.1: The energy-bin weights optimized with CERN test beam data as a function of the estimated particle energy E_{est} . Left: The Si-W ECAL weights. Right: The AHCAL weights (bin 1−8) and the TCMT weight (bin 9).

In previous analyses with a different SC scheme [70,78], weights for each beam energy were forced to follow a monotonic decrease with the bin energy. In the present analysis, no such assumption is built in. The technique used here has the advantage of having a more stable convergence in the weight determination procedure compared to the scheme used in references [70, 78]. On the other hand, the physics interpretation that is provided by enforcing a monotonic descent when increasing the bin number is lost in this purely phenomenological approach, making the interpretation of the

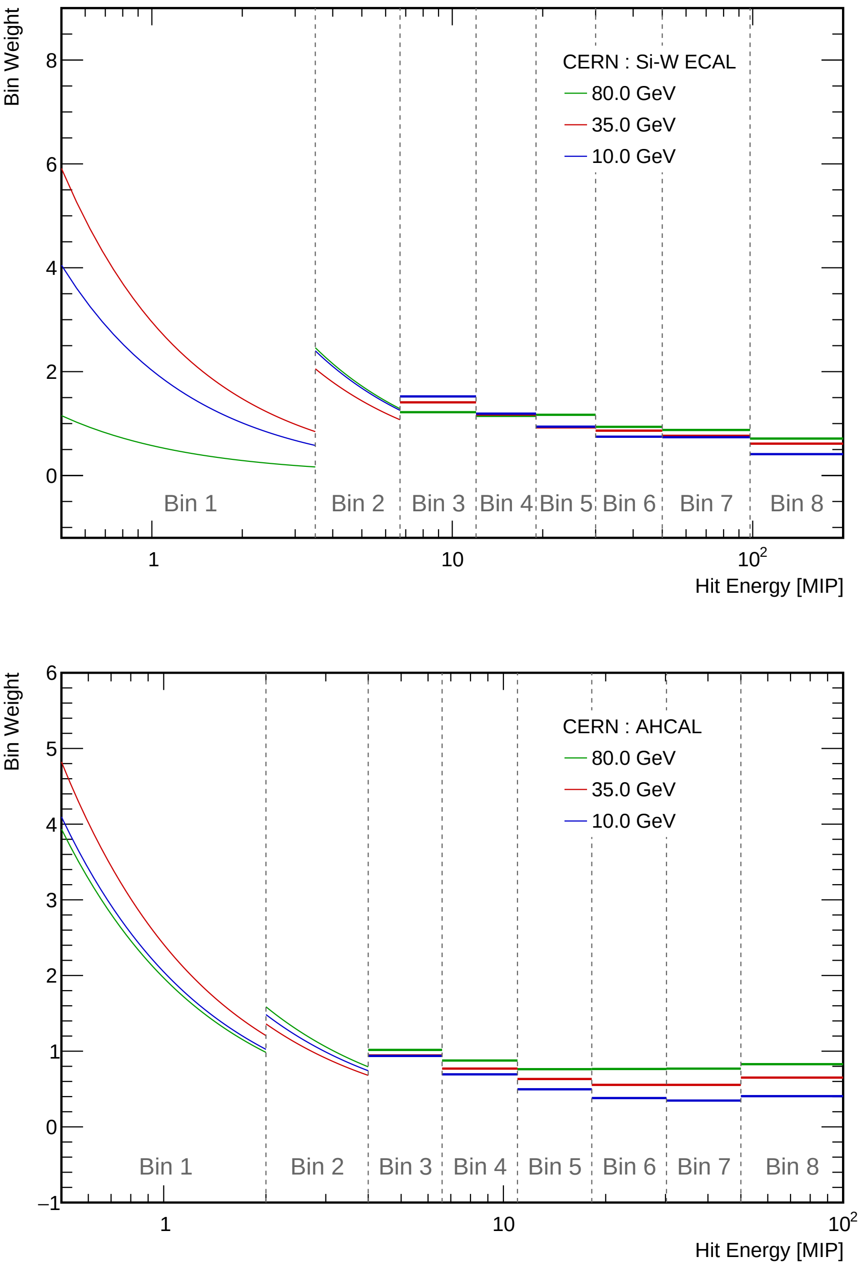

Figure 7.2: The bin weights for 10 GeV, 35 GeV and 80 GeV π^- beams as a function of the hit energies to which these weights are applied. The weights were optimized with CERN data events. Left: Si-W ECAL weights. Right: AHCAL weights. The use of a constant value rather than the individual amplitude of each hit in the first two bins yields energy dependent weights in these bins. The dashed lines indicate the energy range of the each energy-bin.

weights less straightforward. Also because of this, extrapolations beyond the range used for the training of the weights have to be handled with special care, as already mentioned above. As discussed further in section 7.6, this approach does not lead to instabilities in the performance of the algorithm.

7.2 Energy Resolution and Linearity

The software compensation reconstruction methods result in an improved energy resolution when compared to the standard reconstruction method. This is shown in figure 6.2 for the reconstruction of 4 GeV and 80 GeV beams, the lowest and highest energies studied in this analysis. For both cases, the distributions of energies reconstructed with SC are narrower compared to the ones obtained from the standard reconstruction. Moreover, in the distributions obtained from the SC reconstruction, the tail toward higher energies, which is discussed in section 5.4, is substantially reduced. For the same beam energies, the correlation between event energies reconstructed with the standard and the Full SC reconstruction methods is presented in figure 7.3. Similar figures for all other beam energies are given in appendix D.2. For all beam energies, the relation between the reconstructed energies obtained from these reconstruction methods is not linear. Events with lower standard reconstructed energy, presumably due to a high hadronic fraction, get assigned higher reconstructed energy by the SC reconstruction. Likewise events with high standard reconstructed energy, result of above average electromagnetic shower content or nuclear interactions, receive lower SC reconstructed energy.

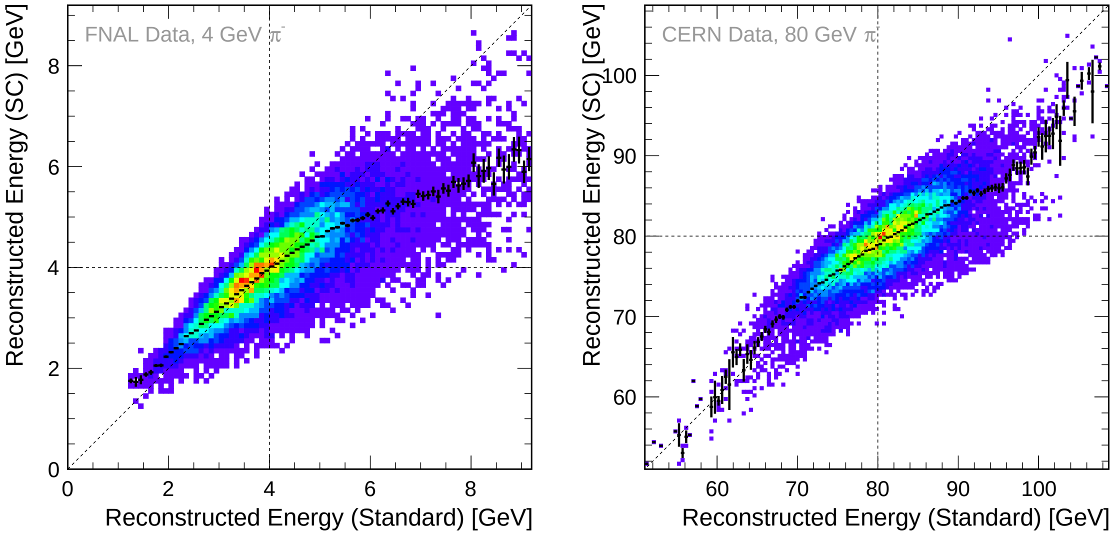

Figure 7.3: The correlation between energies reconstructed with the standard and the Full SC reconstruction methods. Left: reconstructed energies of 4 GeV FNAL beams. Right: reconstructed energies of 80 GeV CERN beams. The black markers show the profile of the mean SC reconstructed energy for bins of the standard reconstructed energy. The dashed lines indicate the beam energy in each axis while the diagonal traces the slope with total correlation.

For each dataset, each reconstruction method produces a set of energy resolutions. To compare the performance of the calorimeter system, the energy resolution as a function of the beam energy in each set is fitted with the following function:

$$\frac{\sigma_{\mathrm{reco}}}{\mathrm{E}_{\mathrm{reco}}} = \frac{a}{\sqrt{\mathrm{E}_{\mathrm{beam}}/\mathrm{GeV}}} \oplus b \oplus \frac{c}{\mathrm{E}_{\mathrm{beam}}}. \tag{7.1}$$

$\mathrm{E}_{\mathrm{beam}}$ is the beam energy and a, b and c are the stochastic, constant and noise contributions,

Table 7.1: Summary of the fit parameters obtained from different reconstructions of CERN, FNAL and the combined datasets.

reco.	a_{Combined} [%]	b_{Combined} [%]	a_{CERN} [%]	b_{CERN} [%]	a_{FNAL} [%]	b_{FNAL} [%]
Standard	55.54±0.13	4.31±0.05	58.40±0.17	3.39±0.08	52.54±0.22	5.91±0.14
SC ECAL	52.66±0.17	3.34±0.08	53.92±0.22	2.83±0.11	51.86±0.28	3.74±0.27
SC HCAL	48.09±0.16	2.90±0.08	46.80±0.20	3.20±0.08	48.10±0.24	2.26±0.36
SC full	44.09±0.14	2.08±0.08	43.32±0.17	2.05±0.09	44.39±0.12	0.00±2.06

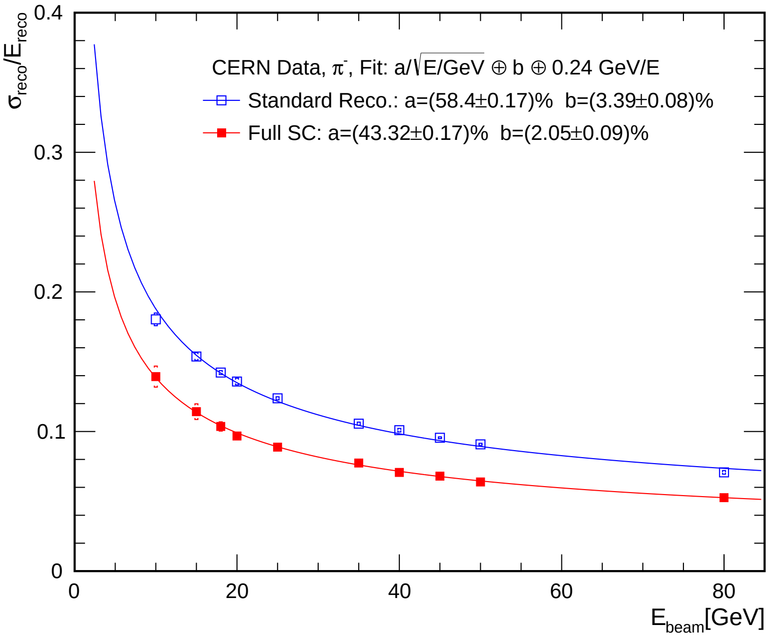

Figure 7.4: The reconstructed energy resolution obtained from the standard (blue) and Full SC (red) reconstruction of CERN dataset. The fit parameters are given in the legend. The total (statistical and systematic) uncertainties are marked with brackets, '[]'.

respectively (see section 3.4 for details). For the CERN and the combined datasets results, the noise term is fixed to 0.24 GeV, while for the FNAL dataset, it is fixed to 0.21 GeV. This corresponds to the noise measurements of the calorimeter system in different test beam setups, which are detailed in appendix B. The fit parameters for the different reconstruction methods in different datasets are summarized in table 7.1. The reduction of both the stochastic and the constant terms with each of the SC schemes indicates an overall better energy resolution when compared to the standard reconstruction. The stochastic and constant terms are highly correlated in the fit; therefore the stochastic term alone is not a robust measure of the overall resolution for which it should be considered along with the constant term. Aside from comparing the fit parameters, energy resolutions obtained from the SC methods are displayed along with those obtained from the standard method as a function of the energy (figures 7.4, 7.5 and 7.6). Furthermore, the ratio between the resolutions, $\sigma_{\mathrm{SC}}/\sigma_{\mathrm{standard}}$, as a function of the beam energy is presented as well in the next sections (figures 7.9 and 7.12).

The reconstructed energy resolutions of CERN and FNAL events obtained from the standard and the Full SC methods are shown in figures 7.4 and 7.5, respectively. In both cases, there is an improvement of the resolution, which can be evaluated from the change in the stochastic term from (58.40±0.17)% to (43.32±0.17)% for the CERN dataset and from (52.54±0.22)% to (44.39±0.12)% for the FNAL dataset. The constant term is also improved in both cases, in particular for the FNAL data. The large change in the constant term for FNAL data explains the somewhat smaller improvement in the stochastic term compared to the CERN dataset.

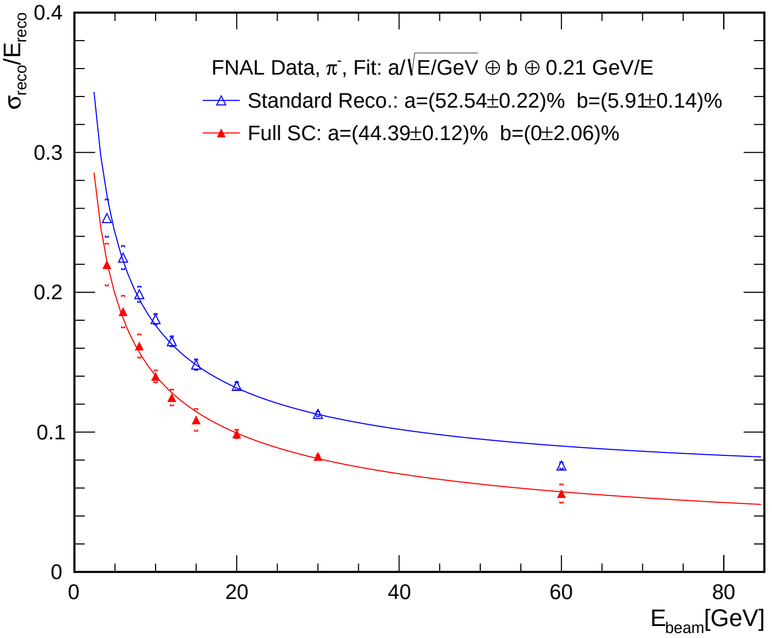

Figure 7.5: The reconstructed energy resolution obtained from the standard (blue) and Full SC (red) reconstruction of FNAL dataset. The fit parameters are given in the legend. The total (statistical and systematic) uncertainties are marked with brackets, '[]'.

Figure 7.6 presents the main result, i.e. the energy resolutions of the combined dataset with the full energy range (4 GeV to 80 GeV). From the Full SC method, the obtained fit parameters are improved compared with the ones obtained from the standard method: the stochastic term decreases from (55.54±0.13)% to (44.09±0.14)% and the constant term decreases by approximately 52%. In figures 7.5 and 7.6, the standard reconstructed 60 GeV data-point shows a lower energy resolution than the fit prediction. This can be explained by the presence of many data-points in the lower energy range, which caused the fit to be dominated by this energy range.

The mean reconstructed energies versus the beam energies, together with the relative residuals to the beam energies, are shown in figure 7.7 for data recorded at CERN and FNAL and for their combination. The agreement with the beam energies is similar for both reconstruction methods in CERN data, reaching deviations up to 3% at worst. For the FNAL data the deviations from the beam

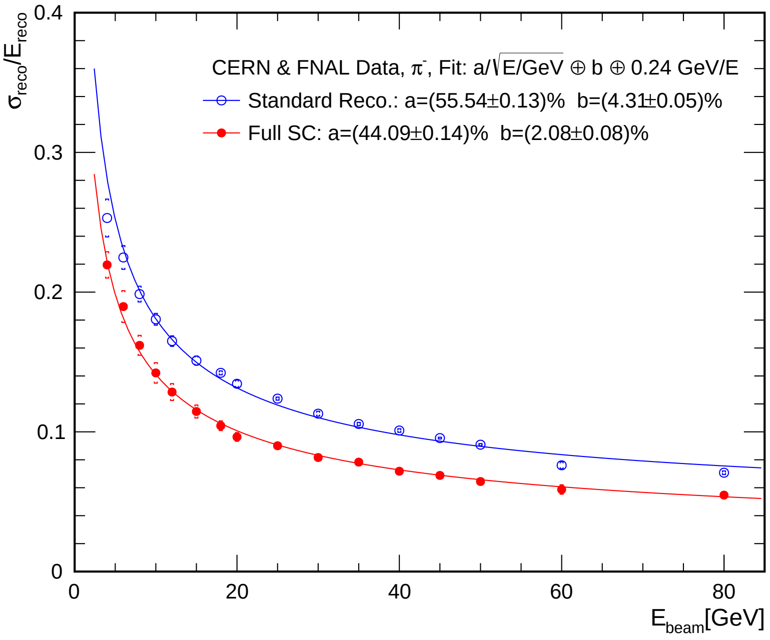

Figure 7.6: The reconstructed energy resolution obtained from the standard (blue) and Full SC (red) reconstruction of the combined dataset. The fit parameters are given in the legend. The total (statistical and systematic) uncertainties are marked with brackets, '[]'.

energy are smaller than 3% when applying the standard reconstruction; however, the deviations of energies obtained from the Full SC method range up to 5%, due to a relatively constant down scaling of these energies in the range of 4 GeV to 20 GeV compared with energies obtained from the standard method. In the combined dataset, both reconstruction methods show a similar linearity level, characterized by deviations smaller than 4%.

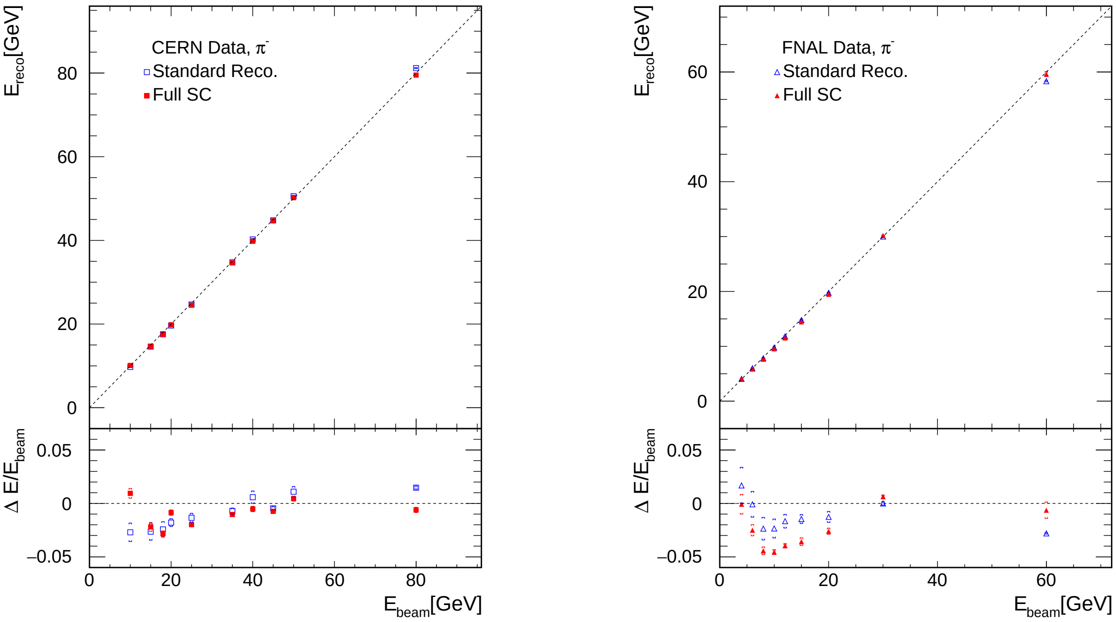

(a) CERN data.

(b) FNAL data

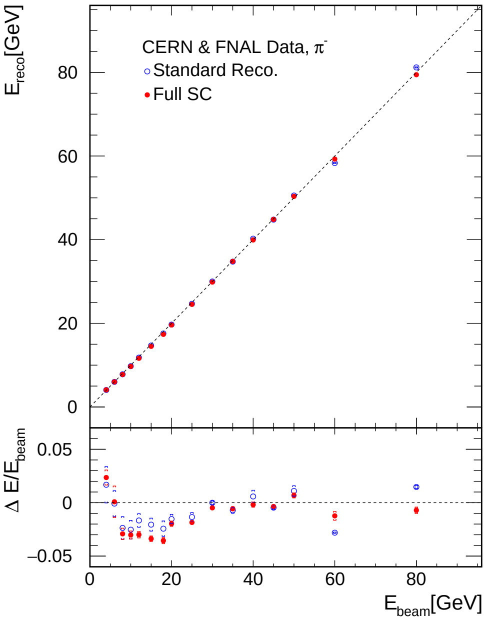

(c) CERN and FNAL data

Figure 7.7: The mean reconstructed energy and relative residual to the beam energy versus beam energy obtained from the standard (blue) and Full SC (red) reconstruction of (a): CERN data. (b): FNAL data. (c): the combined (CERN+FNAL) dataset. The total (statistical and systematic) uncertainties are marked with brackets, '[]'. Dashed lines correspond to $E_{reco} = E_{beam}$.

7.3 Detector Performance in Different Data Taking Campaigns

Between the running periods at CERN in 2007 and at FNAL in 2008, the calorimeter system was completely disassembled and shipped by road, rail and sea from Switzerland to the US. Almost 10% of the front end cards were replaced after transport damage and the detector was reassembled and re-commissioned. This, in addition to differences in the test beam setups and the different beam structures at CERN and FNAL, might have impacted the detector performance.

To evaluate the stability of the detector performance in different data taking campaigns, the results obtained by the CERN and FNAL data are compared. The comparison is extended to also include the combined dataset in order to study the application of the SC method on the larger energy range of the joined data.

Figure 7.8 presents the energy resolution for the different datasets with the standard and Full SC reconstruction. The data-points for the different datasets for both reconstruction methods agree within 6%. The standard reconstruction results of the combined dataset and either the CERN or FNAL data are the same; however the fits are dependent on the energy range and therefore yield different measurements of the energy resolution. With the Full SC scheme, the constant term in each fit is reduced and therefore the fits provide a better description of the higher energy range.

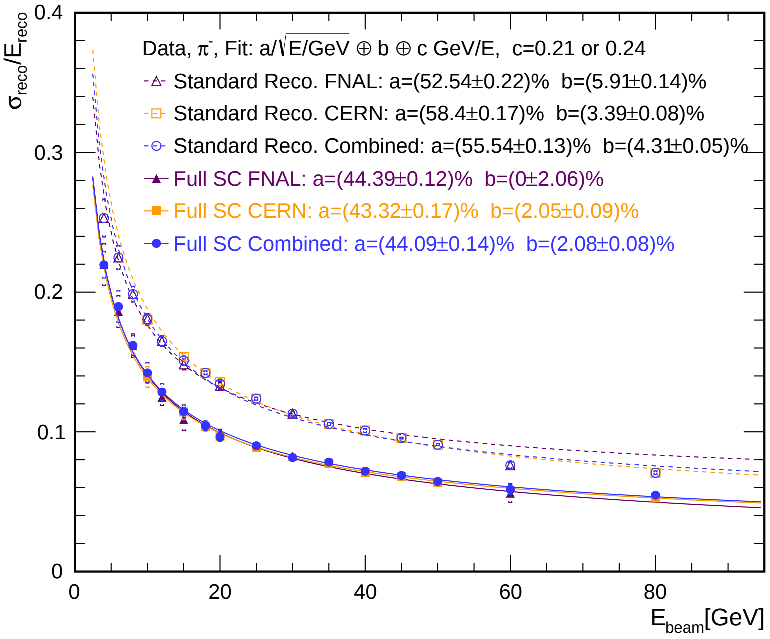

Figure 7.8: The reconstructed energy resolutions obtained from the standard and Full SC reconstruction of FNAL, CERN and the combined (CERN and FNAL) datasets. The fit parameters are given in the legend. The total (statistical and systematic) uncertainties are marked with brackets, '[]'.

The relative improvement between the SC and the standard reconstructed energy resolutions varies between 14% for the lowest beam energy to 30% for higher energies, as shown in figure 7.9. The improved performance of the SC reconstruction at the higher energy range is due to the increase in the electromagnetic fraction, which means more energy depositions from electromagnetic sub-showers

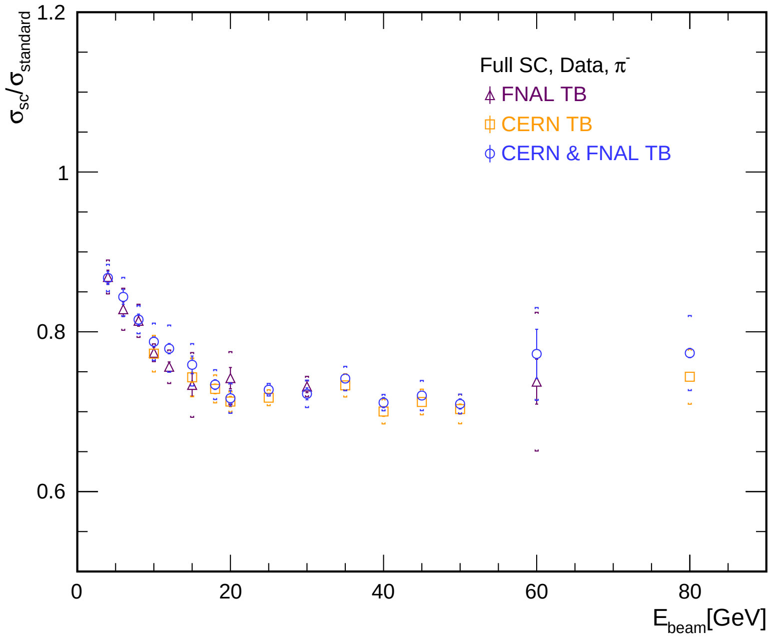

Figure 7.9: The relative improvement of the energy resolutions obtained from the Full SC reconstruction of the different datasets. The total (statistical and systematic) uncertainties are marked with brackets, '[]'.

and therefore more efficient SC reconstruction. Similar improvement in the energy resolution is achieved when reconstructing the different datasets, showing an agreement within 4.5% between the data-points.

The linearity of the detection system is measured with the relative residuals to the beam energy, as can be seen in figure 7.10. The standard reconstruction of 10 GeV, 15 GeV and 20 GeV beams, which were measured at CERN as well as at FNAL, yields compatible reconstructed energies considering the systematic uncertainties. With every dataset, the standard reconstruction energies are obtained within 3% of the beam energies. The SC method results are in a good agreement with the beam energies (<2%) in the higher energy range. For lower beam energies, however, different reconstructed energies are obtained due to the energy dependent optimization procedure of the SC weights. Applying the SC method to the combined data shows to some extent a more stable linearity level.

As mentioned before, in the reconstruction of the combined dataset, data of beam energies measured both at CERN and FNAL are reconstructed separately and the obtained results are averaged. This approach yields similar results to those obtained when combining the data on an event level. It is only for the SC reconstruction of the 10 GeV events that a slightly better energy resolution is obtained when averaging the results (0.139 compared to 0.143); however, for the standard reconstruction and the other energies the differences are smaller than 0.5%.

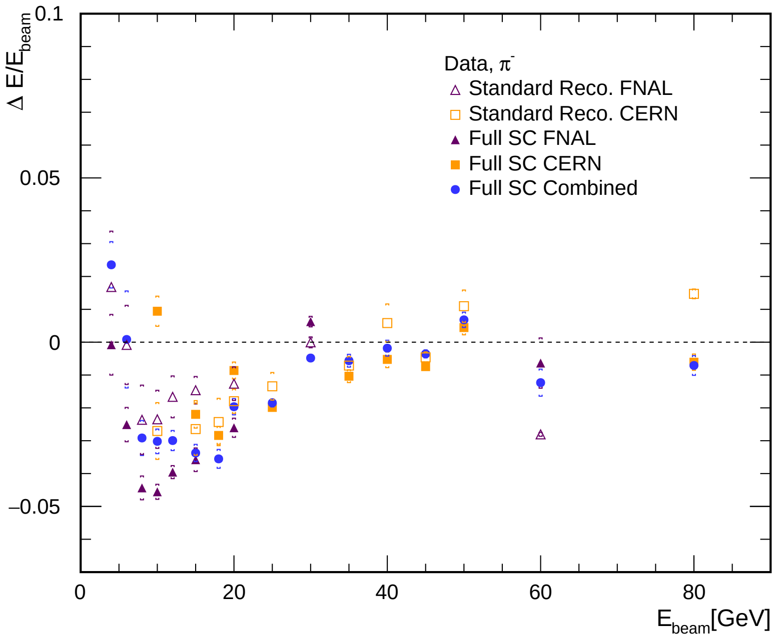

Figure 7.10: The relative residuals to the beam energy obtained from the standard and Full SC reconstruction of the different datasets. The total (statistical and systematic) uncertainties are marked with brackets, '[]'.

7.4 Applying Software Compensation to Different Detectors

The Full SC reconstruction method is applied to every sub-detector in the system and includes an optimization of 51 parameters. The HCAL SC and ECAL SC, which are described in sub-section 6.3.1, are simplified implementations of the method, which include only individual parts of the combined systems. These three SC schemes were applied to the different datasets, together with the standard reconstruction. This study allows to investigate the contributions of different sub-detectors to the performance of Full SC scheme and to test the necessity of such a complicated scheme. In addition, this study is valuable for other studies, including studies of PandoraPFA [30], which use SC only for reconstructing energy depositions in the HCAL.

Figure 7.11 presents the energy resolution for the combined dataset with the different reconstruction methods. With every SC scheme, the energy resolution improves and the constant and stochastic terms given by the fit are reduced. The ECAL SC scheme gives a slightly improved resolution, from a stochastic term of (55.54±0.13)% to (52.66±0.17)%; the HCAL SC reduces it further to (48.09±0.16)%; and the full SC gives the lowest stochastic term of (44.09±0.14)%.

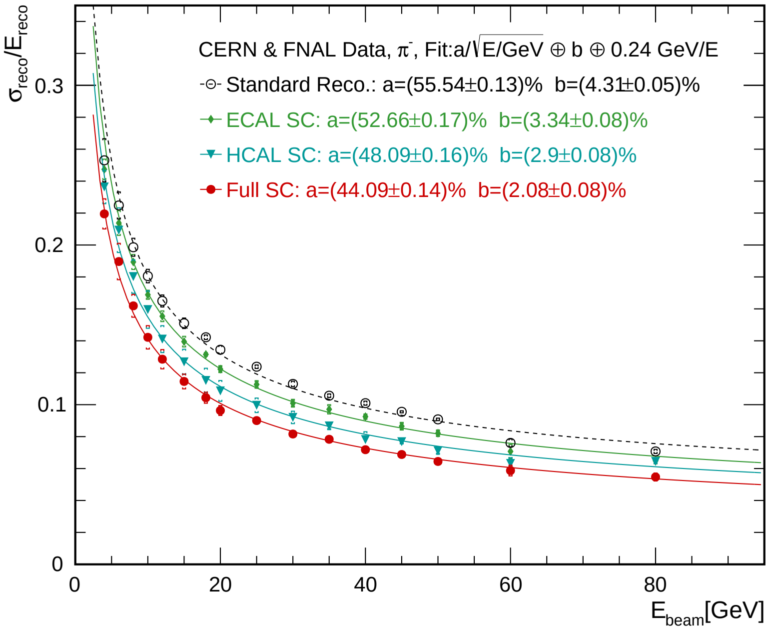

Figure 7.11: The reconstructed energy resolutions obtained from the standard, ECAL SC, HCAL SC and Full SC reconstruction of the combined (CERN and FNAL) dataset. The fit parameters are given in the legend. The total (statistical and systematic) uncertainties are marked with brackets, '[]'.

Figure 7.12 presents the relative improvement of the energy resolutions in which an increasing improvement up to 20 GeV is shown, followed by a considerably flat behavior from this point on. The ECAL SC scheme gives an improvement of only a few percent, while the HCAL SC scheme shows an increasing improvement up to approximately 23%. This is due to the significant larger fraction of the total shower energy that is deposited in the AHCAL. The maximum improvement of approximately 30% is achieved with the Full SC scheme.

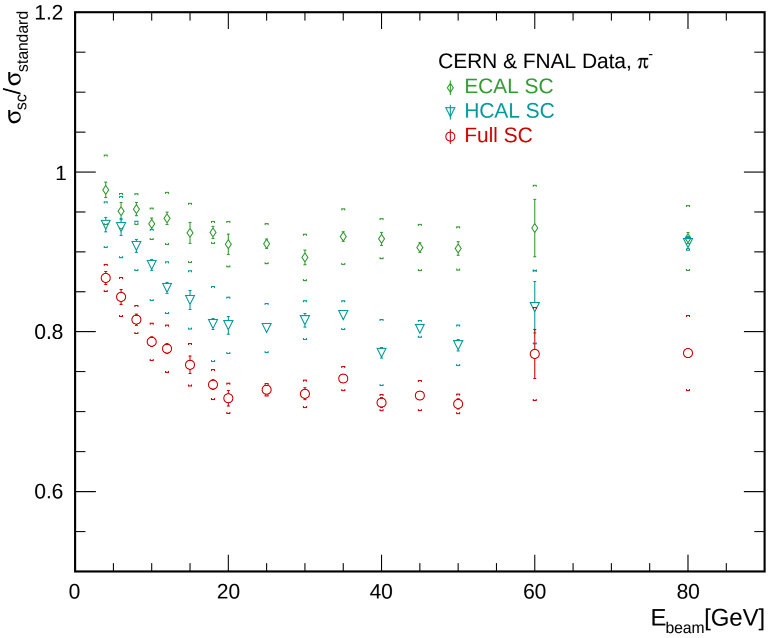

Figure 7.12: Energy dependence of the relative improvement in the combined dataset of the reconstructed energy resolutions with different reconstruction methods. The total (statistical and systematic) uncertainties are marked with brackets, '[]'.

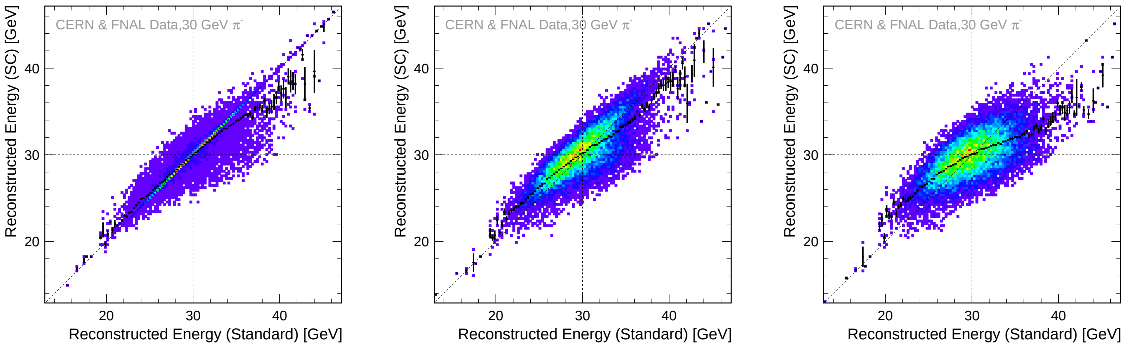

(a) ECAL SC (b) HCAL SC (c) Full SC

Figure 7.13: The correlation between energies reconstructed with the standard and the different SC reconstruction of 30 GeV π^- events. The black markers show the profile of the mean SC reconstructed energy for bins of the standard reconstructed energy. The dashed lines indicate the beam energy in each axis while the diagonal traces the slope with total correlation.

The 'energy compensation' which is applied by the different schemes can be seen in figure 7.13. The figure presents the correlation of the energies reconstructed with the standard method and with different SC schemes. The nearly linear correlation in the ECAL SC figure indicates the small impact of the ECAL SC scheme. For the HCAL SC and the Full SC schemes the relation between the reconstructed energies is non-linear and therefore more compensation takes place.

7.5 Comparison with Previous CALICE Analyses

The CALICE collaboration has performed several studies of different SC techniques to improve the energy resolution in the off-line data analysis. The first preliminary analysis has investigated the hadronic energy resolution of the AHCAL and of the full calorimeter system discussed in this analysis (the Si-W ECAL, the AHCAL and the TCMT) [78]. This has been followed by a publication of the complete analysis, focusing on the AHCAL and the TCMT energy resolution (*AHCAL+TCMT analysis*) [70]. Furthermore, the use of a neural network for improving the energy resolution of hadronic showers in the AHCAL and the TCMT has been explored [81]. In addition to that, a study of the hadronic energy resolution for a combined scintillator-SiPM calorimeter system (*all-Scint setup*), consisting of the ScECAL, the AHCAL and the TCMT, has been performed [82].

The analysis presented in this thesis is compared to the published analysis of the AHCAL and TCMT energy resolution and to the analysis of the hadronic energy resolution in a combined scintillator-SiPM calorimeter system. The AHCAL+TCMT analysis uses the same CERN data that is used in the current analysis, while in the all-Scint setup analysis, the investigated data have been recorded at FNAL test beam facility.

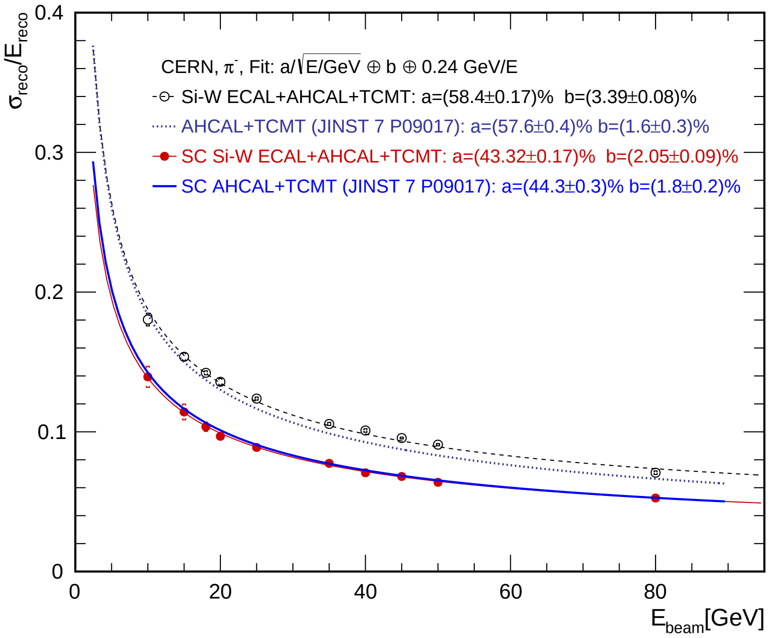

Figure 7.14: The reconstructed energy resolutions obtained from the standard and Full SC reconstruction of CERN data compared to the energy resolution fits published in reference [70]. The published results show the reconstruction of CERN events with a shower start in the first 5 AHCAL layers. The reconstruction was performed with a standard reconstruction and a SC method that apply weights only to the AHCAL and the TCMT hits . The fit parameters are given in the legend. The total (statistical and systematic) uncertainties are marked with brackets, '[]'.

In the AHCAL+TCMT analysis, only events of pion showers with a reconstructed FHI in the first five layers of the AHCAL have been considered in order to avoid longitudinal leakage. Since the Si-W ECAL in these events has contained only the primary track, a fixed value of 200 MeV (equivalent to a MIP) has been used to consider the Si-W ECAL contribution to the total energy [78]. Two reconstruction methods have been investigated in the AHCAL+TCMT analysis: a standard reconstruction method and a SC scheme, which applied weights (with a different parametrization than the HCAL SC scheme) to energy depositions of the AHCAL and the TCMT.

Figure 7.14 shows the energy resolution fits of the AHCAL+TCMT analysis along with the fitted energy resolution points of the CERN data of the current analysis. Although different types of showers are compared, fully contained showers in the AHCAL+TCMT and showers in the full system (with loosen demands on the shower starting), the standard reconstruction in both analyses is compatible within the uncertainties, with a slightly worse resolution for the full system showers. The agreement between the results becomes even better after applying SC: the stochastic terms of the fits agree by 1%, while the constant terms agree by 14%. This result shows a stable performance when applying SC algorithms despite the additional complexity of the full system, which includes different technologies and different sampling structures.

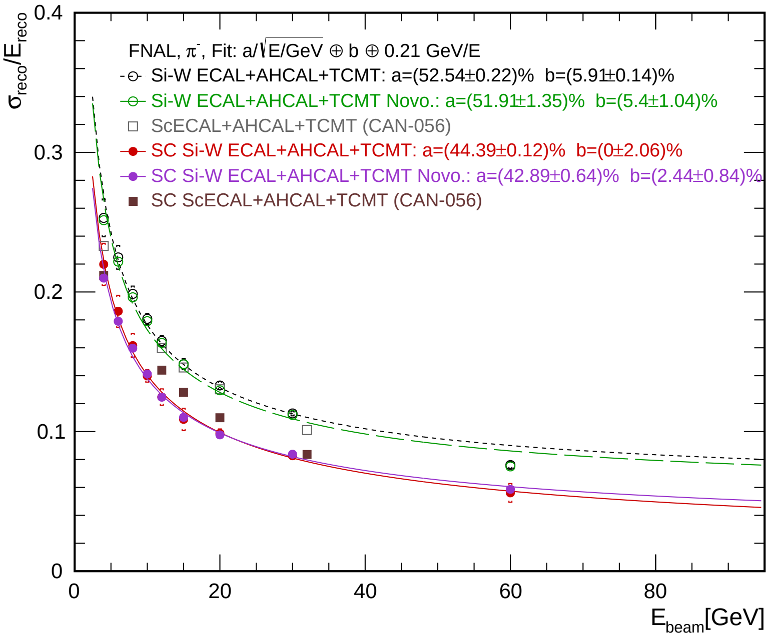

Figure 7.15: The reconstructed energy resolution obtained from the standard and Full SC reconstruction of FNAL data (Si-W ECAL+AHCAL+TCMT) compared to the energy resolution obtained from the analysis of the all-Scint setup (ScECAL+AHCAL+TCMT) [82]. The energy resolution of the Si-W ECAL+AHCAL+TCMT setup are determined by the two-step-Gaussian fit (black and red for the standard and Full SC methods, respectively) and by the Novosibirsk (green and magenta, respectively). The fit parameters are given in the legend. The total (statistical and systematic) uncertainties are marked with brackets, '[]'.

The all-Scint setup analysis have considered as well only events in which the pion showers have a very high probability to be fully contained in the calorimeter system. This has been implemented by selecting only events with a reconstructed FHI in the ScECAL layers or in the first five layers of

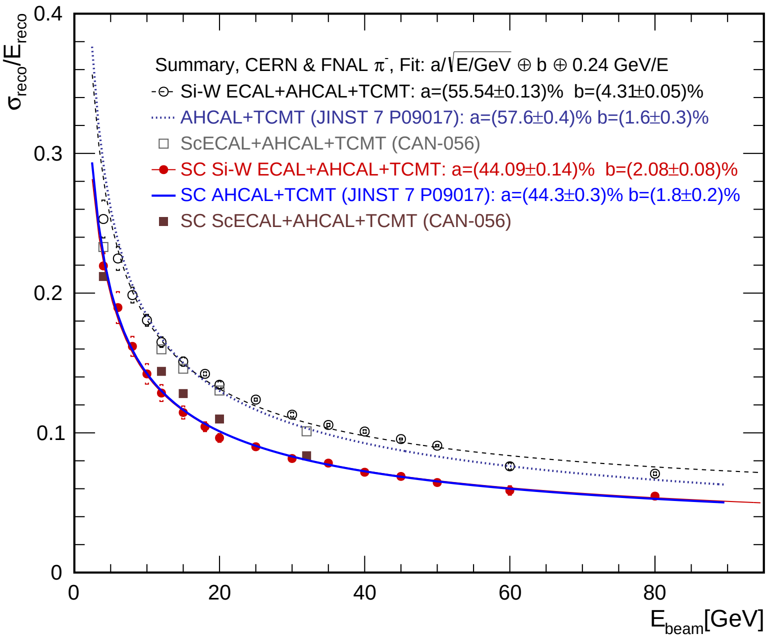

Figure 7.16: The reconstructed energy resolutions obtained from the standard and Full SC reconstruction of the combined dataset compared to the energy resolution fits published in reference [70] and the energy resolutions obtained from the all-Scint setup (ScECAL+AHCAL+TCMT) in reference [82]. The fit parameters are given in the legend. The total (statistical and systematic) uncertainties are marked with brackets, '[]'.

the AHCAL. The reconstructed energies, in the all-Scint setup analysis, have been determined by a fit of the Novosibirsk function rather than the two-step-Gaussian fit (see sub-section 6.2.1). For the comparison of the analysis discussed in this dissertation with the all-Scint analysis, events of the current analysis are fitted with both methods. The different fitting methods result in a difference smaller than 2.7% in the obtained energy resolutions, excluding the 4 GeV and the 60 GeV data-points obtained from the SC reconstruction which differ by 4.7%. The energy resolutions of FNAL data obtained from the different fitting methods are shown in figure 7.15 along with the energy resolution data-points obtained in the all-Scint setup analysis. Both analyses reconstructed 4 GeV, 12 GeV, 15 GeV and 20 GeV data. The SC energy resolutions of the 4 GeV data agree within 1% in both analyses; however for the other beam energies the combined setup considered in this analysis (the Si-W ECAL, the AHCAL and the TCMT) shows a better performance with 12.9% lower energy resolution on average.

In order to summarize the comparison of the analyses, the results for the combined dataset (CERN and FNAL) are shown in figure 7.16 along with the results of the previous analyses, which are discussed above.

7.6 Application of Weights to Different Beam Periods

The robustness of the SC method originating from the training of the SC reconstruction is demonstrated by implementing SC weights obtained from the CERN data on FNAL data and vice-versa. This gives a realistic evaluation of the changes in the expected results obtained from different beams or from the reassembly of the calorimeter. Figures 7.17 and 7.18 show the difference in the reconstructed energy resolutions when using the different weights in the SC reconstruction procedure. Since the weights are optimized for a specific energy range, they are applied only to the measurements in that range.

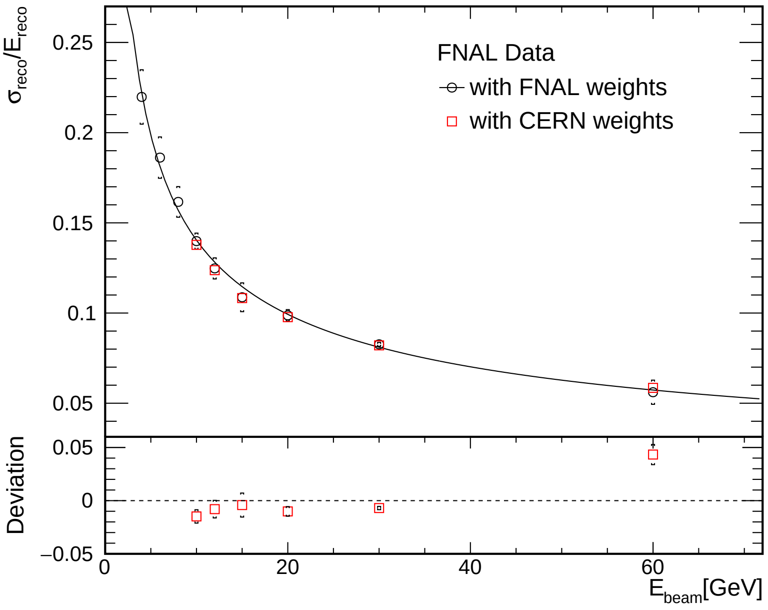

Figure 7.17: The reconstructed energy resolution of FNAL data obtained from SC weights optimized with either FNAL or CERN data, and relative deviations between them. The total (statistical and systematic) uncertainties are marked with brackets, '[]'. The dashed line corresponds to a zero relative deviation.

When CERN weights are applied to the FNAL data, changes within 2% in performance are visible, with the exception of the 60 GeV data-point, where a deterioration of 6% is observed. In the opposite case, a slight energy dependent deterioration of the energy resolution is observed, rising up to 4% at 40 GeV. The overall relatively small changes when transferring the weight calibration between the different datasets demonstrate the robustness of the SC method, and show that the energy dependence of every bin weight, which is trained for a specific dataset, does not have a negative impact on the performance of the algorithm. The inferior performance of the FNAL weights applied to the CERN data suggests that extending the weight optimization procedure to higher energies is beneficial. In this concrete case, such a behavior may be further amplified by the relatively low statistics of the 60 GeV FNAL data-point, which may have a negative impact on the precision of the weights at high energies.

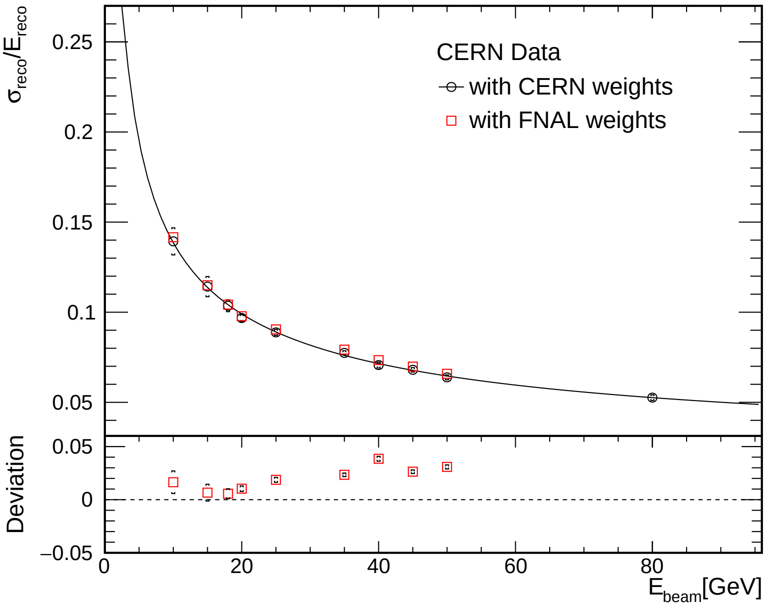

Figure 7.18: The reconstructed energy resolution of CERN data obtained from SC weights optimized with either CERN or FNAL data, and relative deviations between them. The total (statistical and systematic) uncertainties are marked with brackets, '[]'. The dashed line corresponds to a zero relative deviation.

CHAPTER 8

COMPARISON WITH SIMULATIONS

Simulation of the test beam experiments are performed using the FTFP_BERT and the QGSP_BERT physics lists in GEANT4 version 10.1 and the Mokka framework. These two physics lists were studied in previous CALICE analyses [75, 83] and are, at present, the state-of-art lists for simulation of interactions of high energy hadrons with matter.

Simulated events are selected using the same selection criteria optimized previously for data events (detailed in chapter 5). The selected events are reconstructed with the standard and the SC reconstruction schemes using the calibration factors ($C_{\text{Si-W ECAL}}$ and C_{AHCAL}) obtained from the data rather than the ones obtained from the simulations to maintain compatibility with the reconstruction of data events and to provide information on the agreement of the absolute visible energy between data and simulation.

This chapter gives an overall comparison between the detector performance obtained from the test beam data and that predicted with Monte Carlo simulations. The longitudinal profiles in the data and the simulations are discussed in section 8.1. In section 8.2, the SC weights obtained from data and simulation events are compared and section 8.3 contains the reconstruction results of the standard and the Full SC schemes. Section 8.4 presents the ultimate test for the SC method consisting in applying the SC weights from simulation to data events. Finally, section 8.5 presents results of a stand-alone reconstruction of the simulation, by using the calibration factors obtained from the simulated events.

8.1 Longitudinal Profiles

The comparison of shower profiles in data and simulated events provides a deeper insight into the simulation model in terms of the energy scale of the hits as well as the variations in each layer of the detector. Moreover, the discrepancies of the longitudinal profiles between data and simulations are a measure for possible disparities in the energy density in data and simulations, which leads to differences in the reconstruction results.

Figure 8.1 presents the longitudinal profiles of the hit energy and the hit counts in data and simulated events of 15 GeV beams recorded at CERN and FNAL setups. The selection of events with FHI layer greater than or equal to 5 is responsible for the low values in the first five layers.

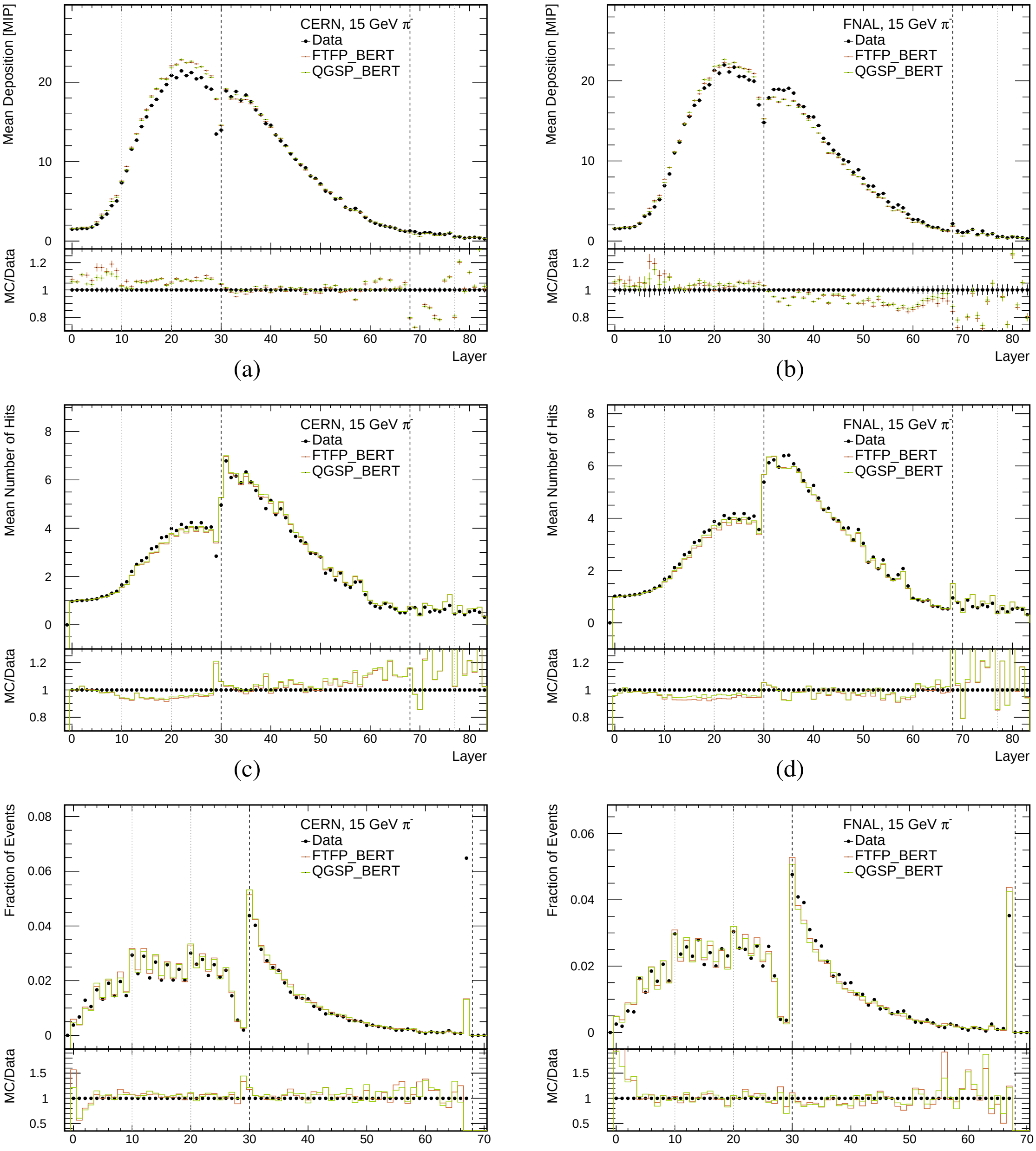

(a) (b)

(c) (d)

(e) (f)

Figure 8.1: Comparison of the layer-to-layer variation of: (a,b) the average mean deposition; (c,d) the average number of hits; and (e,f) the reconstructed FHI layer. Left panel: 15 GeV CERN events. Right panel: 15 GeV FNAL events. Test beam data is marked with black points, the FTFP_BERT simulation is marked in red and the QGSP_BERT simulation is marked in green. Layers 0 – 29 are the Si-W ECAL layers; layers 30 – 67 are the AHCAL layers; layers 68 – 83 are the TCMT layers. The black dashed lines indicate transitions between the sub-detectors. The gray dotted lines indicate transition between absorber thicknesses.

The reduction in the response around layer 29 originates from the lateral leakage in the transition region between the Si-W ECAL and the AHCAL, and the gradual reduction in the last AHCAL layers suggests, on average, a good containment of showers in the detection system. This general shape is well described by the physics lists; however, there are discrepancies between the data and the simulation.

Layers 5 – 29 show a discrepancy of about 8% in both visible energy and the number of hits between data and simulations: the simulations have less hits, but a higher visible energy. This means that the energy density in the simulations is higher. Between layers 30 – 67, the hits are fewer in the simulations by about 5% and the visible energy per layer is lower by up to 10% in FNAL events. For CERN events, the visible energy per layer agrees within around 5% between data and simulations; however, the number of hits is higher in the simulation, fluctuating from layer-to-layer and reaching 20% in the last layers of the AHCAL. This means lower energy density in the simulations of the AHCAL hits in CERN events. In principle, the differences in the mean deposition in MIP units can be reduced in the GeV scale when using the calibration factors obtained from the simulations which, as shown in figure 6.1, have opposite trends.

The distribution of the reconstructed FHI layer (before applying the selection cuts on the FHI layer) for data and simulations is shown in figure 8.1(e) and 8.1(f) for 15 GeV CERN and FNAL events, respectively. The large peak in layer 68 indicates events with no identified FHI layer, which are constituted by muon events and punch-through events (e.g. pions showering in TCMT). These events are rejected in the event selection. The muons in the simulation come from in-flight decay of pions whereas their relative fraction depends on the location of the particle-gun in the simulation model. Since the muon content in data and simulations is quite different, the discrepancy between the two in this layer (layer 68) is expected. The fluctuation between odd and even FHI layers in the Si-W ECAL (layers 0 – 29) reflects the additional material associated with PCB plates and the mechanical support, which adds an additional $\sim 0.008\,\lambda_I$, to every odd layer [84]. The upward steps at layers 9 and 19 are the result of the increasing thickness of the tungsten plates at these locations. These features are all reproduced in the simulations, and are in general well modeled. The large discrepancies between the data and the simulations in the first 4 layers originate from electron contamination in the data, which is removed by the pion selection. For events of interest, selected events with a reconstructed FHI between layers 5 – 55, the shape of the FHI distribution in data is reproduced in the simulations.

The longitudinal profiles in data and simulated events of other beam energies are characterized similarly to those described above for 15 GeV events. The corresponding figures can be found in appendix D.5.

8.2 Software Compensation weights

For the reconstruction of simulated events with the SC methods, the bin weights are optimized from the simulations using the same procedure as the one used for data events, described in section 6.3. This optimization is performed separately for each dataset and therefore results in a different set of weights for each dataset and each SC scheme. The dependence of the bin weight upon the beam energy is compared between weights obtained from data and weights obtained from simulations.

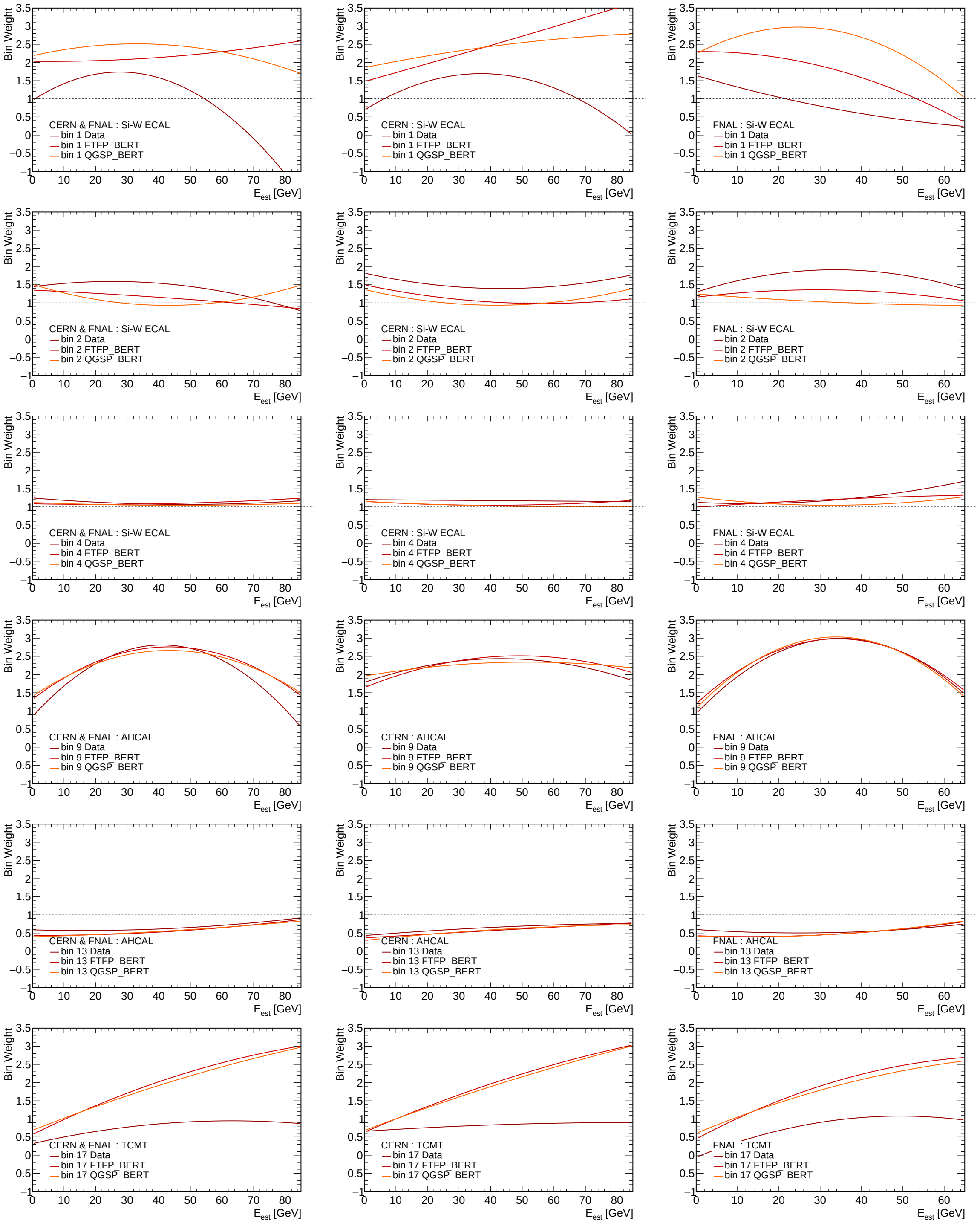

Figure 8.2: Selected bin weights obtained from data and simulations for the Full SC method as a function of the beam energy. Left column: Weights optimized with the combined (CERN+ FNAL) dataset. Middle column: Weights optimized with the CERN dataset. Right column: Weights optimized with the FNAL dataset. The bins are numbered as follows: bins 1 – 8 are the Si-W ECAL bins, bins 9 – 16 are the AHCAL bins and bin 17 is the TCMT bin.

Selected bin weights of the Full SC scheme, which were optimized with the different datasets (CERN, FNAL and the combined datasets) are shown in figure 8.2. The optimization with the different datasets results in a similar level of agreement between the physics list weights and the data weights. The data-driven weights for the AHCAL hits are generally compatible with simulation-driven weights. For the Si-W ECAL hits in the first two energy bins, large discrepancies between data-driven and simulation-driven weights are obtained. The data-driven weight for the TCMT hits differs as well from the simulation-driven weight, likely due to the large differences in the energy density of the hits in data and simulations, which can be seen in figure 8.1.

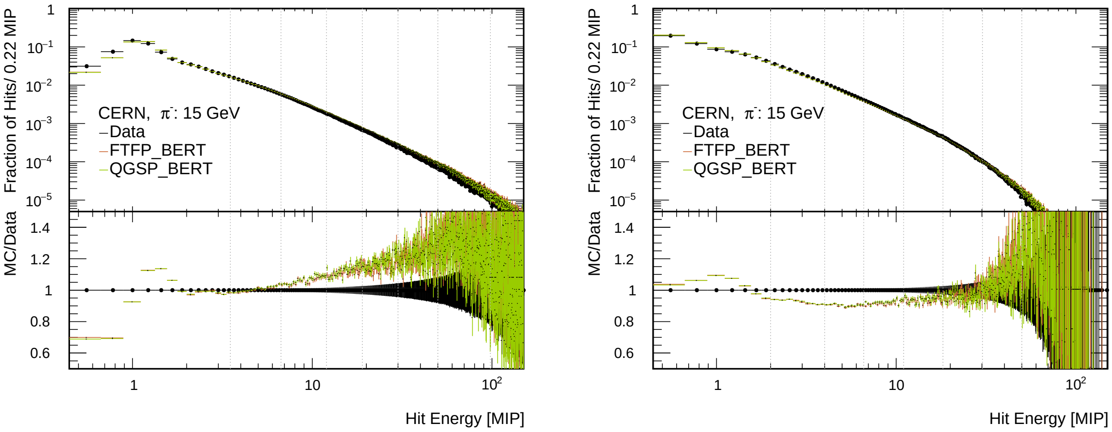

(a) Si-W ECAL CERN

(b) AHCAL CERN

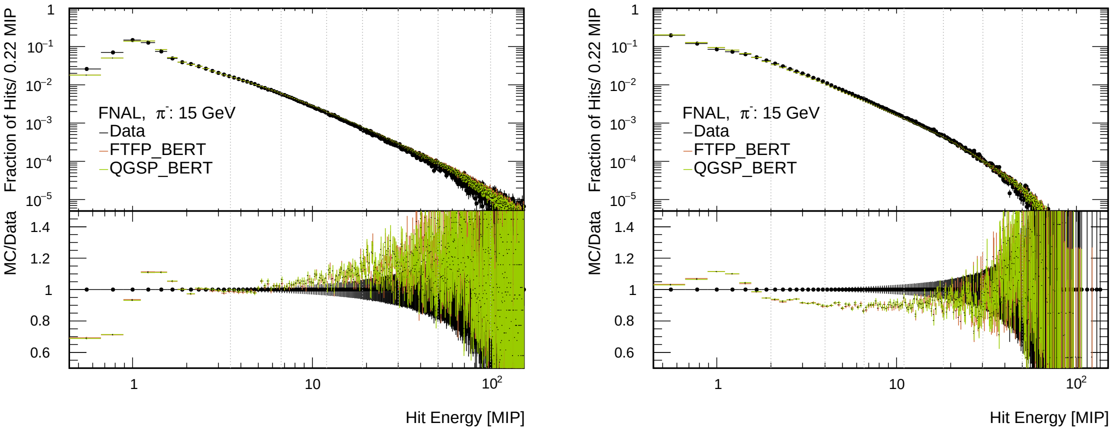

(c) Si-W ECAL FNAL

(d) AHCAL FNAL

Figure 8.3: The hit energy spectra of 15 GeV π^- in test beam data and simulations. Left: Hits in the Si-W ECAL. Right: Hits in the AHCAL. The gray dotted lines indicate the different energy-bins of the SC schemes.

Since the weights are derived from the bin contents, the hit spectra in data and simulations in each sub-detector are compared as well in order to gain a better understanding of the discrepancies between the obtain weights. The comparison of the hit spectra in the Si-W ECAL and the AHCAL is given in figure 8.3 for 15 GeV pions. In the Si-W ECAL, the fraction of low-energy hits in the first energy-bin is lower in the simulations than in data, presumably explaining the higher simulation-driven weights for this bin compare with the corresponding data-driven weight. The variations between the hit spectra in the AHCAL in simulations and real-data seem to have a rather small impact of the corresponding weights, which are, as mentioned before, considerably consistent with

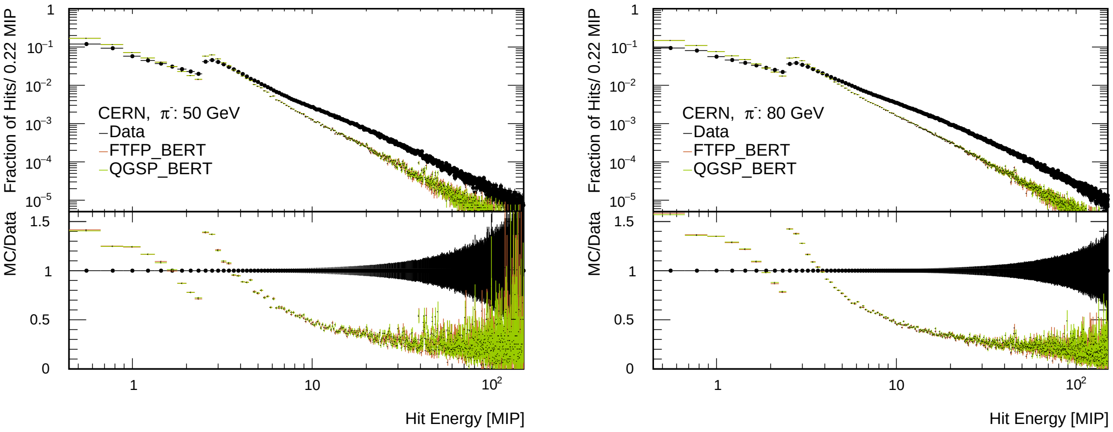

(a) TCMT, 50 GeV CERN (b) TCMT, 80 GeV CERN

Figure 8.4: The TCMT hit energy spectra of (a) 50 GeV and (b) 80 GeV π^- in CERN test beam data and simulations of the physics lists FTFP_BERT and QGSP_BERT.

each other. The hit spectra in the TCMT in data and simulations are shown is figure 8.4 for 50 GeV and 80 GeV events (chosen due to the high statistics of TCMT hits at these energies). The substantially lower fraction of high-energy hits in simulations, reaching up to 90% difference than that fraction in the data, might explain the growing disparities in this energy range between the simulation-driven weights and the data-driven weight for the TCMT hits.

8.3 Reconstruction Results

A comparison of the reconstruction results obtained from data and simulations gives a better understanding of the agreement between the two as well as provides an additional validation for the reconstruction methods. The distributions of the event energies that are reconstructed with the standard method are shown in figures 8.5(a) and 8.5(c) for 4 GeV and 80 GeV beams, respectively. The 4 GeV distributions in the simulations are narrower than those in the data and shifted by approximately 7% towards lower energy. The distributions of 80 GeV events in simulations are broader by about 32% with respect to the data distribution. Similar but much reduced trends in the distribution spreads are shown in figures 8.5(b) and 8.5(d) for the SC reconstruction of 4 GeV and 80 GeV, respectively.

Each of the distributions is fitted as described in section 6.2.1 to determine the mean energy and the energy resolution. The full range of reconstructed energy resolutions is presented in figure 8.6 as a function of the beam energy. Each set of results is fitted with the function described in equation 7.1. The corresponding fit parameters are summarized in table 8.1. For both the simulation and the data, a considerable improvement in the resolution with the Full SC method is visible as well as a reduction of the stochastic and constant terms of the fit. However, the resulting stochastic terms are lower in the simulations than those in the data, while the constant terms follow an opposite trend. This behavior, which is caused by the strong correlation of the fit parameters, makes it difficult to compare the fit results of the data and the physics lists.

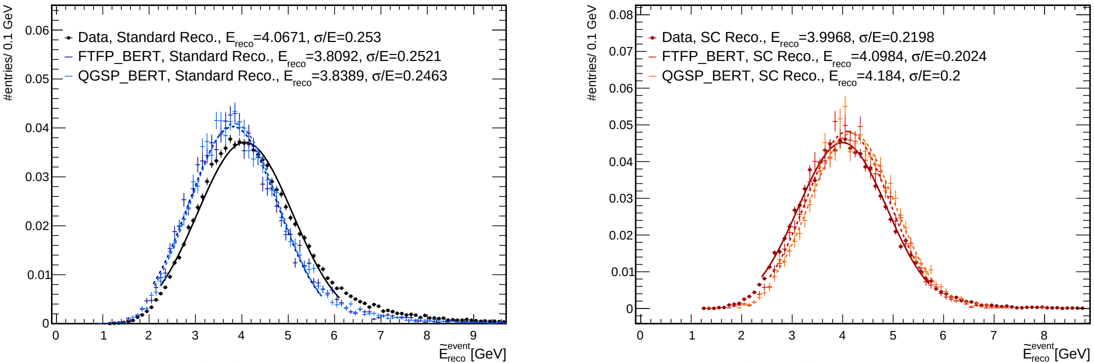

(a) Standard Reco. 4 GeV (b) Full SC 4 GeV

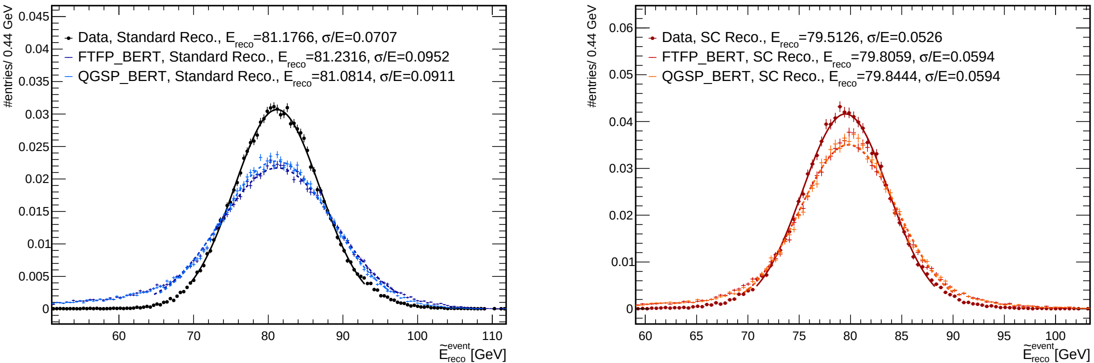

(c) Standard Reco. 80 GeV (d) Full SC 80 GeV

Figure 8.5: The distributions of energies obtained from the standard (left) and Full SC (right) reconstruction of data and simulations of (a,b) 4 GeV FNAL beams and (c,d) 80 GeV CERN beams. The mean energy, $\mathrm{E}_{\mathrm{reco}}$, and the energy resolution, σ/E, of each distribution (obtained from the two-step Gaussian fit) are detailed in the legend.

Looking at the data-points of the standard energy resolutions, an energy dependent deterioration of the data-simulation agreement is visible from the 12 GeV data-point due to an inferior resolution in the simulations. The discrepancies reach 34% for the FTFP_BERT list and 28% for the QGSP_BERT list at 80 GeV. In addition, from the 12 GeV point onwards, the energy resolutions of the QGSP_BERT physics list are lower than the ones of the FTFP_BERT physics list by an average value of 5%. In the lower energy range, the FTFP_BERT physics list performs better than the data, while the QGSP_BERT physics list performs the worst (excluding the 4 GeV data-point).

The SC reconstruction corrects for the large discrepancies in the higher energies and gives an average agreement of 3% between the energy resolutions of data and simulations from 30 GeV until 80 GeV. In the lower energy range of 4 GeV to 25 GeV, an inferior agreement of 6% on average is measured, caused predominantly by a lower energy resolution in the simulations compared to data.

The relative improvement of the energy resolution with the SC methods as a function of the beam energy is presented in figure 8.7. This improvement in simulations tends to have a similar energy dependence when compared to the dependence in data, which is described in section 7.4. The improvement is substantially larger in the simulations than that in the data, with the largest improvement observed for the FTFP_BERT physics list. This is due to the inferior energy resolutions of simulated events when applying the standard reconstruction compared with the

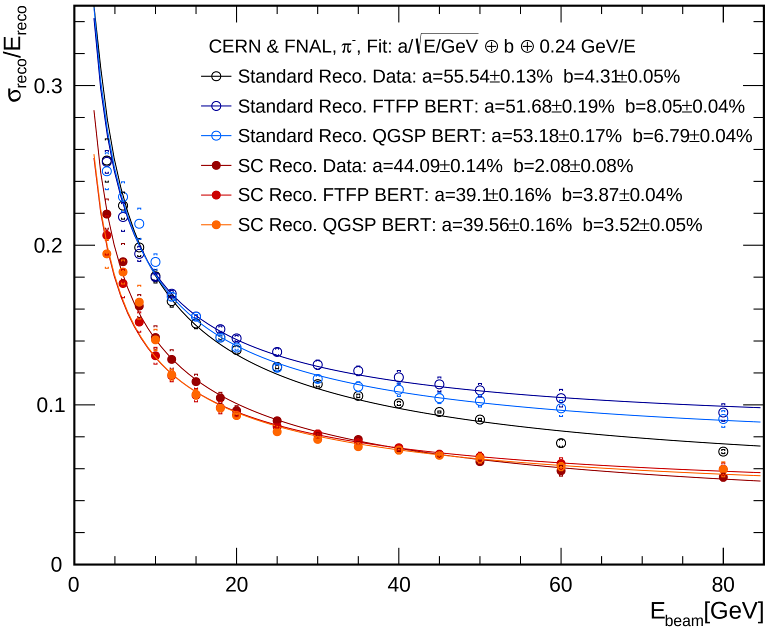

Figure 8.6: The reconstructed energy resolutions obtained from the standard and Full SC reconstruction of the combined (CERN and FNAL) test beam data and simulations. The fit parameters are given in the legend. The total (statistical and systematic) uncertainties are marked with brackets, '[]'.

Table 8.1: The summary of the fit parameters obtained from the standard and the Full SC reconstruction of data and simulations.

reco.	a_{Standard} [%]	b_{Standard} [%]	a_{SC} [%]	b_{SC} [%]
Data	55.54±0.13	4.31±0.05	44.09±0.14	2.08±0.08
FTFP_BERT	51.68±0.19	8.05±0.04	39.10±0.16	3.87±0.04
QGSP_BERT	53.18±0.17	6.79±0.04	39.56±0.16	3.52±0.05

resolutions obtained from the SC methods in the higher energy range.

The performance of different SC schemes in the simulations is similar to the performance in the data. The Full SC produces the best energy resolutions, yet a considerable improvement can already be seen with the HCAL SC method. The energy resolutions of simulated events reconstructed with each SC scheme are compared in appendix D.4.

The linearity in data and simulations is shown in figure 8.8 for the standard and the Full SC methods. For both methods, the reconstructed energies agree within 2.5% from 40 GeV onwards. With the standard reconstruction, the lower energies of simulated events are shifted with respect to the energies of data events (as discussed above for the 4 GeV reconstruction) with up to 10% deviation from the beam energy. This improves with the SC reconstruction, for which the largest deviation is about 7%.

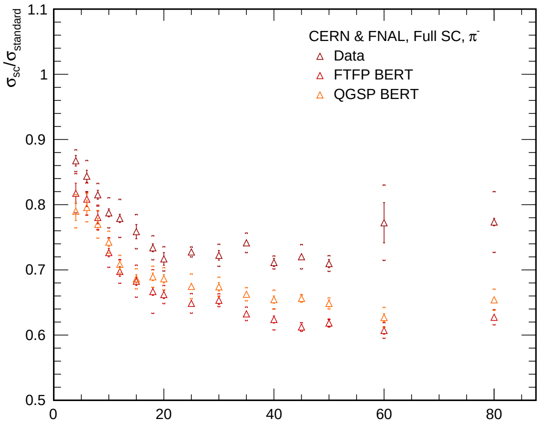

(a) Full SC

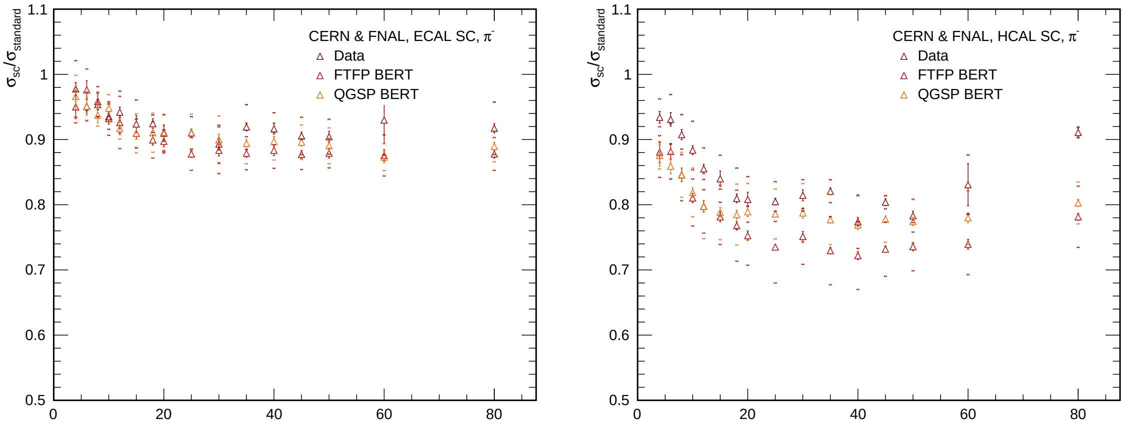

(b) ECAL SC (c) HCAL SC

Figure 8.7: The relative improvement of energy resolutions obtained from the different SC reconstruction of the combined (CERN and FNAL) test beam data and simulations. The total (statistical and systematic) uncertainties are marked with brackets, '[]'.

8.3.1 Implications for PandoraPFA study

In studies performed with PandoraPFA (see sub-section 2.3.1), two methods are used to reconstruct events simulated with the QGSP_BERT physics list. The first method is similar to the standard method presented here, while the second is an SC scheme with a different weight parametrization, in which weights are applied only to the AHCAL hits. These studies show a relative improvement of approximately 13% to 26% in the reconstruction of single neutral hadrons as well as an overall jet energy resolution better than 4% with the SC method [30]. The results for the single hadron reconstruction are compatible with the HCAL SC results presented here.

Since the PandoraPFA is developed for a full detector system in the future collider experiments, the studies can be performed only by means of simulations. The comparison of different reconstruction methods in the current analysis, shows that for real data, comparable results to the results achieved in simulations can be obtained from the SC reconstruction methods. Moreover, the comparison of the SC schemes demonstrates that an implementation of a 'Full system' SC method in PandoraPFA

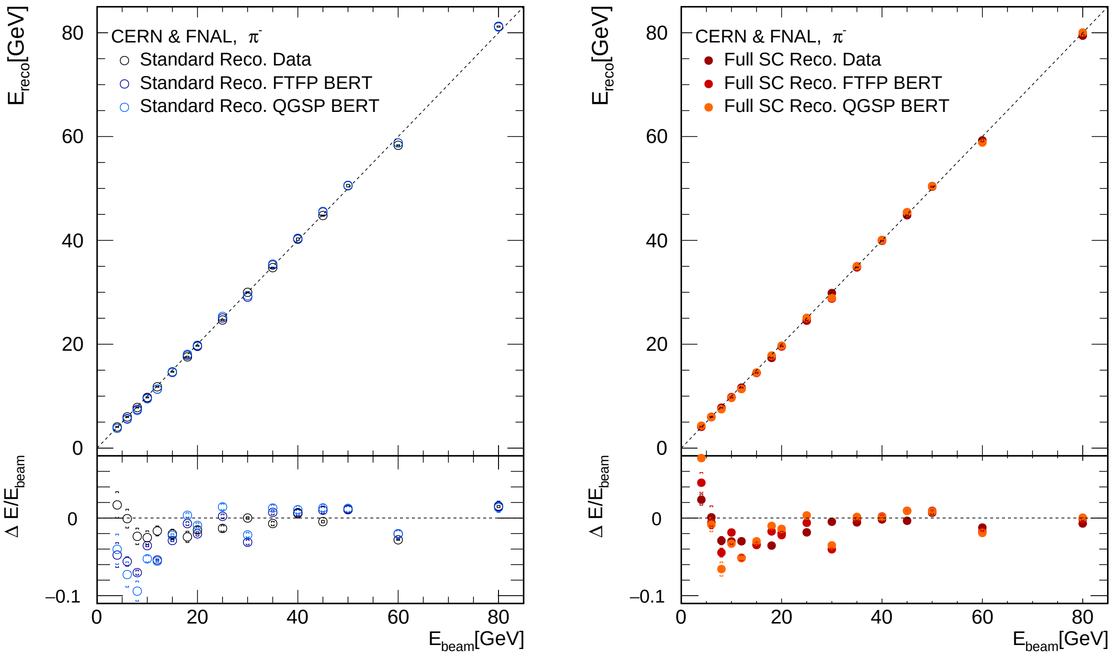

(a) Standart Reconstruction (b) Full SC reconstruction

Figure 8.8: The mean reconstructed energy and the relative residual to the beam energy versus the beam energy of the combined (CERN and FNAL) test beam data and simulations. (a) The standard reconstruction results. (b) The Full SC reconstruction results. The total (statistical and systematic) uncertainties are marked with brackets, '[]'. Dotted lines correspond to $E_{reco} = E_{beam}$.

is likely to further improve the energy resolutions for simulations as well as for data.

8.4 Applying Software Compensation Weights from the Simulations on Data

One of the main questions when developing and testing any reconstruction method is whether the weights obtained from simulated events can be used to reconstruct data events. To answer this question with reference to the Full SC method, the SC weights obtained from simulations with the FTFP_BERT and the QGSP_BERT physics lists are used to reconstruct test beam data events. In this study as well, the energy calibration is done with calibration factors ($C_{\text{Si-W ECAL}}$ and C_{AHCAL}) that were optimized using data. This provides a compatible energy scale to the one of the reconstructed data and corresponds to the common use of an in-situ global calibration of the energy scale in collider experiments.

Figure 8.9 presents the fitted energy resolutions of the Full SC reconstruction which were obtained from the different SC weights. The weights derived from the FTFP_BERT events yield compatible results (<2%) to the ones obtained from the QGSP_BERT weights. Up to the 12 GeV data-point, the energy resolutions reconstructed with the simulation weights are slightly better than the ones reconstructed with the data weights. The discrepancies are larger at the lower beam energies, reaching up to 6% deviation at 4 GeV. From the 12 GeV data-point, the energy resolution obtained

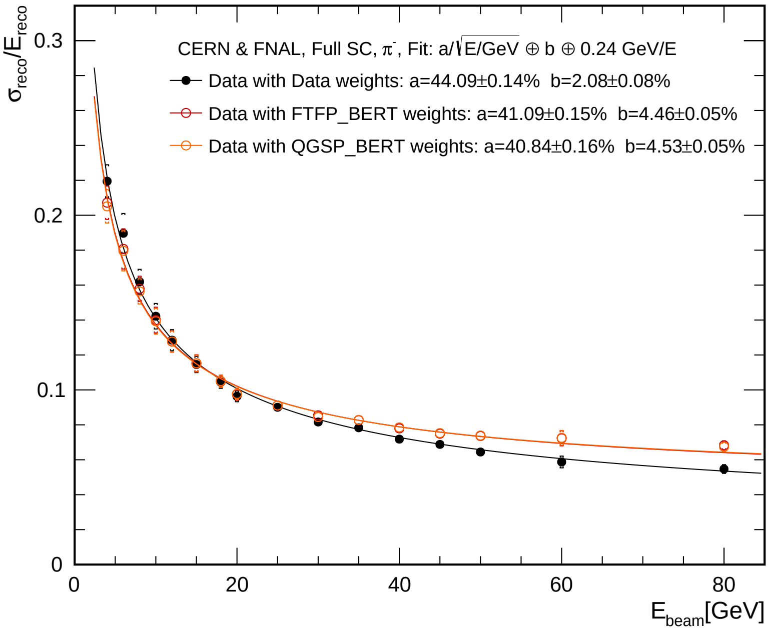

Figure 8.9: The energy resolution of data events reconstructed with the Full SC method using SC weights obtained from the data (black), the FTFP_BERT physics list (red) and the QGSP_BERT physics list (orange). The fit parameters are given in the legend. The total (statistical and systematic) uncertainties are marked with brackets, '[]'.

with the simulation weights deteriorates as the beam energy increases, extending to approximately 24% at 80 GeV. This behavior is consistent with the standard reconstruction of simulated events, which was discussed in the previous section. Since the high energy range in the simulations is modeled with an inferior energy resolution, the SC weights are optimized to reduce the spread of the reconstructed energies. This produces a spread in the SC energies when reconstructing data events with the same weights. An example for this procedure is shown in figure 8.10 for the reconstruction of 80 GeV events. Figure 8.10(a) shows the correlation between the reconstructed energies of FTFP_BERT events, where the standard reconstructed energies are largely spread, in particular towards the lower energy range. The SC reconstruction shifts the lower energies up and produces a finer energy resolution. The same weights, which were optimized for correcting the lower range in the physics list events, are then applied to data events. The resulting correlation between the reconstructed energies is shown in figure 8.10(b). Here, the influence of the weights is similar, i.e. shifting the energies towards higher values, and therefore producing a spread in the SC energies, which results in an inferior energy resolution.

The relative improvement of the SC reconstruction, which is shown figure 8.11, reflects the deterioration of energy resolutions obtained from the simulation weights at high energy. Using the simulation weights produces similar improvement as the data weights only up to 20 GeV, from which the relative improvement deteriorates gradually. Nonetheless, an average improvement of 20% still achieved with these SC weights.

The linearity of the Full SC reconstruction of data events with each of the SC weights is shown in

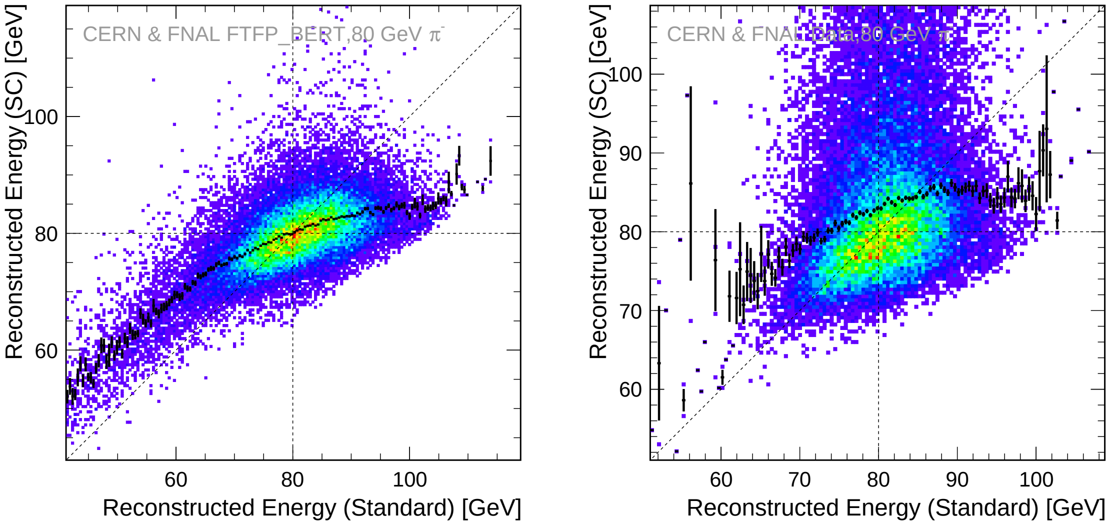

(a) FTFP_BERT events

(b) Data events

Figure 8.10: The correlation between reconstruction of events of 80 GeV beams with the standard method and the Full SC method using FTFP_BERT SC weights of events. (a) The reconstruction of FTFP_BERT events, which the SC weights are optimized for. (b) The reconstruction of data events with FTFP_BERT SC weights. The black markers show the profile of the mean SC reconstructed energy for bins of the standard reconstructed energy. The dashed lines indicate the beam energy in each axis while the diagonal traces the slope with total correlation.

figure 8.12. The energies of 4 GeV and 6 GeV events, which are reconstructed using weights from simulations, are much higher than the corresponding beam energy and deviate by approximately 6%–9% from the energies derived from the data weights. When taking in consideration the rest of the energy range, the agreement between the beam energy and all the reconstructed energies is better than 4%.

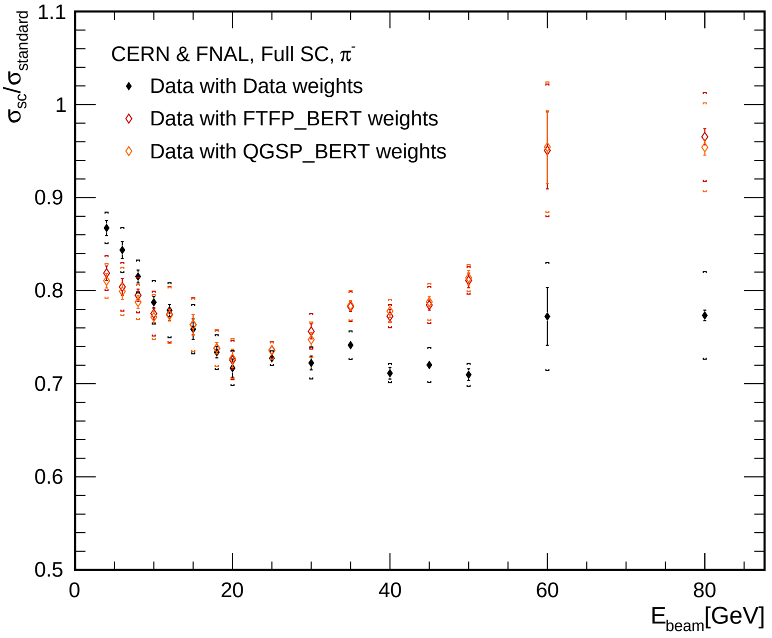

Figure 8.11: The relative improvement of energy resolution reconstructed with the Full SC method using SC weights obtained from the data (black), the FTFP_BERT physics list (red) and the QGSP_BERT physics list (orange). The total (statistical and systematic) uncertainties are marked with brackets, '[]'.

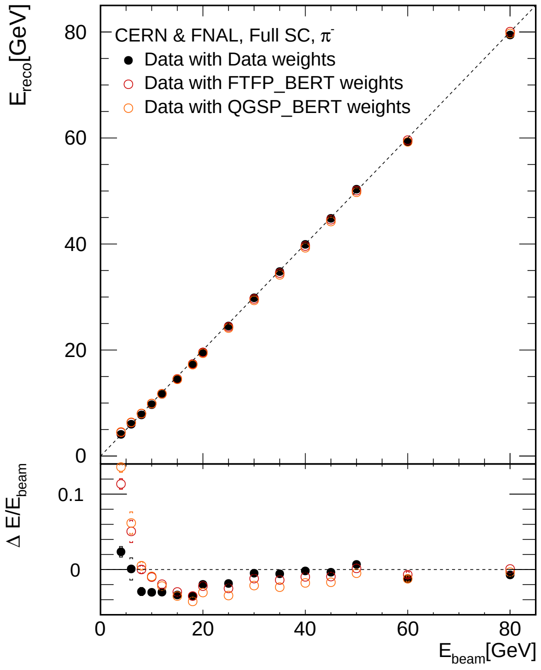

Figure 8.12: The mean reconstructed energy and the relative residual to the beam energy versus the beam energy of data events reconstructed with the Full SC method using SC weights obtained from the data (black), the FTFP_BERT physics list (red) and the QGSP_BERT physics list (orange). The total (statistical and systematic) uncertainties are marked with brackets, '[]'. Dotted lines correspond to $E_{reco} = E_{beam}$.

8.5 Stand-Alone Reconstruction of Simulated Events

All the results presented in this chapter so far are reconstructed with the calibration constants, $C_{\text{Si-W ECAL}}$ and C_{AHCAL}, which are optimized using data events (for a compatible energy scale with the data results). In this section, a stand-alone reconstruction of simulated events, including a MIP-to-GeV calibration optimized from the simulated events, is presented and compared with the previous results.

The optimization process for obtaining a set of calibration factors from each test beam experiment is detailed in section 6.1, together with the calibration factors optimized from the data and from the simulations, which will be referred to from now on as the *data calibration* and the *MC calibration*, respectively. When the data calibration factors are compared with the MC calibration factors, differences of 2% to 8% (with different trends depending on the dataset and the sub-detector) are observed. For the calibration factors of the CERN data, the most pronounced difference is in the $C_{\text{Si-W ECAL}}$, which is lower by 8% when optimized with simulated events. For the FNAL data, the simulation-derived C_{AHCAL} is higher by 6% compared to the data-derived factor.

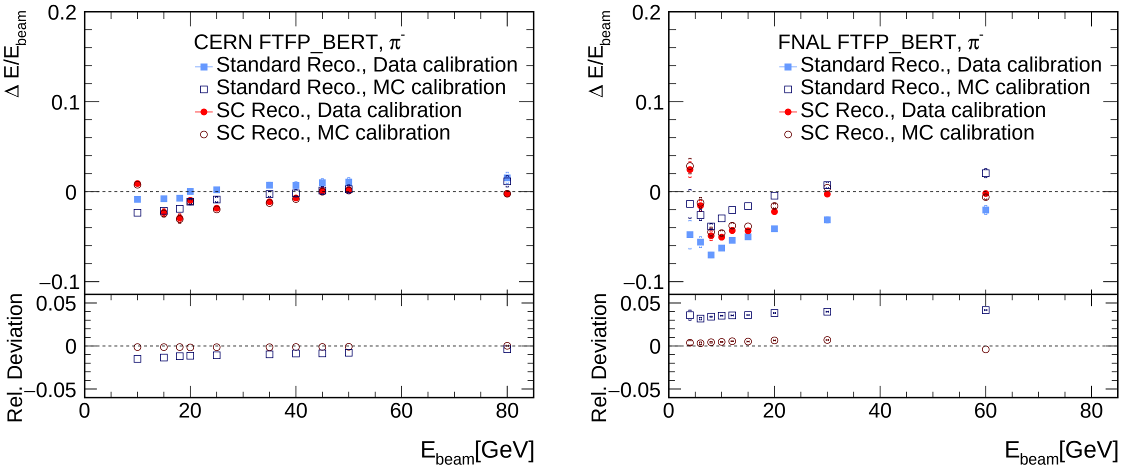

(a) CERN FTFP_BERT (b) FNAL FTFP_BERT

Figure 8.13: The relative deviations of the reconstructed energy from the beam energy of (a) CERN- and (b)FNAL- FTFP_BERT events with the standard and the Full SC methods using the data calibration and the MC calibration in the reconstruction. The dotted line correspond to $E_{\text{reco}} = E_{\text{beam}}$. In the lower panel: the relative deviations of the results obtained from MC calibration from results obtained from data calibration. The dotted line correspond to identical results with both calibrations. The total (statistical and systematic) uncertainties are marked with brackets, '[]'.

The influence of the calibration factors on the standard reconstructed energies can be clearly seen in figure 8.13, which presents the relative deviations of each reconstructed energy from the beam energy of events simulated with the FTFP_BERT physics list (the QGSP_BERT results are similar). The figure also displays the relative deviations of the results obtained from the MC calibration from the results obtained from the data calibration. For the CERN events, the energies reconstructed with the MC calibration implemented in the standard method are slightly lower than the energies reconstructed with the data calibration factors. The discrepancy decreases as the beam energy increases since at higher energies the relative fraction of shower hits in the Si-W ECAL decreases. On the other hand, reconstructed energies of the FNAL data with the standard method are higher when the MC calibration is used than when the reconstruction is done with the data calibration. This time, the relative discrepancies are around 4% – 5% with a slight deterioration towards higher energies, in which the AHCAL contribution gets more dominant.

The SC results are consistent regardless of the calibration factors in use, showing the robustness of the method and its capability to correct for energy scale differences.

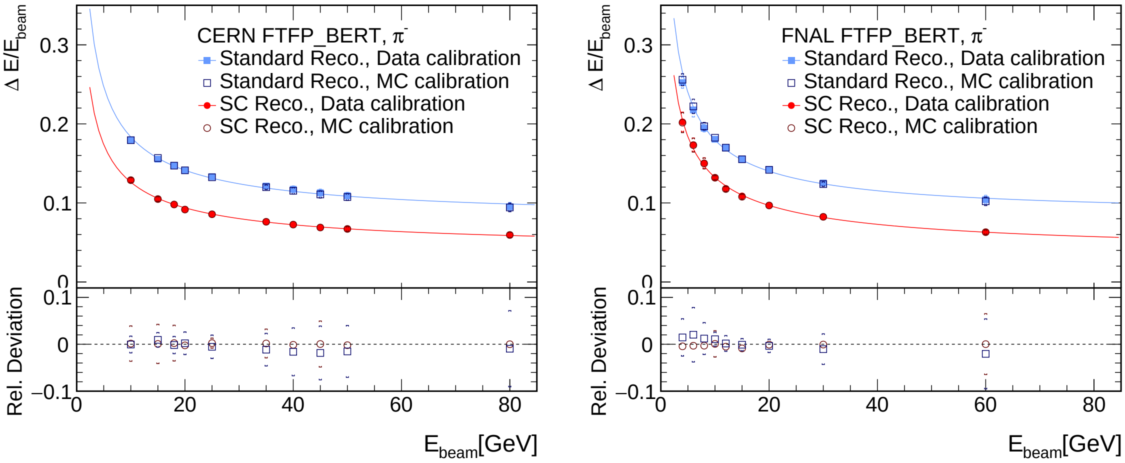

(a) FTFP_BERT (b) QGSP_BERT

Figure 8.14: The reconstructed energy resolution of (a) CERN- and (b)FNAL- FTFP_BERT events with the standard and the Full SC methods using the data calibration and the MC calibration. In the lower panel: the relative deviations of the results obtained from MC calibration from results obtained from data calibration. The dotted line correspond to identical results with both calibrations. The total (statistical and systematic) uncertainties are marked with brackets, '[]'.

The energy resolutions obtained from the standard and the Full SC reconstructed methods using the data calibration and the MC calibration are shown in figure 8.14. Here, the difference between the calibration factors produces relative small discrepancies within 1% for each of the reconstruction methods, showing that the energy scale has no influence of the spread of the reconstructed energies.

8.6 Summary

The key observations from the comparison of data and simulations are as follows:

- For energies above 12 GeV, the standard reconstruction results in a considerable worse energy resolution in simulations than in data. The discrepancy between the two increases with energy.
- The Full SC method yields a consistent energy resolution for data and simulations, in particular at the high energy range.
- Applying SC weights obtained from simulations on data improves the energy resolutions by 20% on average compared to when using the standard reconstruction.
- SC weights obtained from simulations produces similar improvement as the data weights only up to 20 GeV, from which the improvement is reduced gradually. This is consistent with the observed differences in the standard energy reconstruction at higher energies.
- The SC method corrects for energy scale differences and therefore consistent results are obtained from different calibrations.

The simulations obtain energy resolution similar to the data resolution only at the low energy range. From 12 GeV, increasing discrepancies between the two are observed. The SC method corrects for these discrepancies and provides comparable results for data and simulations. Since the improvement of the resolution with the SC method is evaluated with respect to the standard method results, the simulations predict a larger improvement than the one observed in the data; however, the prediction of energy resolution (data-points) with SC method is realistic.

CHAPTER 9

PLASMA WAKEFIELD ACCELERATION

The remarkable success of particle physics, resulting in the establishment and in the experimental confirmation of the Standard Model, is strongly connected with the technological development of particle accelerators over the last century. Since the 1930s, when the first cyclotron was constructed, the energy of accelerators has increased by almost 10 orders of magnitude, allowing beam collisions at ever higher energies, which provided the significant discoveries of each of the Standard Model particles. Nowadays, particle accelerators of different energies have many applications in science and technology, material science, biology, medicine (including cancer therapy), fusion research, and industry. For instance, electron beams with energies of the low GeV scale produce intense picosecond X-ray pulses in synchrotron machines, or more recently even shorter, few femtosecond X-ray pulses in FEL machines. The X-rays of short pulse duration and large brightness are a unique tool to resolve the structure and dynamics of matter on the atomic scale with previously unreached spatial and temporal resolution.

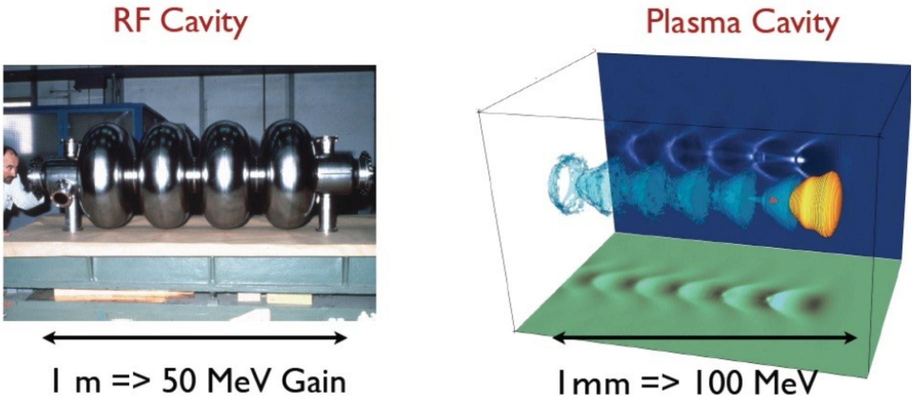

Figure 9.1: Energy gain vs acceleration length. Left: Typical RF cavity structure achieves ~50 MeV in one meter. Right: Simulation of nonlinear laser plasma wakefield. The laser pulse in yellow propagates from left to the right, the iso-electronic density is shown in blue and the electron bunch in red. Adapted from reference [85].

As mentioned in chapter 2, the common acceleration technique in which RF cavities are used is limited to acceleration gradients of about 100 MV/m due to electrical breakdown of the metallic cavity. It is for this reason that an increase of the particle energy requires an increase of the acceleration length. The modern particle accelerators at the terascale such as the future linear collider concepts, ILC and CLIC, are extremely large and costly. A possible solution for linear electron accelerators is plasma-based acceleration, enabling acceleration of electrons to GeV energy in a few centimeters. At the current stage, the quality of the electron beams accelerated with this technique is still not comparable with that of the conventional RF accelerators; however, the concept of plasma wakefield acceleration is an ongoing research field, aiming at providing the next-to-next generation colliders.

Plasma-based acceleration was recognized in 1979 as a possible high-gradient alternative to the conventional RF acceleration [86]. The first suggested scheme included high-intensity laser pulses to drive the plasma wakefield (*laser wakefield acceleration*); however, soon after, in 1985, another scheme in which relativistic charged particle bunches are used for the same purpose, was proposed [87]. The latter scheme, known as *plasma wakefield acceleration*, is discussed in detail in this chapter. Section 9.1 introduces the theoretical fundamentals for this acceleration technique, including the linear and non-linear theories behind the construction of a PWFA. A study of the transition between these theories is presented in section 9.2.

As a first step towards applications in HEP, the use of plasma wakefield acceleration technology in FEL machines is being investigated. Typically, FEL machines require acceleration to energies lower than those needed in collider experiments. Several projects, such as FLASHForward at DESY [88] and EuPRAXIA@SPARC_LAB [89], aim at demonstrating the potential of plasma wakefield accelerators for the production of high-quality electron beams that will support FEL operation. A preliminary study of an FEL scheme with a PWFA, using the possible beam parameters of the SwissFEL operating modes [90], is presented section 9.3.

9.1 Basic Principles of Plasma Wakefield Accelerators

Plasma is a collection of free electrons and ions with an overall zero charge that behave in a collective way due to attractive and repelling electric forces between free charges. The enormous number of free electrons inside a plasma can be manipulated altogether in a coherent fluid-like manner, providing the capability of plasmas to support considerably high acceleration gradients.

A charged particle beam which propagates in the plasma, a *drive bunch*, interacts electromagnetically with the plasma electrons. The space-charge field of the particle bunch displaces the plasma electrons, predominantly in a transverse direction to the bunch propagation. In the case of a negatively charged particle bunch (e.g. an electron bunch), the plasma electrons are expelled from the bunch volume, leaving behind the plasma ions, which are much heavier and considered immobile on the electrons' time scale*. At the next moment, when the particle bunch moves further in the plasma, the electromagnetic force of the positively charged ions attract the plasma electrons back toward the axis (of the bunch propagation). However, due to the kinetic energy gained from the electric field, these electrons overshoot and sustain plasma oscillation at the plasma (angular)

---

*The ions can move over the same time scale as the electrons when the drive bunch density is much larger than the plasma density. In this case, the ion motion need to be considered as well [91–93].

frequency ω_{pe}. ω_{pe} is defined[†] as

$$\omega_{pe} = \sqrt{\frac{n_{pe} e^2}{\varepsilon_0 m_e}}, \tag{9.1}$$

where n_{pe} stands for the local plasma density, e and m_e represent the electron mass and charge, respectively, and ε_0 is the vacuum permittivity. The plasma oscillation sets up a coherent plasma density fluctuation which propagates at the velocity of the drive bunch, i.e. the *plasma wakefield wave*.

Excited plasma wakefields have longitudinal and transverse components. The longitudinal wakefield is defined as the longitudinal electric field of the beam-plasma system, $W_z = E_z$. The transverse wakefield, on the other hand, is defined by the Lorentz force exerted on the unit charge that experiences the plasma wake and move with velocity close to the speed of light, $W_r \cong E_r - cB_\theta$ (in cylindrical coordinates) [94–96]. The longitudinal component generates a periodic pattern of acceleration and deceleration, while the transverse component induces a periodic pattern of focusing and defocusing. These patterns co-move with the driving beam and can extend to several plasma periods behind the beam, before heating effects dominate. Figure 9.2(a) illustrates the formation of a wakefield by a drive bunch and shows the characteristic fields.

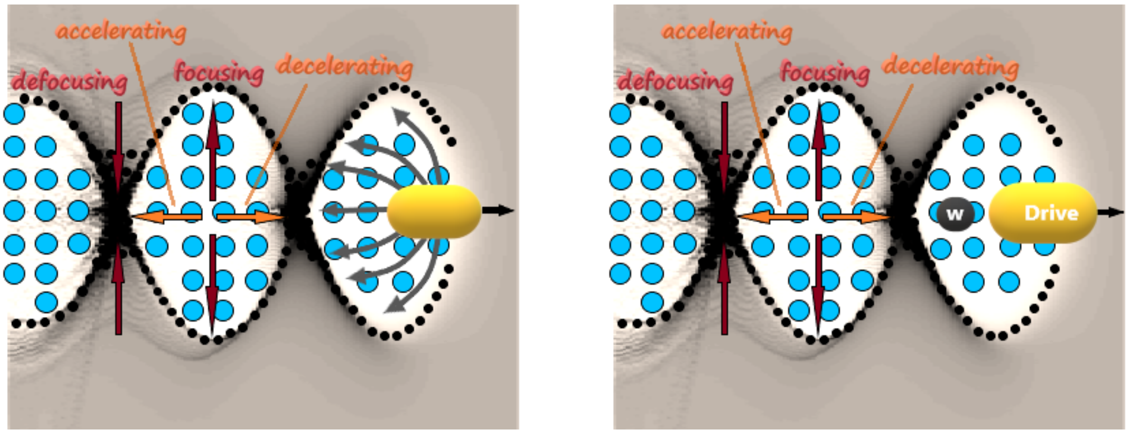

(a) (b)

Figure 9.2: An illustration of the PWFA principles. (a) A beam of negative charged particles (yellow) drives the wakefield by displacing the plasma electrons (black). The plasma ions (blue), which stay static in this time frame, draw the electrons back to the axis, setting up an electron density oscillation. The corresponding electric field components of the wakefield are depicted (W_z in orange; W_r in dark red), where the labels state the effect of these field on a negatively charged beam. (b) A witness bunch of negative charges (light black) is placed behind the drive bunch in the useful phase, in which the fields are simultaneously accelerating and focusing.

In a PWFA, the drive bunch velocity is typically close to the speed of light, $v_b \cong c$. Relativistic beams with high γ[‡] can maintain their longitudinal size over a propagation of several meters since the *dephasing length* ΔL for particles with γ and $\gamma + \Delta\gamma$ over the distance L is equal to $\frac{1}{\gamma^2}\frac{\Delta\gamma}{\gamma}L$.

[†] In SI unit system.

[‡] Lorentz factor, which is also a measure to the kinetic energy via the relation $E_k = (\gamma - 1)m_0 c^2$.

Since the phase velocity v_{ph} of the plasma wave is approximately equal to that of the drive bunch, the plasma wave number k_{pe} can be expressed as $\frac{\omega_{pe}}{v_b} \cong \frac{\omega_{pe}}{c}$ and its wavelength as $\lambda_{pe} = \frac{2\pi c}{\omega_{pe}}$. Previous studies [97, 98] have shown that for a bi-Gaussian beam with the longitudinal and radial size of σ_{zb} and σ_{rb}, respectively, the maximal wakefield can be obtained when the following relations are fulfilled:

$$\begin{aligned} k_{pe}\sigma_{zb} &\simeq \sqrt{2} \\ k_{pe}\sigma_{rb} &\lesssim 1, \end{aligned} \tag{9.2}$$

which means that bunch length is of the order of the wave period.

As the drive bunch propagates in the plasma, it loses its energy to the wakefield, which then transfers it to the accelerated beam, the *witness bunch*. In order to achieve an efficient acceleration, the witness bunch should be placed in the *useful phase*, i.e. the phase of the wake that is both accelerating and focusing, as illustrated in figure 9.2(b). For this, a relativistic bunch (on the order of MeV) is fired directly along the axis of propagation, with highly accurate timing and alignment. It is important to note that the PWFA scheme requires a pre-acceleration of both bunches to relativistic energies, which is performed with the conventional RF accelerators.

A typical measure of the efficiency with which the energy is transformed from a drive bunch to a witness bunch is the *transformer ratio*. It is defined by

$$R_{\text{trans}} = \frac{E_{\text{witness max}}}{E_{\text{drive max}}}, \tag{9.3}$$

where $E_{\text{witness max}}$ is the maximum accelerating wakefield behind the drive bunch and $E_{\text{drive max}}$ is the maximum decelerating wakefield inside the bunch. Higher values of the transformer ratio mean that more energy was transferred to the witness bunch. The transformer ratio is a value that can be obtained comparatively easily in experiments when assuming that the acceleration length for the witness beam is equal to the deceleration length for the drive beam and considering that the witness beam is accelerated at the peak accelerating field. In that case, the transformer ratio can be observed in the electron energy spectrum as the maximum energy gain of the witness beam divided by the maximum energy loss of the drive beam.

Two distinct regimes of plasma wakefield acceleration are defined by the ratio between the drive bunch density n_b and the plasma density, $\frac{n_b}{n_{pe}}$: the *linear regime* and the *non-linear regime*. In the linear regime the plasma density perturbation Δn, which is approximately equal to the beam density $\Delta n \cong n_b$, is smaller than the natural plasma density, $n_b \ll n_{pe}$, whereas the non-linear regime is characterized by denser drive bunches. A brief theoretical description of these regimes is given in the following sub-sections.

9.1.1 Linear Theory

Plasma wakefield acceleration in the linear regime can be described analytically using a cold, non-relativistic model for the plasma. The linear theory considers a uniform natural plasma density, which is free of thermal effects (i.e. cold). The ions motion is neglected as they respond on a much longer time scale than the electrons. In addition, the model uses a two dimensional system with cylindrical symmetry and considers only the first order perturbation of the plasma. A complete analytical description in all three dimensions including all relevant physical interactions is not possible. In this simplified analytical model, the wakefield is driven by a relativistic bunch characterized by a charge density distribution with uncorrelated longitudinal and transverse components, $n_{b\parallel}(\xi)$ and $n_{b\perp}(r)$, of the form:

$$n_b\left(\xi = z - ct, r\right) = n_{b\parallel}(\xi) \cdot n_{b\perp}(r). \tag{9.4}$$

The variable $\xi = z - ct$ measures the distance behind the bunch in the moving beam-plasma system. The full calculation, which is given in references [99, 100], results in the following expressions for the wakefields in the propagation direction $\hat{z}$ and the transverse direction $\hat{r}$:

$$W_z(\xi, r) = Z(\xi)R(r) = \frac{e}{\varepsilon_o}\int_{-\infty}^{\xi} n_{b\parallel}(\xi') \cdot cos\left(k_{pe}\left(\xi' - \xi\right)\right) d\xi' \cdot R(r) \tag{9.5}$$

$$W_r(\xi, r) = \frac{e}{\varepsilon_o k_{pe}}\int_{-\infty}^{\xi} n_{b\parallel}(\xi') \cdot sin\left(k_{pe}\left(\xi' - \xi\right)\right) d\xi' \cdot \frac{dR(r)}{dr} \tag{9.6}$$

$Z(\xi)$ and $R(r)$ represent the longitudinal and transverse components of W_z, which are given by

$$Z(\xi) = \frac{e}{\varepsilon_o}\int_{-\infty}^{\xi} n_{b\parallel}(\xi') \cdot cos\left(k_{pe}\left(\xi' - \xi\right)\right) d\xi' \tag{9.7}$$

$$R(r) = k_{pe}^2\int_{o}^{r} r'dr'n_{b\perp}(r')I_o(k_{pe}r')K_o(k_{pe}r) + k_{pe}^2\int_{r}^{\infty} r'dr'n_{b\perp}(r')I_o(k_{pe}r)K_o(k_{pe}r') \tag{9.8}$$

where I_0 and K_0 are the zeroth order modified Bessel functions of the first and the second kind [101].

For every beam profile, which follows equation 9.4, the corresponding wakefields travel at the speed of light and oscillate sinusoidally with a frequency determined by the plasma density. The sinusoidal patterns of the wakefields are shown in figures 9.3(a), 9.3(c) and 9.3(e). Since the fields have continuous longitudinal and radial variations, different longitudinal and radial parts of the bunch are accelerated and focused differently. This results in a broad energy spread and an emittance growth, respectively, of the witness bunch. The wakefields are symmetrical with respect to sign of the bunch charge, which means that in the linear regime, positron and electron bunches generate similar fields, differing only by a phase factor of $\pi/2$.

Since the propagating disturbance in the linear regime is relatively small, it is possible to analytically study additional characteristics of the wakefields. For instance, the maximum field amplitude in the linear regime can be estimated by using the Gauss's law with the assumption that all electrons oscillate with the same frequency. The resulting field amplitude, which is referred to as the *cold non-relativistic wave-breaking field*, is given by

$$W_{WB} = \frac{m_e c \omega_{pe}}{e}. \tag{9.9}$$

For a plasma with a neutral density $n_{pe} = 10^{16}\,\mathrm{cm}^{-3}$, this equation results in an accelerating field of 10 GV/m. In addition, studies of the transformer ratio in the linear regime have shown that for a single drive bunch with a symmetric current profile, the transformer ratio has a maximum value of 2 [102]. For an asymmetric current profile larger values can be obtained [103]; however, these asymmetric profiles are difficult to realize experimentally.

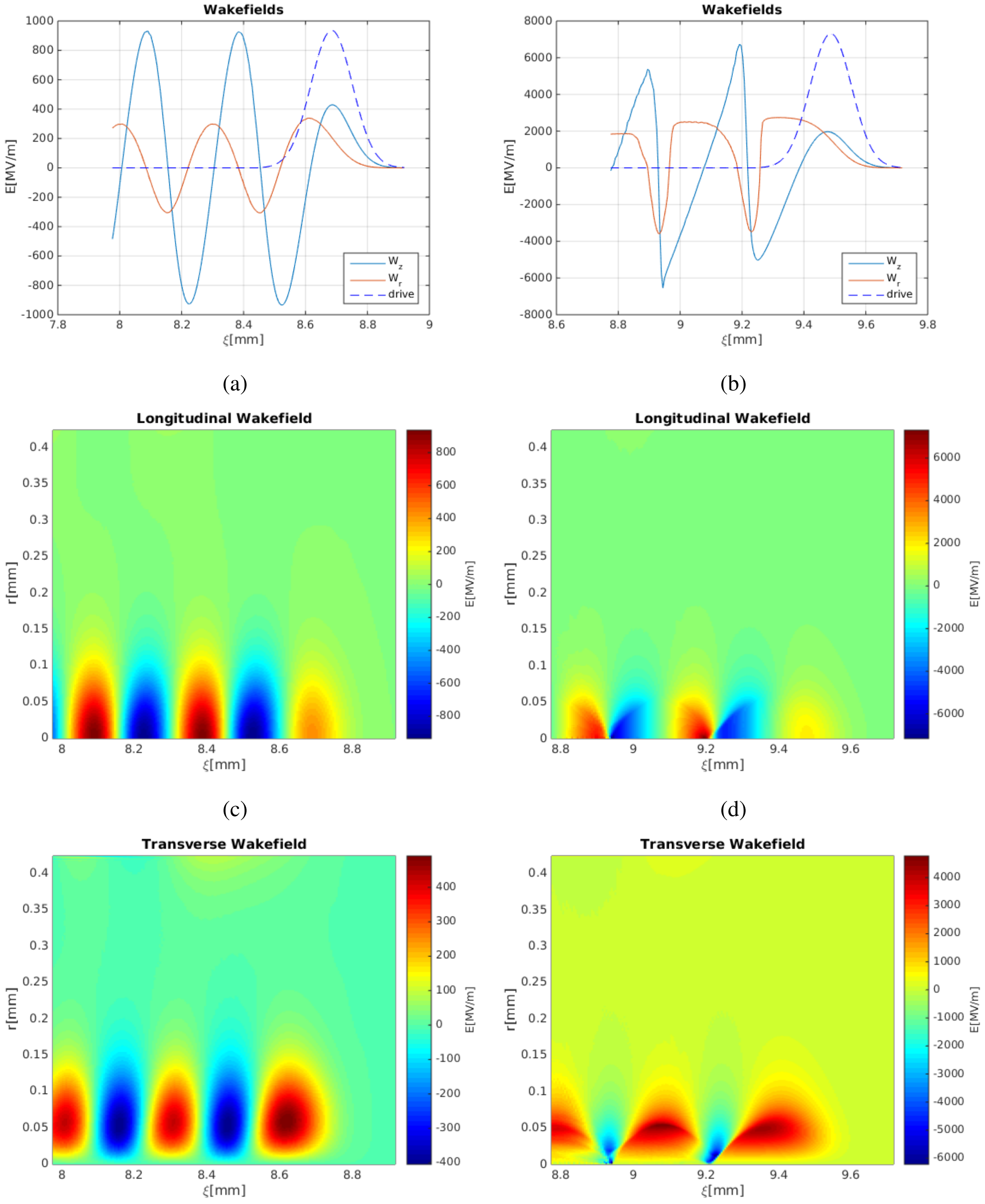

(a) (b)

(c) (d)

(e) (f)

Figure 9.3: 2D cylindrical simulation of linear (left) and non-linear (right) plasma wakefields using the OSIRIS particle-in-cell code. Figures (a) and (b): 1D cuts of the bi-Gaussian drive bunch (blue dashed line) propagating from left to right, the longitudinal field (blue) at the propagation axis, $W_z(0)$, and the transverse field (red) at radial length of the drive bunch, $W_r(\sigma_{rb})$. Figures (c) and (d): W_z in 2D. Figures (e) and (f): W_r in 2D.

9.1.2 The Non-Linear Theory

The operation of PWFA in the non-linear regime is considered to be the second generation of PWFAs. This regime, which is characterized by a beam density greater than or equal to the plasma density ($n_b \geqslant n_{pe}$), has significant advantages over the linear regime (considering a negatively charged drive bunch). The acceleration scheme in the non-linear regime is more efficient, characterized with transformer ratios larger than 2 [104]. In addition, both the energy spread and emittance growth that are seen in the linear regime, are considerably reduced when denser beams are used.

While in the linear regime, the small disturbance changes slightly the plasma density in a sinusoidally form, with a denser bunch the radial space-charge fields of the beam are strong enough to radially expel all electrons in a defined volume, leaving behind a 'channel' of unshielded ions around the core of the bunch. This leads to the formation of a spherical cavity (or a *bubble*) behind the driver [105, 106]. On the boundary of this cavity, a thin electron sheath composed of the expelled electrons is formed. This bubble structure is illustrates in figure 9.4. Eventually the space-charge of the ions pulls the electrons back, thereby creating the plasma wave wake.

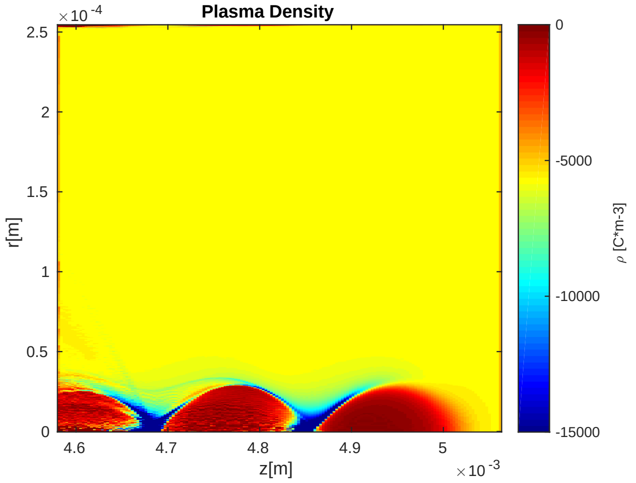

Figure 9.4: An illustration of the plasma density behind a drive bunch with density larger than the plasma density, propagating from left to right in a relativistic velocity. Simulated in 2D cylindrical coordinate system using the OSIRIS particle-in-cell code.

Due to its complex nonlinear nature, this regime, which is also referred to as the *blowout regime*, is commonly studied numerically with the use of the *Particle-in-Cell (PIC)* simulation method [107]. Previous studies [105, 106, 108] have shown that the radial wakefield inside each bubble scales linearly with the radius, and stays constant along the propagation direction. This effect is visible in figures 9.3(b) and 9.3(f). This transverse focusing field can maintain both the drive bunch and the witness bunch to a small transverse size against their natural tendency to diverge due to their emittance or transverse temperature. In addition, within each bubble the longitudinal wakefield, W_z, is independent of the radius and thus equally accelerates particles with the same longitudinal position. These field characteristics support a table acceleration of electrons. The longitudinal field, however, varies linearly with the longitudinal position, as shown in figures 9.3(b) and 9.3(d). This linearity induce an energy spread of the accelerated witness bunch [105, 106].

9.1.3 Beam Loading

In both the linear and the non-linear regimes, potential witness bunches exhibit energy spread due to the variation of the longitudinal fields in the propagation direction. These variation are sinusoidal in the linear regime, while in the non-linear regime they are approximately linear with the longitudinal position. The different energies of individual electrons in the bunch becomes substantial, as the acceleration length increases.

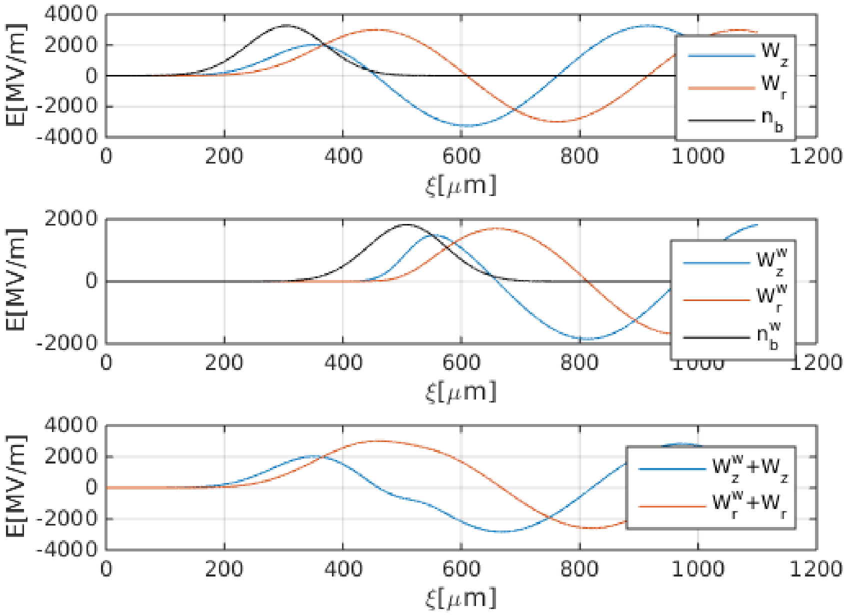

Figure 9.5: Beam loading in the linear regime, numerical solution using equations 9.5 and 9.6. The beams are bi-Gaussian relativistic bunches which propagate from right to left. Upper panel: wakefields of the drive bunch (W_z in blue, W_r in red) and beam density profile n_b (black). Middle panel: wakefields of the witness bunch (W_z^w in blue, W_r^w in red) and beam density profile n_b^w (black). Lower panel: the total wakefields in the longitudinal (blue) and transverse (red) directions. In the region of the witness bunch the longitudinal field is flattened.

For efficient acceleration, the witness bunch is located in the useful phase, which typically characterized by large variations in W_z. Since the witness bunch produces also wakefields, one of the proposed solutions is *beam loading*, i.e. placing the witness bunch such that the longitudinal wakefield it generates would opposed to the drive bunch wakefield. In this way, the gradient of the total W_z is reduced and therefore most particles of the witness bunch can undergo similar acceleration by the flattened accelerating field. Figure 9.5 depicts beam loading in the linear regime, in which both bunches propagate from right to the left in the plasma (opposite direction of the one shown before) and a relatively flattened acceleration field of approximately 800 MV/m is achieved.

Achieving an efficient beam loading requires optimization of the witness bunch parameters: charge, length, relative position, etc. More details for beam loading in the linear and the non-linear regimes can be found in [109] and [110], respectively.

9.2 From the Linear Theory to the Non-Linear Theory

For studying the dependence of the wakefield amplitudes on the driving bunch charge, simulations of a PWFA scheme of a bi-Gaussian drive bunch propagating in plasma were performed with the OSIRIS PIC code. In these type of simulations, the plasma wavelength determines the simulation settings and therefore for this study a constant plasma density of $n_{pe} = 1.8 \cdot 10^{18}\,\text{cm}^{-3}$ was used. The simulation resolution was fixed to 60 cells per λ_{pe} in the longitudinal direction and 30 cells per λ_{pe} the transverse direction. The drive bunch sizes were set to $\sigma_{zb} = 52.8\,\mu\text{m}$ and $\sigma_{rb} = 100\,\mu\text{m}$ (chosen for illustration purposes). The charge density of the bunch was varied so that the transition between the linear and the non-linear regimes could be investigated. The initial wakefields (after 5 mm propagation in the plasma) in each simulation were sampled at the maximal focusing position, which typically corresponds to the useful phase.

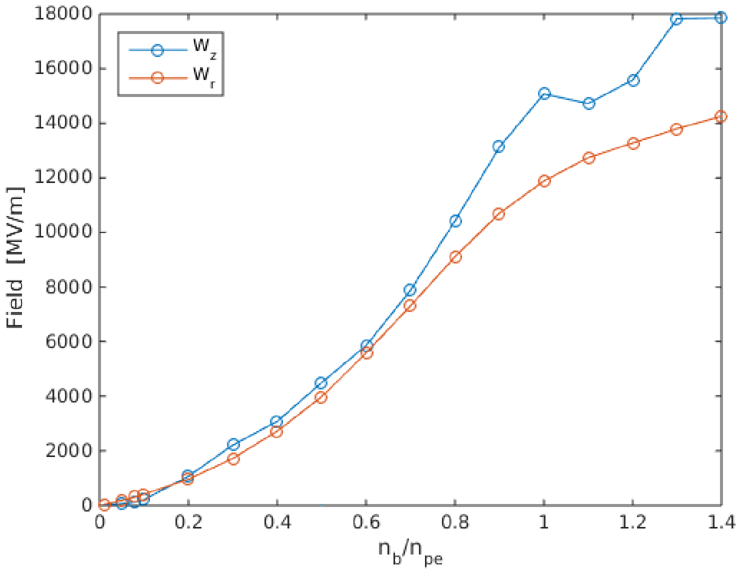

Figure 9.6: Amplitudes of the longitudinal (blue) and the transverse (red) wakefields as a function of $\frac{n_b}{n_{pe}}$. Both fields are sampled at the maximal focusing position. Obtained from a 2D cylindrical simulation with the OSIRIS particle-in-cell code, using plasma density of $n_{pe} = 1.8 \cdot 10^{18}\,\text{cm}^{-3}$ and bi-Gaussian electron beam with $\sigma_{zb} = 52.8\,\mu\text{m}$ and $\sigma_{rb} = 100\,\mu\text{m}$.

Figure 9.6 presents the amplitude of the longitudinal and transverse fields as a function of the ratio between the beam and plasma densities $\frac{n_b}{n_{pe}}$. In general, with the increasing charge larger field amplitudes are obtained (excluding $\frac{n_b}{n_{pe}}$=1.1 for W_z). A quadratic dependence is shown for both W_z and W_r up to $\frac{n_b}{n_{pe}}$=0.9, above which the non-linear effects become more dominant. In addition, from around $\frac{n_b}{n_{pe}}$=0.8 the amplitude of W_z becomes substantially larger than that of W_r.

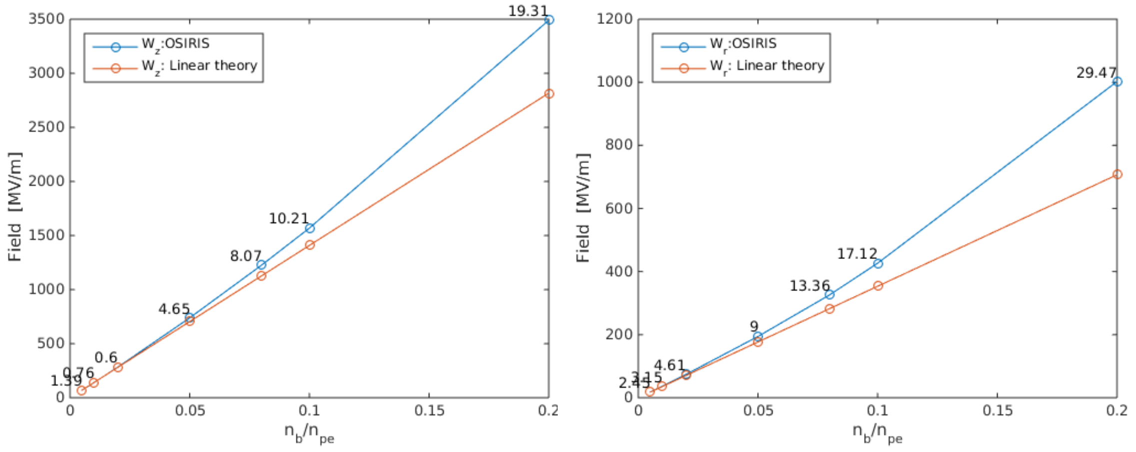

(a) (b)

Figure 9.7: Amplitudes of (a) longitudinal and (b) transverse wakefields at the maximal focusing position as a function of $\frac{n_b}{n_{pe}}$. Comparison between simulation results obtained from a 2D cylindrical simulation with the OSIRIS particle-in-cell code (blue) and analytical calculation in the linear regime using equations 9.5 and 9.6 (red) of a PWFA scheme with plasma density of $n_{pe} = 1.8 \cdot 10^{18}\,\mathrm{cm}^{-3}$ and bi-Gaussian electron beam with $\sigma_{zb} = 52.8\,\mu\mathrm{m}$ and $\sigma_{rb} = 100\,\mu\mathrm{m}$. The relative deviation between each simulation and calculation result is given in the figure near the simulation result.

In figure 9.7, the results obtained from the simulations are compared with results obtained from equations 9.5 and 9.6 for the linear regime. At $\frac{n_b}{n_{pe}}$=0.1, the relative deviations between W_z and W_r are larger than 10%, with 10.2% and 17.1%, respectively. Therefore, for the considered PWFA scheme, the linear regime is valid only for $n_b < 0.1n_{pe}$.

9.3 Application of a PWFA to an X-ray Free Electron Laser

The synchrotron radiation of highly accelerated electron bunches provides an advanced lasing technology, characterized by short wavelengths. The radiation wavelengths achievable with Free electron lasers are down to just a few tenths of a nanometer. These machines provide very intense and tightly focused X-ray beams, which can be used to map the atomic structure of materials, including the dynamics of chemical processes or even details of the motion of atoms in matter.

The energy of the radiating electron bunches determines the lasing power as well as the radiation wavelength. Placing a PWFA after the conventional linear accelerator (*linac*), as illustrated in figure 9.8(a), gives the possibility to double the electron energy in a much shorter distance than that of the linac and therefore to generate a pulse with higher energy and an even shorter wavelength.

This section presents a preliminary study of such an acceleration scheme for the *SwissFEL* [90], which is currently being constructed at the Paul Scherrer Institute. The SwissFEL aims at providing a coherent photon emission of 0.1 nm to 7 nm from relativistic electron bunches of 5.8 GeV energy. The total length of the project is approximately 700 meters, as shown in figure 9.8(b).

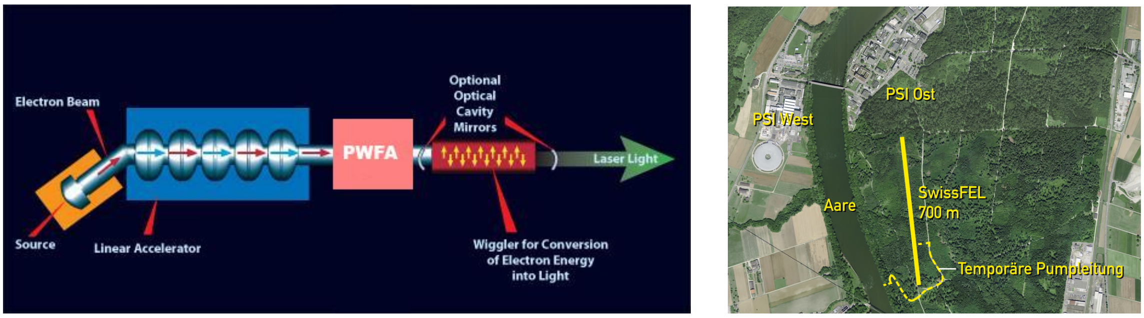

(a)

(b)

Figure 9.8: (a) Schematic depiction of an FEL with a PWFA (not to scale). Adapted from reference [111]. (b) The future location of the SwissFEL in relation to the current PSI site. [112].

9.3.1 The Working Mechanism of a Free Electron Laser

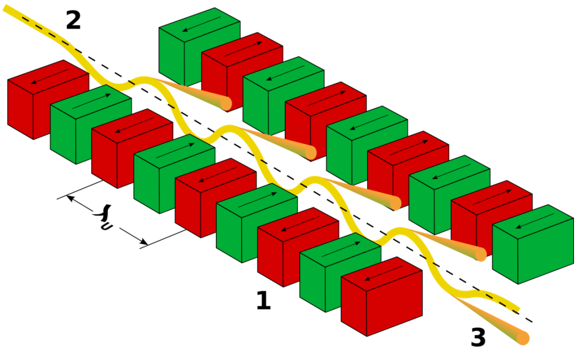

Figure 9.9: The working principle of an undulator. 1: the alternating magnets with a period of λ_U. 2: the electron beam enters from the upper left and starts oscillating with the magnetic field. 3: synchrotron radiation exiting to the lower right [113].

An FEL takes electron bunches from an electron source and accelerates them to relativistic velocities, using an RF linac (which is typically the largest part in the FEL design). After the acceleration, the bunches pass through an *undulator* (or a *wiggler*), i.e. a periodic arrangement of magnets with alternating poles (figure 9.9). The alternating magnetic field together with the electron charge stimulate the Lorentz force, which forces the electrons in the beam to travel along a sinusoidal path about the axis of the undulator. As the electrons are transversely accelerated, they emit synchrotron radiation. At first, each electron undergoes the process independently without being influence by any neighboring emissions and therefore the emission is incoherent. However, if the quality of the electron beam is sufficiently high (in terms of charge density, emittance and energy spread), the emitted photons interact back with the electron beam in such a way that the electrons organize themselves into a regularly spaced pattern of *microbunches*. The radiation of these microbunches is coherent. During the process of microbunching the radiation intensity grows exponentially up to a saturation level where maximum bunching is reached.

The undulator strength is determined with the dimensionless undulator parameter K, given by

$$K = \frac{eB_0\lambda_U}{2\pi m_e c} = 0.934 \cdot B_0 \cdot \lambda_U \,[\mathrm{T} \cdot \mathrm{cm}], \tag{9.10}$$

where λ_U is the undulator period and B_0 is the maximal amplitude of the magnetic field. The wavelength of the emitted radiation is given by

$$\lambda_{ph} = \frac{\lambda_U}{2\gamma^2}\left(1 + \frac{K^2}{2}\right), \tag{9.11}$$

in which γ is the electron energy in units of the rest energy $m_e c^2$. Electron bunches with higher energies can provide shorter radiation wavelength as well as a higher intensity beam [114].

9.3.2 Parameter of the SwissFEL

The SwissFEL design is optimized for generating X-ray radiation with wavelengths of 0.1 nm to 7 nm. The undulator design was optimized for a wavelength of 0.1 nm with a period of λ_U =15 mm and an undulator parameter of 1.2 [90]. The SwissFEL linac provides electron beams of different size and charge density: the bunch size ranges between 10 μm and 20 μm, while the beam charge changes from 10 pC to 200 pC. Table 9.1 summarizes the SwissFEL possible operation modes.

Table 9.1: A Summary of the relevant SwissFEL Parameters.

λ_{ph}	0.1 – 7 nm
λ_U	15 mm
K	1.2
γ	5.8 GeV
σ_z	10 – 20 μm
Q	10 – 200 pC

9.3.3 The PWFA Scheme

The SwissFEL accelerates electron bunches with an RF linac to an energy of 5.8 GeV and then transfers them to the undulator for producing X-ray radiation. Extending the acceleration stage by placing a PWFA between the linac and the undulator can bring the electron bunches to much higher energies in a relatively short acceleration length. In such a FEL design, two accelerated bunches are used: the first as the drive bunch and the second as the witness bunch. The beam properties were optimized separately according to the possible parameter range of the SwissFEL operating modes.

Table 9.2: The parameters of the PWFA scheme.

n_{pe}	$3.53 \cdot 10^{16}$ cm^{-3}
bunch separation	100 μm
initial energy	5.8 GeV
σ_{zb}	20 μm
σ_{rb}	10 μm
Q_b	400 pC
σ_{zw}	10 μm
σ_{rw}	10 μm
Q_w	170 pC

A non-linear PWFA scheme was optimized by means of numerical simulations for doubling the energy of the SwissFEL electron bunches. The optimization was performed with the OSIRIS PIC code using 2D cylindrical symmetry. The simulation resolution was fixed to 60 cells per λ_{pe} in the longitudinal direction and 30 cells per λ_{pe} the transverse direction. The starting point for the PWFA optimization was a bi-Gaussian drive bunch with a charge of 400 pC [115]. Accordingly, the plasma density was optimized to $3.53 \cdot 10^{16}$ cm^{-3} and the longitudinal and transverse lengths of the bunch were optimized to σ_{zb}=20 μm and σ_{rb}=10 μm, respectively. The witness bunch parameters were optimized according to the beam loading principles described in reference [116] for reducing the final energy spread. The optimization for a bi-Gaussian witness bunch yielded a charge of 170 pC and both longitudinal and transverse lengths of ($\sigma_{zw} = \sigma_{rw} =$) 10 μm. The peak-to-peak bunch separation was optimized to $5 \cdot \sigma_{zb}$. For simplicity, the bunches were assumed to be mono-energetic with an energy of 5.8 GeV at injection in the plasma. The preliminary PWFA scheme parameters are summarized in table 9.2.

The initial wakefields generated by the optimized drive bunch are shown in figure 9.10(a). A constant focusing field is visible along with a high accelerating field, which shows a linear dependence to longitudinal position. The loading of the witness bunch is presented in figure 9.10(b), where the accelerating wakefield within the bunch is flattened and reaches about 3.5 GeV/m. From this, the average energy gain after an acceleration length of 0.5 m in the plasma, can be estimate by a simple calculation to a value of 1.75 GeV.

After propagating the bunches for 0.5 m in the plasma with the numerical simulations, the beam loading scheme was investigated by plotting the energy distributions of the electrons in each bunch. The initial and final energy distributions are presented in figure 9.11. The final distribution of the witness bunch has mean value of 7.82 GeV and a *Full Width at Half Maximum (FWHM)* of 80.32 MeV, which includes 57% of the bunch particles. The distribution of the drive bunch has a mean value of 4.13 GeV and a FWHM of 2.1 GeV. This means that the witness bunch gained 2.04 GeV in half a meter, while the drive bunch lost 1.67 GeV. According to this result, doubling of

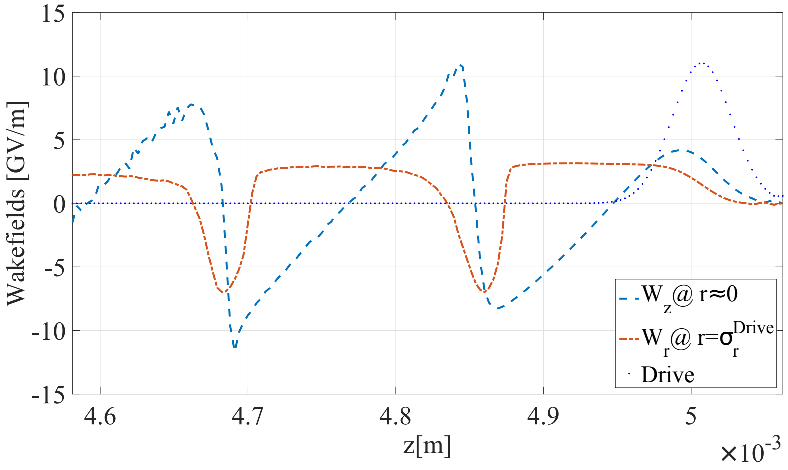

(a)

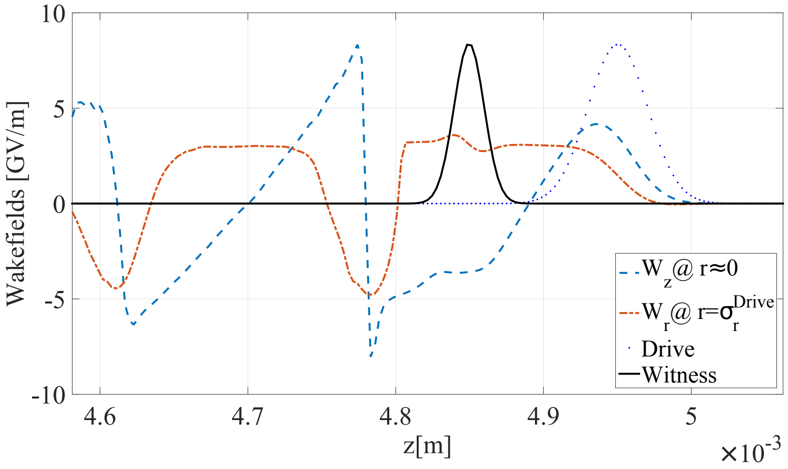

(b)

Figure 9.10: The longitudinal wakefield $W_z(0)$ on axis (blue) and the transverse wakefield at $W_r(\sigma_{rb})$ (red) after a propagation of 5 mm in the plasma. (a) The wakefields of the drive bunch. (b) Beam loading, the total wakefields of the drive and witness bunches. The drive and witness bunches are marked by dotted and solid lines, respectively. These results obtained from a numerical simulation with a 2D cylindrical symmetry with the OSIRIS PIC code. The simulation parameters are summarized in Table 9.2.

the beam energy is possible in a PWFA with a length of a few meters.

Although the energy spread of the witness bunch is about 80.3 MeV (about 1% of the beam energy), the operation requirements of the SwissFEL are much stringent, demanding a maximum energy spread of 350 keV. Selection of particles with an energy range of ±175 keV around the maximum distribution value would give the suitable energy range; however, this would reduce the applicable charge for the lasing, which can result at worst in an incoherent radiation. More advanced studies addressing all aspects of the PWFA process (optimizing the beam parameters, generating witness bunch, designing the plasma cell, optimizing the plasma stability, releasing and capturing accelerated beams, etc.) are being carried out in several projects [88, 89]. The concept of doubling the beam energy by placing a PWFA after a linac may also be a viable option to increase the collision energy of the future linear colliders ILC and CLIC. Such options are already investigated by several research groups [117–119].

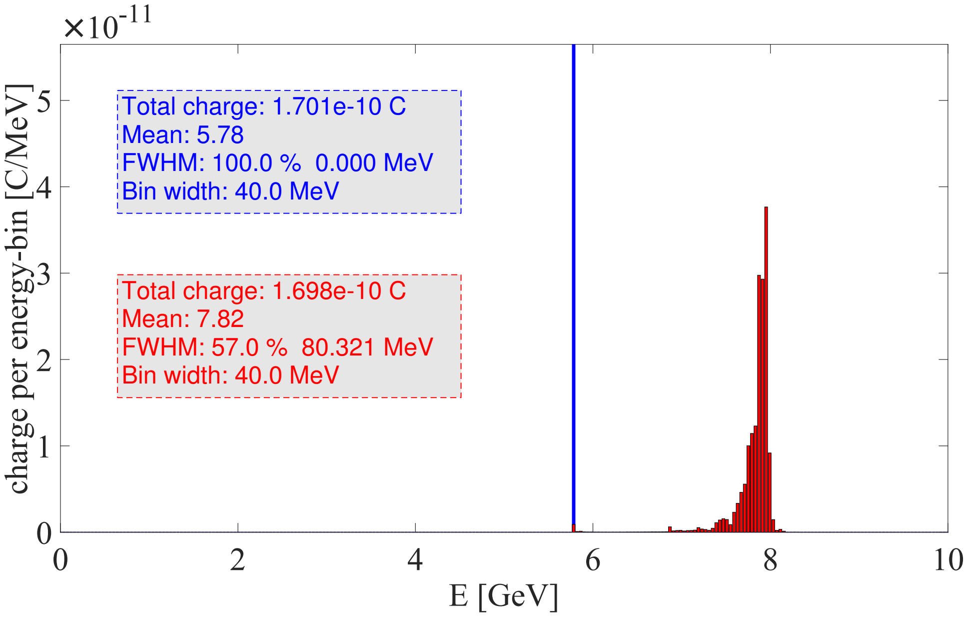

(a) Witness Bunch

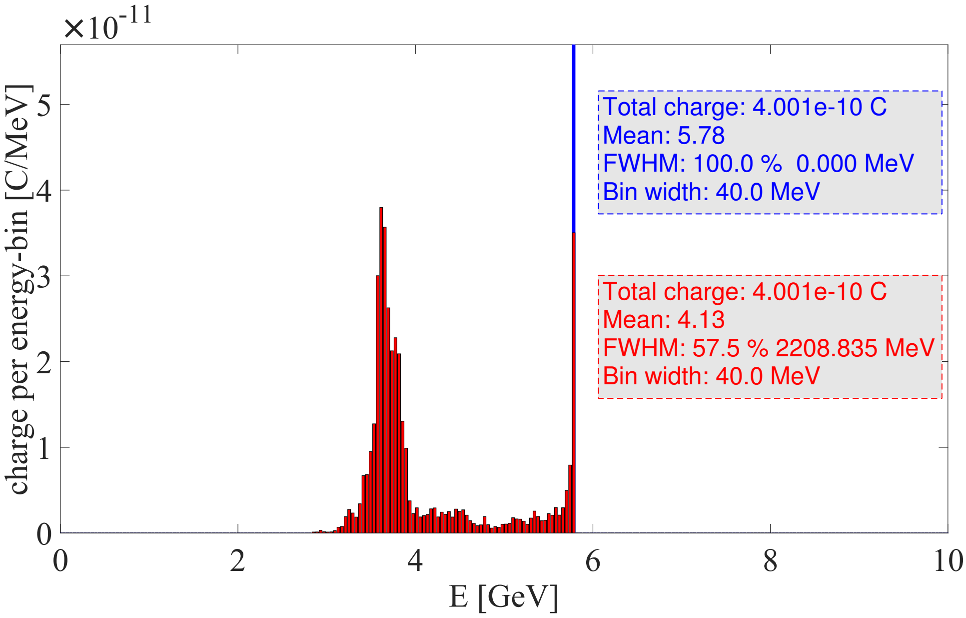

(b) Drive Bunch

Figure 9.11: The energy distributions of the (a) witness and (b) drive bunches before (blue) and after (red) propagation of 0.5 m inside the plasma. After 0.5 m: the witness bunch distribution has a mean value at 7.82 GeV and FWHM of 80.32 MeV (including 57% of particles of the initial beam), while the drive bunch distribution has a mean value of 4.13 GeV with FWHM of 2.2 GeV (52% of the particles).

CHAPTER 10

CONCLUSIONS AND OUTLOOK

High-energy physics experiments strive to precisely study the elementary particles and their interactions and to search for new physics beyond the Standard Model. Linear electron-positron colliders with high center-of-mass energies will provide more precise measurements than possible with current collider experiments, leading to a substantial additional discovery potential. These highly precise measurements are achievable only with an advanced detector system with unprecedented resolution accompanied by modern reconstruction approaches such as Particle Flow Algorithms.

The CALICE collaboration develops calorimeter prototypes with high spatial granularities for future linear collider experiments. Different calorimeter concepts have been developed by the collaboration, differing by their absorber materials, readout techniques and granularities. Three CALICE physics prototypes, the Silicon-Tungsten Electromagnetic Calorimeter (Si-W ECAL), the Analog Hadron Calorimeter (AHCAL) and the Tail Catcher and Muon Tracker (TCMT), have been installed together and tested as a combined system in test beam experiments. These experiments provide the possibility to evaluate the performance of the calorimeter prototypes in realistic detector configurations. In the full calorimeter system, layers of tungsten and steel of various thickness are implemented as absorber materials, while the active detector elements are silicon sensors and plastic scintillators with silicon photomultipliers.

To study the performance of the calorimeter system in this thesis, data collected in negative pion beams at the CERN and FNAL test beam facilities are used. In each of the test beam campaigns, different beam instrumentation has been installed in the beam line. In addition, the beams provided at FNAL exhibit a larger contamination with additional particles or particles of different types compared to the beams at CERN. The dataset studied here consists of pion data from 10 GeV to 80 GeV recorded at CERN, and from 4 GeV to 60 GeV recorded at FNAL. For removing the contamination of muon, electron and multi-particle events from the data sample, considering the different beam compositions and energy ranges at the test beam campaigns, a sophisticated multi-step selection process is applied to the data to select events with a single pion shower.

The selected events of the CERN data are reconstructed separately from the FNAL data events. For accounting for differences in the detector configuration and operation, different sets of calibration factors for the conversion from the MIP calibration scale to energy units are used. These calibration factors are derived from the respective energy depositions in CERN or FNAL events. For evaluating the performance of the full energy range from 4 GeV to 80 GeV, a combination of the CERN and FNAL data, the combined dataset, is reconstructed as well.

Two different methods for reconstructing the hadron energy in the calorimeter system are evaluated. The first reconstruction method, the standard reconstruction, uses constant weights per sub-detector, taking into account the varying thickness of the absorber structure in the Si-W ECAL and the TCMT as well as the different response to MIPs and to electromagnetic showers in the Si-W ECAL. The second reconstruction method, the Software Compensation (SC) reconstruction, attempts to correct for the inherent differences in the detector response to electromagnetic and to purely hadronic showers, one of the limiting factors for the hadronic energy resolution. The method aims at distinguishing energy depositions of the electromagnetic sub-showers in the hadronic showers by the deposited energy in each hit. Accordingly, optimized weights are applied to individual cell energies for equalizing the electromagnetic and the hadronic components and therefore improving the energy resolution. A new SC scheme which forces less dependencies on the weight shapes is validated in this analysis. Three schemes of this method are tested by applying weights to different sub-detectors (Full SC, HCAL SC and ECAL SC).

The SC method results in a sizeable improvement of the energy resolution with every SC scheme. While the standard reconstruction of the energy resolution of the combined CERN and FNAL dataset yields a stochastic term of $(55.54\pm0.13)\%/\sqrt{E/\mathrm{GeV}}$ and a constant term of $(4.31\pm0.05)\%$, with software compensation these terms are reduced to $(44.09\pm0.14)\%/\sqrt{E/\mathrm{GeV}}$ and $(2.08\pm0.08)\%$, respectively. The improvement in resolution with software compensation is up to 30% at energies above 20 GeV. When applying software compensation only to one of the sub-detectors, the improvement in energy resolution is reduced. In the Si-W ECAL alone, an improvement of up to 7% is achieved, while software compensation in the AHCAL and the TCMT yields up to 23% improvement. This shows the importance of software compensation in the hadron calorimeter. These results are consistent with previously published results of software compensation for showers starting in the AHCAL, demonstrating the success of the inter-calibration of the different sub-systems, despite their different geometries and different readout technologies. A similar analysis of a combined CALICE calorimeter system of scintillator-SiPM prototypes shows a comparable performance with slightly worse resolutions with the SC reconstruction than the ones shown for the combined setup that is investigated in this thesis.

GEANT4-based detector simulations covering the same energy range and detector configurations as the test beam data are reconstructed as well with the same methods in order to test the robustness of the reconstruction methods and to validate the simulation models. The energy resolution obtained from the standard reconstruction are considerably worse in simulations than in the data at energies above 12 GeV; however, when using the SC reconstruction the obtained resolutions are consistent for data and simulation also at high energies. Using SC weights optimized with simulations to reconstruct the data produces an average improvement of 20% compared to the standard reconstruction; however, the achieved improvement is comparable to the one obtained from weights optimized with data only up to 20 GeV. The reduced improvement at higher energies suggests differences on the local shower structure between data and simulations, which is also visible by the disagreement observed for the standard energy resolution at high energies.

The analysis of the combined calorimeter system demonstrates the feasibility of a full 4π detector system of the same technologies and shows an overall better performance with the SC reconstruction method. The comparison between reconstruction results of data and simulation with different reconstruction schemes is valuable for studies of the PFA in a full detector system for future collider experiments, which can be performed only by means of simulations.

In the further future, it is expected that an additional increase of the collision energy of collider experiments will be required. Plasma wakefield acceleration is one of the leading options for linear colliders for increasing the beam energies. One possible scheme of such energy upgrades is placing Plasma Wakefield Accelerators (PWFAs) after the main RF accelerators. In this way, beams which are accelerated in the conventional way are used to drive wakefields with high amplitudes inside a plasma cell. The energy of these wakefields is then transferred to a chasing witness beam which is placed in a specific phase relative to the driving beam for an efficient acceleration. A preliminary study of the method demonstrates an energy gain of approximately 2 GeV in half a meter, i.e. an accelerating gradient about 100 times higher than that of the superconducting structures developed for the ILC. This result suggests the possibility for a substantial increase in the collision energies of linear colliders with the plasma acceleration technique.

APPENDIX A

DETERMINATION OF THE FIRST HADRONIC INTERACTION LAYER

The reconstruction of the First Hadronic Interaction (FHI) layer is based on the differences in the layer energies before the shower start and at the starting point. In this analysis several algorithms from previous analyses [74–76] were used. The search for the FHI layer is done consecutively, starts with the Si-W ECAL and resumes with the AHCAL. First, two criteria optimized for the Si-W ECAL are used for the Si-W ECAL layers, one after the other:

- The absolute energy increase criterion:
  The deposited energy E_l in MIP units in each layer is compared with a threshold energy defined as E_{cut}, which was optimized to 8 MIPs in reference [75]. The layer is identifies as the FHI layer if the deposited energies in thiss layer and in two subsequent layers are larger than the threshold energy:

  $$E_l > E_{cut} \text{ and } E_{l+1} > E_{cut} \text{ and } E_{l+2} > E_{cut}. \tag{A.1}$$

  This criterion is not effective for the last two layers in the Si-W ECAL.

- The relative energy increase criterion:
  This criterion is based on the relative increase the deposited energy in the layer, using a threshold ratio F_{cut} set to 6, as in previous Si-W ECAL analyses [74, 75]. The condition to define the FHI layer is in the form:

  $$\frac{E_l + E_{l+1}}{E_{l-1} + E_{l-2}} > F_{cut} \text{ and } \frac{E_{l+1} + E_{l+2}}{E_{l-1} + E_{l-2}} > F_{cut}, \tag{A.2}$$

When the FHI layer is still not identified within the Si-W ECAL layers, an technique optimized for the AHCAL is used for both the Si-W ECAL and the AHCAL layers. This technique, referred to as the moving average criterion, is taken from the Primary Track Finder algorithm [76].

For each layer, from the Si-W ECAL front layer till the last AHCAL layer, two values are calculated:

- M_l - The moving average of the visible energy in 10 successive layers up to l-th layer.
- N_l - The number of hits in the l-th layer .

Layer l is considered as the FHI layer when two conditions are fulfilled:

$$(\mathrm{M}_l + \mathrm{M}_{l+1}) > \mathrm{M}_{\mathrm{thr}} \text{ and } (\mathrm{N}_l + \mathrm{N}_{l+1}) > \mathrm{N}_{\mathrm{thr}}. \tag{A.3}$$

$\mathrm{M}_{\mathrm{thr}}$ and $\mathrm{N}_{\mathrm{thr}}$ are thresholds optimized in reference [120] to $\mathrm{M}_{\mathrm{thr}} = \left(6.0 + 0.1\frac{\mathrm{E}_{\mathrm{beam}}}{\mathrm{GeV}}\right)$ MIPs and $\mathrm{N}_{\mathrm{thr}} = 3.77 + 1.44 \cdot \ln\left(\frac{\mathrm{E}_{\mathrm{beam}}}{\mathrm{GeV}}\right)$.

The distributions of the reconstructed FHI layer in CERN and FNAL events are shown in figures 8.1, D.25,D.26, D.31 and D.30.

APPENDIX B

NOISE MEASUREMENTS

The measurement of the noise in the calorimeter system is performed for the selected events of the runs given in table 5.1. In order to select noise events, the following cuts are applied to the data:

- Beam Events Rejection: As the beam trigger provided by two coincidence scintillation plate identifies beam events, only events with no valid beam trigger are selected.
- Random Trigger Events: Selecting events of random triggers, which were recorded during data-taking in order to monitor pedestals and noise.
- Calibration Event Rejection: Removing events in which a calibration of the SiPMs is performed with a LED system (as is detailed in section 4.5).
- Electron Event Rejection in FNAL data: Rejection of electron events from the 4 GeV−30 GeV FNAL data sample is performed using the information recorded by the Cherenkov detector veto.

The noise level is measured for each test beam setup separately due to the different settings in CERN and FNAL experiments. The hits, i.e. energy depositions larger than 0.5 MIP, in the Si-W ECAL and the TCMT are scaled with the appropriate weighting for the absorber thickness, c_t, which is defined in section 6.1. For each sub-detector, the hit energies in MIP units are set out in a histogram. The noise level in each calorimeter is extracted from the spread (RMS) of the histogram. The contribution of the Si-W ECAL is negligible compared to the other calorimeters. To determine the overall noise level in each test beam setup, the noise contributions of the AHCAL and the TCMT are added in quadrature. Figures B.1 and B.1 present the distribution of the hit energies in FNAL and CERN events, respectively. The measurement yields a noise level of 0.24 GeV in the CERN setup and 0.21 GeV in the FNAL setup.

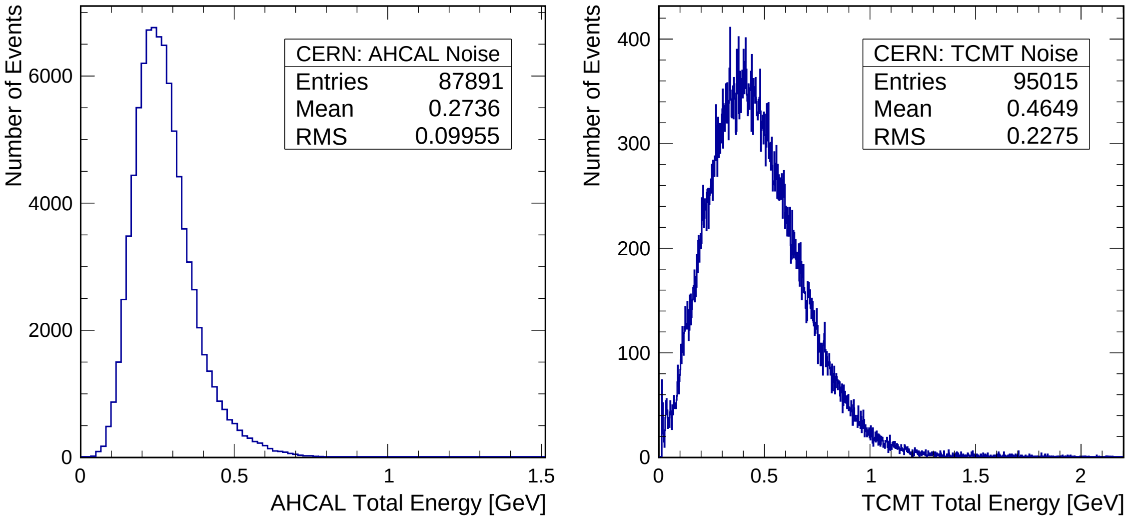

Figure B.1: The measurement of noise events recorded at CERN test beam experiment. The distributions of hit energies in the AHCAL (left) and in the TCMT (right) give respective noise level of 0.1 GeV and 0.22 GeV.

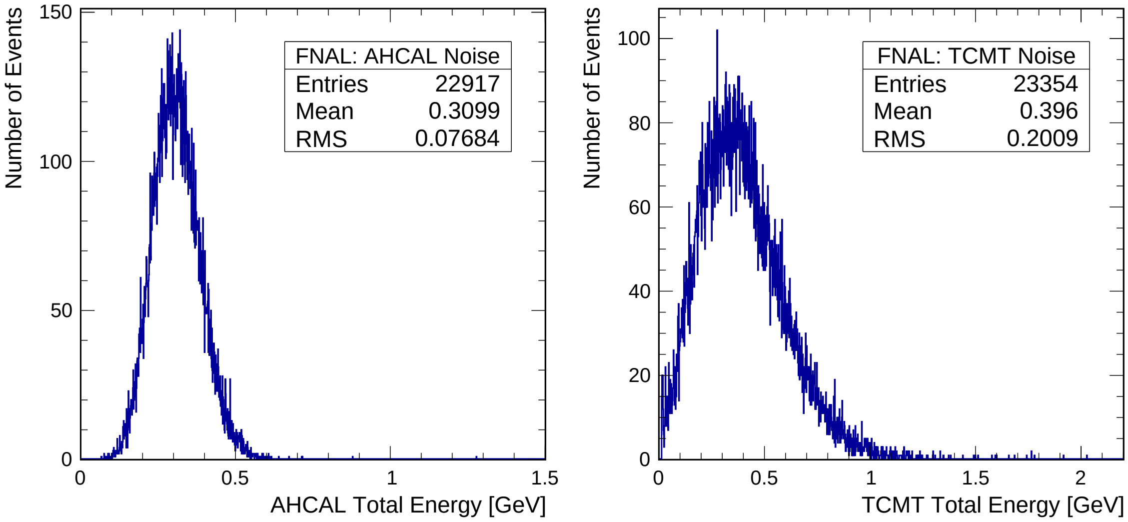

Figure B.2: The measurement of noise events recorded at FNAL test beam experiment. The distributions of hit energies in the AHCAL (left) and in the TCMT (right) give respective noise level of 0.08 GeV and 0.2 GeV.

APPENDIX C

SYSTEMTIC UNCERTAINTIES ADDITIONAL DETAILS

C.1 Electron Rejection Cut

The uncertainties obtained from the implementation of a tighter electron rejection cut in the event selection by rejecting events with FHI layer in the first module of the Si-W ECAL (10th layer instead of the 5th layer).

CERN Dataset

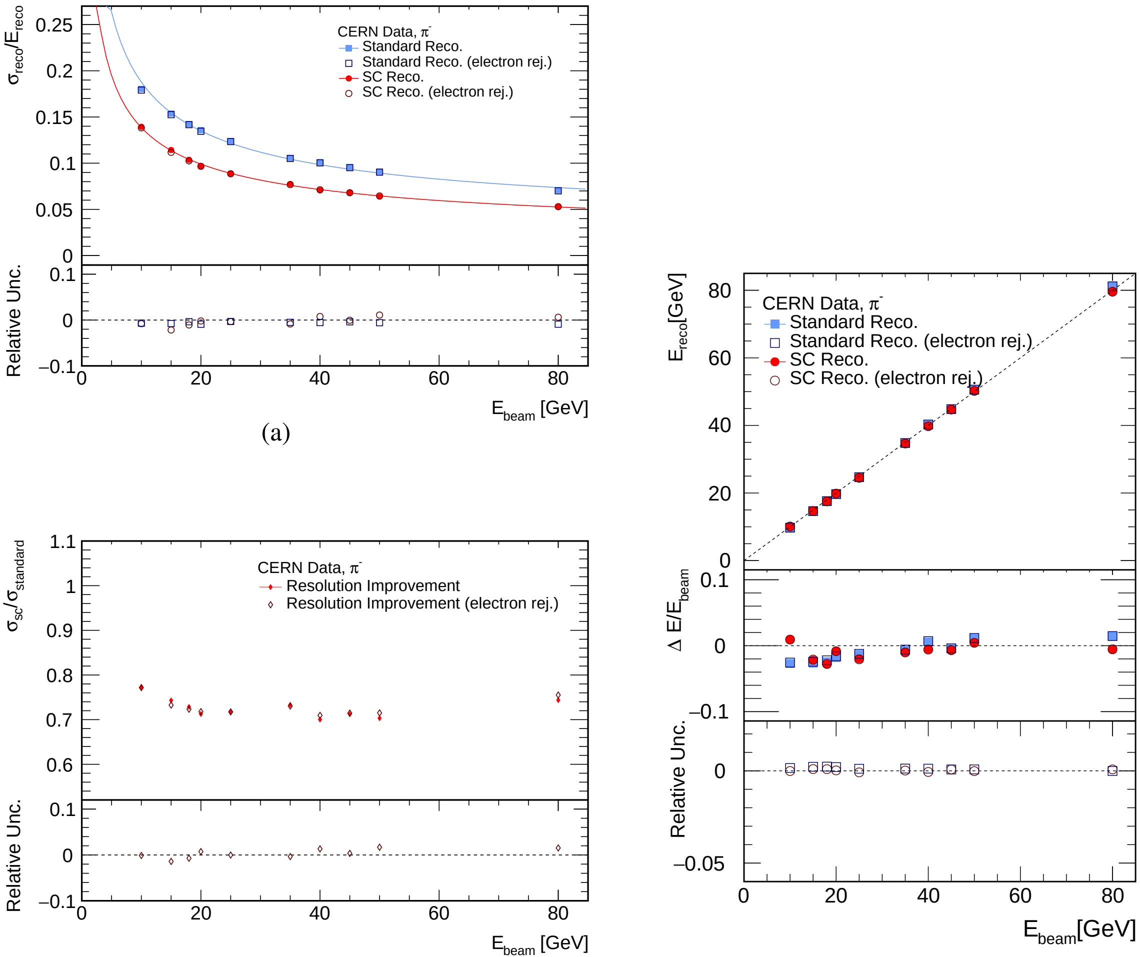

(a)

(b)

(c)

Figure C.1: The variations in the reconstruction results of CERN data after implementing a tighter electron rejection cut in the event selection (selecting events with FHI>9 instead of FHI>4). Upper panel in each figure: reconstruction results of events selected with the original and the modified event selection criteria. Lower panel in each figure: the relative uncertainty obtained from modifying the event selection; The dashed line corresponds to a zero relative uncertainty. (a) The energy resolutions obtained from the standard and the Full SC methods. (b) The relative improvement of the SC reconstructed energy resolutions. (c) The mean reconstructed energy and relative residuals to the beam energy obtained from the standard and the Full SC methods.

FNAL Dataset

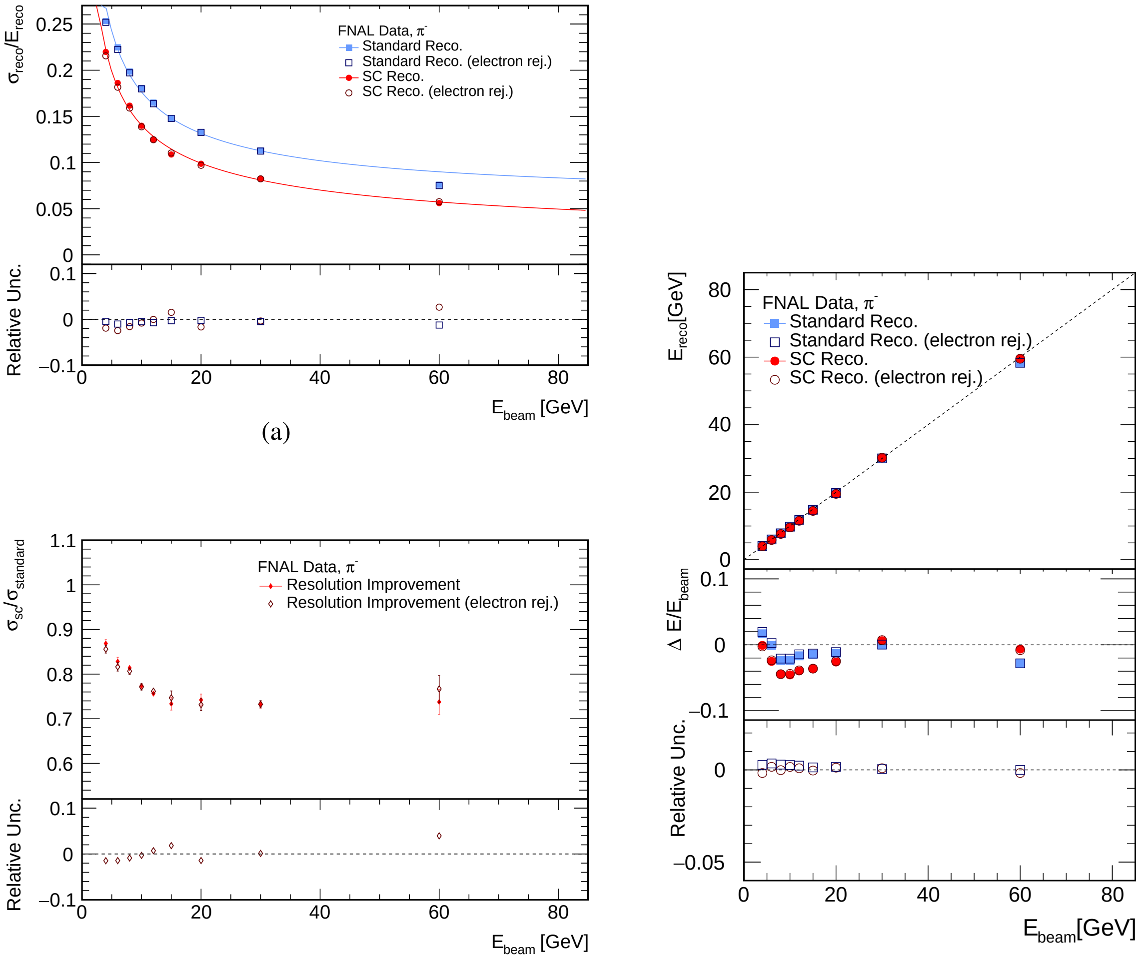

(a)

(b)

(c)

Figure C.2: The variations in the reconstruction results of FNAL data after implementing a tighter electron rejection cut in the event selection (selecting events with FHI>9 instead of FHI>4). Upper panel in each figure: reconstruction results of events selected with the original and the modified event selection criteria. Lower panel in each figure: the relative uncertainty obtained from modifying the event selection; The dashed line corresponds to a zero relative uncertainty. (a) The energy resolutions obtained from the standard and the Full SC methods. (b) The relative improvement of the SC reconstructed energy resolutions. (c) The mean reconstructed energy and relative residuals to the beam energy obtained from the standard and the Full SC methods.

The Combined Dataset

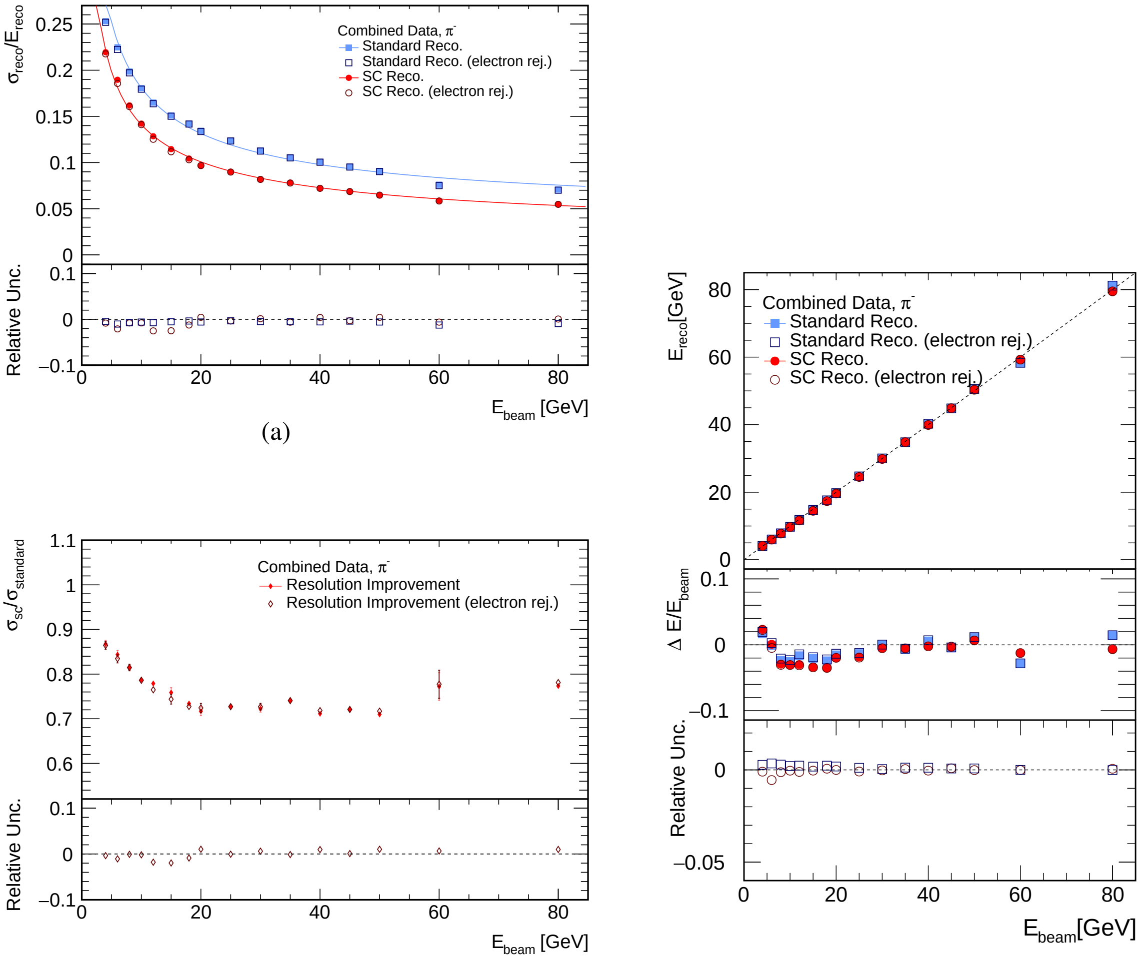

(a) (b) (c)

Figure C.3: The variations in the reconstruction results of the combined dataset after implementing a tighter electron rejection cut in the event selection (selecting events with FHI>9 instead of FHI>4). Upper panel in each figure: reconstruction results of events selected with the original and the modified event selection criteria. Lower panel in each figure: the relative uncertainty obtained from modifying the event selection; The dashed line corresponds to a zero relative uncertainty. (a) The energy resolutions obtained from the standard and the Full SC methods. (b) The relative improvement of the SC reconstructed energy resolutions. (c) The mean reconstructed energy and relative residuals to the beam energy obtained from the standard and the Full SC methods.

C.2 Full Shower Containment Cut

The uncertainties obtained from the implementation of a tighter cut for full shower containment in the event selection by rejecting events with FHI after the 5th layer of the AHCAL (35th layer of the full calorimeter system, instead of layer 56).

CERN Dataset

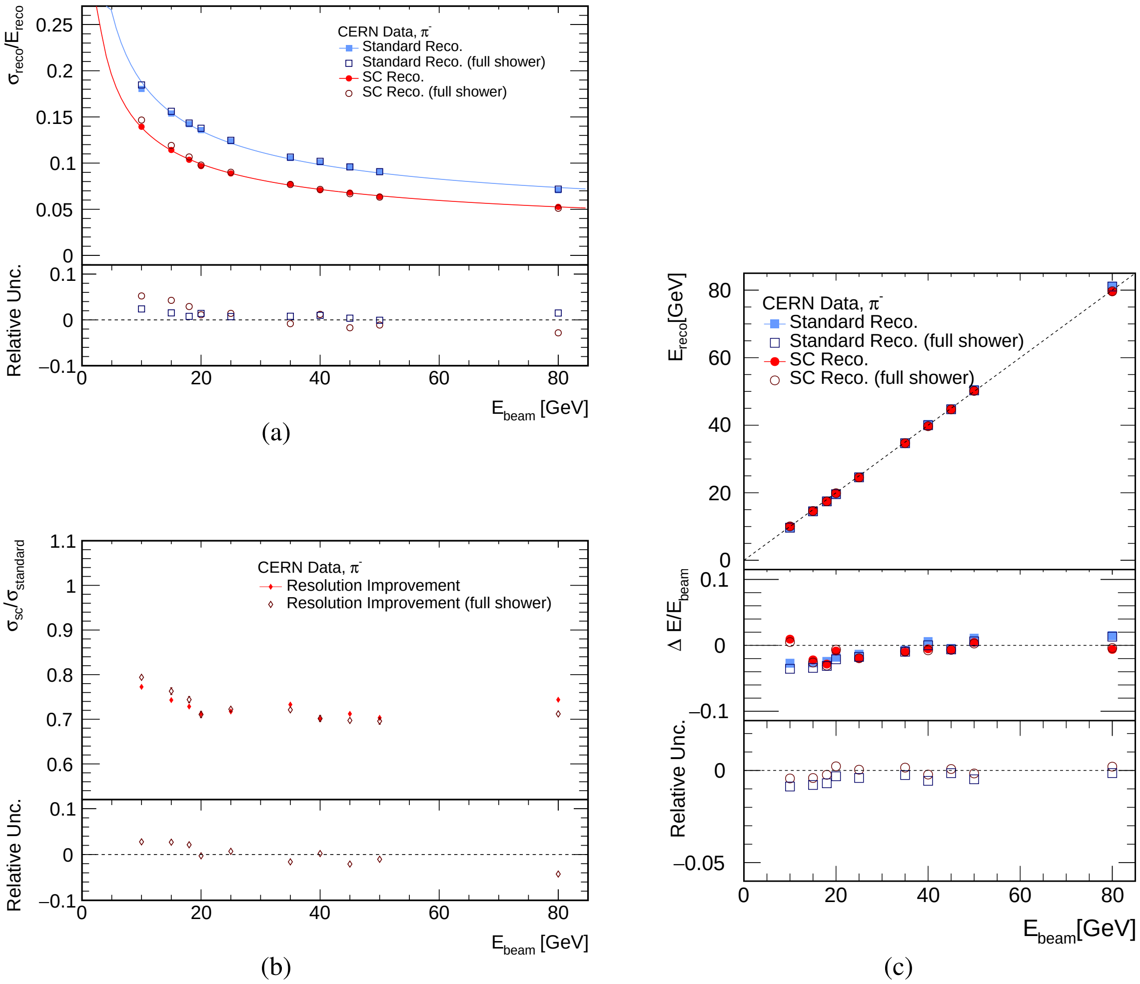

(a)

(b)

(c)

Figure C.4: The variations in the reconstruction results of CERN data after implementing a tighter cut for full shower containment in the event selection (selecting events with FHI<35 instead of FHI<56). Upper panel in each figure: reconstruction results of events selected with the original and the modified event selection criteria. Lower panel in each figure: the relative uncertainty obtained from modifying the event selection; The dashed line corresponds to a zero relative uncertainty. (a) The energy resolutions obtained from the standard and the Full SC methods. (b) The relative improvement of the SC reconstructed energy resolutions. (c) The mean reconstructed energy and relative residuals to the beam energy obtained from the standard and the Full SC methods.

FNAL Dataset

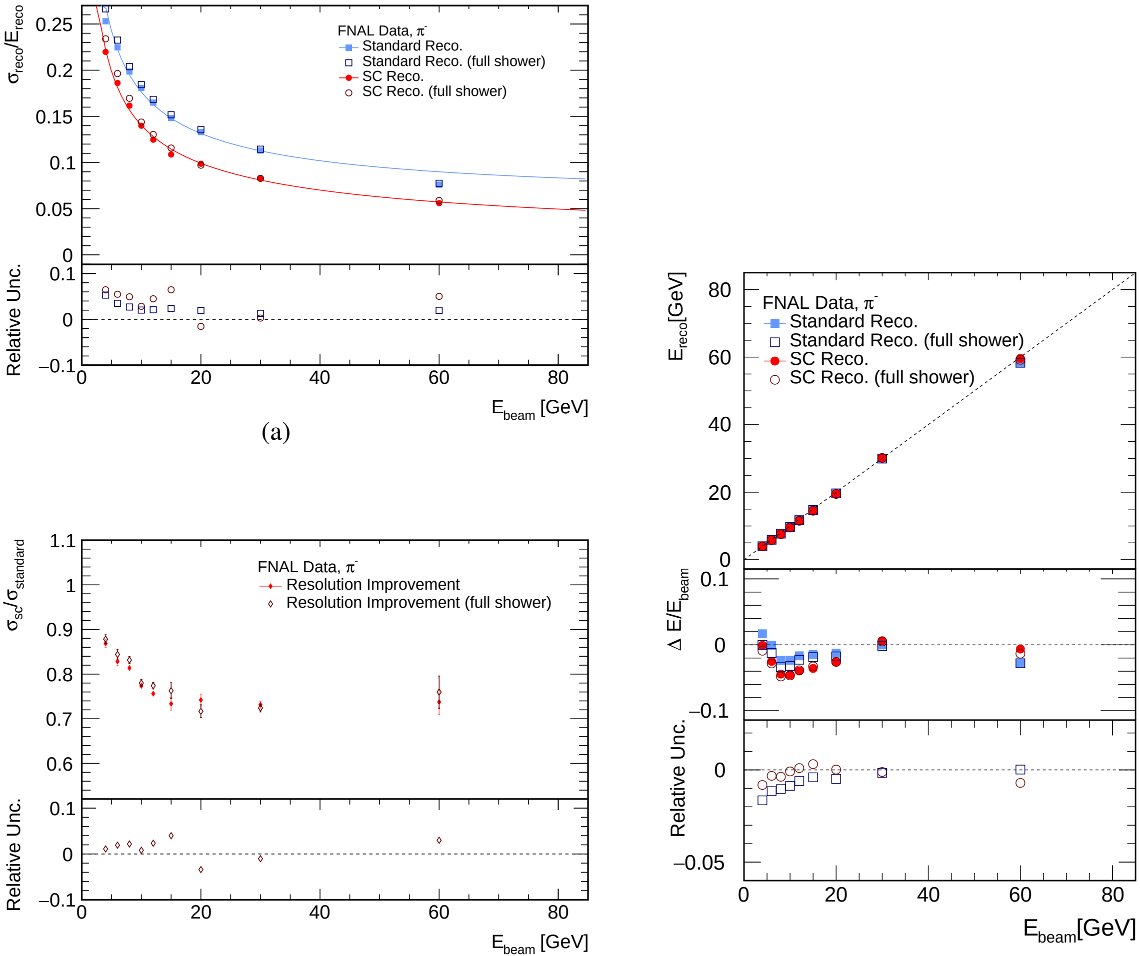

(a)

(b)

(c)

Figure C.5: The variations in the reconstruction results of FNAL data after implementing a tighter cut for full shower containment in the event selection (selecting events with FHI<35 instead of FHI<56). Upper panel in each figure: reconstruction results of events selected with the original and the modified event selection criteria. Lower panel in each figure: the relative uncertainty obtained from modifying the event selection; The dashed line corresponds to a zero relative uncertainty. (a) The energy resolutions obtained from the standard and the Full SC methods. (b) The relative improvement of the SC reconstructed energy resolutions. (c) The mean reconstructed energy and relative residuals to the beam energy obtained from the standard and the Full SC methods.

The Combined Dataset

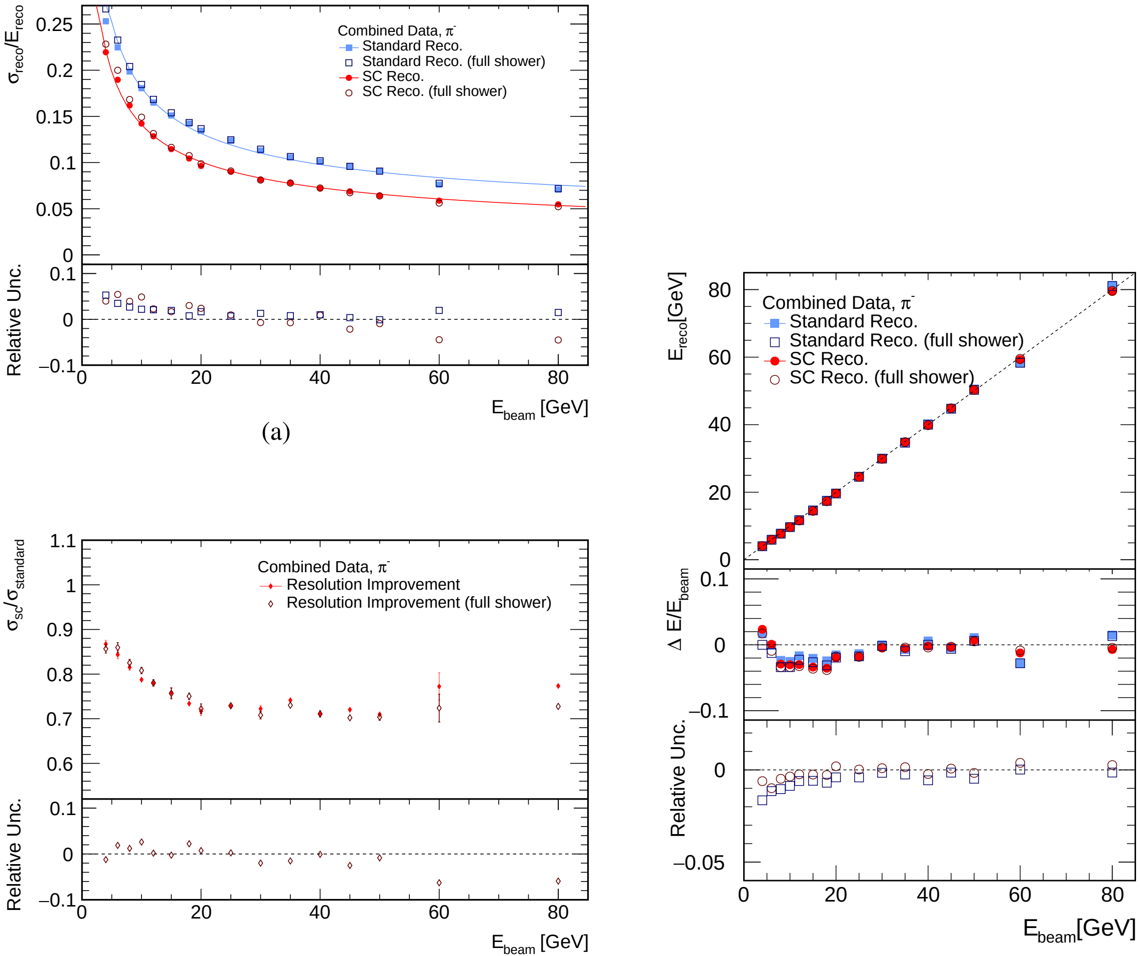

(a)

(b)

(c)

Figure C.6: The variations in the reconstruction results of the combined dataset after implementing a tighter cut for full shower containment in the event selection (selecting events with FHI<35 instead of FHI<56). Upper panel in each figure: reconstruction results of events selected with the original and the modified event selection criteria. Lower panel in each figure: the relative uncertainty obtained from modifying the event selection; The dashed line corresponds to a zero relative uncertainty. (a) The energy resolutions obtained from the standard and the Full SC methods. (b) The relative improvement of the SC reconstructed energy resolutions. (c) The mean reconstructed energy and relative residuals to the beam energy obtained from the standard and the Full SC methods.

C.3 Muon Rejection Cut

The uncertainties obtained from the implementation of a looser muon rejection in the event selection by removing the cut on the reconstructed energy, which is destined for rejecting low-energy muons (including events from $E_{beam} \geqslant 15$ GeV with $E_{reco} < E_{beam}/2.6$).

CERN Dataset

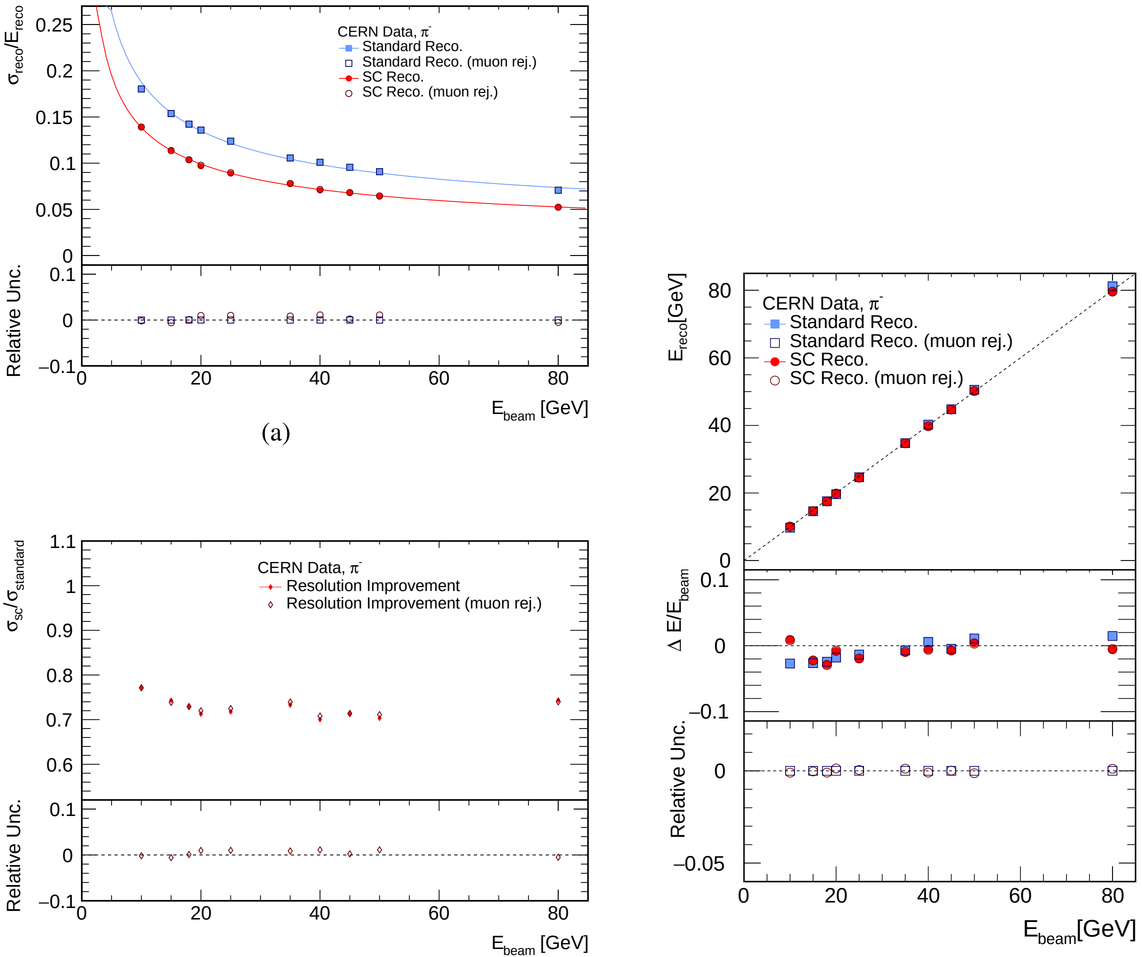

(a)

(b)

(c)

Figure C.7: The variations in the reconstruction results of CERN data after implementing a looser muon rejection cut for full shower containment in the event selection (including events from $E_{beam} \geqslant 15$ GeV with $E_{reco} < E_{beam}/2.6$). Upper panel in each figure: reconstruction results of events selected with the original and the modified event selection criteria. Lower panel in each figure: the relative uncertainty obtained from modifying the event selection; The dashed line corresponds to a zero relative uncertainty. (a) The energy resolutions obtained from the standard and the Full SC methods. (b) The relative improvement of the SC reconstructed energy resolutions. (c) The mean reconstructed energy and relative residuals to the beam energy obtained from the standard and the Full SC methods.

FNAL Dataset

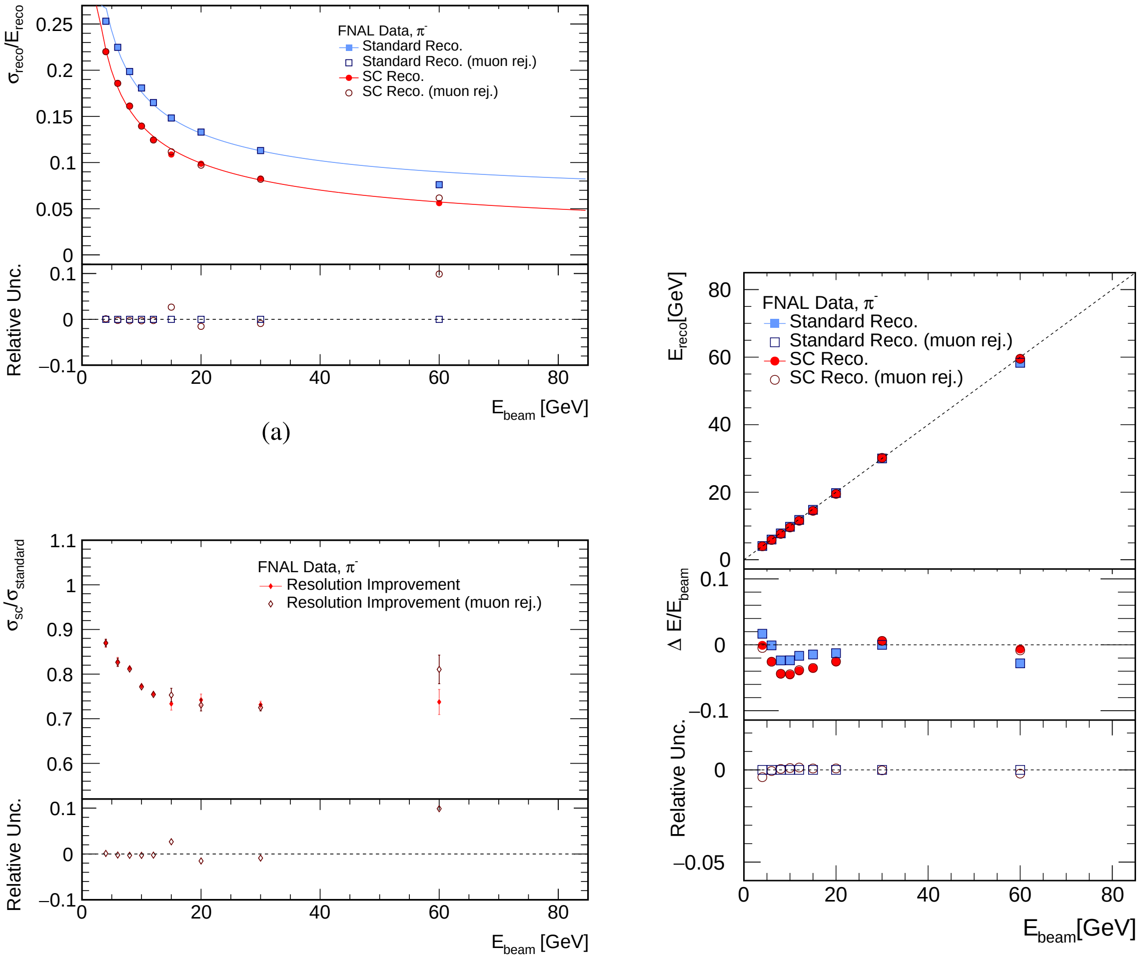

(a)

(b)

(c)

Figure C.8: The variations in the reconstruction results of FNAL data after implementing a looser muon rejection cut for full shower containment in the event selection (including events from $E_{beam} \geqslant 15$ GeV with $E_{reco} < E_{beam}/2.6$). Upper panel in each figure: reconstruction results of events selected with the original and the modified event selection criteria. Lower panel in each figure: the relative uncertainty obtained from modifying the event selection; The dashed line corresponds to a zero relative uncertainty. (a) The energy resolutions obtained from the standard and the Full SC methods. (b) The relative improvement of the SC reconstructed energy resolutions. (c) The mean reconstructed energy and relative residuals to the beam energy obtained from the standard and the Full SC methods.

The Combined Dataset

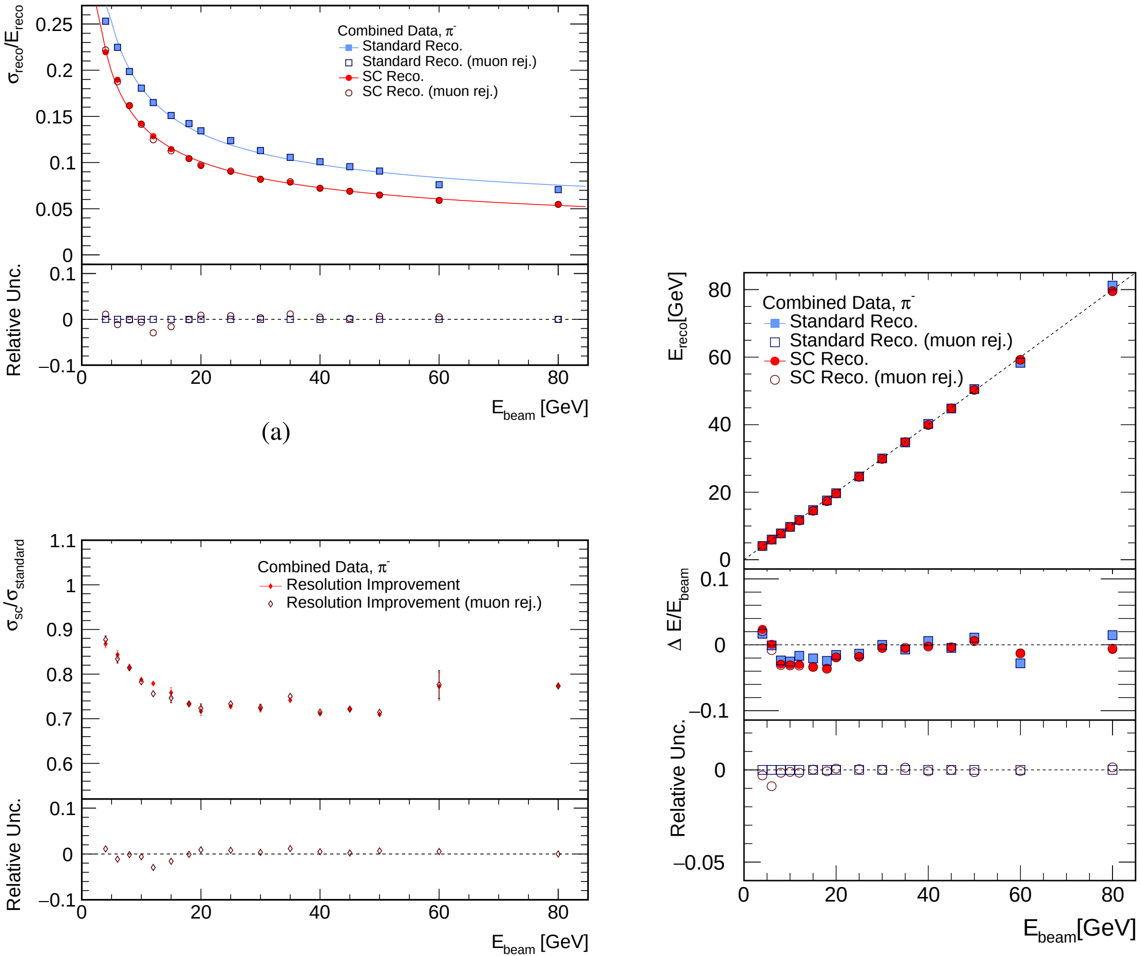

(a)

(b)

(c)

Figure C.9: The variations in the reconstruction results of the combined dataset after implementing a looser muon rejection cut for full shower containment in the event selection (including events from $E_{beam} \geqslant 15$ GeV with $E_{reco} < E_{beam}/2.6$). Upper panel in each figure: reconstruction results of events selected with the original and the modified event selection criteria. Lower panel in each figure: the relative uncertainty obtained from modifying the event selection; The dashed line corresponds to a zero relative uncertainty. (a) The energy resolutions obtained from the standard and the Full SC methods. (b) The relative improvement of the SC reconstructed energy resolutions. (c) The mean reconstructed energy and relative residuals to the beam energy obtained from the standard and the Full SC methods.

C.4 Clustering Distance

The uncertainties obtained from the implementation of a looser clustering requirement for multi-particle rejection in the event selection by clustering hits within d_{th}=20 mm (instead of d_{th}=12 mm).

CERN Dataset

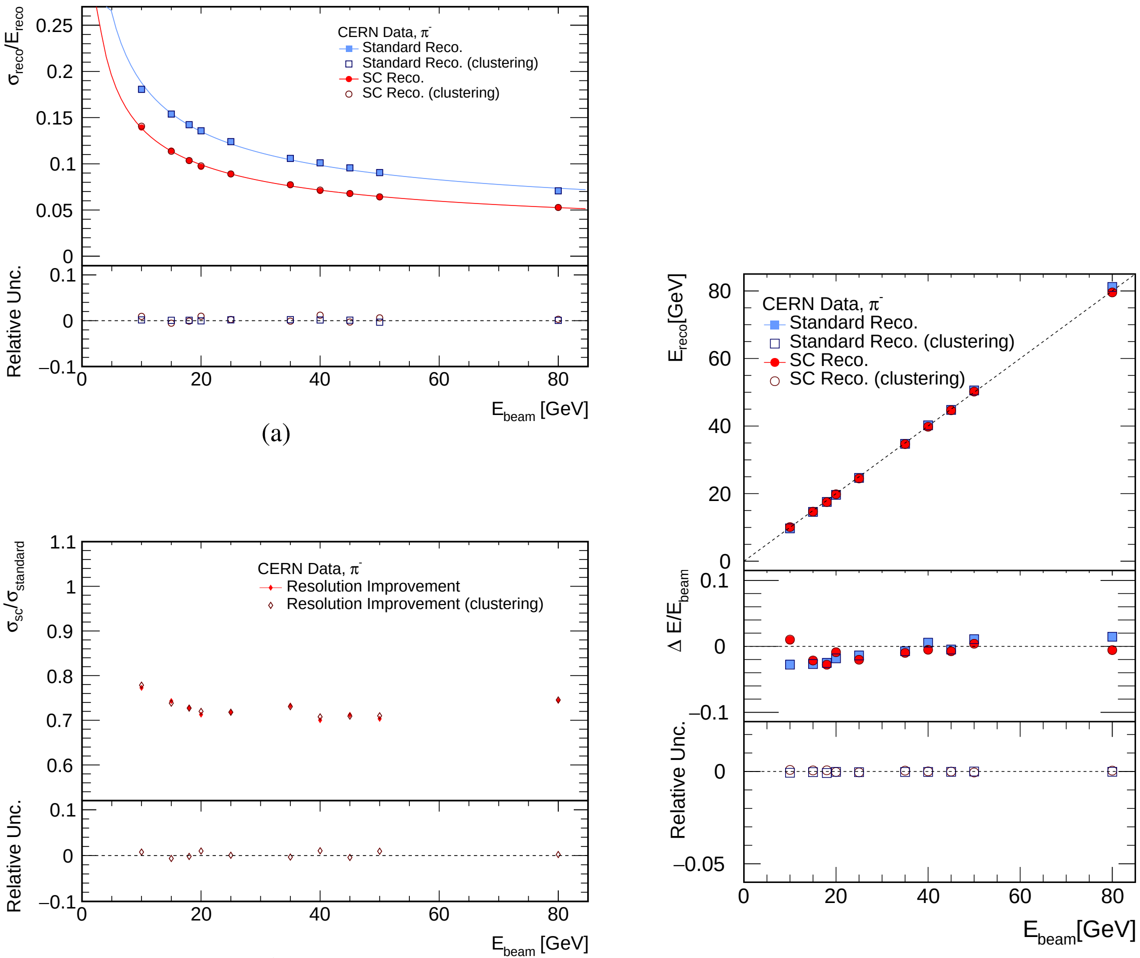

(a) (b) (c)

Figure C.10: The variations in the reconstruction results of CERN data after implementing a looser clustering requirement for multi-particle rejection in the event selection (d_{th}=20 mm instead of d_{th}=12 mm). Upper panel in each figure: reconstruction results of events selected with the original and the modified event selection criteria. Lower panel in each figure: the relative uncertainty obtained from modifying the event selection; The dashed line corresponds to a zero relative uncertainty. (a) The energy resolutions obtained from the standard and the Full SC methods. (b) The relative improvement of the SC reconstructed energy resolutions. (c) The mean reconstructed energy and relative residuals to the beam energy obtained from the standard and the Full SC methods.

FNAL Dataset

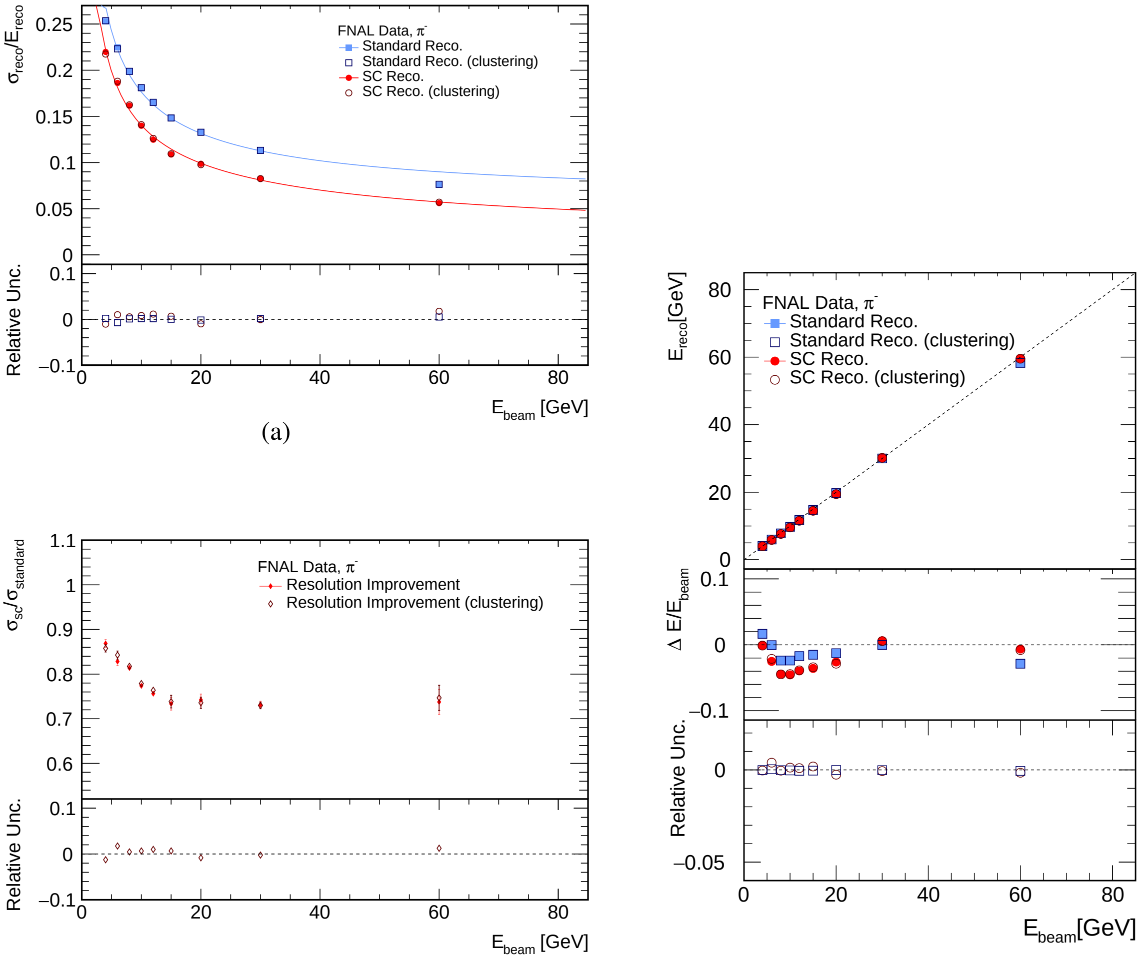

(a)

(b)

(c)

Figure C.11: The variations in the reconstruction results of FNAL data after implementing a looser clustering requirement for multi-particle rejection in the event selection (d_{th}=20 mm instead of d_{th}=12 mm). Upper panel in each figure: reconstruction results of events selected with the original and the modified event selection criteria. Lower panel in each figure: the relative uncertainty obtained from modifying the event selection; The dashed line corresponds to a zero relative uncertainty. (a) The energy resolutions obtained from the standard and the Full SC methods. (b) The relative improvement of the SC reconstructed energy resolutions. (c) The mean reconstructed energy and relative residuals to the beam energy obtained from the standard and the Full SC methods.

The Combined Dataset

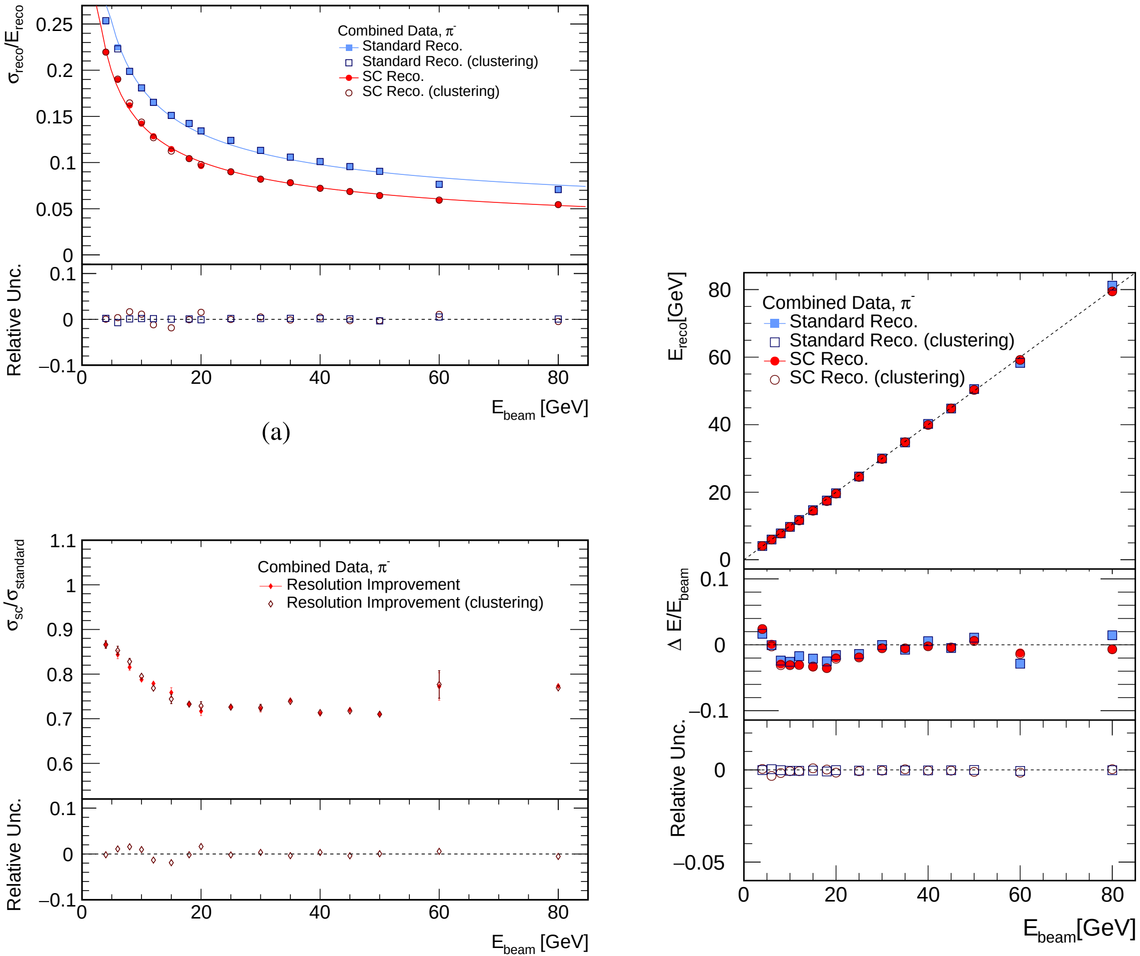

(a)

(b)

(c)

Figure C.12: The variations in the reconstruction results of the combined dataset after implementing a looser clustering requirement for multi-particle rejection in the event selection (d_{th}=20 mm instead of d_{th}=12 mm). Upper panel in each figure: reconstruction results of events selected with the original and the modified event selection criteria. Lower panel in each figure: the relative uncertainty obtained from modifying the event selection; The dashed line corresponds to a zero relative uncertainty. (a) The energy resolutions obtained from the standard and the Full SC methods. (b) The relative improvement of the SC reconstructed energy resolutions. (c) The mean reconstructed energy and relative residuals to the beam energy obtained from the standard and the Full SC methods.

C.5 Systematic Uncertainties for Simulated Events

The total systematic uncertainties for the standard and the Full SC reconstruction of events simulated with the FTFP_BERT and QGSP_BERT GEANT4 physics lists.

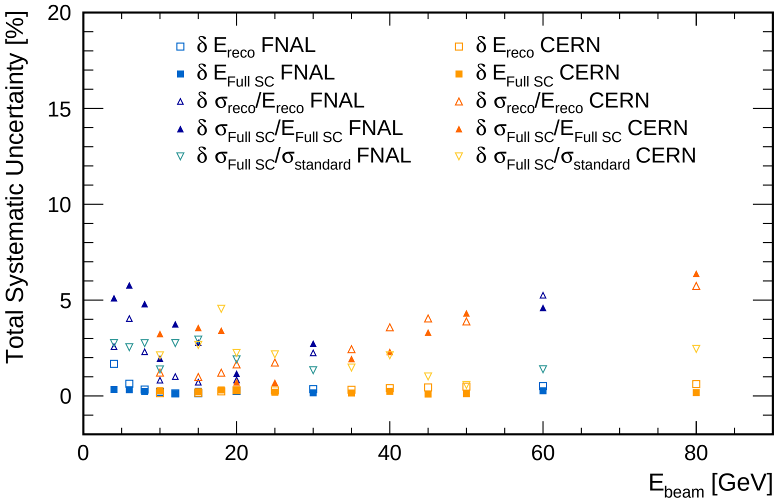

Figure C.13: Summary of the total systematic uncertainties obtained from the standard and the Full SC reconstruction of FTFP_BERT simulations of CERN and FNAL events.

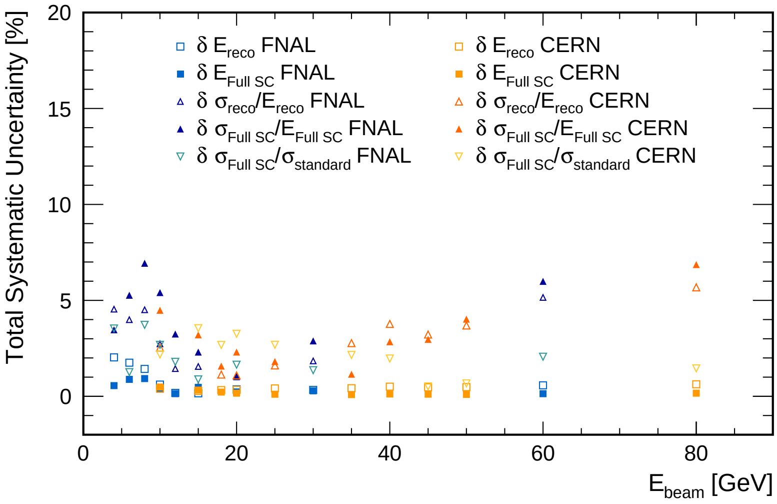

Figure C.14: Summary of the total systematic uncertainties obtained from the standard and the Full SC reconstruction of QGSP_BERT simulations of CERN and FNAL events.

APPENDIX D

ADDITIONAL FIGURES

D.1 Software Compensation Weights

CERN Dataset

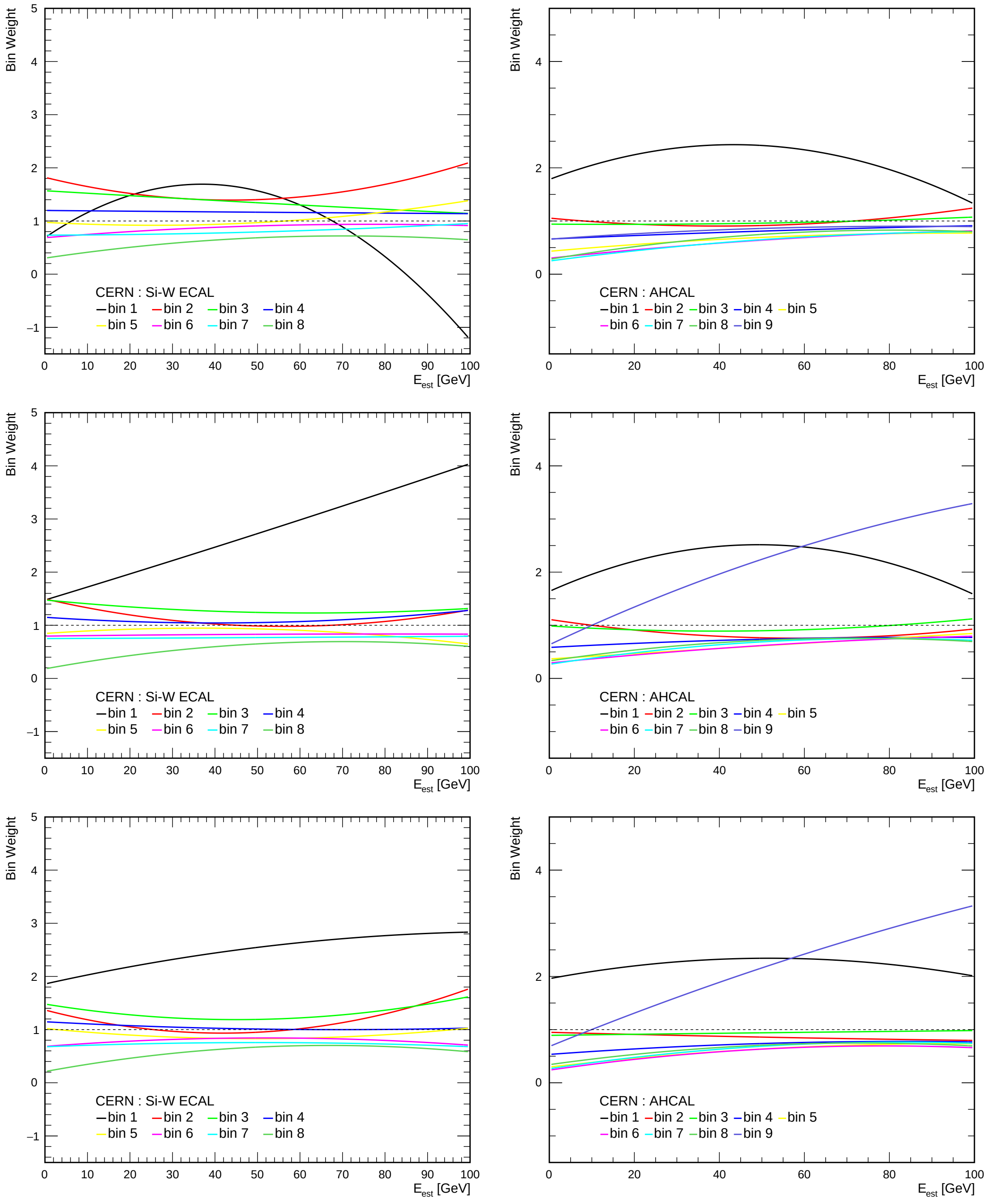

Figure D.1: The energy-bin weights as a function of the estimated particle energy E_{est}. Left: Si-W ECAL weights. Right: AHCAL weights (bin 1 – 8) and TCMT weight (bin 9). Upper panel: Weights obtained from CERN data events. Middle panel: Weights obtained from CERN FTFP_BERT events. Lower panel: Weights obtained from CERN QGSP_BERT events.

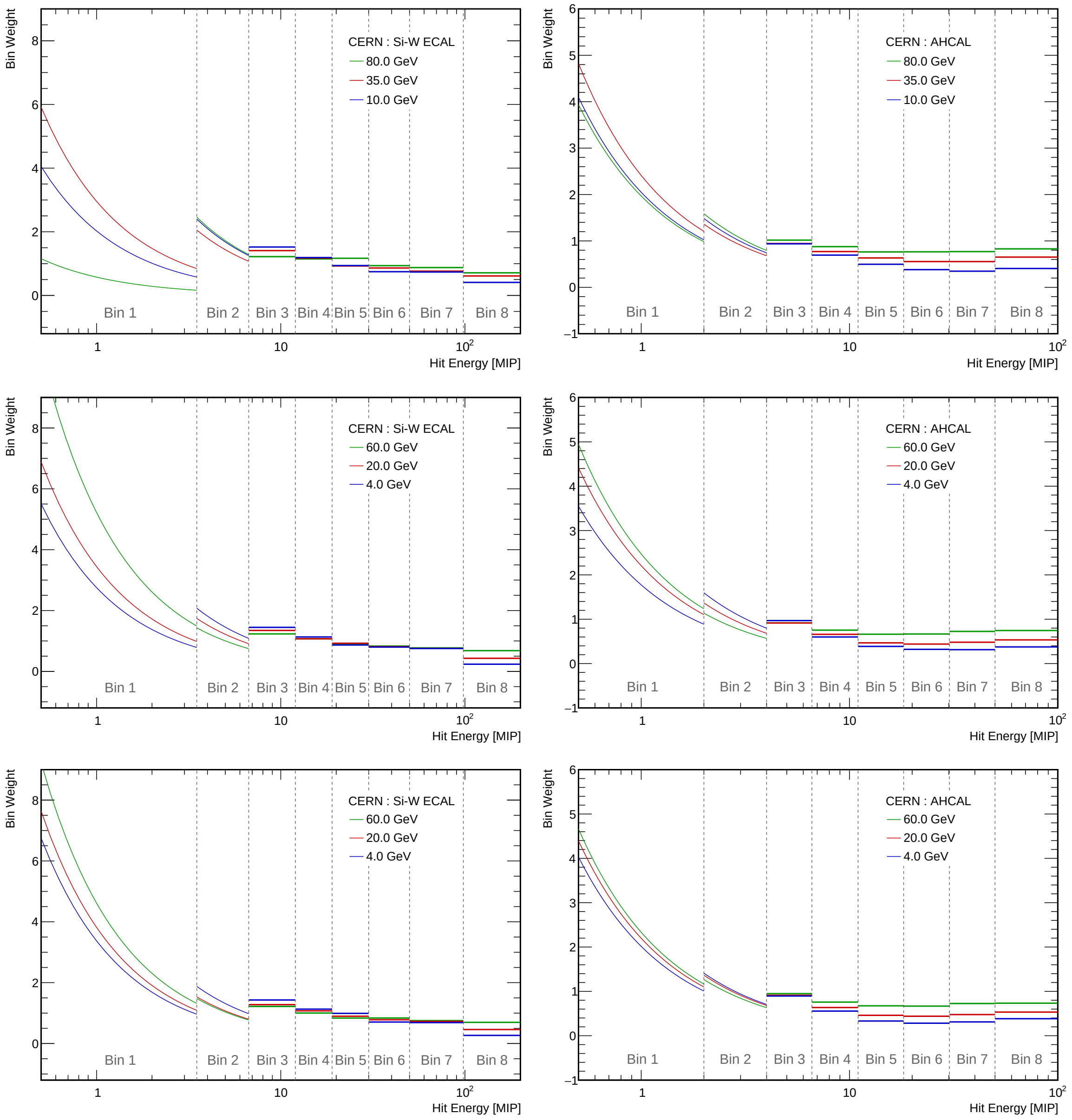

Figure D.2: The optimized bin weights for 4 GeV, 20 GeV and 60 GeV π^- beams as a function of the hit energies to which these weights are applied. Left: Si-W ECAL weights. Right: AHCAL weights. Upper panel: Weights obtained from CERN data events. Middle panel: Weights obtained from CERN FTFP_BERT events. Lower panel: Weights obtained from CERN QGSP_BERT events. The dashed lines indicate the energy range of the different energy-bins.

FNAL Dataset

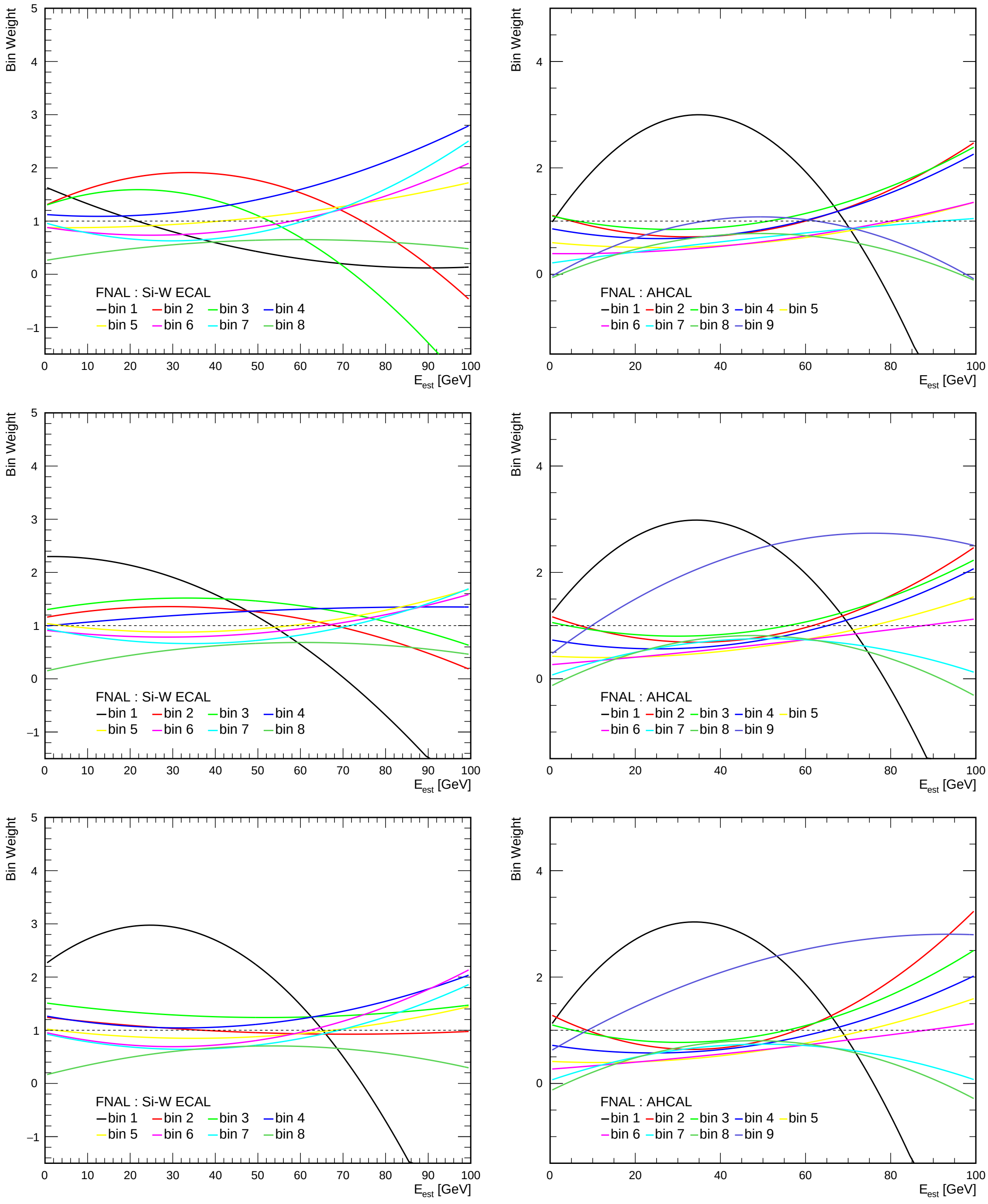

Figure D.3: The energy-bin weights as a function of the estimated particle energy E_{est}. Left: Si-W ECAL weights. Right: AHCAL weights (bin 1 – 8) and TCMT weight (bin 9). Upper panel: Weights obtained from FNAL data events. Middle panel: Weights obtained from FNAL FTFP_BERT events. Lower panel: Weights obtained from FNAL QGSP_BERT events.

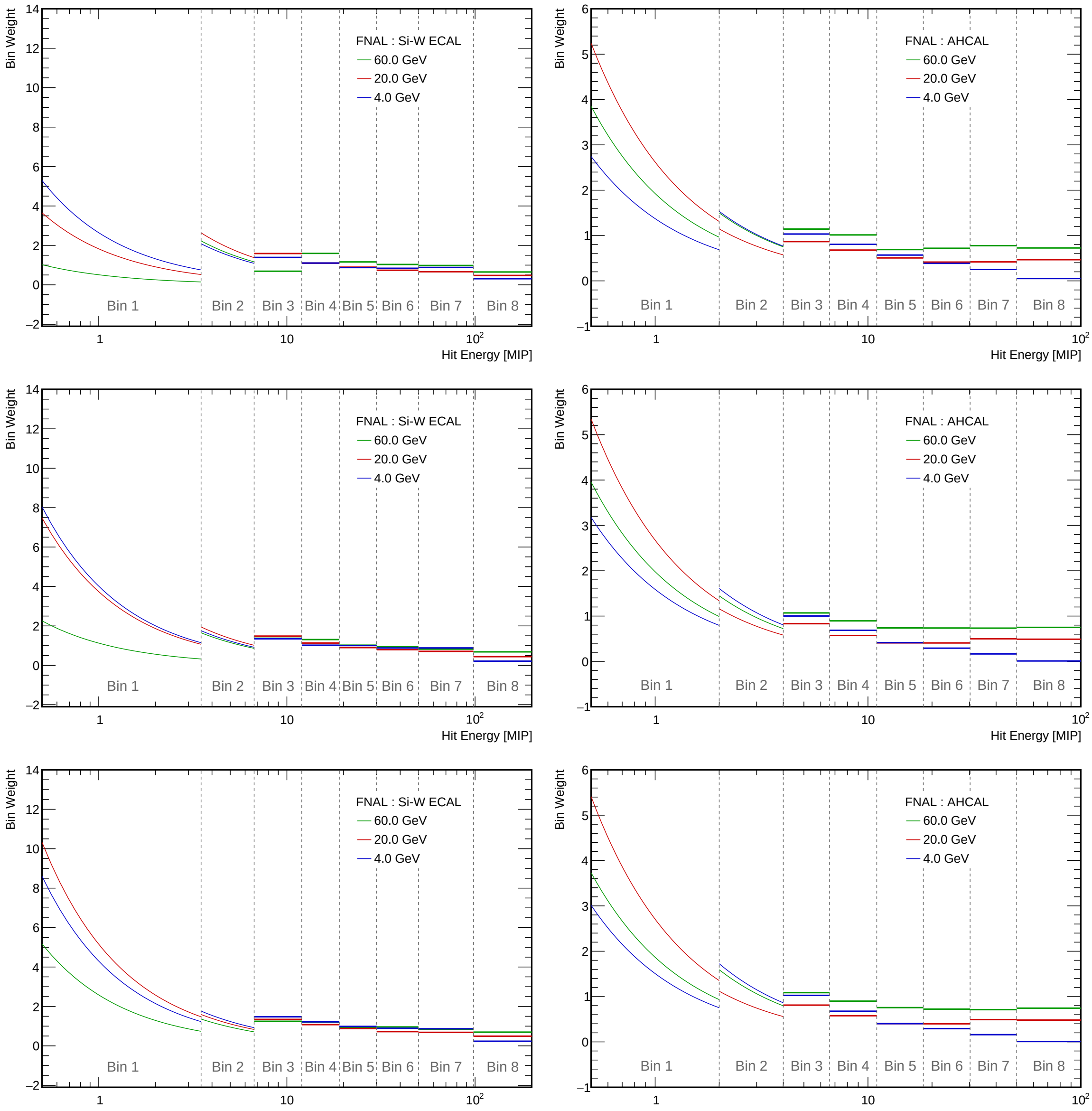

Figure D.4: The optimized bin weights for 4 GeV, 20 GeV and 60 GeV π^- beams as a function of the hit energies to which these weights are applied. Left: Si-W ECAL weights. Right: AHCAL weights. Upper panel: Weights obtained from FNAL data events. Middle panel: Weights obtained from FNAL FTFP_BERT events. Lower panel: Weights obtained from FNAL QGSP_BERT events. The dashed lines indicate the energy range of the different energy-bins.

Combined Dataset

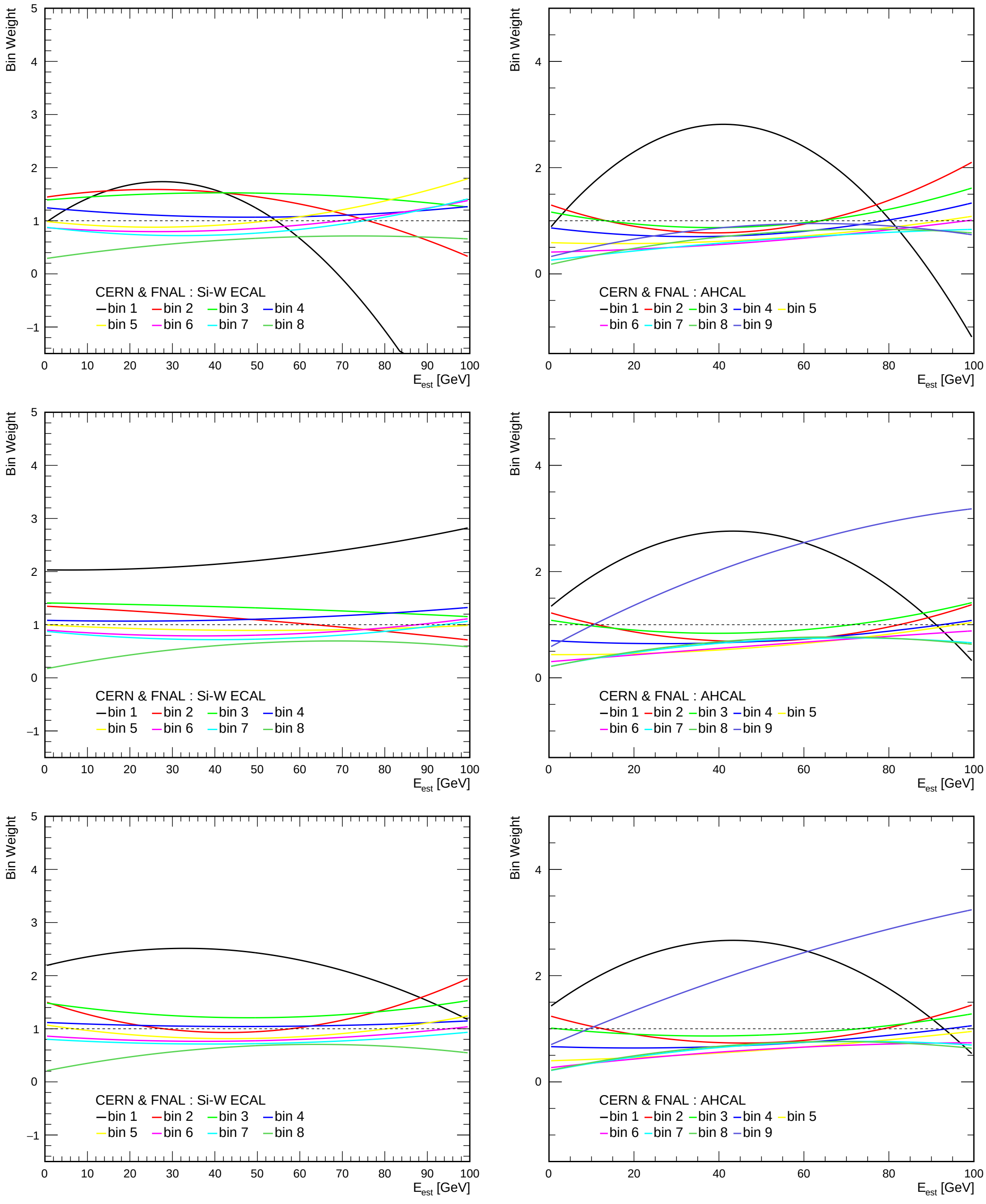

Figure D.5: The energy-bin weights as a function of the estimated particle energy E_{est}. Left: Si-W ECAL weights. Right: AHCAL weights (bin 1 – 8) and TCMT weight (bin 9). Upper panel: Weights obtained from Combined data events. Middle panel: Weights obtained from combined FTFP_BERT events. Lower panel: Weights obtained from combined QGSP_BERT events.

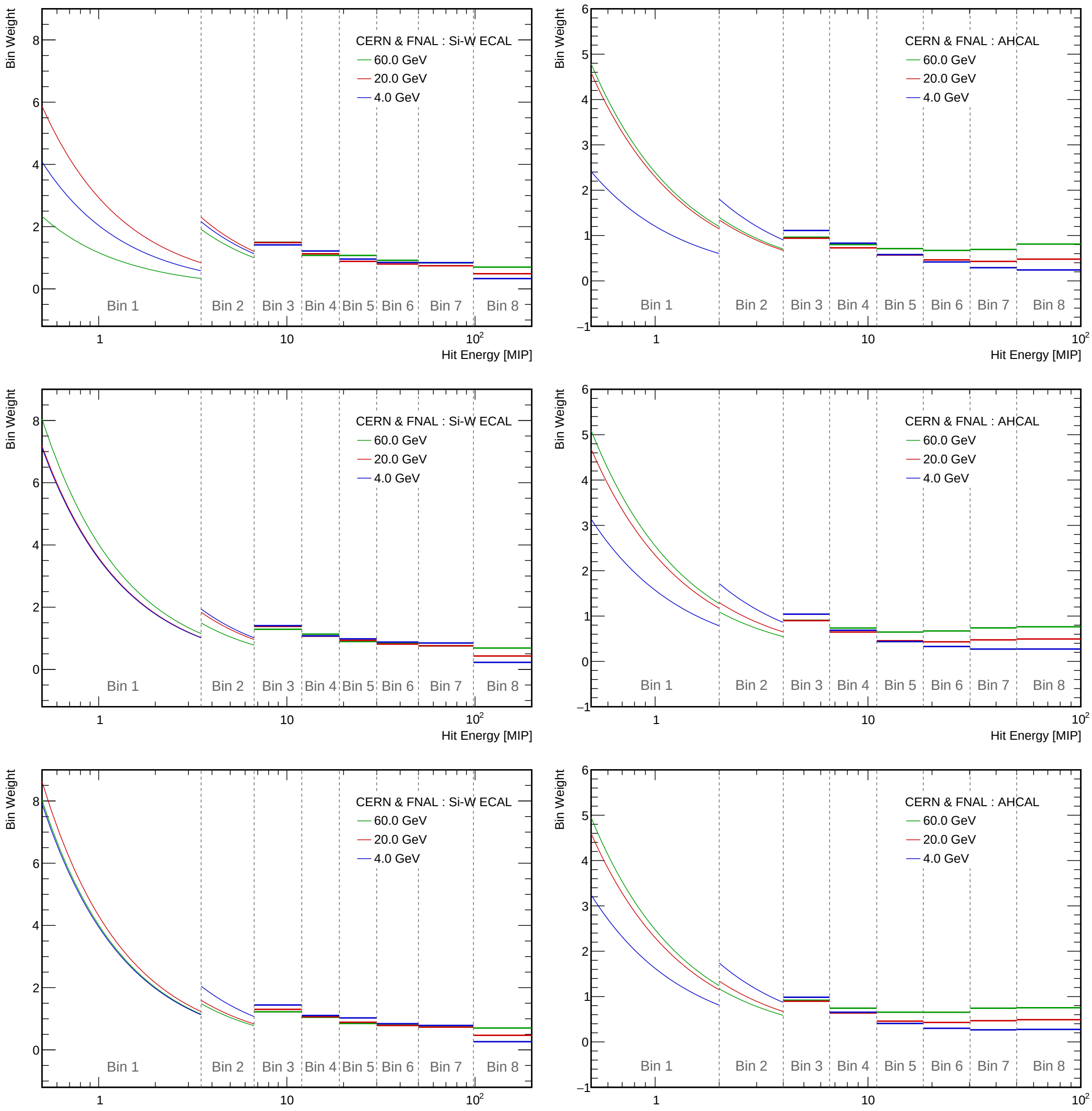

Figure D.6: The optimized bin weights for 4 GeV, 20 GeV and 60 GeV π^- beams as a function of the hit energies to which these weights are applied. Left: Si-W ECAL weights. Right: AHCAL weights. Upper panel: Weights obtained from combined data events. Middle panel: Weights obtained from combined FTFP_BERT events. Lower panel: Weights obtained from combined QGSP_BERT events. The dashed lines indicate the energy range of the different energy-bins.

D.2 Reconstructed Energies

CERN Dataset

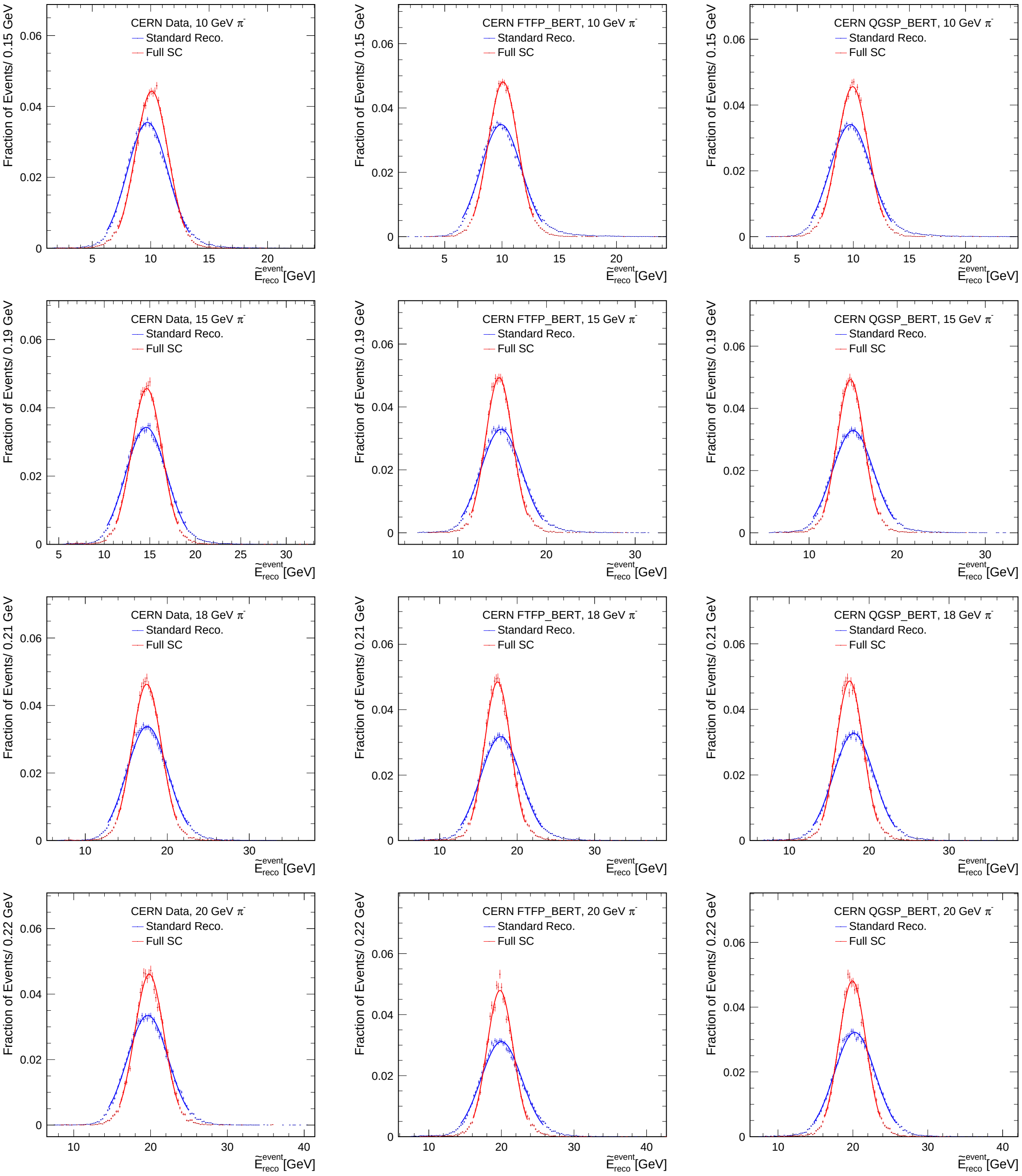

Figure D.7: The distribution of reconstructed energies with the standard (blue) and Full SC (red) reconstruction of CERN events (10 GeV, 15 GeV, 18 GeV, 20 GeV). Left: Data events. Middle: FTFP_BERT events. Right: QGSP_BERT events.

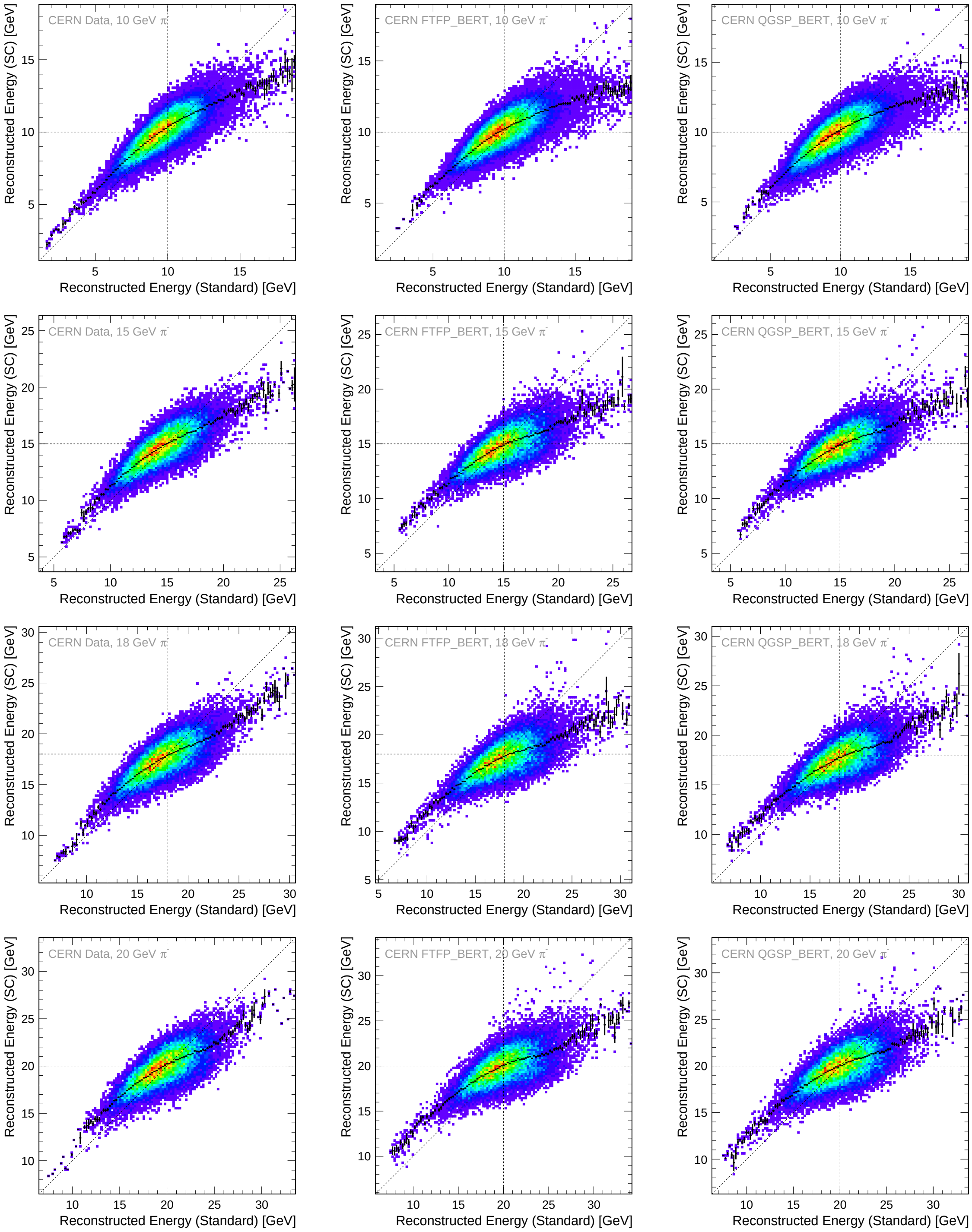

Figure D.8: The correlation between energies reconstructed with the standard and the Full SC reconstruction methods of CERN events (10 GeV, 15 GeV, 18 GeV, 20 GeV). Left: Data events. Middle: FTFP_BERT events. Right: QGSP_BERT events. The black markers show the profile of the mean SC reconstructed energy for bins of the standard reconstructed energy. The dashed lines indicate the beam energy in each axis while the diagonal traces the slope with total correlation.

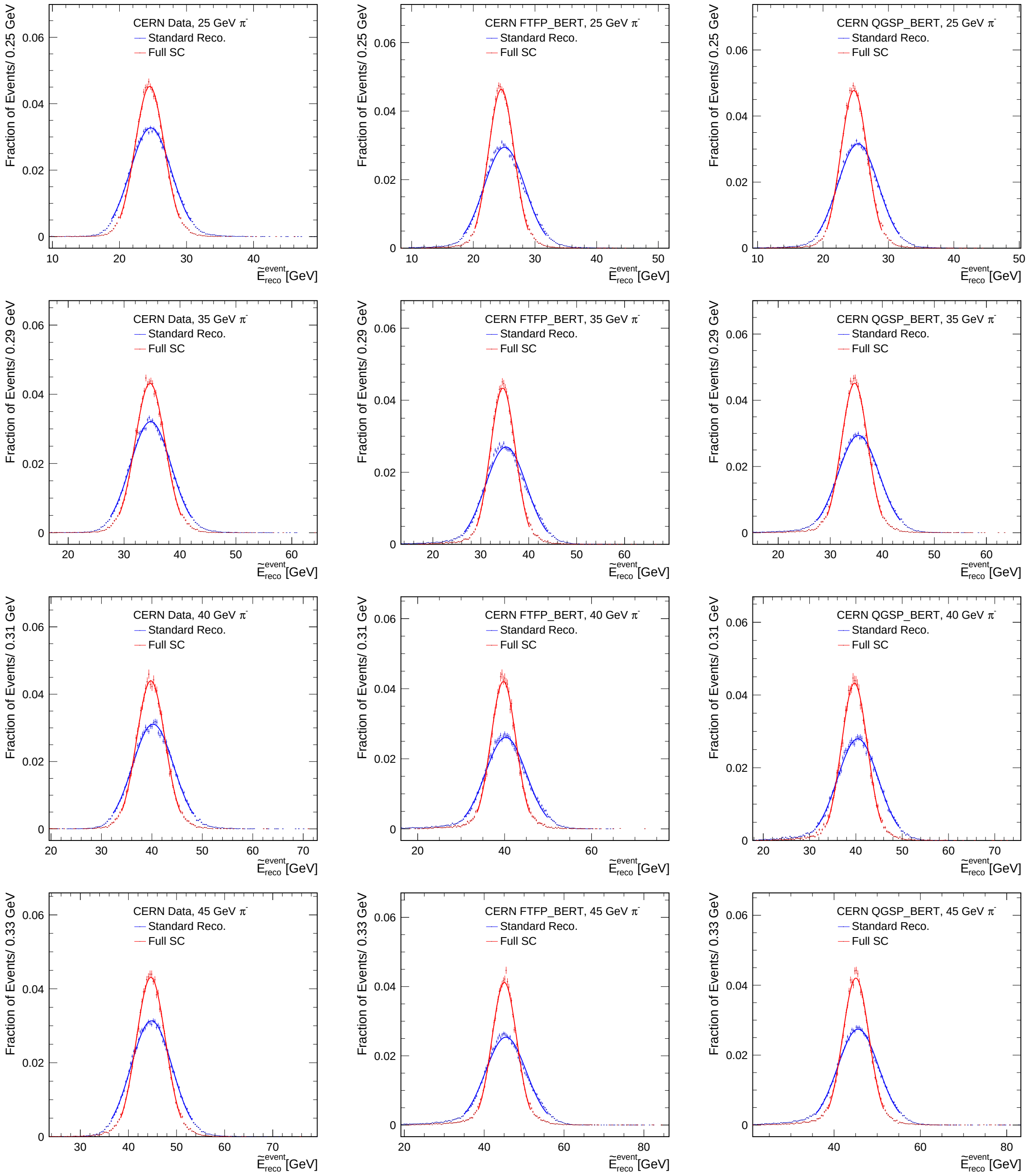

Figure D.9: The distribution of reconstructed energies with the standard (blue) and Full SC (red) reconstruction of CERN events (25 GeV, 35 GeV, 40 GeV, 45 GeV). Left: Data events. Middle: FTFP_BERT events. Right: QGSP_BERT events.

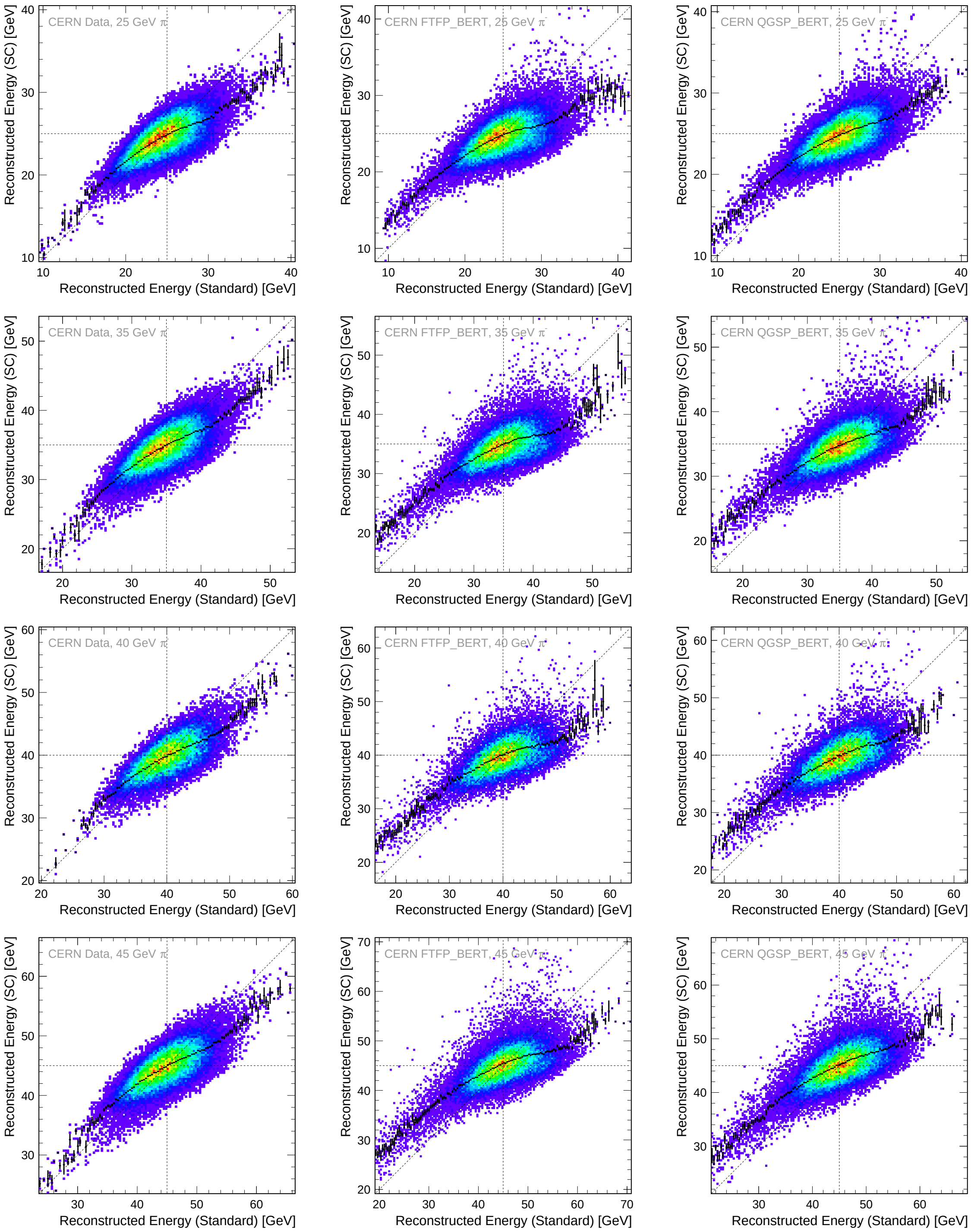

Figure D.10: The correlation between energies reconstructed with the standard and the Full SC reconstruction methods of CERN events (25 GeV, 35 GeV, 40 GeV, 45 GeV). Left: Data events. Middle: FTFP_BERT events. Right: QGSP_BERT events. The black markers show the profile of the mean SC reconstructed energy for bins of the standard reconstructed energy. The dashed lines indicate the beam energy in each axis while the diagonal traces the slope with total correlation.

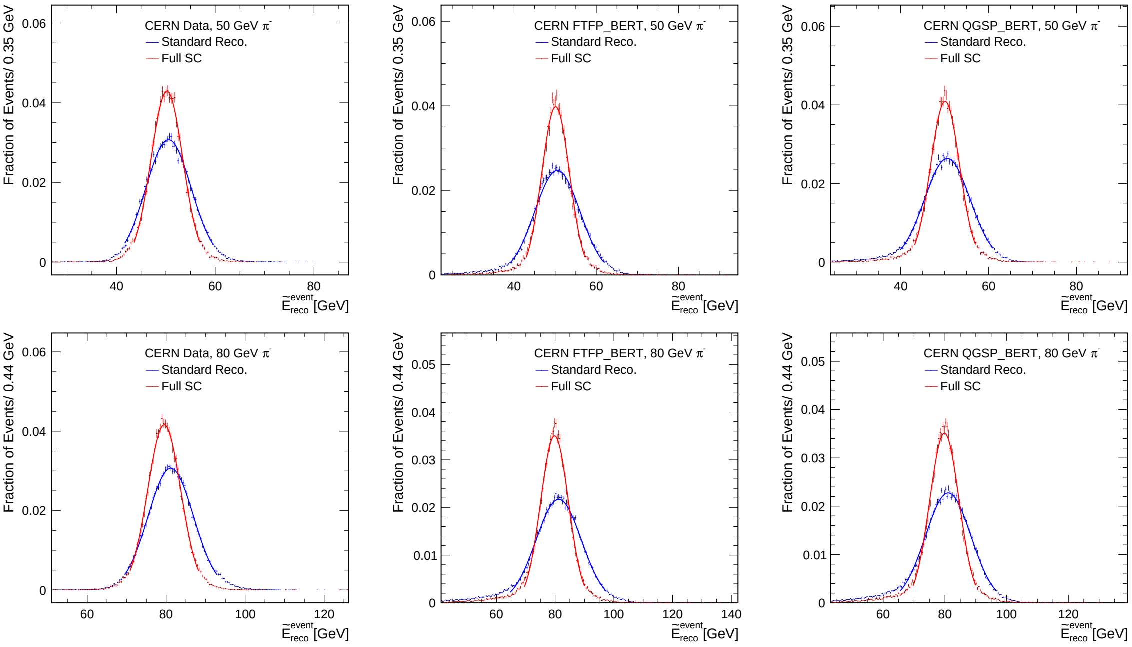

Figure D.11: The distribution of reconstructed energies with the standard (blue) and Full SC (red) reconstruction of CERN events (50 GeV, 80 GeV). Left: Data events. Middle: FTFP_BERT events. Right: QGSP_BERT events.

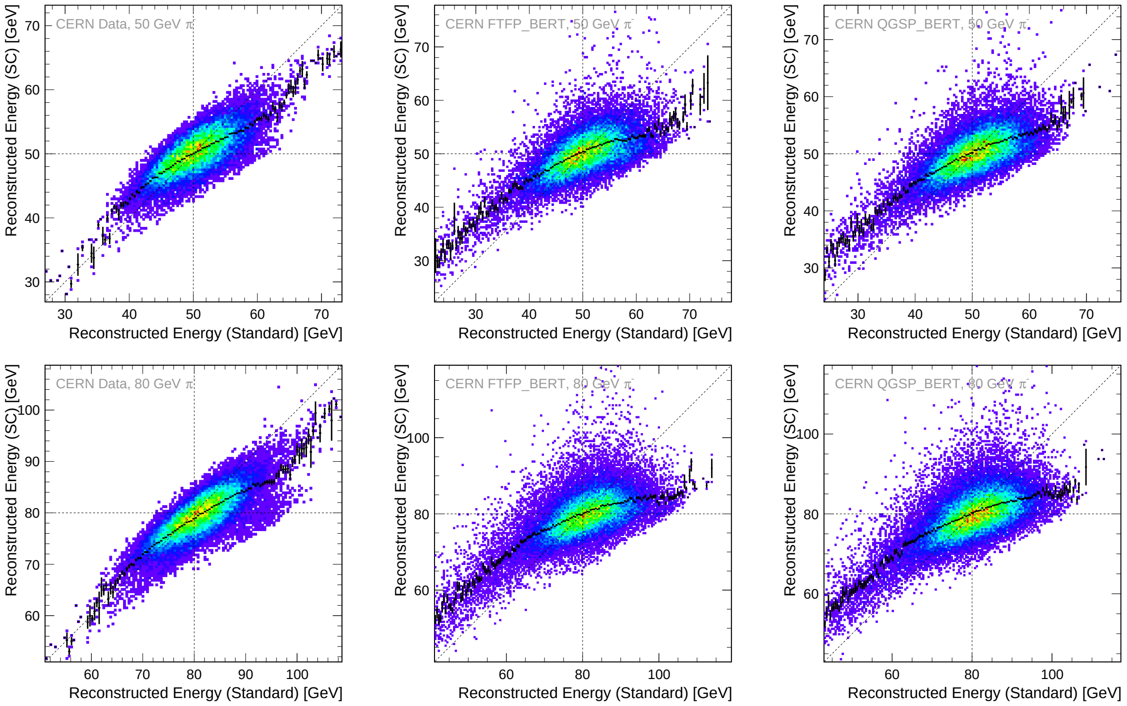

Figure D.12: The correlation between energies reconstructed with the standard and the Full SC reconstruction methods of CERN events (50 GeV, 80 GeV). Left: Data events. Middle: FTFP_BERT events. Right: QGSP_BERT events. The black markers show the profile of the mean SC reconstructed energy for bins of the standard reconstructed energy. The dashed lines indicate the beam energy in each axis while the diagonal traces the slope with total correlation.

FNAL Dataset

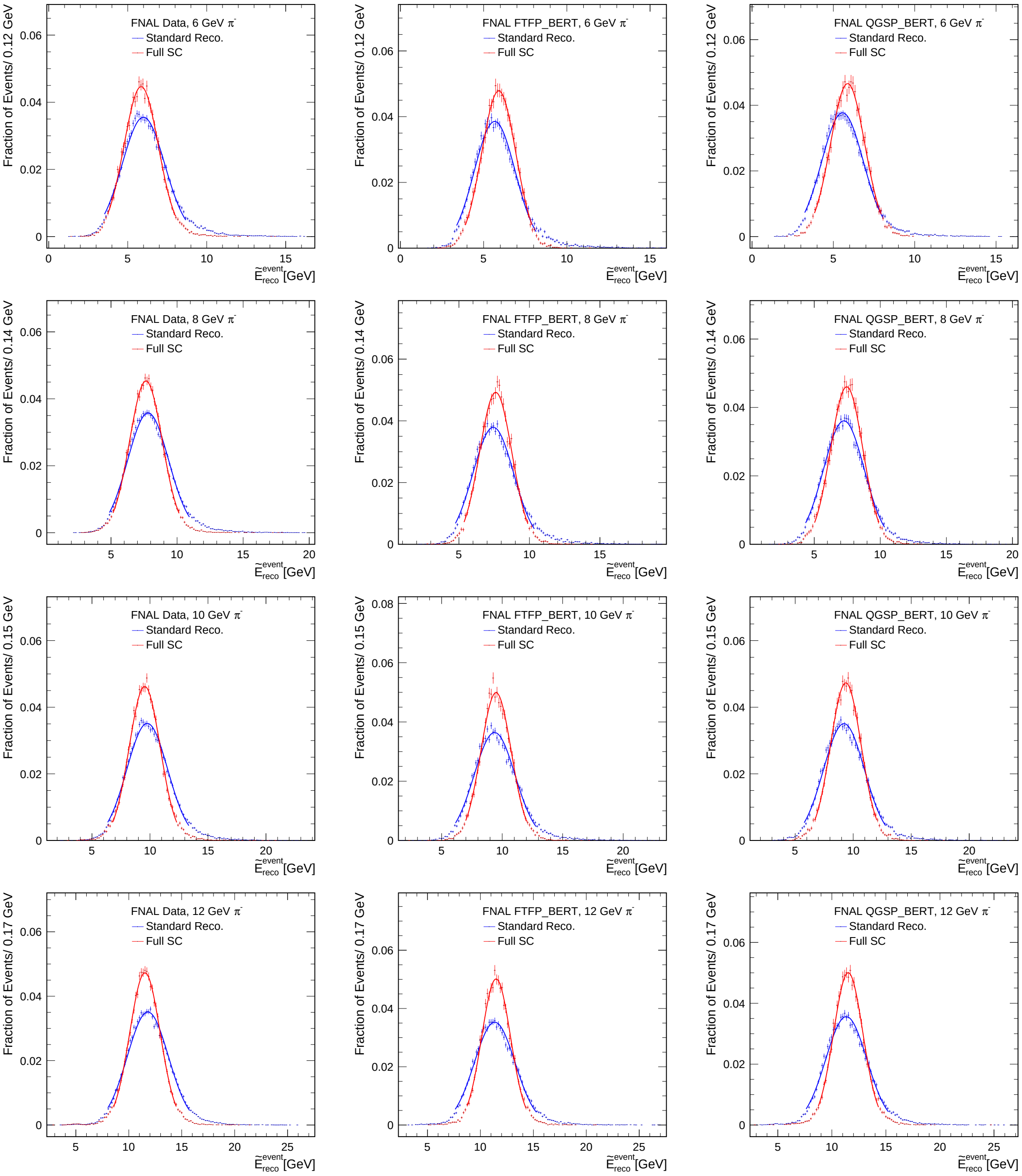

Figure D.13: The distribution of reconstructed energies with the standard (blue) and Full SC (red) reconstruction of FNAL events (6 GeV, 8 GeV, 10 GeV, 12 GeV). Left: Data events. Middle: FTFP_BERT events. Right: QGSP_BERT events.

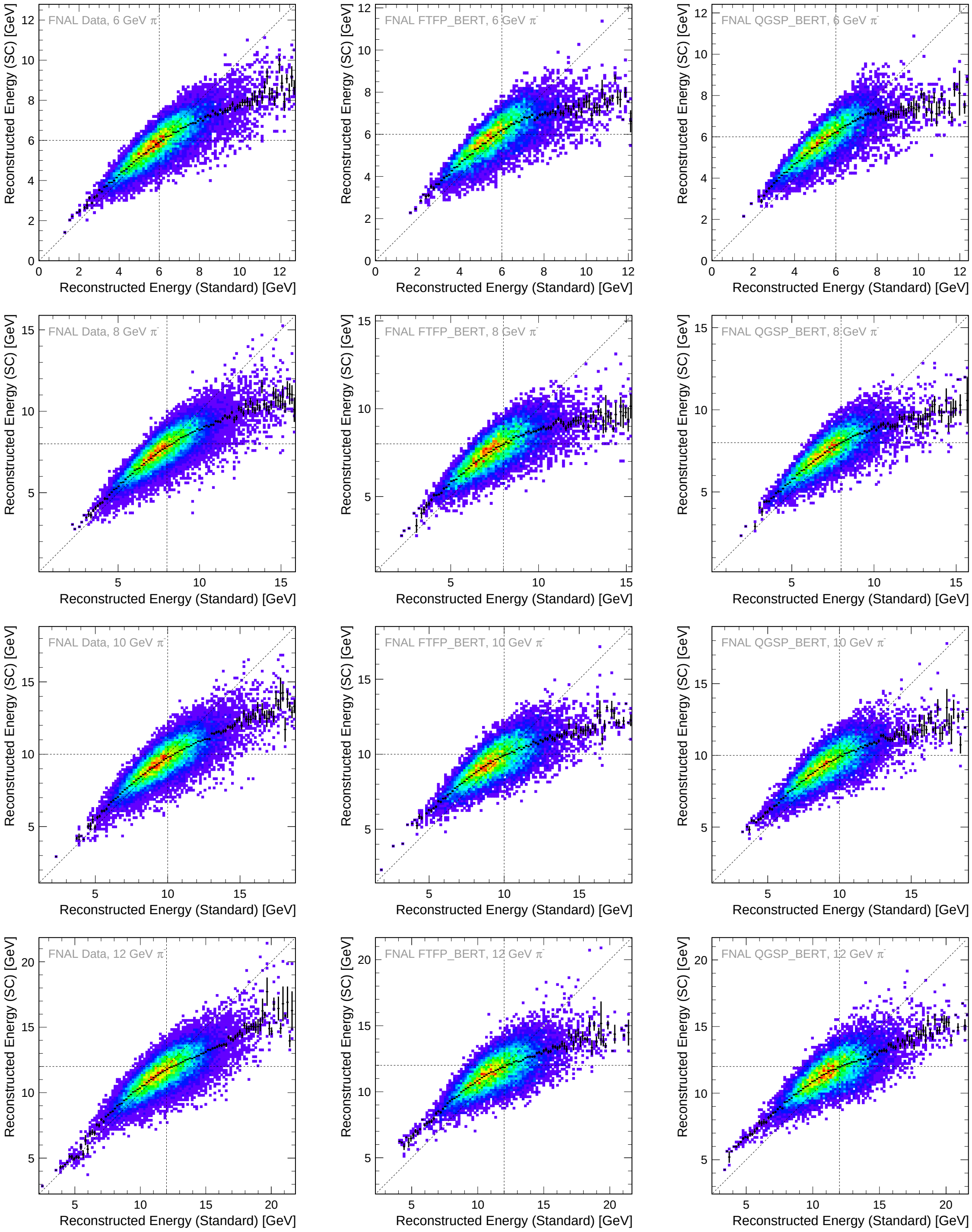

Figure D.14: The correlation between energies reconstructed with the standard and the Full SC reconstruction methods of FNAL events (6 GeV, 8 GeV, 10 GeV, 12 GeV). Left: Data events. Middle: FTFP_BERT events. Right: QGSP_BERT events. The black markers show the profile of the mean SC reconstructed energy for bins of the standard reconstructed energy. The dashed lines indicate the beam energy in each axis while the diagonal traces the slope with total correlation.

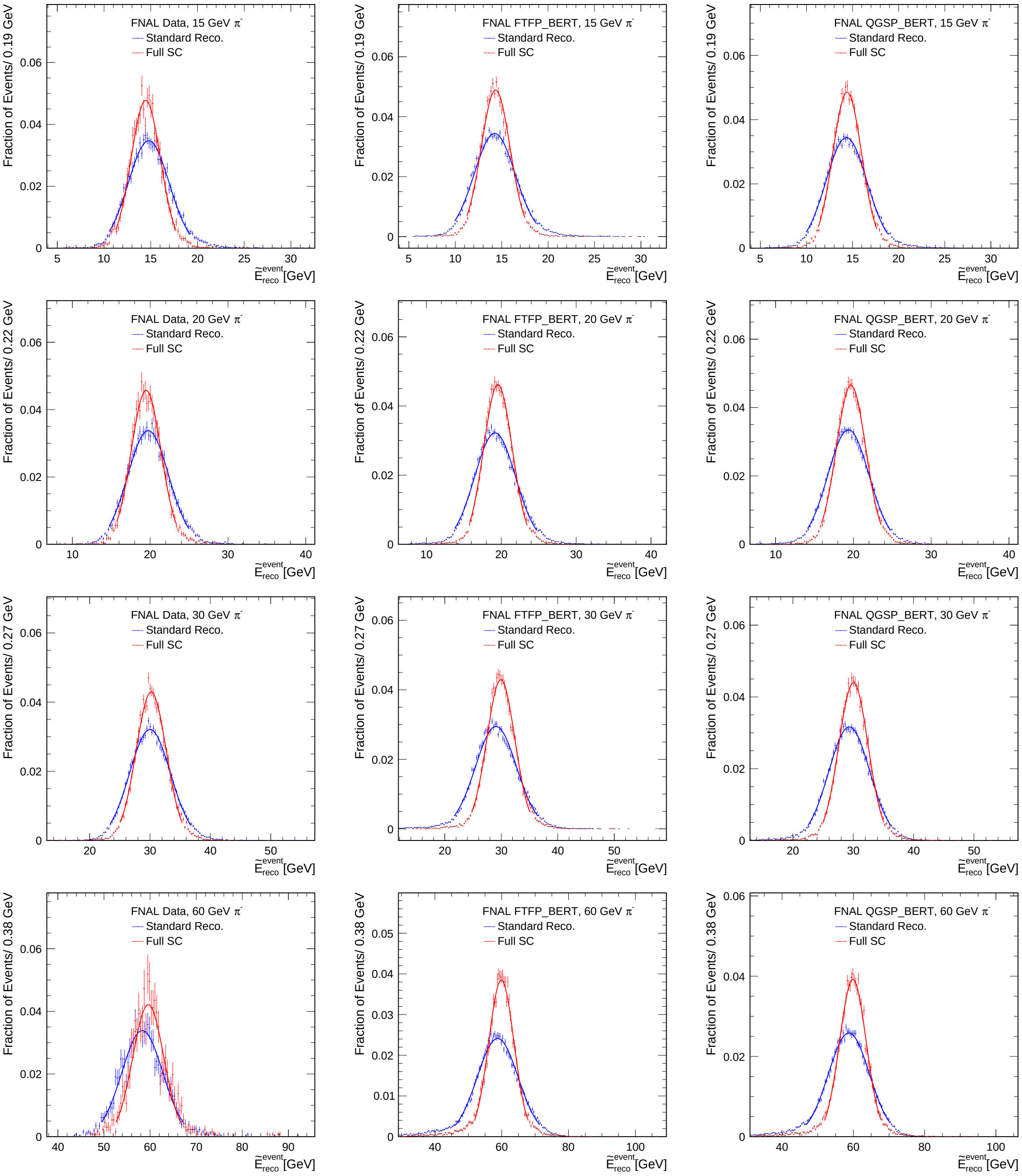

Figure D.15: The distribution of reconstructed energies with the standard (blue) and Full SC (red) reconstruction of FNAL events (15 GeV, 20 GeV, 30 GeV, 60 GeV). Left: Data events. Middle: FTFP_BERT events. Right: QGSP_BERT events.

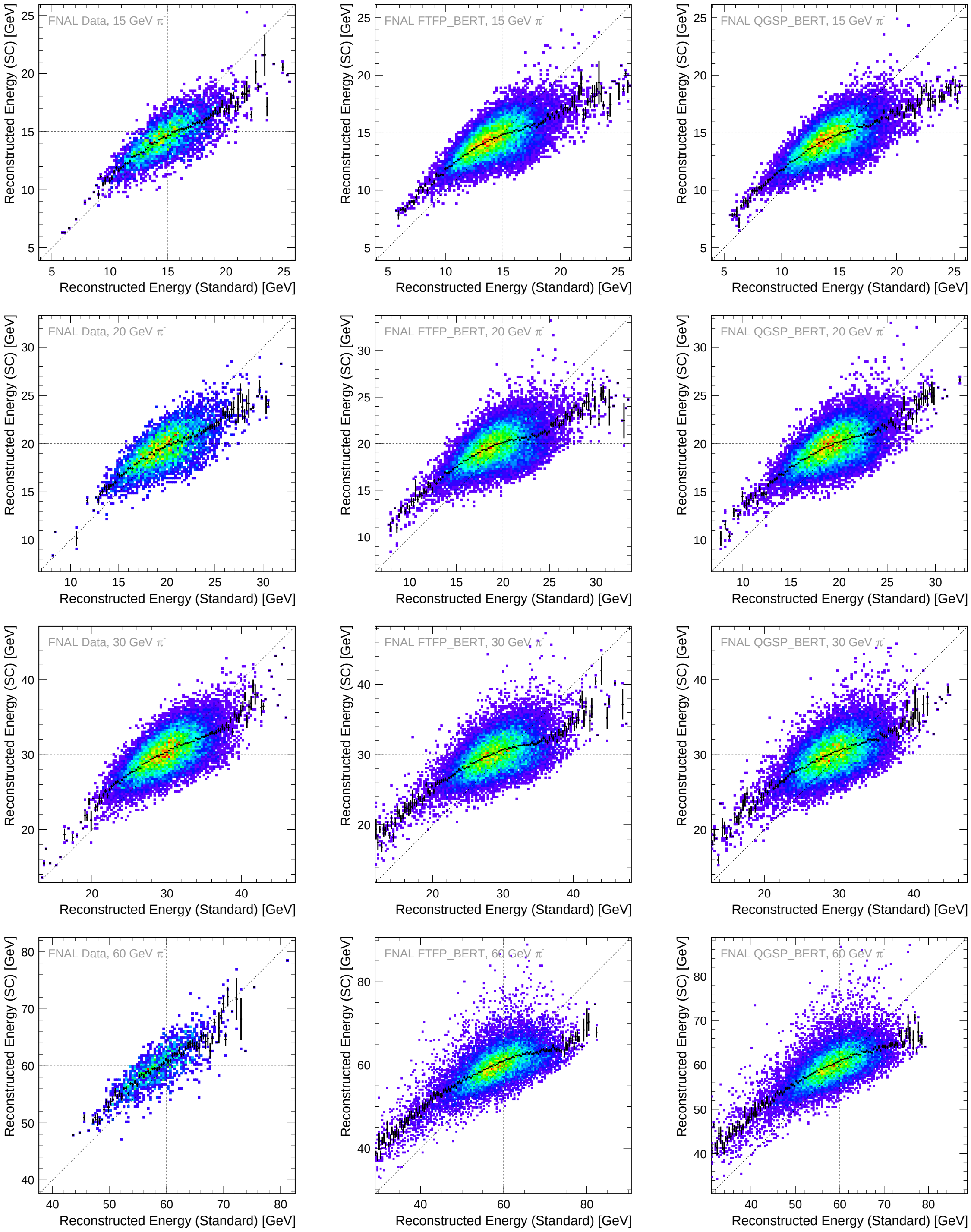

Figure D.16: The correlation between energies reconstructed with the standard and the Full SC reconstruction methods of FNAL events (15 GeV, 20 GeV, 30 GeV, 60 GeV). Left: Data events. Middle: FTFP_BERT events. Right: QGSP_BERT events. The black markers show the profile of the mean SC reconstructed energy for bins of the standard reconstructed energy. The dashed lines indicate the beam energy in each axis while the diagonal traces the slope with total correlation.

D.3 Linearity in Simulations

FTFP_BERT

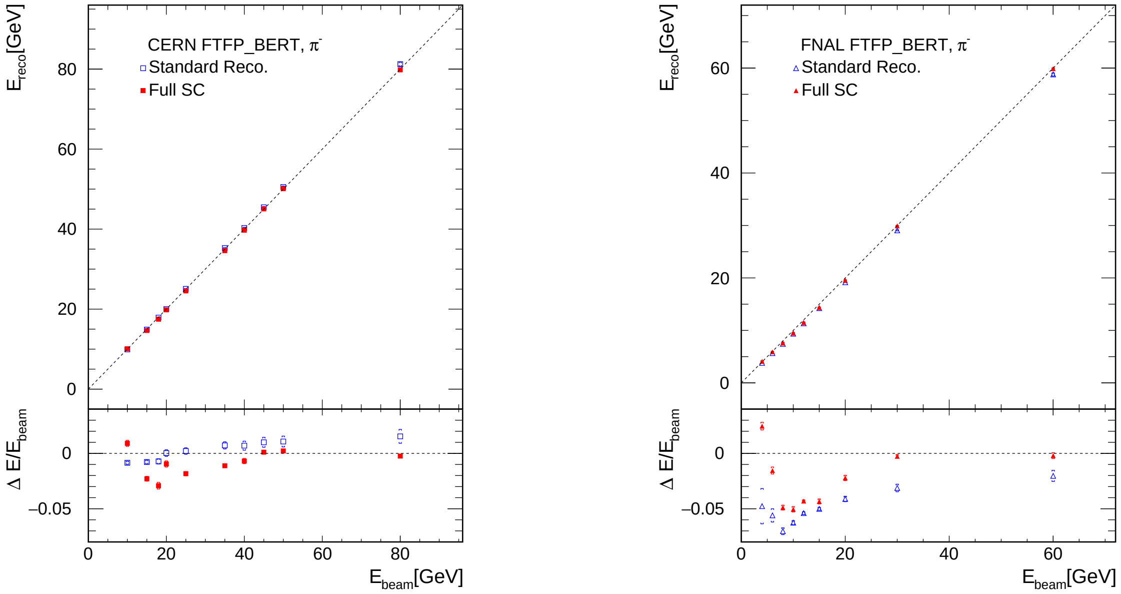

(a) CERN FTFP_BERT (b) FNAL FTFP_BERT

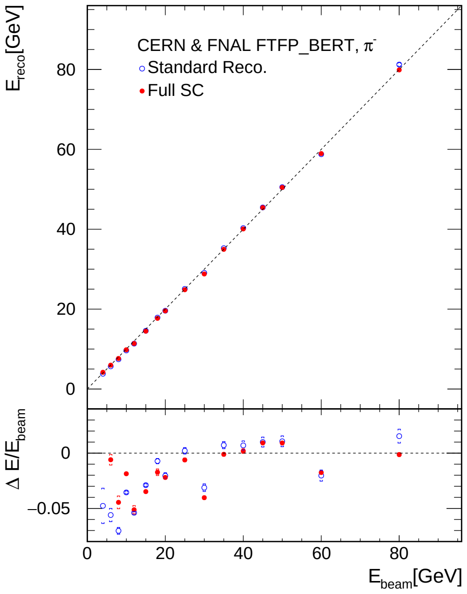

(c) CERN and FNAL FTFP_BERT

Figure D.17: The mean reconstructed energy and relative residual to the beam energy versus beam energy obtained from the standard (blue) and Full SC (red) reconstruction of (a): FTFP_BERT simulations of CERN data. (b): FTFP_BERT simulations of FNAL data. (c): FTFP_BERT simulations of the combined (CERN+FNAL) dataset. The total (statistical and systematic) uncertainties are marked with brackets, '[]'. Dashed lines correspond to $E_{reco} = E_{beam}$.

QGSP_BERT

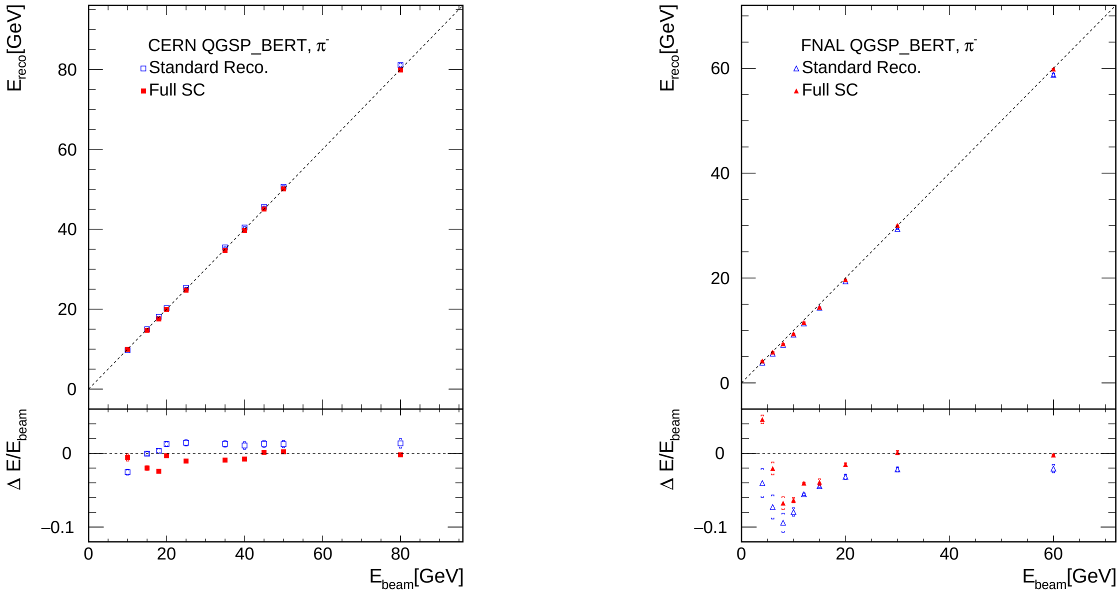

(a) CERN QGSP_BERT (b) FNAL QGSP_BERT

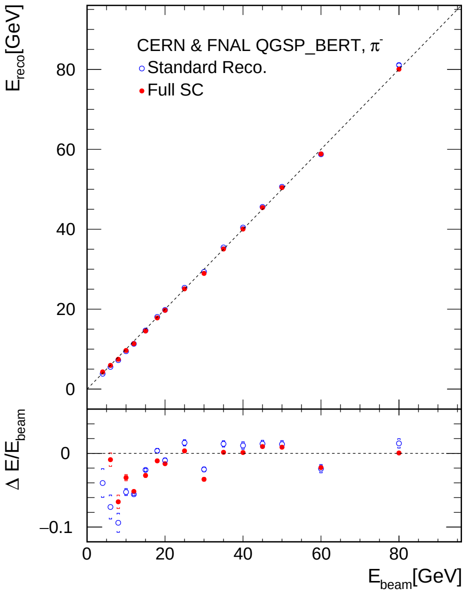

(c) CERN and FNAL QGSP_BERT

Figure D.18: The mean reconstructed energy and relative residual to the beam energy versus beam energy obtained from the standard (blue) and Full SC (red) reconstruction of (a): (a): QGSP_BERT simulations of CERN data. (b): QGSP_BERT simulations of FNAL data. (c): QGSP_BERT simulations of the combined (CERN+FNAL) dataset. The total (statistical and systematic) uncertainties are marked with brackets, '[]'. Dashed lines correspond to $E_{reco} = E_{beam}$.

D.4 Applying Software Compensation to Different Detectors

CERN Dataset

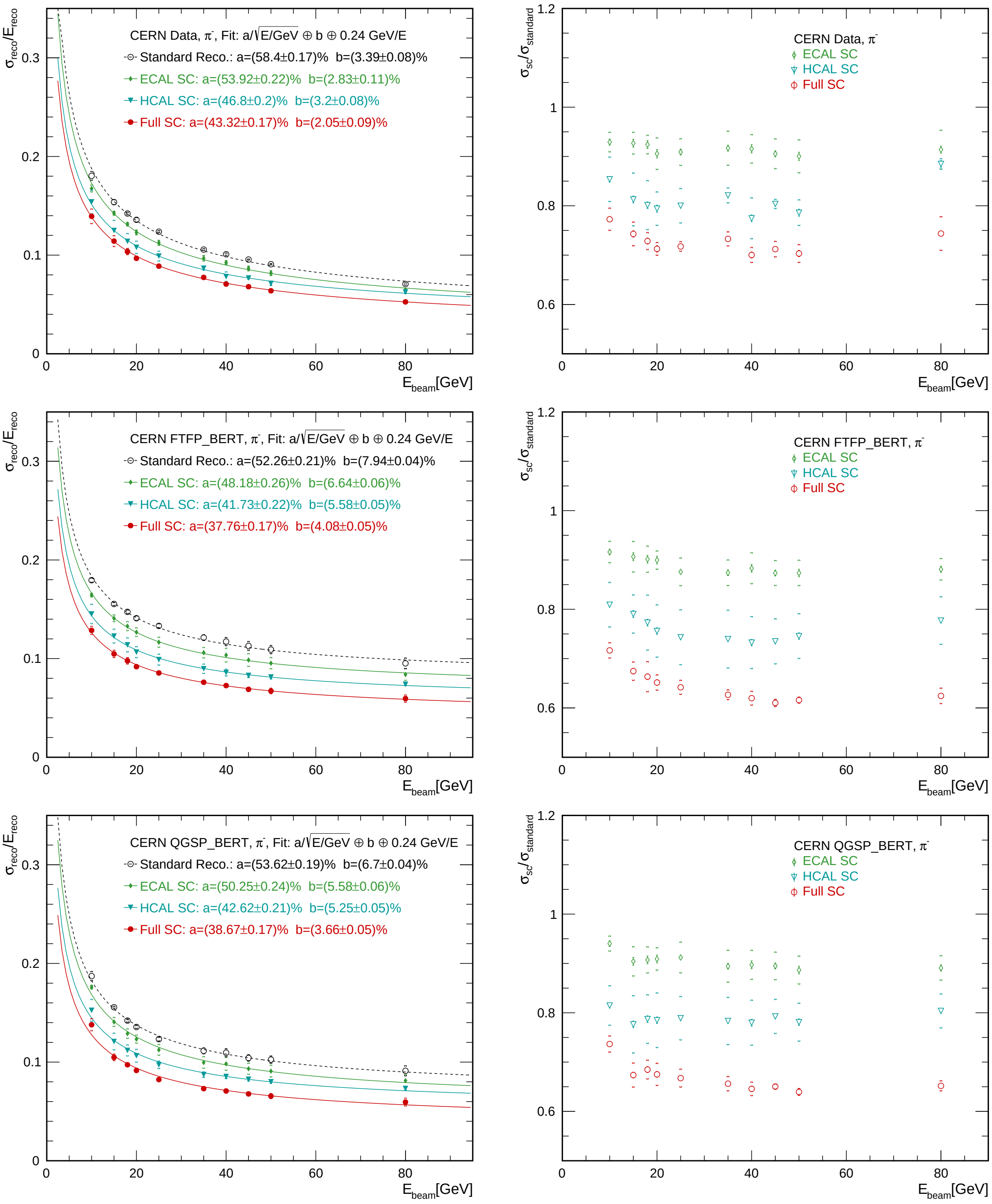

Figure D.19: Left: Fitted energy resolutions obtained from the standard, ECAL SC, HCAL SC and Full SC reconstruction of CERN dataset. The fit parameters are given in the legend. Right: The relative improvement in energy resolutions obtained from the SC reconstruction of CERN dataset. Upper panel: Results obtained from CERN data events. Middle panel: Results obtained from CERN FTFP_BERT events. Lower panel: Results obtained from CERN QGSP_BERT events. The total (statistical and systematic) uncertainties are marked with brackets, '[]'.

FNAL Dataset

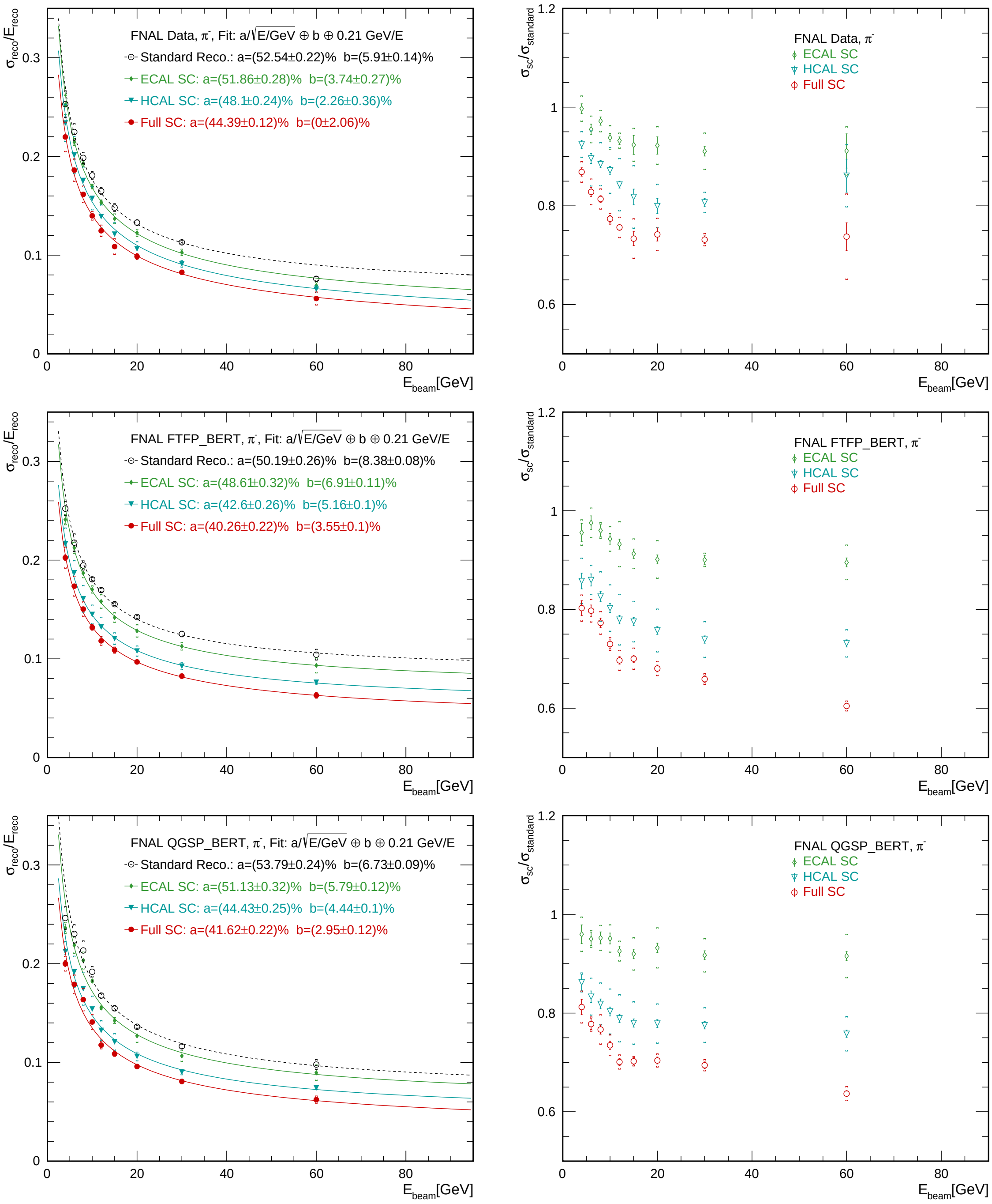

Figure D.20: Left: Fitted energy resolutions obtained from the standard, ECAL SC, HCAL SC and Full SC reconstruction of FNAL dataset. The fit parameters are given in the legend. Right: The relative improvement of energy resolutions obtained from the SC reconstruction of FNAL dataset. Upper panel: Results obtained from FNAL data events. Middle panel: Results obtained from FNAL FTFP_BERT events. Lower panel: Results obtained from FNAL QGSP_BERT events. The total (statistical and systematic) uncertainties are marked with brackets, '[]'.

Combined Dataset

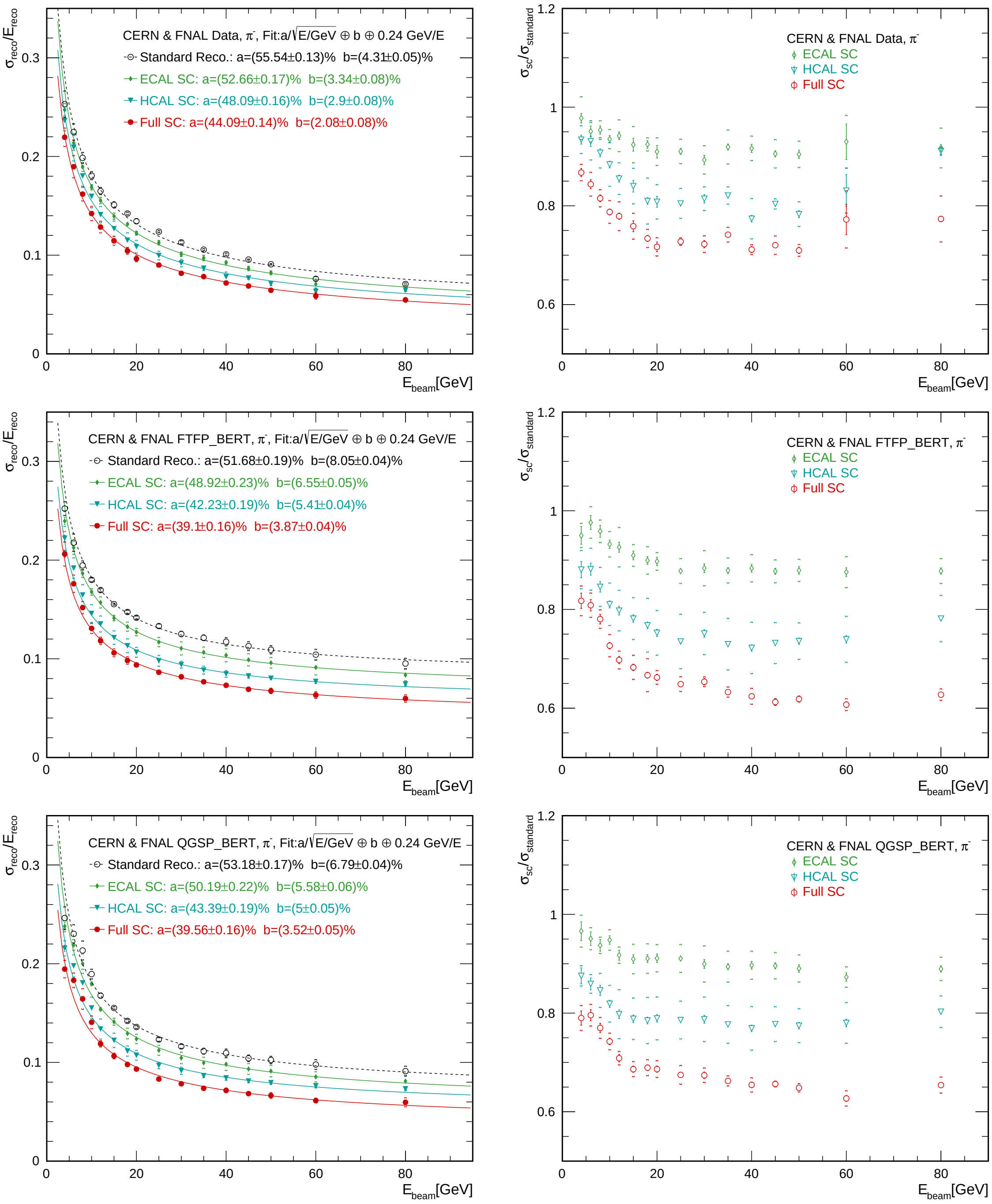

Figure D.21: Left: Fitted energy resolutions obtained from the standard, ECAL SC, HCAL SC and Full SC reconstruction of combined dataset. The fit parameters are given in the legend. Right: The relative improvement of energy resolutions obtained from the SC reconstruction of combined dataset. Upper panel: Results obtained from combineddata events. Middle panel: Results obtained from combined FTFP_BERT events. Lower panel: Results obtained from combined QGSP_BERT events. The total (statistical and systematic) uncertainties are marked with brackets, ’[]’.

D.5 Longitudinal Profiles

CERN dataset

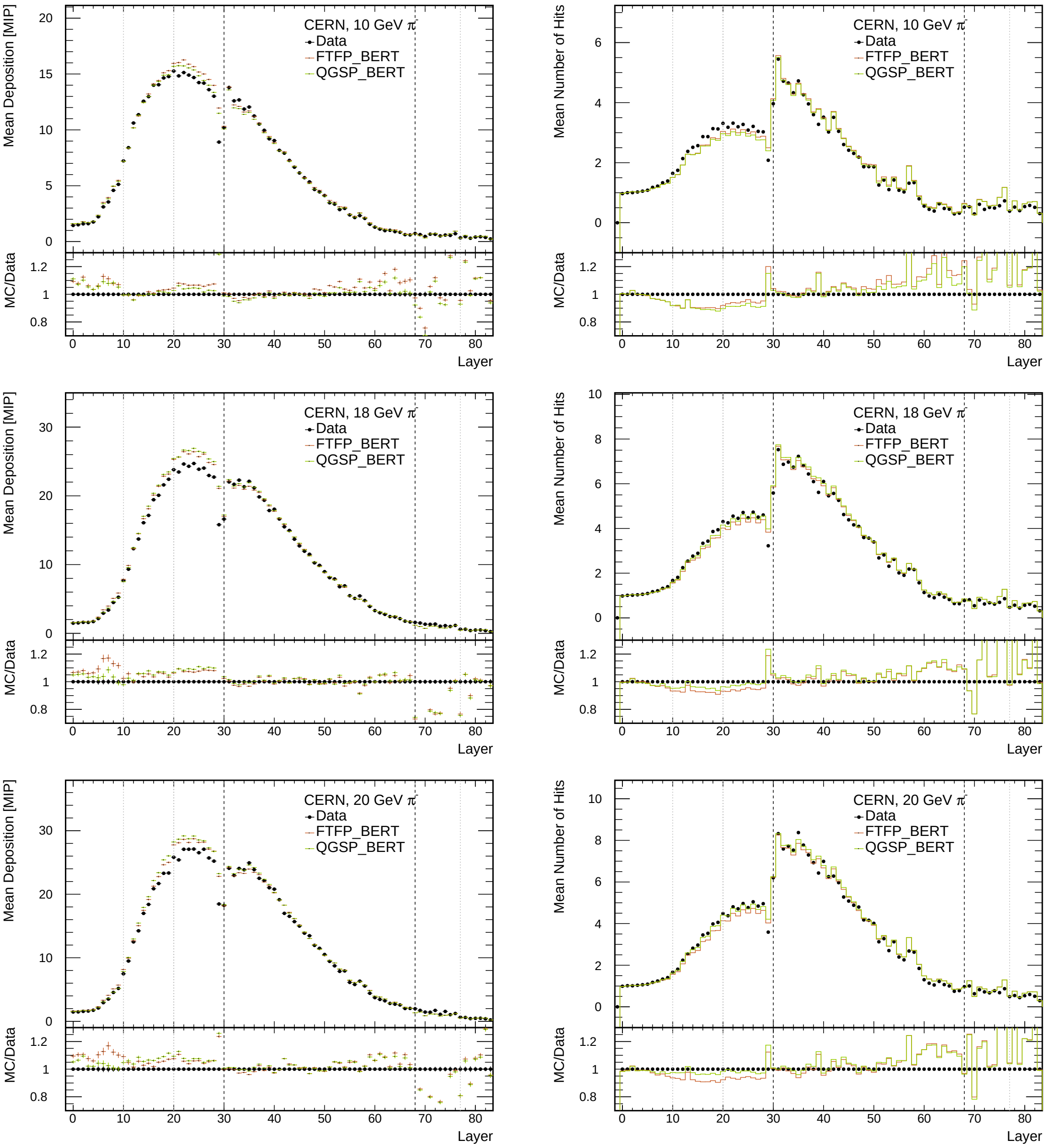

Figure D.22: Comparison of the layer-to-layer variation in CERN events (10 GeV, 18 GeV, 20 GeV). Left: The average mean deposition. Right: The average number of hits. Test beam data is marked with black points, the FTFP_BERT simulation is marked in red and the QGSP_BERT simulation is marked in green. Layers 0 – 29 are the Si-W ECAL layers; layers 30 – 67 are the AHCAL layers; layers 68 – 83 are the TCMT layers. The black dashed lines indicate transitions between the sub-detectors. The gray dotted lines indicate transition between absorber thicknesses.

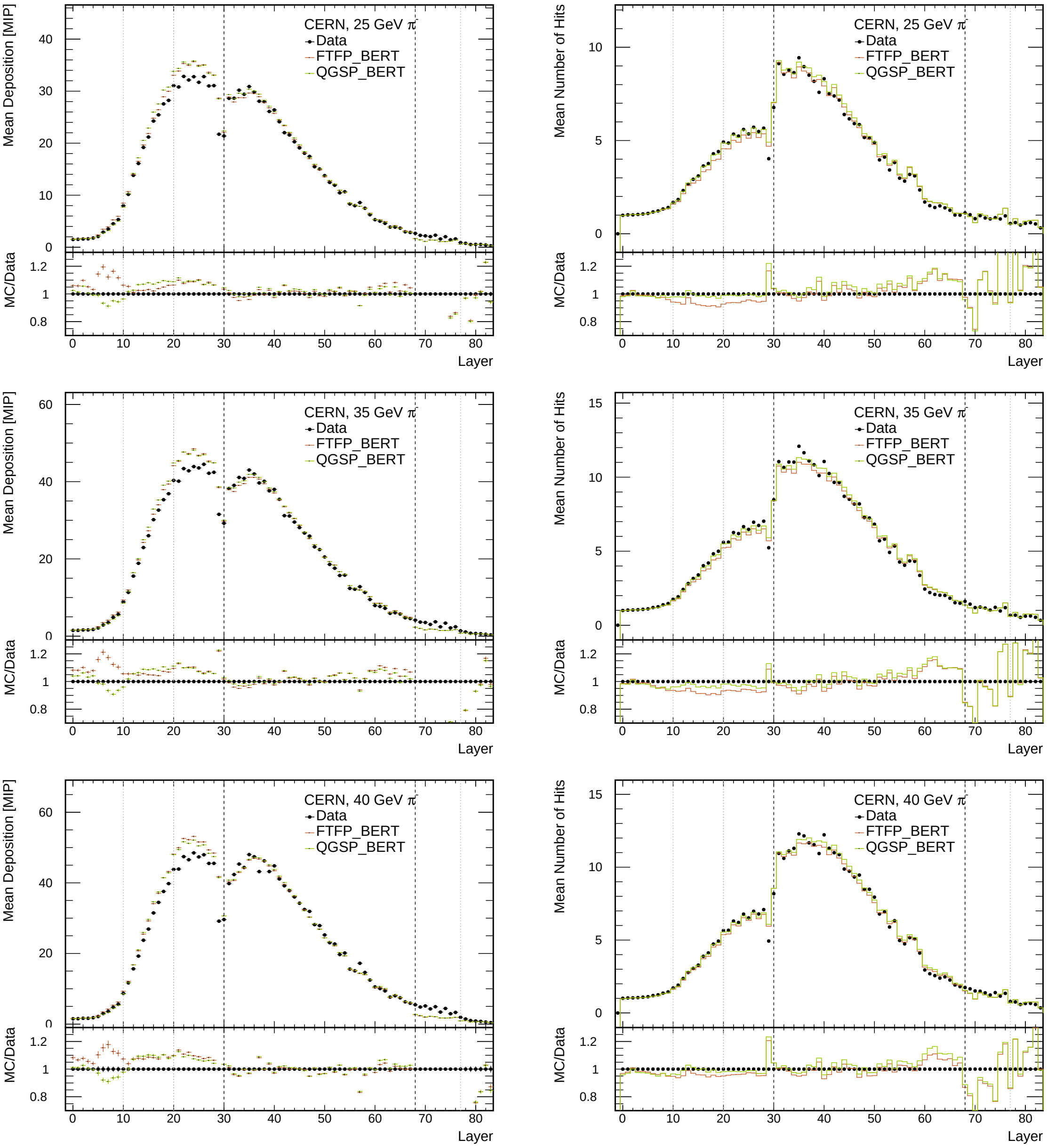

Figure D.23: Comparison of the layer-to-layer variation in CERN events (25 GeV, 35 GeV, 40 GeV). Left: The average mean deposition. Right: The average number of hits. Test beam data is marked with black points, the FTFP_BERT simulation is marked in red and the QGSP_BERT simulation is marked in green. Layers 0 – 29 are the Si-W ECAL layers; layers 30 – 67 are the AHCAL layers; layers 68 – 83 are the TCMT layers. The black dashed lines indicate transitions between the sub-detectors. The gray dotted lines indicate transition between absorber thicknesses.

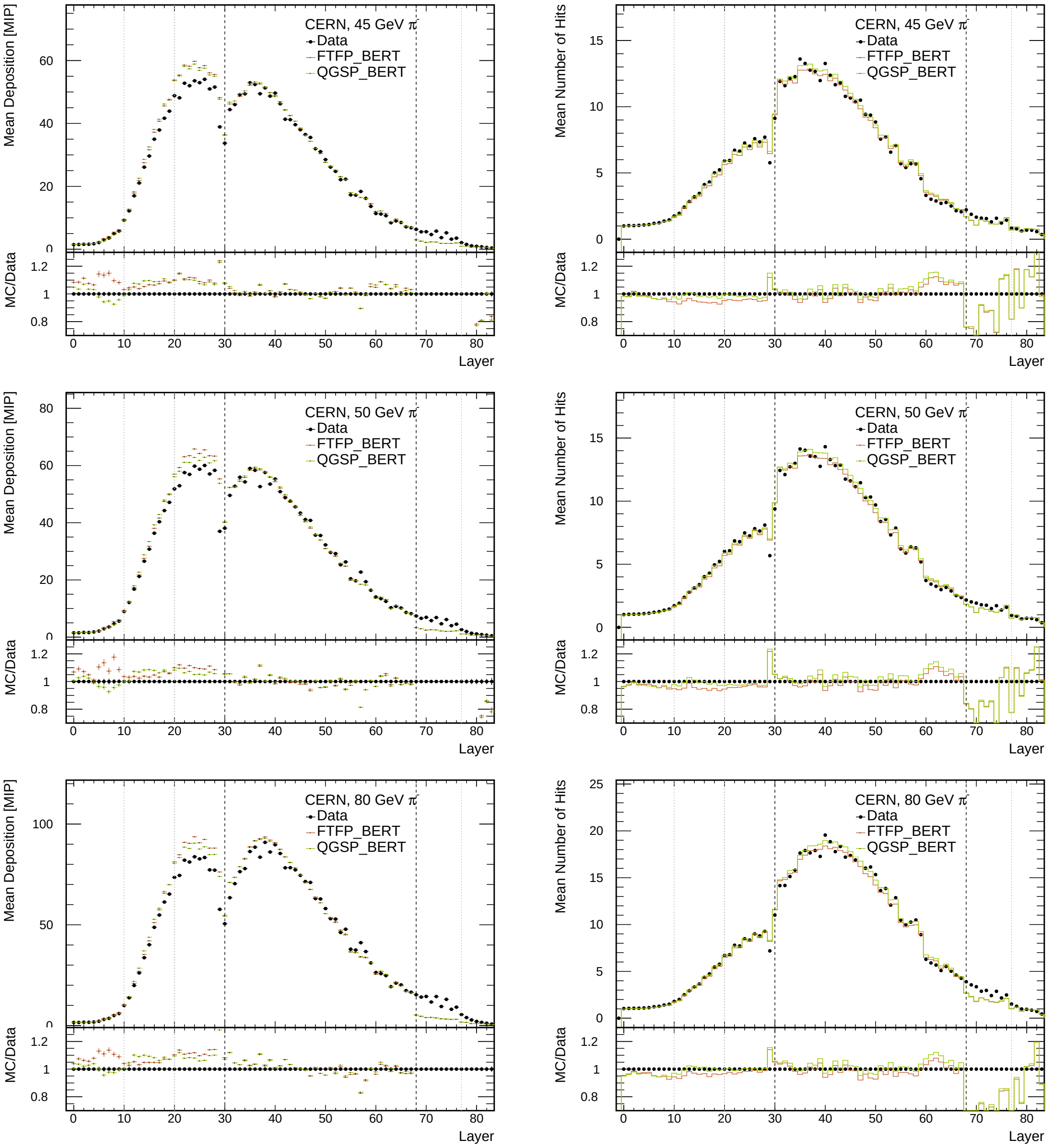

Figure D.24: Comparison of the layer-to-layer variation in CERN events (45 GeV, 50 GeV, 80 GeV). Left: The average mean deposition. Right: The average number of hits. Test beam data is marked with black points, the FTFP_BERT simulation is marked in red and the QGSP_BERT simulation is marked in green. Layers 0 – 29 are the Si-W ECAL layers; layers 30 – 67 are the AHCAL layers; layers 68 – 83 are the TCMT layers. The black dashed lines indicate transitions between the sub-detectors. The gray dotted lines indicate transition between absorber thicknesses.

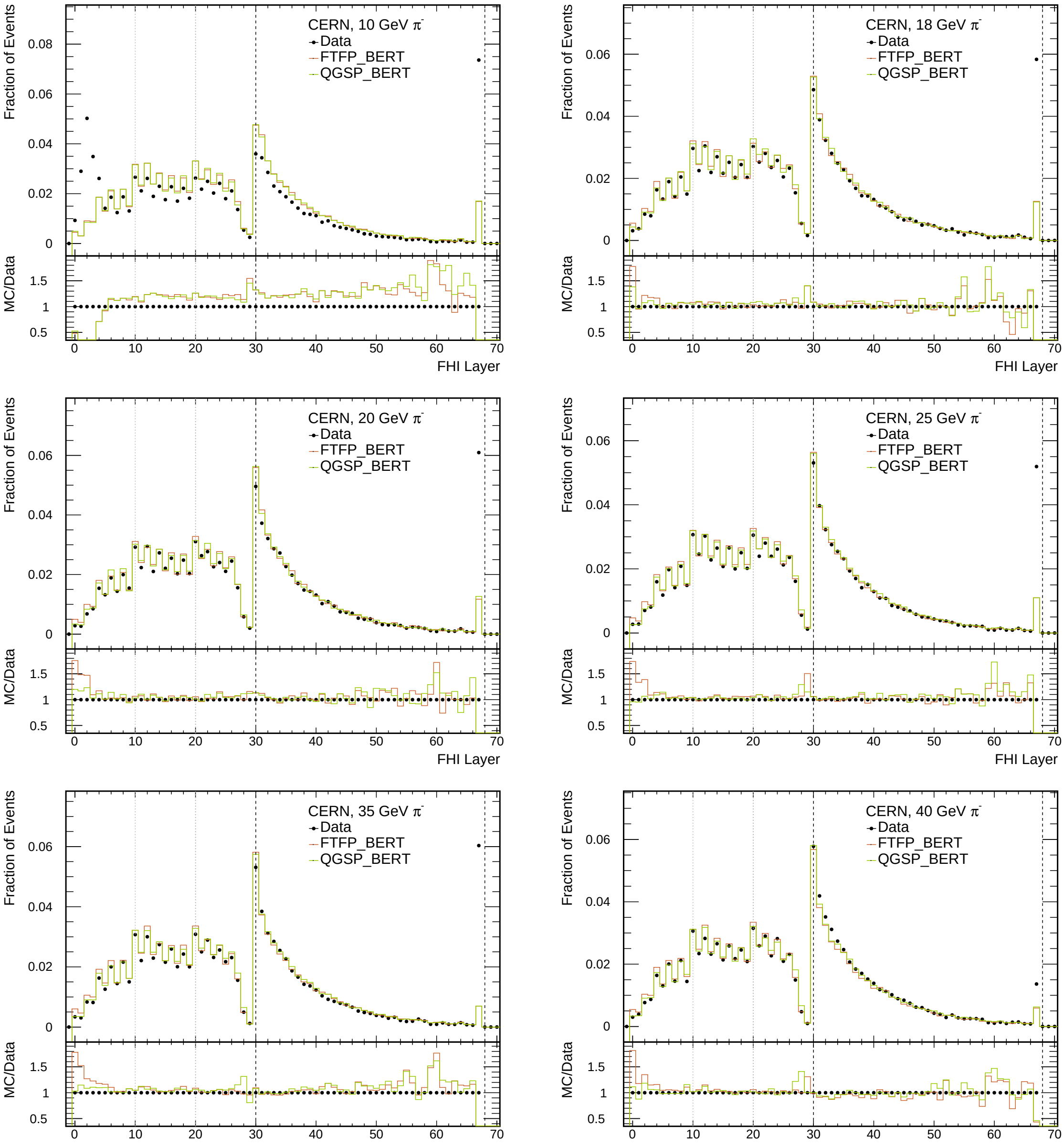

Figure D.25: Comparison of the layer-to-layer variation of the reconstructed FHI layer in CERN events (10 GeV, 18 GeV, 20 GeV, 25 GeV, 35 GeV). Test beam data is marked with black points, the FTFP_BERT simulation is marked in red and the QGSP_BERT simulation is marked in green. Layers 0 – 29 are the Si-W ECAL layers; layers 30 – 67 are the AHCAL layers; layers 68 – 83 are the TCMT layers. The black dashed lines indicate transitions between the sub-detectors. The gray dotted lines indicate transition between absorber thicknesses.

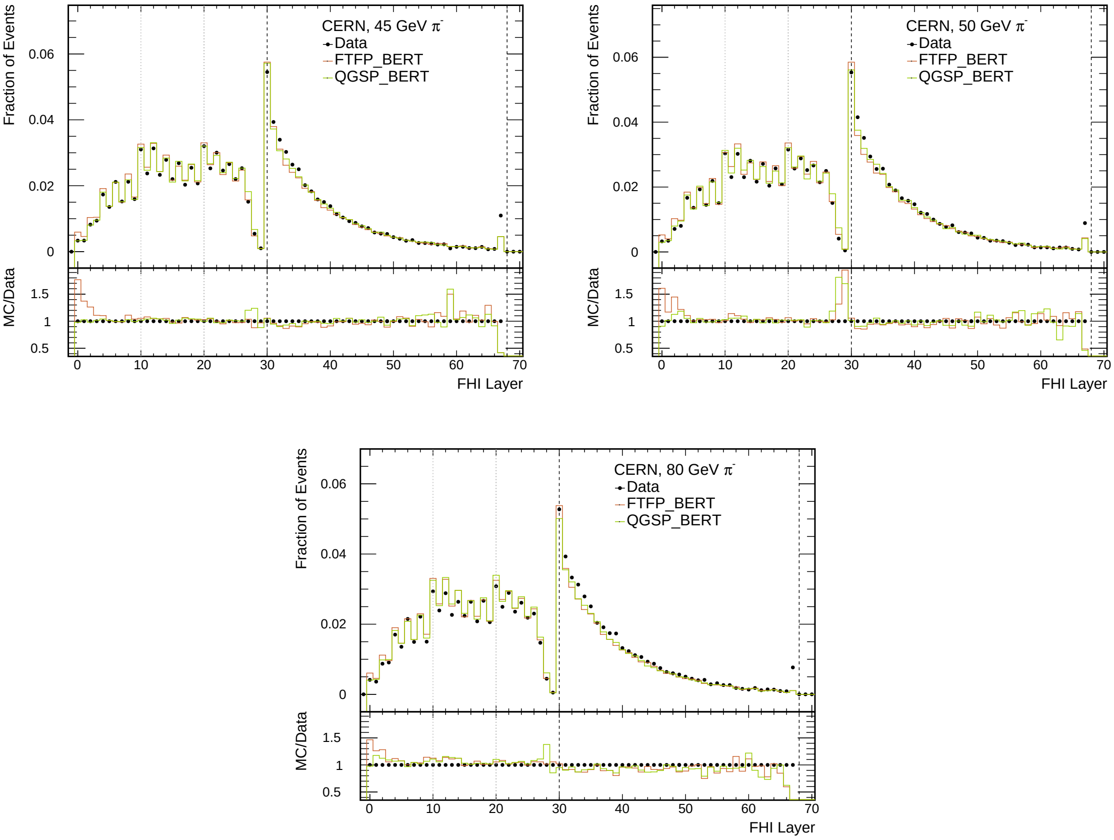

Figure D.26: Comparison of the layer-to-layer variation of the reconstructed FHI layer in CERN events (45 GeV, 50 GeV, 80 GeV). Test beam data is marked with black points, the FTFP_BERT simulation is marked in red and the QGSP_BERT simulation is marked in green. Layers 0 – 29 are the Si-W ECAL layers; layers 30 – 67 are the AHCAL layers; layers 68 – 83 are the TCMT layers. The black dashed lines indicate transitions between the sub-detectors. The gray dotted lines indicate transition between absorber thicknesses.

FNAL dataset

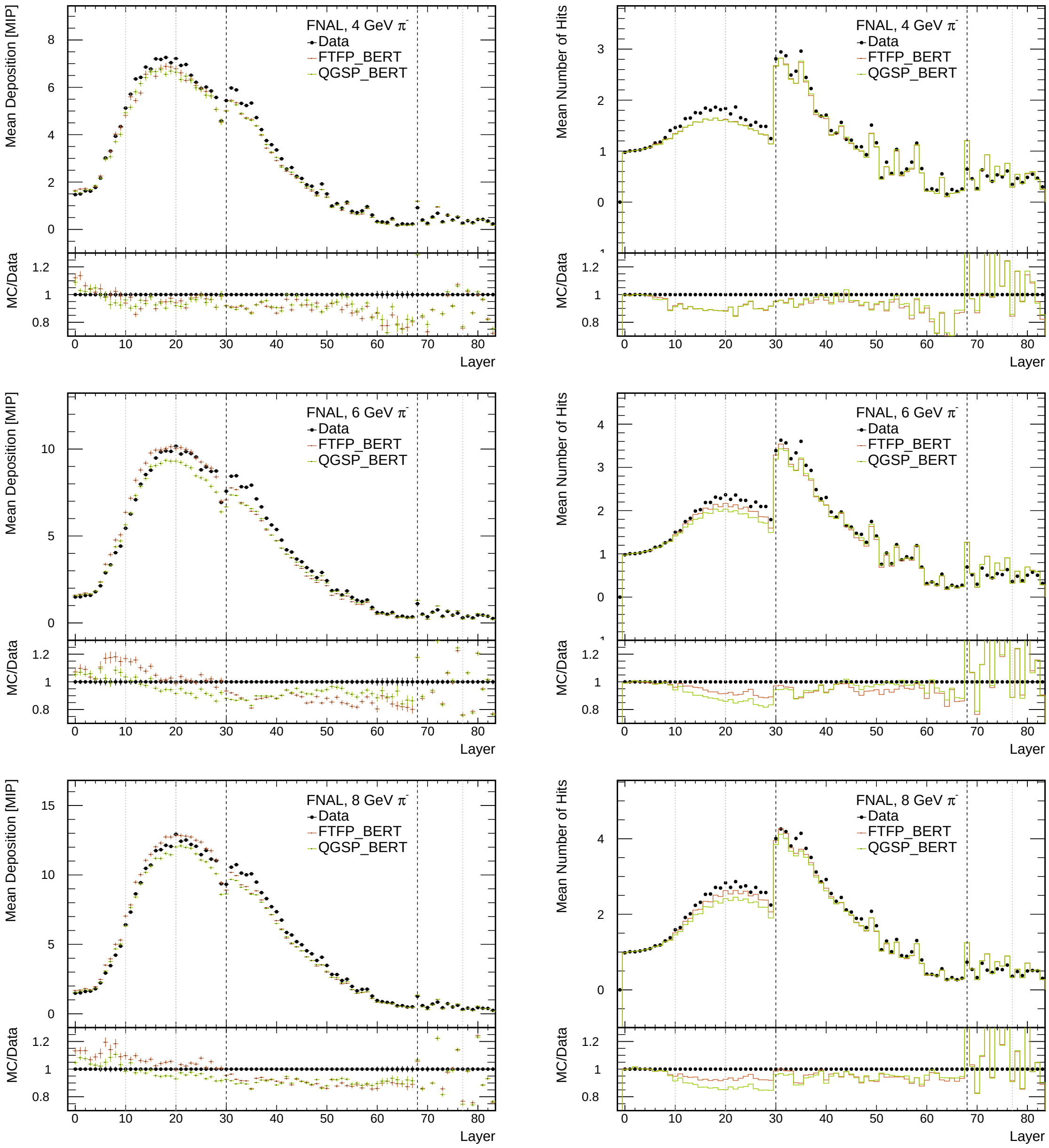

Figure D.27: Comparison of the layer-to-layer variation in FNAL events (4 GeV, 6 GeV, 8 GeV). Left: The average mean deposition. Right: The average number of hits. Test beam data is marked with black points, the FTFP_BERT simulation is marked in red and the QGSP_BERT simulation is marked in green. Layers 0 – 29 are the Si-W ECAL layers; layers 30 – 67 are the AHCAL layers; layers 68 – 83 are the TCMT layers. The black dashed lines indicate transitions between the sub-detectors. The gray dotted lines indicate transition between absorber thicknesses.

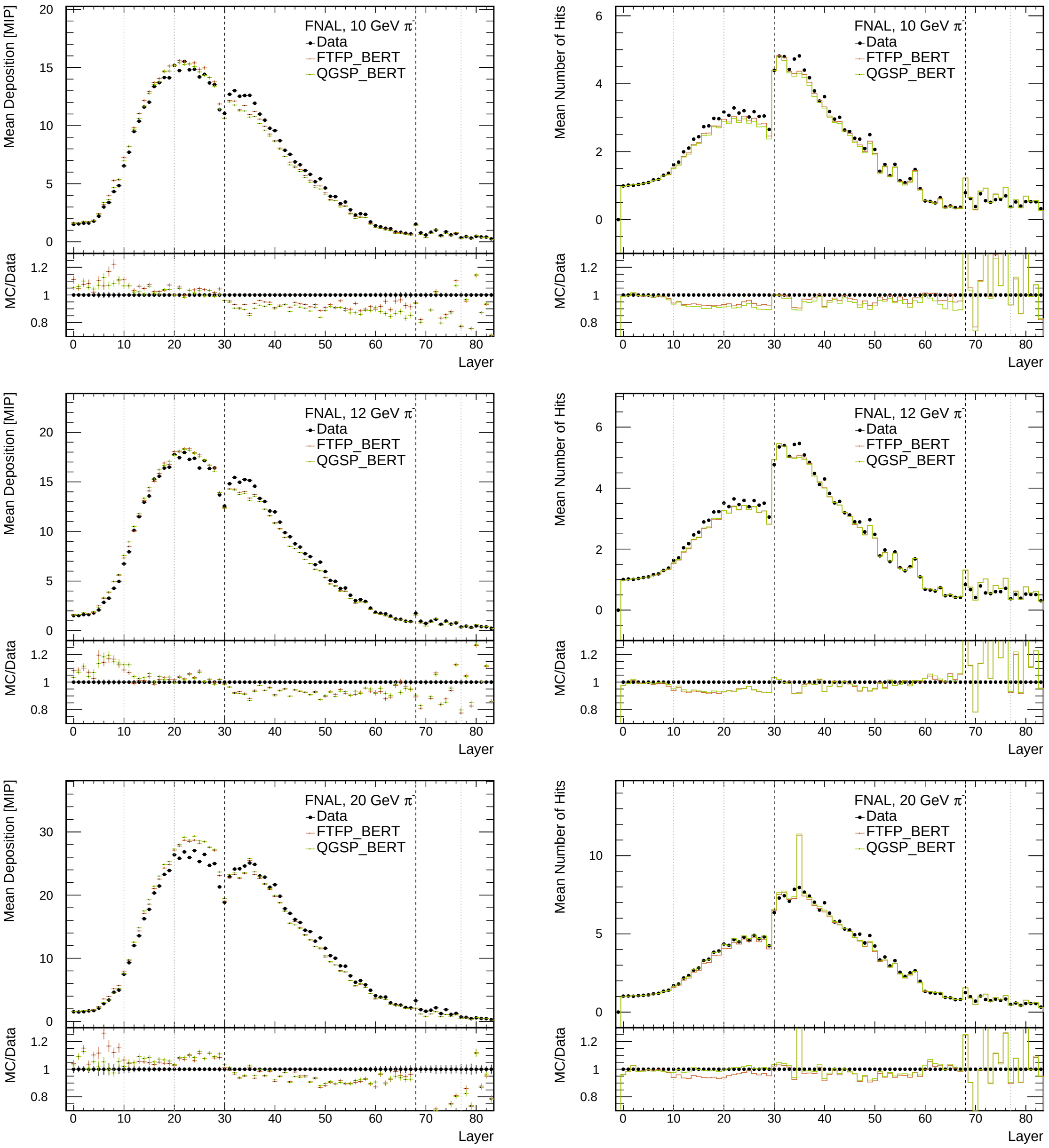

Figure D.28: Comparison of the layer-to-layer variation in FNAL events (10 GeV, 12 GeV, 20 GeV). Left: The average mean deposition. Right: The average number of hits. Test beam data is marked with black points, the FTFP_BERT simulation is marked in red and the QGSP_BERT simulation is marked in green. Layers 0 – 29 are the Si-W ECAL layers; layers 30 – 67 are the AHCAL layers; layers 68 – 83 are the TCMT layers. The black dashed lines indicate transitions between the sub-detectors. The gray dotted lines indicate transition between absorber thicknesses.

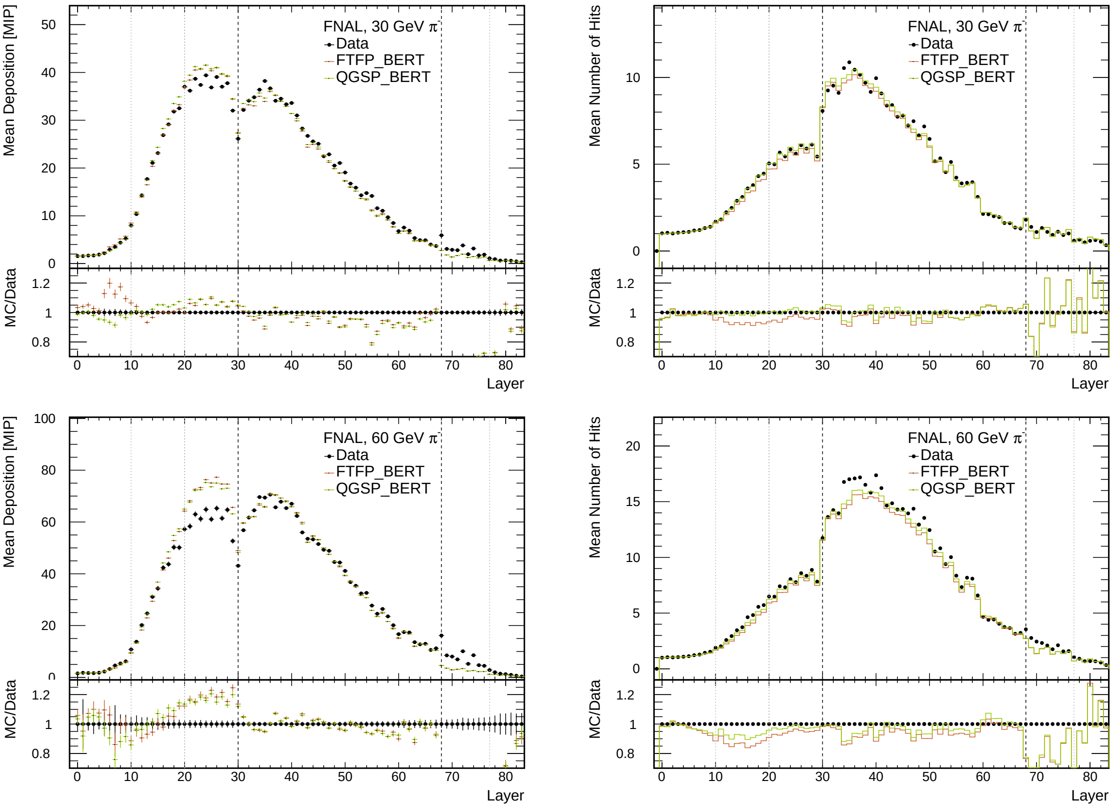

Figure D.29: Comparison of the layer-to-layer variation in FNAL events (30 GeV, 60 GeV). Left: The average mean deposition. Right: The average number of hits. Test beam data is marked with black points, the FTFP_BERT simulation is marked in red and the QGSP_BERT simulation is marked in green. Layers 0 – 29 are the Si-W ECAL layers; layers 30 – 67 are the AHCAL layers; layers 68 – 83 are the TCMT layers. The black dashed lines indicate transitions between the sub-detectors. The gray dotted lines indicate transition between absorber thicknesses.

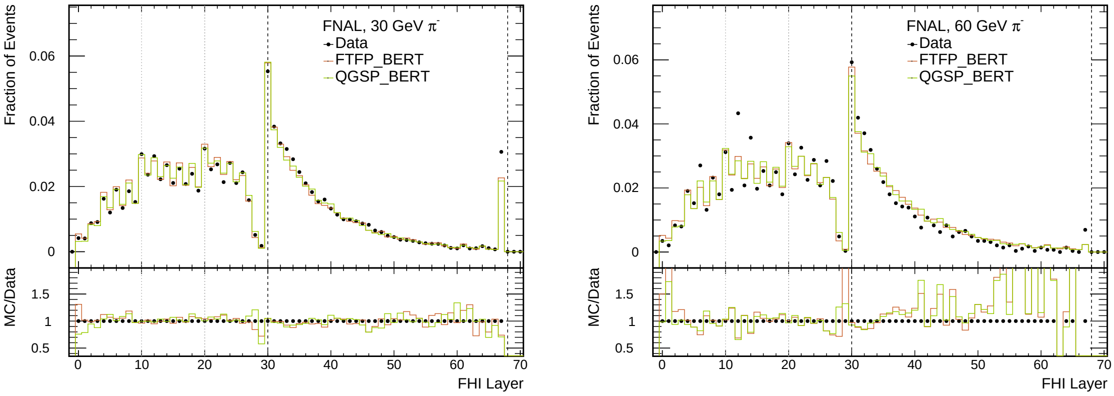

Figure D.30: Comparison of the layer-to-layer variation of the reconstructed FHI layer in FNAL events (30 GeV, 60 GeV). Test beam data is marked with black points, the FTFP_BERT simulation is marked in red and the QGSP_BERT simulation is marked in green. Layers 0 – 29 are the Si-W ECAL layers; layers 30 – 67 are the AHCAL layers; layers 68 – 83 are the TCMT layers. The black dashed lines indicate transitions between the sub-detectors. The gray dotted lines indicate transition between absorber thicknesses.

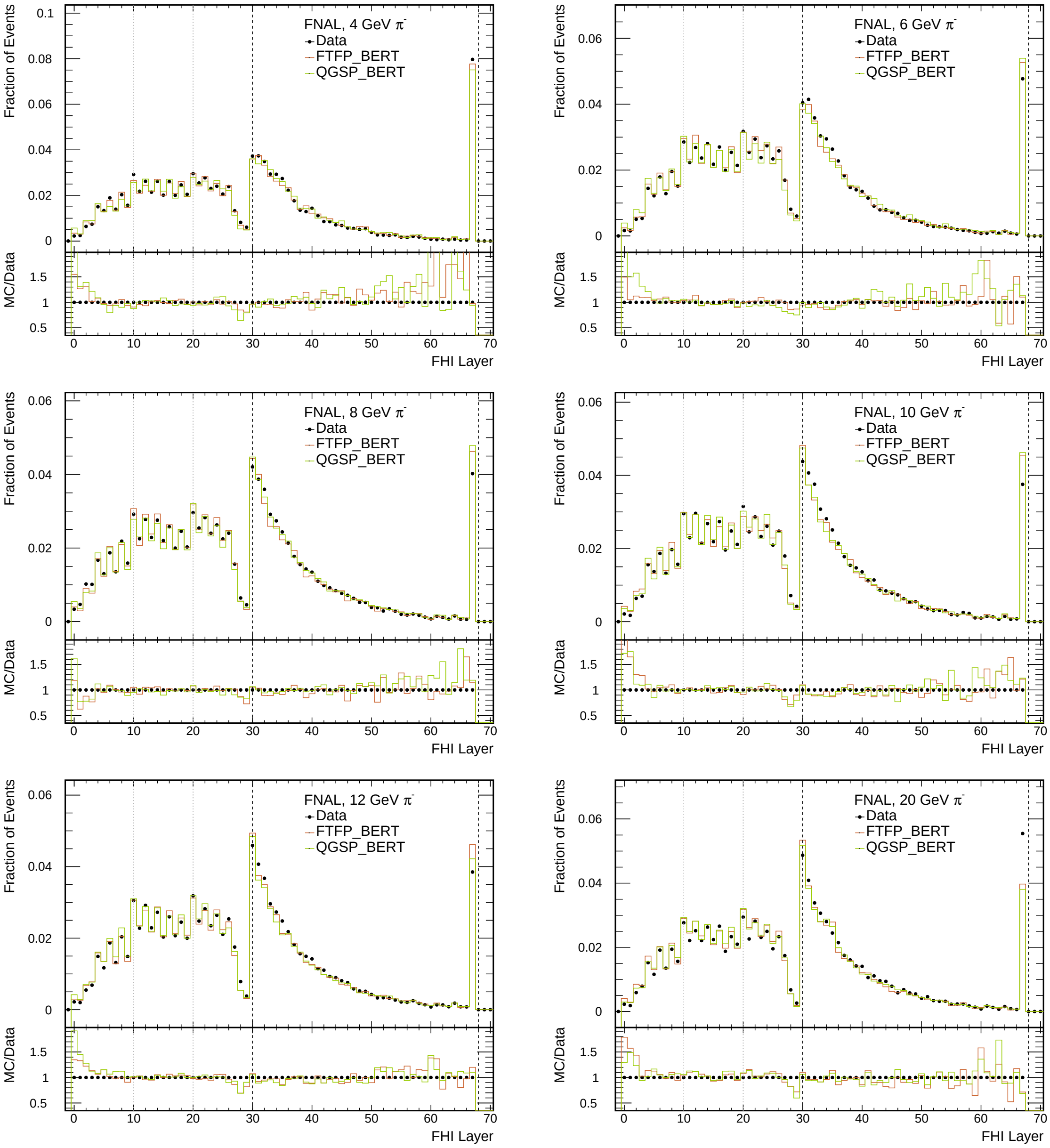

Figure D.31: Comparison of the layer-to-layer variation of the reconstructed FHI layer in FNAL events (4 GeV, 6 GeV, 8 GeV, 10 GeV, 12 GeV, 20 GeV). Test beam data is marked with black points, the FTFP_BERT simulation is marked in red and the QGSP_BERT simulation is marked in green. Layers 0 – 29 are the Si-W ECAL layers; layers 30 – 67 are the AHCAL layers; layers 68 – 83 are the TCMT layers. The black dashed lines indicate transitions between the sub-detectors. The gray dotted lines indicate transition between absorber thicknesses.

D.6 Comparison of Data and Simulation Results

D.6.1 Software Compensation Weights

CERN dataset

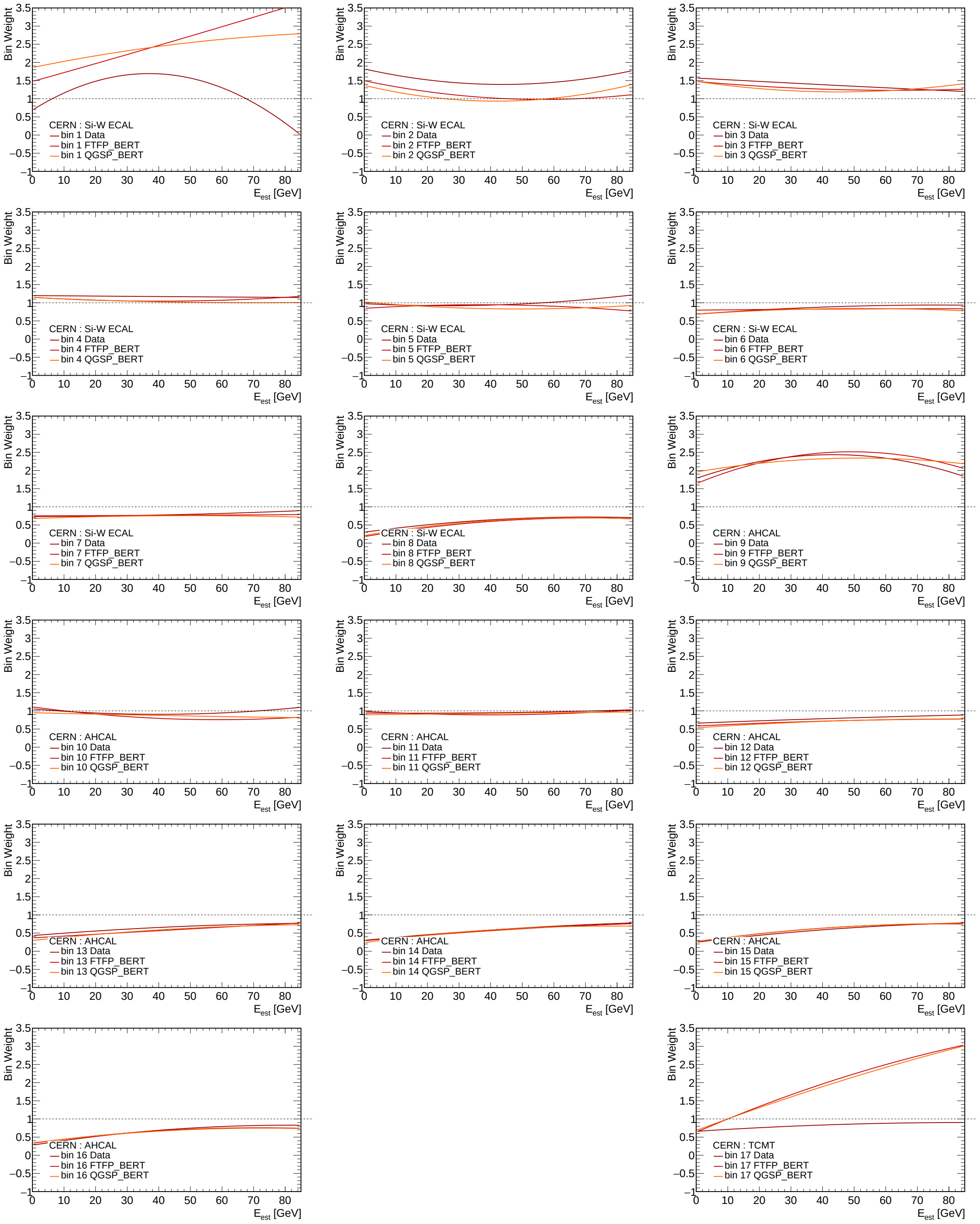

Figure D.32: The bin weights optimized with CERN data and simulations for the Full SC method as a function of the beam energy. The bins are numbered as follows: bins 1 – 8 are the Si-W ECAL bins, bins 9 – 16 are the AHCAL bins and bin 17 is the TCMT bin.

FNAL dataset

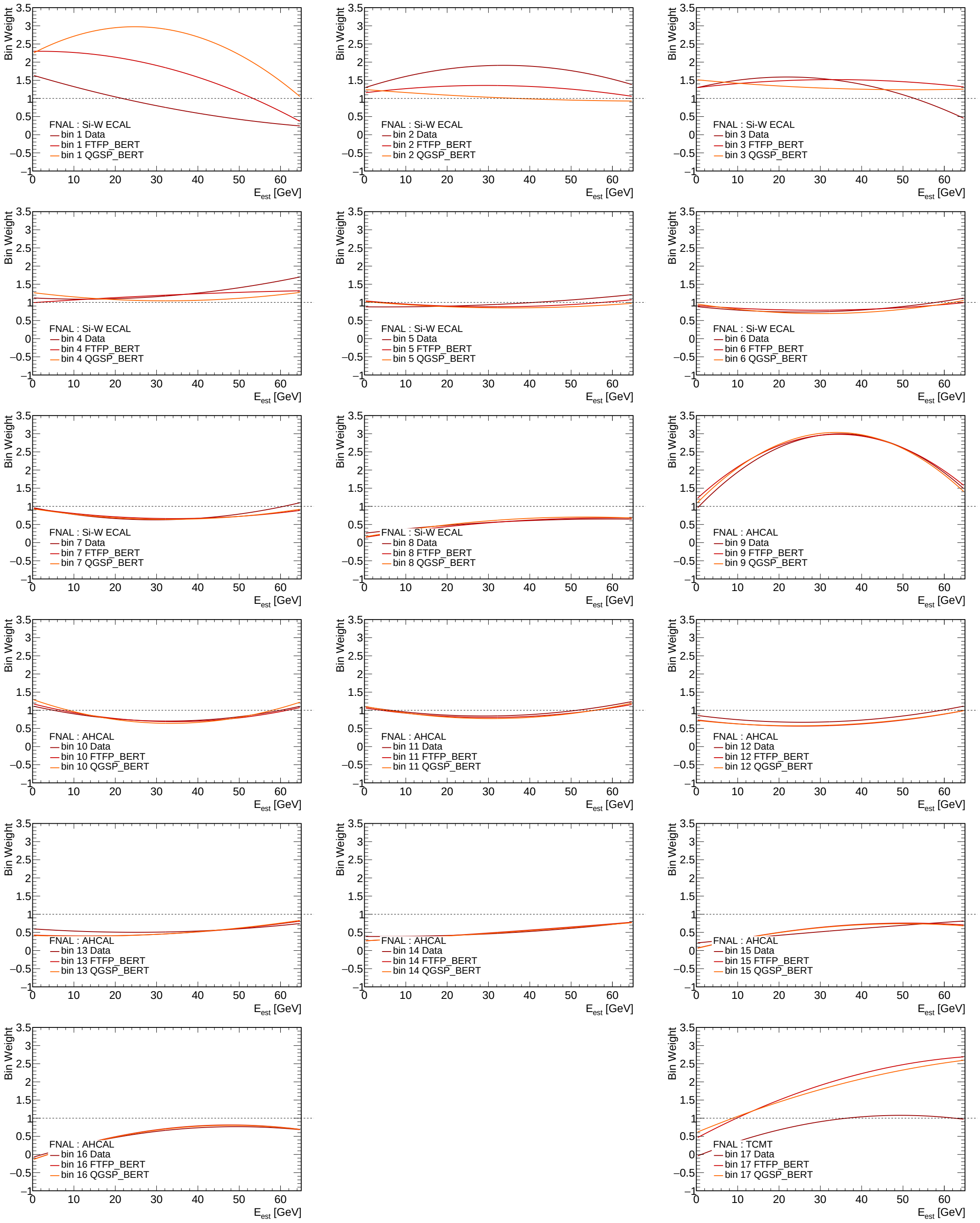

Figure D.33: The bin weights optimized with FNAL data and simulations for the Full SC method as a function of the beam energy. The bins are numbered as follows: bins 1 – 8 are the Si-W ECAL bins, bins 9 – 16 are the AHCAL bins and bin 17 is the TCMT bin.

Combined Dataset

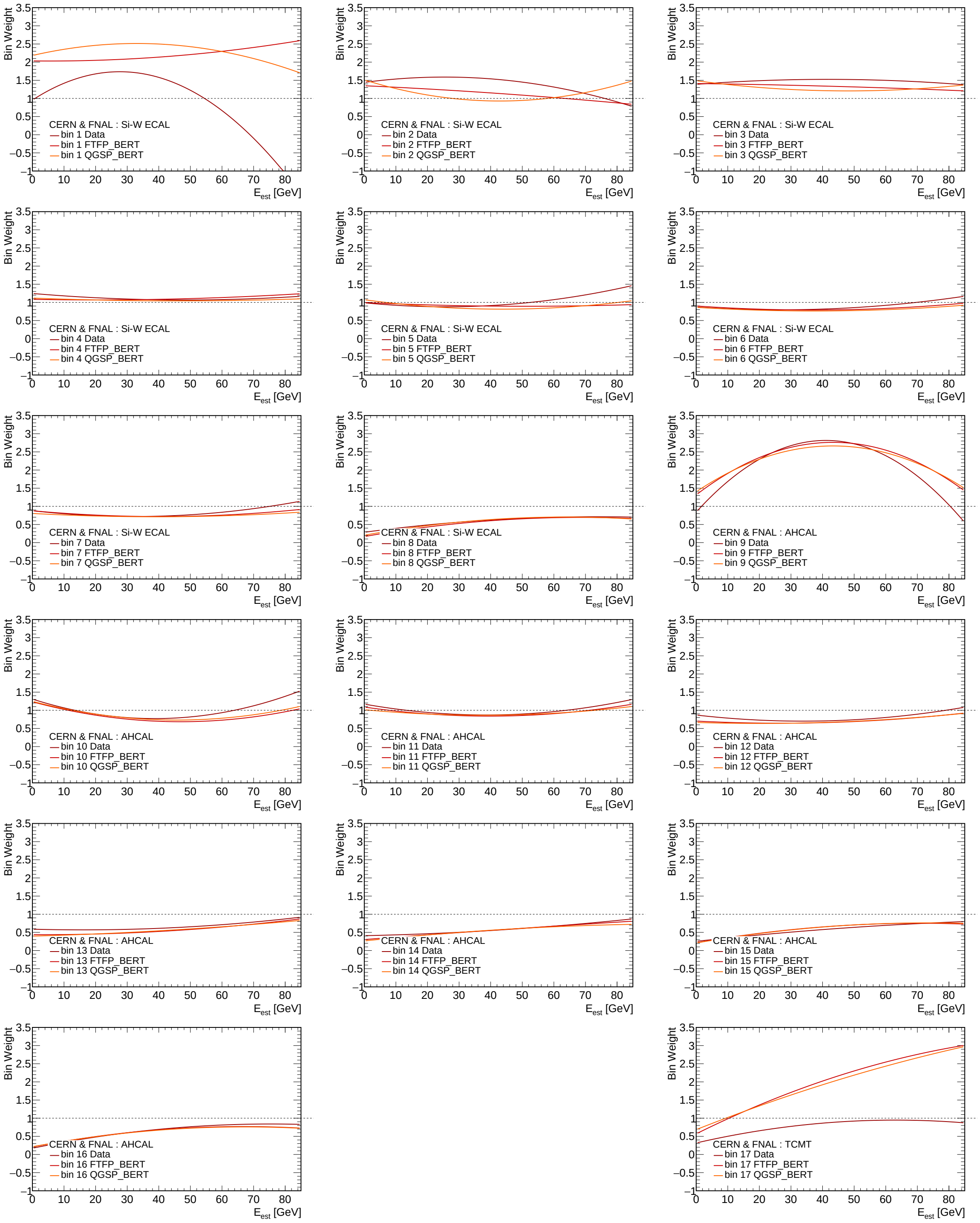

Figure D.34: The bin weights optimized with the combined (CERN+ FNAL) data and simulations for the Full SC method as a function of the beam energy. The bins are numbered as follows: bins 1 – 8 are the Si-W ECAL bins, bins 9 – 16 are the AHCAL bins and bin 17 is the TCMT bin.

D.6.2 Reconstructed Energies

CERN Dataset

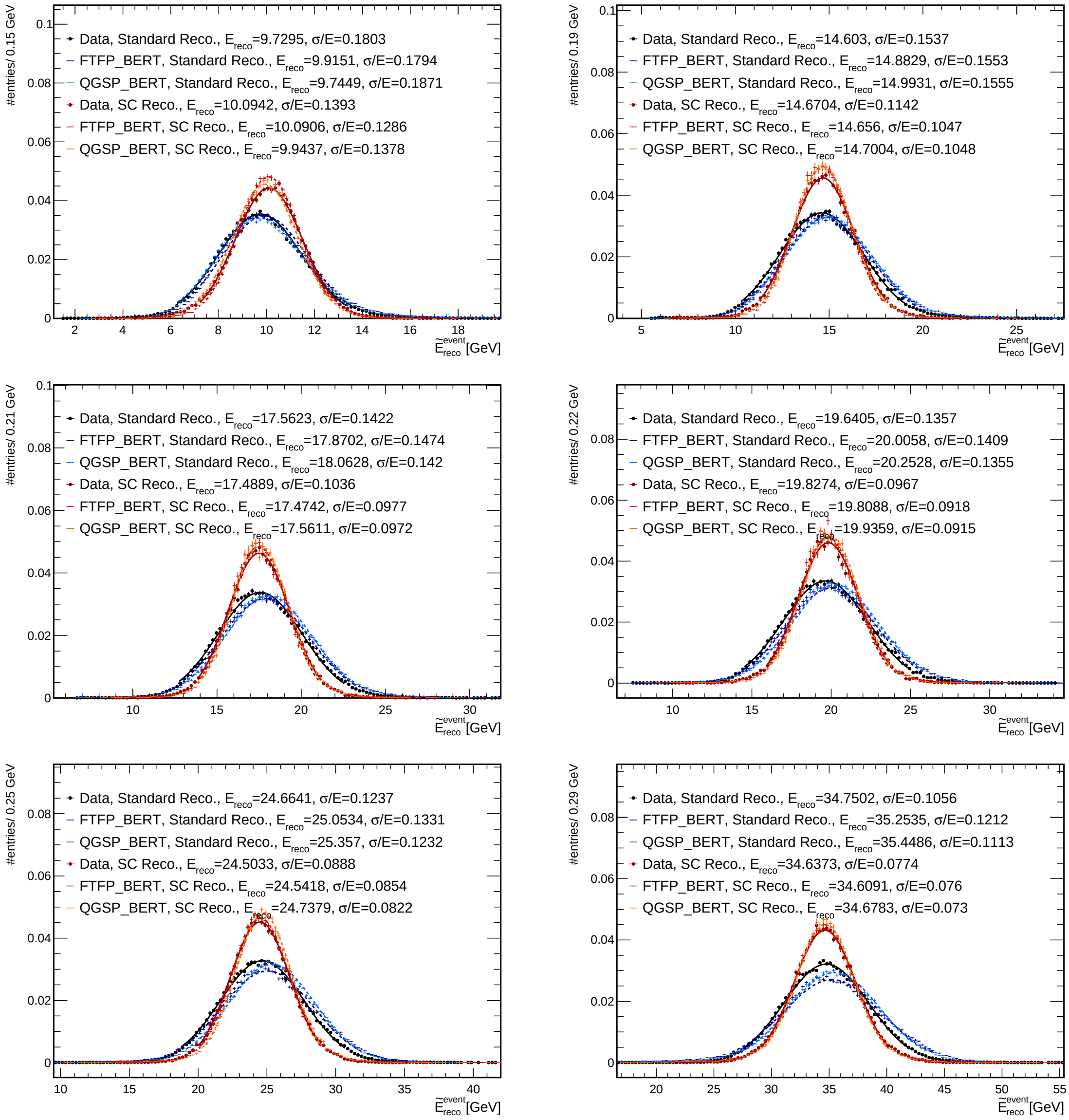

Figure D.35: The distributions of reconstructed energies of CERN data and simulations (10 GeV, 15 GeV, 18 GeV, 20 GeV, 25 GeV, 35 GeV) obtained from the standard and the Full SC methods. The mean energy, E_{reco}, and the energy resolution, σ/E, of each distribution (obtained from the two-step Gaussian fit) are detailed in the legend.

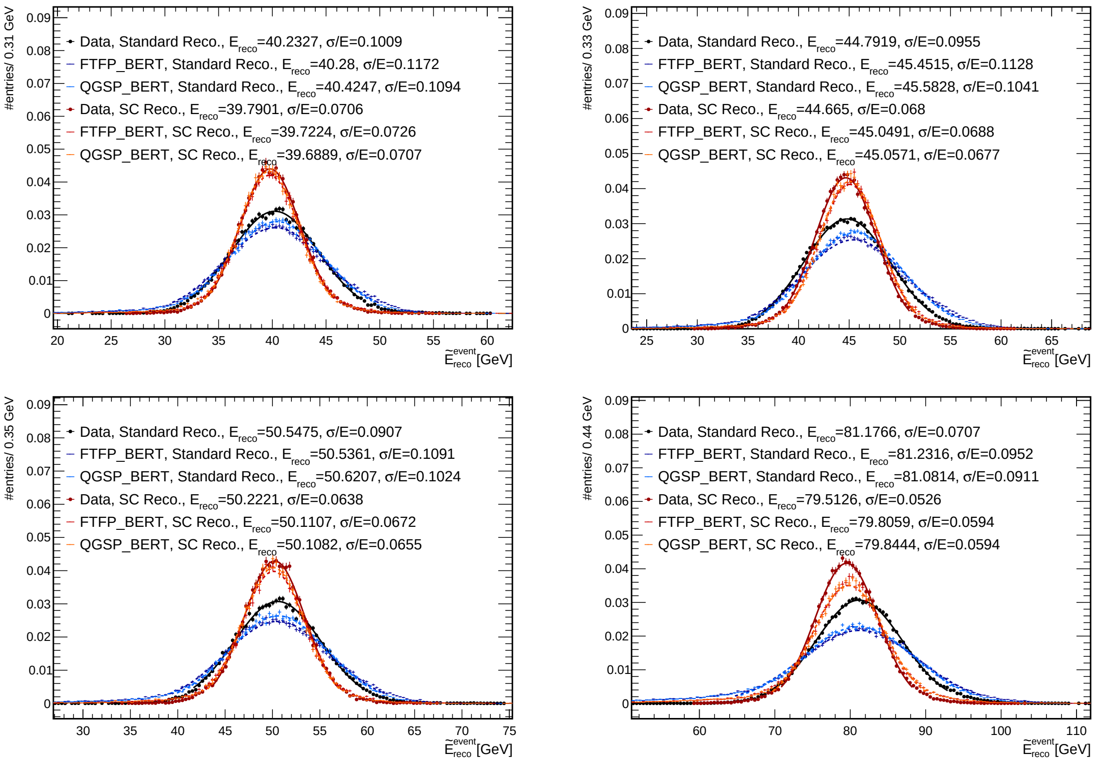

Figure D.36: The distributions of reconstructed energies of CERN data and simulations (40 GeV, 45 GeV, 50 GeV, 80 GeV) obtained from the standard and the Full SC methods. The mean energy, E_{reco}, and the energy resolution, σ/E, of each distribution (obtained from the two-step Gaussian fit) are detailed in the legend.

FNAL Dataset

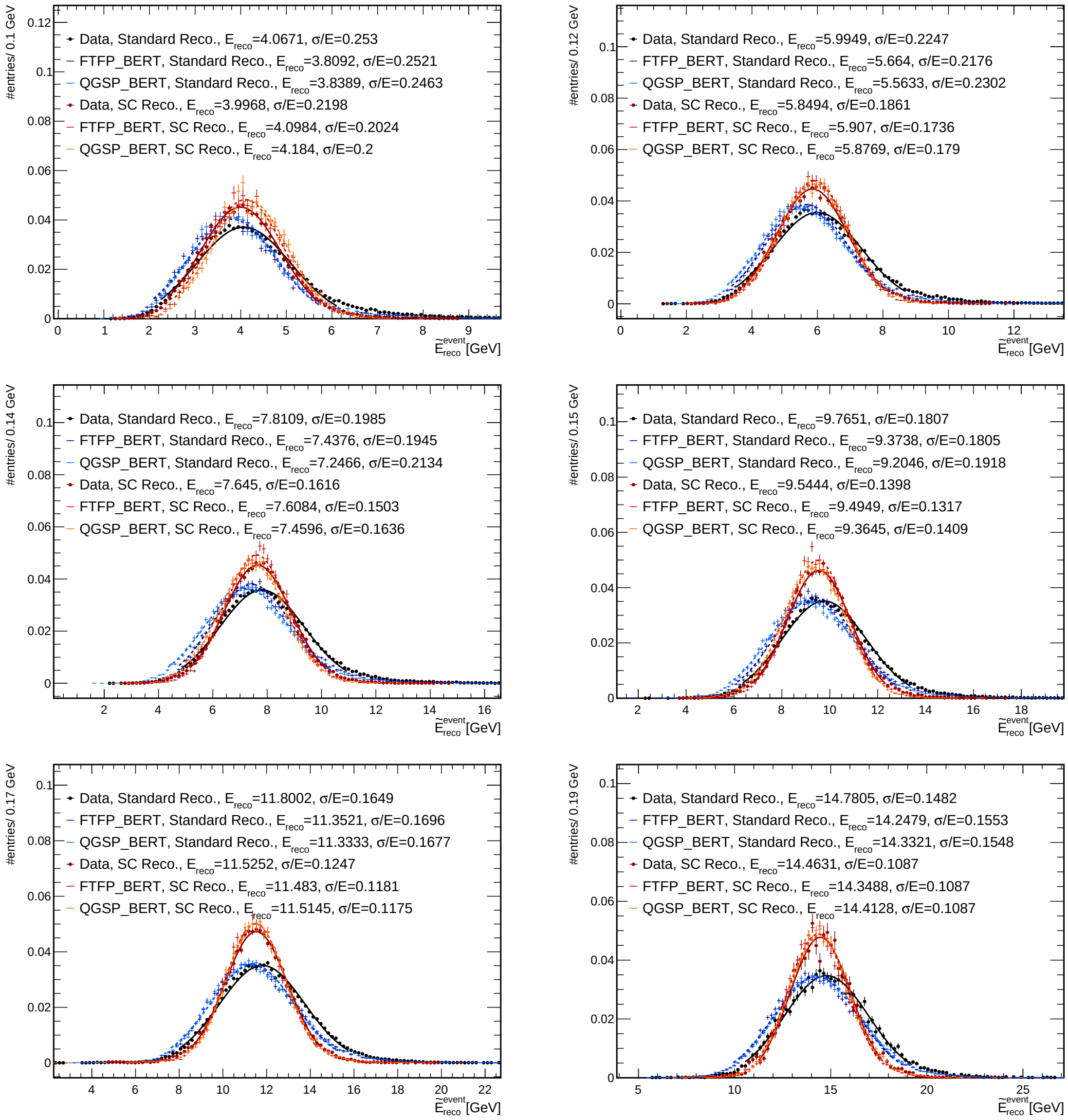

Figure D.37: The distributions of reconstructed energies of FNAL data and simulations (4 GeV, 6 GeV, 8 GeV, 10 GeV, 12 GeV, 15 GeV) obtained from the standard and the Full SC methods. The mean energy, E_{reco}, and the energy resolution, σ/E, of each distribution (obtained from the two-step Gaussian fit) are detailed in the legend.

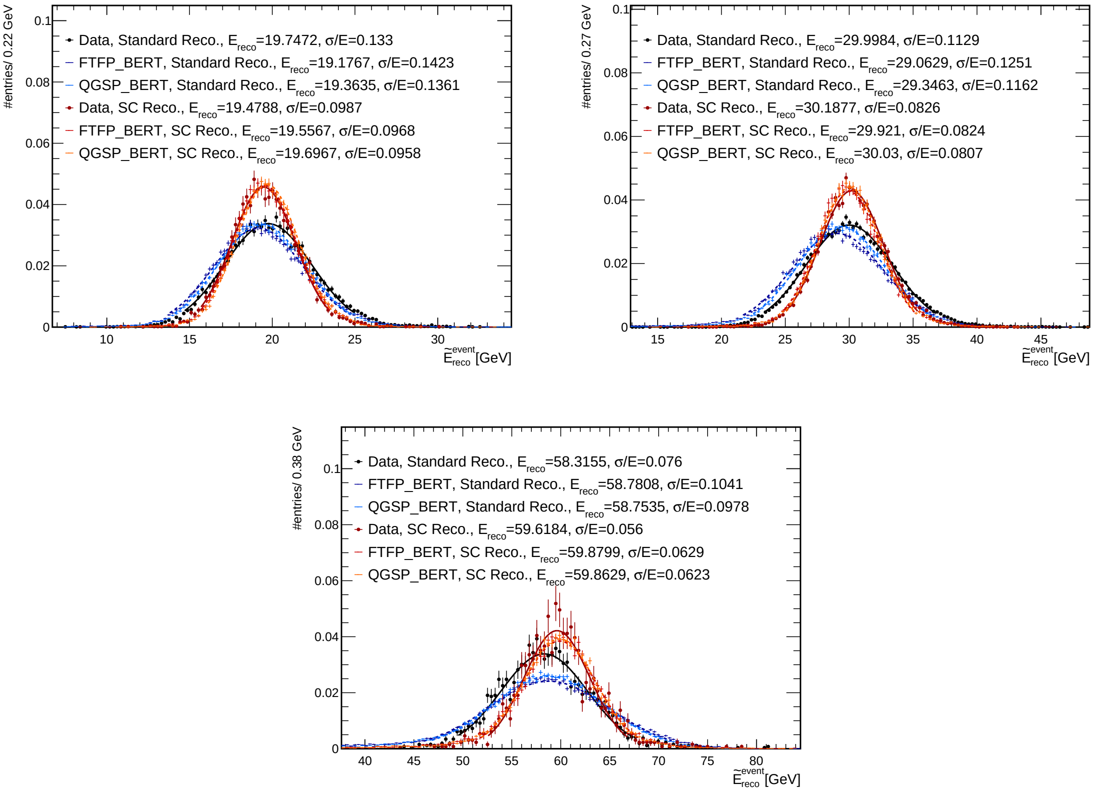

Figure D.38: The distributions of reconstructed energies of FNAL data and simulations (20 GeV, 30 GeV, 60 GeV) obtained from the standard and the Full SC methods. The mean energy, E_{reco}, and the energy resolution, σ/E, of each distribution (obtained from the two-step Gaussian fit) are detailed in the legend.

D.6.3 Linearity

CERN dataset

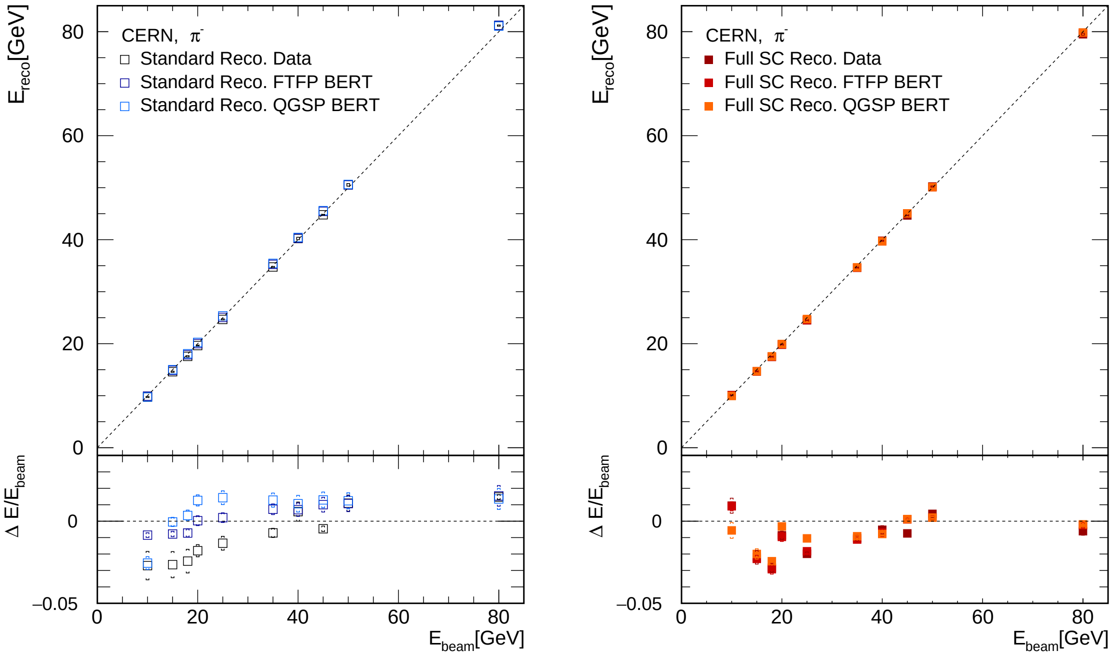

(a) Standart Reconstruction

(b) Full SC reconstruction

Figure D.39: The mean reconstructed energy and the relative residual to the beam energy versus the beam energy of CERN test beam data and simulations. (a) The standard reconstruction results. (b) The Full SC reconstruction results. The total (statistical and systematic) uncertainties are marked with brackets, ’[]’. Dotted lines correspond to $E_{reco} = E_{beam}$.

FNAL Dataset

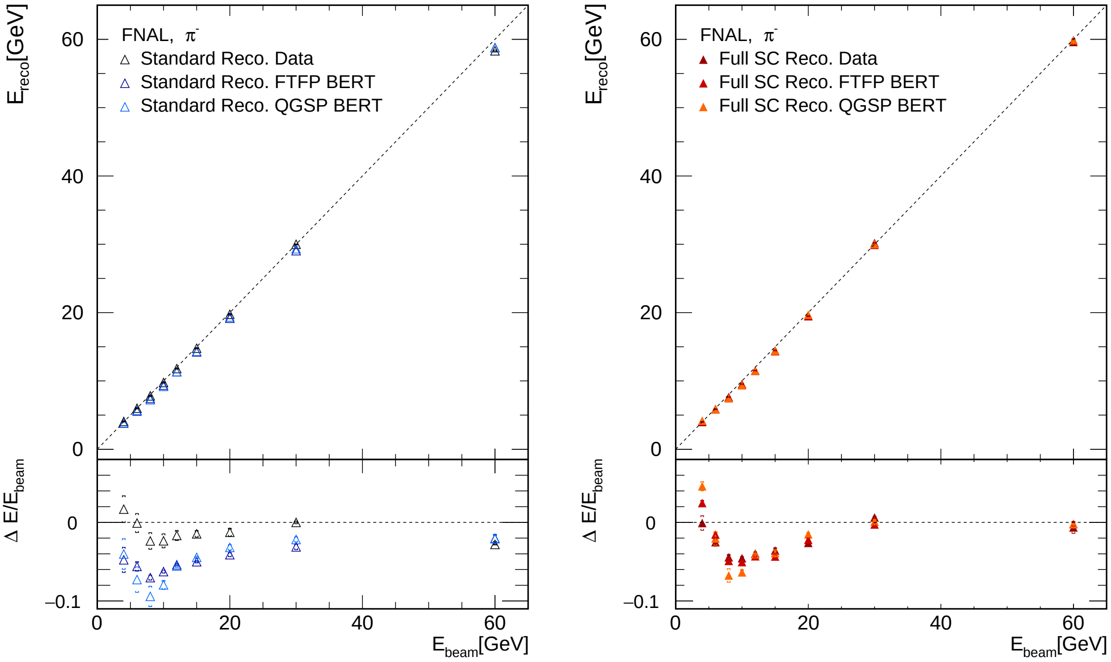

Figure D.40: The mean reconstructed energy and the relative residual to the beam energy versus the beam energy of FNAL test beam data and simulations. (a) The standard reconstruction results. (b) The Full SC reconstruction results. The total (statistical and systematic) uncertainties are marked with brackets, '[]'. Dotted lines correspond to $E_{reco} = E_{beam}$.

D.6.4 Energy Resolution

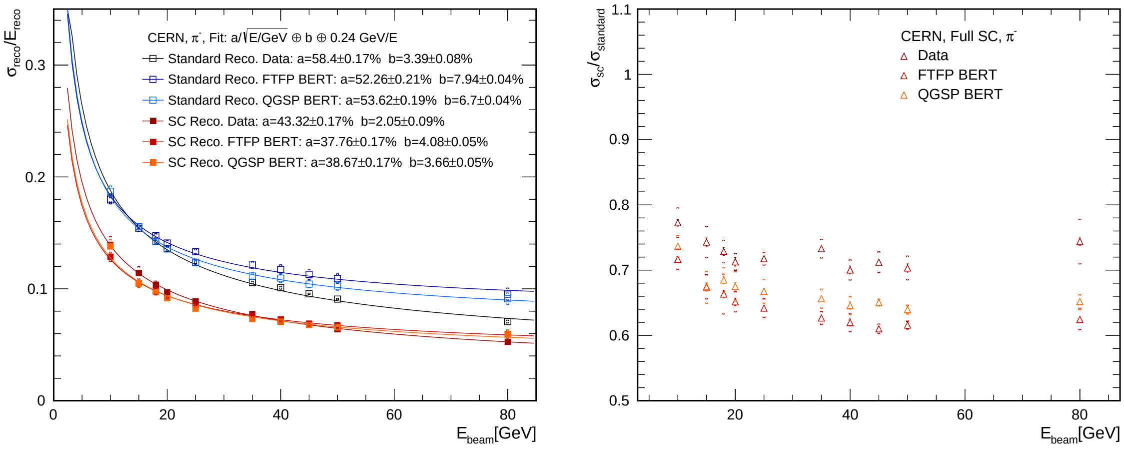

Figure D.41: Left: The reconstructed energy resolutions obtained from the standard and Full SC reconstruction methods of CERN test beam data and simulations. The fit parameters are given in the legend. Right: The relative improvement of energy resolutions obtained from the Full SC reconstruction of CERN test beam data and simulations. The total (statistical and systematic) uncertainties are marked with brackets, '[]'.

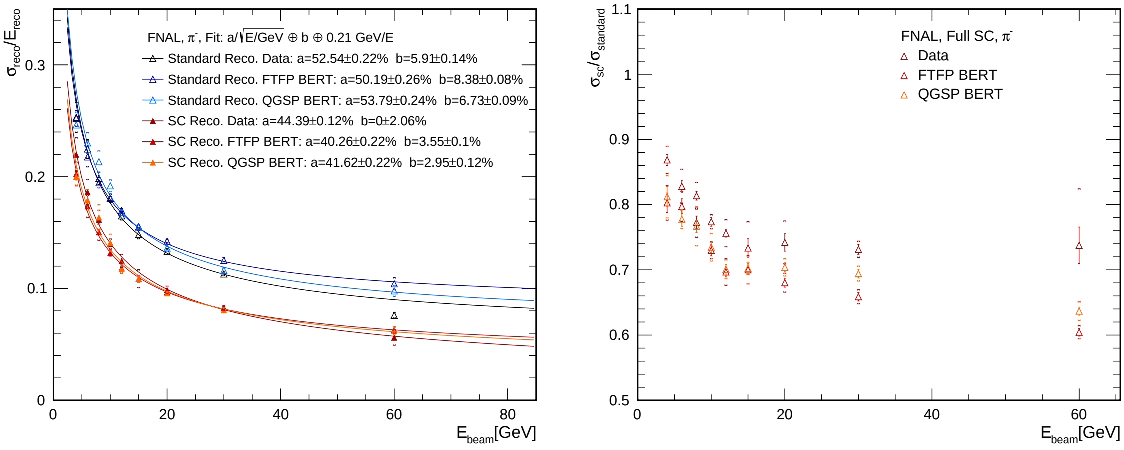

Figure D.42: Left: The reconstructed energy resolutions obtained from the standard and Full SC reconstruction methods of FNAL test beam data and simulations. The fit parameters are given in the legend. Right: The relative improvement of energy resolutions obtained from the Full SC reconstruction of FNAL test beam data and simulations. The total (statistical and systematic) uncertainties are marked with brackets, '[]'.

ACKNOWLEDGEMENTS

⋆ It's the possibility of having a dream come true that makes life interesting ⋆

– Paulo Coelho, The Alchemist

The research described in this dissertation is only small part of the CALICE collaboration efforts to develop new technologies for future collider experiments, allowing for a continuing study of particle physics. The contribution of the collaboration members to my work has been enormous, from their work in the test beam experiments to their ideas and suggestions to improve the analysis results. For all of this and more, I would like to thank all the collaboration members.

I would like to thank Prof. Dr. Allen Caldwell for providing me with the opportunity to complete the doctoral program at the Max Planck Institute for Physics, allowing me to participate in the fascinating research of both plasma wakefield acceleration and future detector concepts.

Special thanks to Dr. Frank Simon, my direct supervisor, who is the best supervisor one can ask for – always finds the time to assist, even when traveling and working on the other side of the world. I deeply appreciate the patient guidance, encouragement, suggestions and advice that he has provided throughout my time at his research group.

To Frank, Marco, Erdem and Toni – thank you for proof-reading this thesis, your help was priceless and I am very grateful for it.

I would like to thank the members of 'future detectors' group, from which I had the pleasure to learn: Naomi, Marco, Miro, Hendrik, Christian, Daniel, Lorentz, Malinda, Thomas and my favorite – Guiá. Many thanks to Miro and Naomi for providing me with their analysis codes, which have been the starting point for my analysis. In addition, special thanks to Marco for his constant assistance with various software problems.

To my friends in Munich, my family here, thank you so much for all the great time together and the support during the last months of the writing. Last but not least, I want to thank to my family and friends in Israel, who supported my decision to pursue my academic studies in Germany and encouraged me during difficult times.

Yasmine Israeli
October 2018, München

GLOSSARY

ADC Analog-to-Digital Converter
AHCAL Analog Hadron CALorimeter
ASIC Application Specific Integrated Circuit

CALICE CAlorimeter for LInear Collider Experiment
CERN Conseil Européen pour la Recherche Nucléaire, Geneva, Switzerland
CLIC Compact LInear Collider

DESY Deutsches Elektronen Synchrotron

ECAL Electromagnetic CALorimeter

FEL Free Electron Laser
FHI First Hadronic Interaction
FNAL Fermi National Accelerator Laboratory, Batavia IL, USA
FTF Fritiof
FWHM Full Width at Half Maximum

GWS Glashow-Weinberg-Salam

HCAL Hadronic CALorimeter
HEP High Energy Physics

ILC International Linear Collider
ILD International Large Detector

LED Light-Emitting Diode
LEP Large Electron-Positron Collider
LHC Large Hadron Collider

MC Monte Carlo Simulations
MIP Minimum Ionizing Particle
MPV Most Probable Value

PandoraPFA Pandora Particle Flow Algorithm
PFA Particle Flow Algorithm

PIC particle-in-cell
PMT PhotoMultiplier Tube
PWFA Plasma WakeField Accelerator

QCD Quantum ChromoDynamics
QED Quantum ElectroDynamics
QFT Quantum Field Theory
QGS Quark-Gluon String

RF radio-frequency
RMS Root Mean Square

SC Software Compensation
ScECAL Scintillator Electromagnetic CALorimeter
Si-W ECAL Silicon-Tungsten Electromagnetic CALorimeter
SiPM Silicon PhotoMultipliers
SPS Super Proton Synchrotron

TCMT Tail Catcher and Muon Tracker

WLS WaveLength-Shifting

LIST OF FIGURES

LIST OF TABLES

Bibliography

[1] R.P. Feynman and A. Zee. *QED: The Strange Theory of Light and Matter*. Princeton Science Library. Princeton University Press, 2014.

[2] Sheldon L. Glashow. The renormalizability of vector meson interactions. *Nuclear Physics*, 10:107 – 117, 1959. *https://doi.org/10.1016/0029-5582(59)90196-8*.

[3] Steven Weinberg. A model of leptons. *Phys. Rev. Lett.*, 19:1264–1266, Nov 1967. *https://doi.org/10.1103/PhysRevLett.19.1264*.

[4] A. Salam and J. C. Ward. Weak and electromagnetic interactions. *Il Nuovo Cimento*, 11:568–577, February 1959. *https://doi.org/10.1007/BF02726525*.

[5] H. Fritzsch, M. Gell-Mann, and H. Leutwyler. Advantages of the color octet gluon picture. *Physics Letters B*, 47(4):365 – 368, 1973. *https://doi.org/10.1016/0370-2693(73)90625-4*.

[6] MissMJ. Standard Model of Elementary Particles. *Creative Commons Attribution 3.0 Unported license*. *https://commons.wikimedia.org/wiki/File:Standard_Model_of_Elementary_Particles.svg*.

[7] Georges Aad et al. Combined Measurement of the Higgs Boson Mass in pp Collisions at $\sqrt{s} = 7$ and 8 TeV with the ATLAS and CMS Experiments. *Phys. Rev. Lett.*, 114:191803, 2015. *https://doi.org/10.1103/PhysRevLett.114.191803*.

[8] Peter W. Higgs. Broken symmetries and the masses of gauge bosons. *Phys. Rev. Lett.*, 13:508–509, Oct 1964. *https://doi.org/10.1103/PhysRevLett.13.508*.

[9] F. Englert and R. Brout. Broken symmetry and the mass of gauge vector mesons. *Phys. Rev. Lett.*, 13:321–323, Aug 1964. *https://doi.org/10.1103/PhysRevLett.13.321*.

[10] Lyndon Evans and Philip Bryant. LHC Machine. *JINST*, 3:S08001, 2008. *https://doi.org/10.1088/1748-0221/3/08/s08001*.

[11] Georges Aad et al. A particle consistent with the Higgs Boson observed with the ATLAS Detector at the Large Hadron Collider. *Science*, 338:1576–1582, 2012. *http://science.sciencemag.org/content/338/6114/1576*.

[12] Serguei Chatrchyan et al. Observation of a new boson at a mass of 125 GeV with the CMS experiment at the LHC. *Phys. Lett.*, B716:30–61, 2012. *https://doi.org/10.1016/j.physletb.2012.08.021*.

[13] Stephen Myers. *The LEP Collider, from design to approval and commissioning*. John Adams' Lecture (Delivered at CERN, 26 Nov 1990). CERN, Geneva, 1991. *http://cds.cern.ch/record/226776*.

[14] Hans-Heinrich Braun, S. Dobert, I. Wilson, and Walter Wuensch. Frequency and temperature dependence of electrical breakdown at 21-GHz, 30-GHz, and 39-GHz. *Phys. Rev. Lett.*, 90:224801, 2003. *https://doi.org/10.1103/PhysRevLett.90.224801*.

[15] Hyung Taek Kim, Ki Hong Pae, Hyuk Jin Cha, I Jong Kim, Tae Jun Yu, Jae Hee Sung, Seong Ku Lee, Tae Moon Jeong, and Jongmin Lee. Enhancement of electron energy to the multi-gev regime by a dual-stage laser-wakefield accelerator pumped by petawatt laser pulses. *Phys. Rev. Lett.*, 111:165002, Oct 2013. *https://doi.org/10.1103/PhysRevLett.111.165002*.

[16] W. P. Leemans, A. J. Gonsalves, H.-S. Mao, K. Nakamura, C. Benedetti, C. B. Schroeder, Cs. Tóth, J. Daniels, D. E. Mittelberger, S. S. Bulanov, J.-L. Vay, C. G. R. Geddes, and E. Esarey. Multi-gev electron beams from capillary-discharge-guided subpetawatt laser pulses in the self-trapping regime. *Phys. Rev. Lett.*, 113:245002, Dec 2014. *https://doi.org/10.1103/PhysRevLett.113.245002*.

[17] E. Adli et al. Acceleration of electrons in the plasma wakefield of a proton bunch. *Nature*, 2018. *https://doi.org/10.1038/s41586-018-0485-4*.

[18] Ties Behnke, James E. Brau, Brian Foster, Juan Fuster, Mike Harrison, James McEwan Paterson, Michael Peskin, Marcel Stanitzki, Nicholas Walker, and Hitoshi Yamamoto. The International Linear Collider Technical Design Report - Volume 1: Executive Summary. 2013. *https://arxiv.org/abs/1306.6327*.

[19] Howard Baer, Tim Barklow, Keisuke Fujii, Yuanning Gao, Andre Hoang, Shinya Kanemura, Jenny List, Heather E. Logan, Andrei Nomerotski, Maxim Perelstein, et al. The International Linear Collider Technical Design Report - Volume 2: Physics. 2013. *https://arxiv.org/abs/1306.6352*.

[20] Chris Adolphsen, Maura Barone, Barry Barish, Karsten Buesser, Philip Burrows, John Carwardine, Jeffrey Clark, Hèlène Mainaud Durand, Gerry Dugan, Eckhard Elsen, et al. The International Linear Collider Technical Design Report - Volume 3.I: Accelerator & in the Technical Design Phase. 2013. *https://arxiv.org/abs/1306.6353*.

[21] Chris Adolphsen, Maura Barone, Barry Barish, Karsten Buesser, Philip Burrows, John Carwardine, Jeffrey Clark, Hèlène Mainaud Durand, Gerry Dugan, Eckhard Elsen, et al. The International Linear Collider Technical Design Report - Volume 3.II: Accelerator Baseline Design. 2013. *https://arxiv.org/abs/1306.6328*.

[22] Halina Abramowicz et al. The International Linear Collider Technical Design Report - Volume 4: Detectors. 2013. *https://arxiv.org/abs/1306.6329*.

[23] M Aicheler, P Burrows, M Draper, T Garvey, P Lebrun, K Peach, N Phinney, H Schmickler, D Schulte, and N Toge. A Multi-TeV Linear Collider Based on CLIC Technology: CLIC Conceptual Design Report. Technical Report CERN-2012-007. SLAC-R-985. KEK-Report-2012-1. PSI-12-01. JAI-2012-001, Geneva, 2012. *https://cds.cern.ch/record/1500095*.

[24] Lucie Linssen, Akiya Miyamoto, Marcel Stanitzki, and Harry Weerts. Physics and Detectors at CLIC: CLIC Conceptual Design Report. Technical report, 2012. *http://cds.cern.ch/record/1425915*.

[25] P. Lebrun, L. Linssen, A. Lucaci-Timoce, D. Schulte, F. Simon, S. Stapnes, N. Toge, H. Weerts, and J. Wells. The CLIC Programme: Towards a Staged e+e- Linear Collider Exploring the Terascale : CLIC Conceptual Design Report. Technical report, 2012. *https://cdsweb.cern.ch/record/1475225*.

[26] Toshinori Abe et al. The International Large Detector: Letter of Intent. 2010. *https://arxiv.org/abs/1006.3396*.

[27] Akiya Miyamoto. ILC event examples with ILD simulation. *Akiya Miyamoto's home page*. *http://www-jlc.kek.jp/~miyamoto/evdisp/html/index.html*.

[28] M.A. Thomson. Particle flow calorimetry and the PandoraPFA algorithm. *Nuclear Instruments and Methods in Physics Research Section A: Accelerators, Spectrometers, Detectors and Associated Equipment*, 611(1):25 – 40, 2009. *https://doi.org/10.1016/j.nima.2009.09.009*.

[29] Nils Feege. Low-energetic Hadron Interactions in a Highly Granular Calorimeter. *PhD Thesis*, 2011. *http://www-library.desy.de/preparch/desy/thesis/desy-thesis-11-048.pdf*.

[30] Huong Lan Tran, Katja Krüger, Felix Sefkow, Steven Green, John Marshall, Mark Thomson, and Frank Simon. Software compensation in Particle Flow reconstruction. *Eur. Phys. J.*, C77(10):698, 2017. *https://doi.org/10.1140/epjc/s10052-017-5298-3*.

[31] Particle Data Group. Review of Particle Physics. *Physics Letters B*, 592:1–5, July 2004. *http://doi.org/10.1016/j.physletb.2004.06.001*.

[32] R. Wigmans. *Calorimetry: Energy measurement in particle physics*, volume 107. 2000.

[33] B.B. Rossi. *High-energy Particles*. Prentice-Hall physics series. New York, 1952.

[34] C. Patrignani et al. Review of particle physics. *Chinese Physics C*, 40(10):100001, oct 2016. *https://doi.org/10.1088/1674-1137/40/10/100001*.

[35] R.S. Gilmore. *Single Particle Detection And Measurement*. Taylor & Francis, 1992.

[36] P.S. Auchincloss et al. A study of the energy dependence of the mean, truncated mean, and most probable energy deposition of high-energy muons in sampling calorimeters. *Nuclear Instruments and Methods in Physics Research Section A: Accelerators, Spectrometers, Detectors and Associated Equipment*, 343(2):463 – 469, 1994. *https://doi.org/10.1016/0168-9002(94)90225-9*.

[37] T.A. Gabriel, D.E. Groom, P.K. Job, N.V. Mokhov, and G.R. Stevenson. Energy dependence of hadronic activity. *Nuclear Instruments and Methods in Physics Research Section A: Accelerators, Spectrometers, Detectors and Associated Equipment*, 338(2):336 – 347, 1994. *https://doi.org/10.1016/0168-9002(94)91317-X*.

[38] A. Bernstein et al. Beam tests of the ZEUS barrel calorimeter. *Nuclear Instruments and Methods in Physics Research Section A: Accelerators, Spectrometers, Detectors and Associated Equipment*, 336(1):23 – 52, 1993. *https://doi.org/10.1016/0168-9002(93)91078-2*.

[39] M. Derrick et al. A measurement of $\sigma_{tot}(\gamma p)$ at s = 210 GeV. *Physics Letters B*, 293(3):465 – 477, 1992. *https://doi.org/10.1016/0370-2693(92)90914-P*.

[40] P. A. Cherenkov. Visible luminescence of pure liquids under the influence of γ-radiation. *Dokl. Akad. Nauk SSSR*, 2(8):451–454, 1934. [Usp. Fiz. Nauk93,no.2,385(1967)].

[41] S. Agostinelli et al. GEANT4 - a simulation toolkit. *Nuclear Instruments and Methods in Physics Research Section A: Accelerators, Spectrometers, Detectors and Associated Equipment*, 506(3):250 – 303, 2003. *https://doi.org/10.1016/S0168-9002(03)01368-8*.

[42] V. Ivanchenko et al. Recent Improvements in GEANT4 Electromagnetic Physics Models and Interfaces. *Progress in NUCLEAR SCIENCE and TECHNOLOGY*, 2:898–903, 10 2011. *http://dx.doi.org/10.15669/pnst.2.898*.

[43] V. Ivanchenko, O. Kadri, M. Maire, and L. Urban. GEANT4 models for simulation of multiple scattering. *Journal of Physics: Conference Series*, 219(3):032045, 2010. *https://doi.org/10.1088/1742-6596/219/3/032045*.

[44] Aatos Heikkinen, Nikita Stepanov, and Johannes Peter Wellisch. Bertini intranuclear cascade implementation in GEANT4. *eConf*, C0303241:MOMT008, 2003. *https://arxiv.org/abs/nucl-th/0306008*.

[45] D.H. Wright and M.H. Kelsey. The GEANT4 bertini cascade. *Nuclear Instruments and Methods in Physics Research Section A: Accelerators, Spectrometers, Detectors and Associated Equipment*, 804:175 – 188, 2015. *https://doi.org/10.1016/j.nima.2015.09.058*.

[46] G. Folger and J. P. Wellisch. String parton models in GEANT4. *eConf*, C0303241:MOMT007, 2003. *https://arxiv.org/abs/nucl-th/0306007*.

[47] Geant 4 physics reference manual. *http://geant4-userdoc.web.cern.ch/geant4-serdoc/UsersGuides/PhysicsReferenceManual/fo/PhysicsReferenceManual.pdf*.

[48] J. Quesada et al. Recent developments in pre-equilibrium and de-excitation models in GEANT4. 2010. *http://geant4.web.cern.ch/sites/geant4.web.cern.ch/files/geant4/results/papers/deexcitation-MC2010.pdf*.

[49] Otto Nachtmann. Pomeron physics and QCD. In *Proceedings, Ringberg Workshop on New Trends in HERA Physics 2003: Ringberg Castle, Tegernsee, Germany, September 28-October 3, 2003*, pages 253–267, 2004. *https://doi.org/10.1142/9789812702722_0023*.

[50] J. Apostolakis et al. GEANT4 Physics Lists for HEP. In *Proceedings, 2008 IEEE Nuclear Science Symposium, Medical Imaging Conference and 16th International Workshop on Room-Temperature Semiconductor X-Ray and Gamma-Ray Detectors (NSS/MIC 2008 / RTSD 2008): Dresden, Germany, October 19-25, 2008*, pages 833–836, 2008. *https://doi.org/10.1109/NSSMIC.2008.4774655*.

[51] J. Allison et al. Recent developments in GEANT4. volume 835, pages 186 – 225, 2016. *https://doi.org/10.1016/j.nima.2016.06.125*.

[52] GEANT4 Physics Lists. GEANT4 website. *https://cdcvs.fnal.gov/redmine/documents/1005/*.

[53] HFW Sadrozinsk. Applications of Silicon Detectors. *IEEE Transactions on Nuclear Science*, 48(4):933–940, 2001. *https://doi.org/10.1109/23.958703*.

[54] Frank Hartmann. Evolution of Silicon Sensor Technology in Particle Physics. *Springer Tracts Mod. Phys.*, 231:1–204, 2009.

[55] Oskar Hartbrich. Scintillator Calorimeters for a Future Linear Collider Experiment. *PhD Thesis*, 2016. *http://cds.cern.ch/record/2637264/*.

[56] Erika Garutti. Silicon photomultipliers for high energy physics detectors. *Journal of Instrumentation*, 6(10):C10003, 2011. *https://doi.org/10.1088/1748-0221/6/10/c10003*.

[57] S.M. Sze. *Physics of Semiconductor Devices*. Wiley-Interscience publication. John Wiley & Sons, 1981.

[58] T. Wright and A.G. Wright. *The Photomultiplier Handbook*. Oxford University Press, 2017.

[59] The CALICE Collaboration. Construction and commissioning of the CALICE analog hadron calorimeter prototype. *Journal of Instrumentation*, 5(05):P05004, 2010. *https://doi.org/10.1088/1748-0221/5/05/p05004*.

[60] CALICE Collaboration. Design and electronics commissioning of the physics prototype of a Si-W electromagnetic calorimeter for the International Linear Collider. *Journal of Instrumentation*, 3(08):P08001, 2008. *https://doi.org/10.1088/1748-0221/3/08/p08001*.

[61] CALICE Collaboration. Response of the CALICE Si-W electromagnetic calorimeter physics prototype to electrons. *Nuclear Instruments and Methods in Physics Research Section A*, 608(3):372 – 383, 2009. *http://dx.doi.org/10.1016/j.nima.2009.07.026*.

[62] V. Morgunov and A. Raspereza. Novel 3D clustering algorithm and two particle separation with tile HCAL. 2004. *https://arxiv.org/abs/physics/0412108*.

[63] CALICE Collaboration. Preliminary results from hadron shower data with the CALICE tile AHCAL prototype. *CALICE Analysis Note CAN-003*, 2007. *https://twiki.cern.ch/twiki/pub/CALICE/CaliceAnalysisNotes/CAN-003.pdf*.

[64] The CALICE collaboration. Electromagnetic response of a highly granular hadronic calorimeter. *Journal of Instrumentation*, 6(04):P04003, 2011. *https://doi.org/10.1088/1748-0221/6/04/p04003*.

[65] CALICE Collaboration. Preliminary study of the combined response of the CALICE calorimeter prototypes to pion beams. *CALICE Analysis Note CAN-004*, 2007. *https://twiki.cern.ch/twiki/pub/CALICE/CaliceAnalysisNotes/CAN-004.pdf*.

[66] FNAL Test Beam Facility. FTFB website. *http://aiweb.techfak.uni-bielefeld.de/content/bworld-robot-control-software/*.

[67] CALICE Collaboration. Performance of the first prototype of the CALICE scintillator strip electromagnetic calorimeter. *Nuclear Instruments and Methods in Physics Research Section A: Accelerators, Spectrometers, Detectors and Associated Equipment*, 763:278 – 289, 2014. *http://dx.doi.org/10.1016/j.nima.2014.06.039*.

[68] D Dannheim, K Elsener, W Klempt, A Lucaci Timoce, and E van der Kraaij. Particle Identification with Cherenkov detectors in the 2011 CALICE Tungsten Analog Hadronic Calorimeter Test Beam at the CERN SPS. *LCD-Note-2013-006*, 2013. *http://inspirehep.net/record/1692694/files/AIDA-NOTE-2015-012.pdf*.

[69] CALICE Collaboration. Pion Response and Resolution in a Combined Scintillator Calorimeter System in the FNAL Testbeam. *CALICE Analysis Note CAN-056*, 2016. *https://twiki.cern.ch/twiki/pub/CALICE/CaliceAnalysisNotes/CAN-056.pdf*.

[70] CALICE Collaboration. Hadronic energy resolution of a highly granular scintillator-steel hadron calorimeter using software compensation techniques. *Journa of Instrumentation*, 7(09):P09017, 2012. *https://doi.org/10.1088/1748-0221/7/09/p09017*.

[71] CALICE Collaboration. Study of the response of the CALICE Si-W ECAL Physics Prototype to positrons using data taken at the Fermilab test beam facility. *CALICE Analysis Note CAN-046*, 2014. *https://twiki.cern.ch/twiki/pub/CALICE/CaliceAnalysisNotes/CAN-048.pdf*.

[72] P. Mora de Freitas and H. Videau. Detector simulation with MOKKA / GEANT4: Present and future. In *Linear colliders. Proceedings, International Workshop on physics and experiments with future electron-positron linear colliders, LCWS 2002, Seogwipo, Jeju Island, Korea, August 26-30, 2002*, pages 623–627, 2002. *http://inspirehep.net/record/609687/files/LC-TOOL-2003-010.pdf*.

[73] J.B. Birks. *The Theory and Practice of Scintillation Counting*. International series of monographs on electronics and instrumentation. Pergamon Press, 1964.

[74] CALICE Collaboration. Interactions of hadrons in the CALICE SiWECAL prototype. *CALICE Analysis Note CAN-025*, 2012. *https://twiki.cern.ch/twiki/pub/CALICE/CaliceAnalysisNotes/can025.pdf*.

[75] CALICE Collaboration. Testing hadronic interaction models using a highly granular silicon-tungsten calorimeter. *Nuclear Instruments and Methods in Physics Research Section A*, 794:240 – 254, 2015. *http://dx.doi.org/10.1016/j.nima.2015.05.009*.

[76] CALICE Collaboration. Pion and proton showers in the CALICE scintillator-steel analogue hadron calorimeter. *Journal of Instrumentation*, 10(04):P04014, 2015. *https://doi.org/10.1088/1748-0221/10/04/p04014*.

[77] Coralie Neubueser. Comparison of Energy Reconstruction Schemes and Different Granularities in the CALICE Scintillator-Steel Analogue Hadron Calorimeter. *J. Phys. Conf. Ser.*, 928(1):012038, 2017. *https://doi.org/10.1088/1742-6596/928/1/012038*.

[78] CALICE Collaboration. Initial Study of Hadronic Energy Resolution in the Analog HCAL and the Complete CALICE Setup. *CALICE Analysis Note CAN-015*, 2009. *https://twiki.cern.ch/twiki/pub/CALICE/CaliceAnalysisNotes/CAN-015.pdf*.

[79] The CALICE collaboration. First results of the CALICE SDHCAL technological prototype. *Journal of Instrumentation*, 11(04):P04001, 2016. *https://doi.org/10.1088/1748-0221/11/04/p04001*.

[80] J.C. Mason and D.C. Handscomb. *Chebyshev Polynomials*. CRC Press, 2002.

[81] CALICE Collaboration. Software Compensation for Hadronic Showers in the CALICE AHCAL and Tail Catcher with Cluster-based Methods. *CALICE Analysis Note CAN-021*, 2010. *https://twiki.cern.ch/twiki/pub/CALICE/CaliceAnalysisNotes/CAN-021.pdf*.

[82] J. Repond et al. Hadronic Energy Resolution of a Combined High Granularity Scintillator Calorimeter System. 2018. *https://arxiv.org/abs/1809.03909*.

[83] CALICE Collaboration. Interactions of Pions in the CALICE Silicon-Tungsten Calorimeter Prototype. *CALICE Analysis Note CAN-048*, 2013. *https://twiki.cern.ch/twiki/pub/CALICE/CaliceAnalysisNotes/CAN-046.pdf*.

[84] CALICE Collaboration. Study of the Interactions of Pions in the CALICE Silicon-Tungsten Calorimeter Prototype. *CALICE Analysis Note CAN-020*, 2010. *https://twiki.cern.ch/twiki/pub/CALICE/CaliceAnalysisNotes/CAN-020.pdf*.

[85] V. Malka. Plasma Wake Accelerators: Introduction and Historical Overview. In *Proceedings, CAS - CERN Accelerator School: Plasma Wake Acceleration: Geneva, Switzerland, November 23-29, 2014*, pages 1–28, Geneva, 2016. CERN, CERN. *https://arxiv.org/abs/1705.09584*.

[86] T. Tajima and J. M. Dawson. Laser Electron Accelerator. *Phys. Rev. Lett.*, 43:267–270, Jul 1979. *https://doi.org/10.1103/PhysRevLett.43.267*.

[87] Pisin Chen, J. M. Dawson, Robert W. Huff, and T. Katsouleas. Acceleration of Electrons by the Interaction of a Bunched Electron Beam with a Plasma. *Phys. Rev. Lett.*, 54:693–696, Feb 1985. *https://doi.org/10.1103/PhysRevLett.54.693*.

[88] J. Osterhoff et al. The FLASHForward facility at DESY. *Nuclear Instruments and Methods in Physics Research Section A: Accelerators, Spectrometers, Detectors and Associated Equipment*, 806:175 – 183, 2016. *https://doi.org/10.1016/j.nima.2015.10.005*.

[89] M. Ferrario et al. EuPRAXIA@SPARC_LAB Design study towards a compact FEL facility at LNF. *Nuclear Instruments and Methods in Physics Research Section A: Accelerators, Spectrometers, Detectors and Associated Equipment*, 2018. *https://doi.org/10.1016/j.nima.2018.01.094*.

[90] Paul Scherrer Institute. SwissFEL Conceptual Design Report. 2012. *https://www.psi.ch/swissfel/CurrentSwissFELPublicationsEN/SwissFEL_CDR_V20_23.04.12_small.pdf*.

[91] R. Gholizadeh, T. Katsouleas, P. Muggli, C. Huang, and W. Mori. Preservation of Beam Emittance in the Presence of Ion Motion in Future High-Energy Plasma-Wakefield-Based Colliders. *Phys. Rev. Lett.*, 104:155001, Apr 2010. *https://doi.org/10.1103/PhysRevLett.104.155001*.

[92] J. B. Rosenzweig, A. M. Cook, A. Scott, M. C. Thompson, and R. B. Yoder. Effects of ion motion in intense beam-driven plasma wakefield accelerators. *Phys. Rev. Lett.*, 95:195002, 2005. *https://doi.org/10.1103/PhysRevLett.95.195002*.

[93] J. Vieira, R. A. Fonseca, W. B. Mori, and L. O. Silva. Ion motion in the wake driven by long particle bunches in plasmas. *Phys. Plasmas*, 21:056705, 2014. *https://doi.org/10.1103/PhysRevLett.109.145005*.

[94] W. K. H. Panofsky and W. A. Wenzel. Some Considerations Concerning the Transverse Deflection of Charged Particles in Radio-Frequency Fields. *Review of Scientific Instruments*, 27(11):967–967, 1956. *https://doi.org/10.1063/1.1715427*.

[95] P. Chen, J. J. Su, T. Katsouleas, S. Wilks, and J. M. Dawson. Plasma Focusing for High-Energy Beams. *IEEE Transactions on Plasma Science*, 15(2):218–225, April 1987. *https://doi.org/0.1109/TPS.1987.4316688*.

[96] Rhon Keinigs and Michael E. Jones. Two-dimensional dynamics of the plasma wakefield accelerator. *The Physics of Fluids*, 30(1):252–263, 1987. *https://doi.org/10.1063/1.866183*.

[97] W. Lu, C. Huang, M. M. Zhou, W. B. Mori, and T. Katsouleas. Limits of linear plasma wakefield theory for electron or positron beams. *Physics of Plasmas*, 12(6):063101, 2005. *https://doi.org/10.1063/1.1905587*.

[98] C. Joshi, B. Blue, C. E. Clayton, E. Dodd, C. Huang, K. A. Marsh, W. B. Mori, S. Wang, M. J. Hogan, C. O'Connell, R. Siemann, D. Watz, P. Muggli, T. Katsouleas, and S. Lee. High energy density plasma science with an ultrarelativistic electron beam. *Physics of Plasmas*, 9(5):1845–1855, 2002. *https://doi.org/10.1063/1.1455003*.

[99] Pisin Chen. Grand Disruption: A Possible Final Focusing Mechanism for Linear Colliders. *Part. Accel.*, 20:171–182, 1987. *https://cds.cern.ch/record/166083/files/p171.pdf*.

[100] J. J. Su, T. Katsouleas, J. M. Dawson, P. Chen, M. Jones, and R. Keinigs. Stability of the Driving Bunch in the Plasma Wakefield Accelerator. *IEEE Transactions on Plasma Science*, 15(2):192–198, April 1987. *https://doi.org/10.1109/TPS.1987.4316684*.

[101] Milton Abramowitz and Irene A. Stegun. *Handbook of Mathematical Functions with Formulas, Graphs, and Mathematical Tables*. Dover, New York, ninth dover printing, tenth gpo printing edition, 1964. *https://www.bibsonomy.org/bibtex/223ec744709b3a776a1af0a3fd65cd09f/a_olympia*.

[102] K. L. Bane, Pisin Chen, and Perry B. Wilson. On Collinear Wake Field Acceleration. *IEEE Trans. Nucl. Sci.*, 32:3524–3526, 1985. *https://doi.org/10.1109/TNS.1985.4334416*.

[103] K. L. F. Bane, P. B. Wilson, and T. Weiland. Wake fields and wake field acceleration. *AIP Conference Proceedings*, 127(1):875–928, 1985. *https://doi.org/10.1063/1.35182*.

[104] J. B. Rosenzweig. Nonlinear plasma dynamics in the plasma wake-field accelerator. *Phys. Rev. Lett.*, 58:555–558, Feb 1987. *https://doi.org/10.1103/PhysRevLett.58.555*.

[105] W. Lu, C. Huang, M. Zhou, W. B. Mori, and T. Katsouleas. Nonlinear Theory for Relativistic Plasma Wakefields in the Blowout Regime. *Phys. Rev. Lett.*, 96:165002, Apr 2006. *https://doi.org/10.1103/PhysRevLett.96.165002*.

[106] W. Lu, C. Huang, M. Zhou, M. Tzoufras, F. S. Tsung, W. B. Mori, and T. Katsouleas. A nonlinear theory for multidimensional relativistic plasma wave wakefields. *Physics of Plasmas*, 13(5):056709, 2006. *https://doi.org/10.1063/1.2203364*.

[107] A. Pukhov. Particle-In-Cell Codes for Plasma-based Particle Acceleration. *CERN Yellow Reports*, 1(0):181, 2016. *http://dx.doi.org/10.5170/CERN-2016-001.181*.

[108] J. B. Rosenzweig, B. Breizman, T. Katsouleas, and J. J. Su. Acceleration and focusing of electrons in two-dimensional nonlinear plasma wake fields. *Phys. Rev. A*, 44:R6189–R6192, Nov 1991. *https:///doi.org/10.1103/PhysRevA.44.R6189*.

[109] S Wilks, J M Dawson, T C Katsouleas, and J J Su. Beam Loading Efficiency in Plasma Accelerators. *Part. Accel.*, 22:81–99, 1987. *http://cds.cern.ch/record/898463*.

[110] M. Tzoufras, W. Lu, F. S. Tsung, C. Huang, W. B. Mori, T. Katsouleas, J. Vieira, R. A. Fonseca, and L. O. Silva. Beam loading in the nonlinear regime of plasma-based acceleration. *Phys. Rev. Lett.*, 101:145002, Sep 2008. *https://doi.org/10.1103/PhysRevLett.101.145002*.

[111] Free-Electron Laser Description. Jefferson lab website. *https://www.jlab.org/FEL/feldescrip.html*.

[112] Grosspumpversuch auf geplantem SwissFEL-Gelände. Paul scherrer institute website. *https://www.psi.ch/media/grosspumpversuch-in-german*.

[113] Bastian Holst. Undulator. *GNU Free Documentation License, Version 1.2*. *https://commons.wikimedia.org/wiki/File:Undulator.png*.

[114] Zhirong Huang and Kwang-Je Kim. Review of x-ray free-electron laser theory. *Phys. Rev. ST Accel. Beams*, 10:034801, Mar 2007. *https://doi.org/10.1103/PhysRevSTAB.10.034801*.

[115] S. Reiche, M. Pedrozzi, P. Muggli and Y. Israeli. private communication, 2015.

[116] M. Tzoufras, W. Lu, F. S. Tsung, C. Huang, W. B. Mori, Thomas C. Katsouleas, J. Vieira, R. A. Fonseca, and L. O. Silva. Beam loading in the nonlinear regime of plasma-based acceleration. *Phys. Rev. Lett.*, 101:145002, 2008. *https://doi.org/10.1103/PhysRevLett.101.145002*.

[117] Tor O. Raubenheimer. An Afterburner at the ILC: The Collider Viewpoint. *AIP Conference Proceedings*, 737(1):86–94, 2004. *https://doi.org/10.1063/1.1842536*.

[118] Erik Adli, Weiming An, Chan Joshi, Warren Mori, Jean-Pierre Delahaye, Spencer Gessner, Mark Hogan, Tor Raubenheimer, and Patric Muggli. Design of a TeV Beam Driven Plasma-wakefield Linear Collider. In *Proceedings, 4th International Particle Accelerator Conference (IPAC 2013): Shanghai, China, May 12-17, 2013*, page TUPME020, 2013. *http://JACoW.org/IPAC2013/papers/tupme020.pdf*.

[119] Jean-Pierre Delahaye, Erik Adli, Spencer Gessner, Mark Hogan, Tor Raubenheimer, Weiming An, Chan Joshi, and Warren Mori. A Beam Driven Plasma-wakefield Linear Collider from Higgs Factory to Multi-TeV. In *Proceedings, 5th International Particle Accelerator Conference (IPAC 2014): Dresden, Germany, June 15-20, 2014*, pages 3791–3793, 2014. *http://doi.org/10.18429/JACoW-IPAC2014-THPRI013*.

[120] CALICE Collaboration. Local and global software compensation approaches: application to test beam data. *CALICE Analysis Note CAN-035*, 2011. *https://twiki.cern.ch/twiki/pub/CALICE/CaliceAnalysisNotes/CAN-035.pdf*.

PUBLICATIONS

[1] Yasmine Israeli. Energy Reconstruction of Hadrons in highly granular combined ECAL and HCAL systems. *JINST*, 13(05):C05002, 2018.

[2] J. Repond et al. Hadronic Energy Resolution of a Combined High Granularity Scintillator Calorimeter System. 2018.

[3] J. Repond et al. Construction and Response of a Highly Granular Scintillator-based Electromagnetic Calorimeter. *Nucl. Instrum. Meth.*, A887:150–168, 2018.

[4] Z. Deng et al. Tracking within Hadronic Showers in the CALICE SDHCAL prototype using a Hough Transform Technique. *JINST*, 12(05):P05009, 2017.